Development and Performance Investigation of Parabolic Trough Solar Collector and Latent Heat Storage Units for Indoor Cooking Application

A

Thesis submitted

for the award of the degree of

DOCTOR OF PHILOSOPHY

By

BERIHU GEBREYOHANNES ABREHA

CENTER FOR ENERGY

INDIAN INSTITUTE OF TECHNOLOGY GUWAHATI

GUWAHATI-781039, ASSAM, INDIA

MAY 2021

Declaration

I certify that

a. The work contained in this thesis is original, and has been done by myself under the general supervision of my supervisors.
b. The work has not been submitted to any other institute for any degree or diploma.
c. Whenever I have used materials (data, theoretical analysis, results) from other sources, I have given due credit to them by citing it in the text of the thesis and giving their details in the references.
d. Whenever I have quoted written materials from other sources, I have put them under quotation marks and given due credit to the sources by citing them and giving required details in the references.

Place: I.I.T Guwahati

Date: ***12-06-2021***

Berihu Gebreyohannes Abreha
Research Scholar
Centre for Energy
Indian Institute of Technology Guwahati,
Guwahati 781039, Assam INDIA

CERTIFICATE

This is to certify that the work contained in the thesis entitled **Development and Performance Investigation of Parabolic Trough Solar Collector and Latent Heat Storage Units for Indoor Cooking Application** by **Berihu Gebreyohannes Abreha**, a student of the **Center for Energy** Indian Institute of Technology Guwahati, for the award of the degree of **Doctor of Philosophy** has been carried out under our supervision and that thesis has not been submitted elsewhere for any degree or diploma.

Gaurav Trivedi

Dr. Gaurav Trivedi
Associate Professor
Department of Electronics & Electrical Engineering
Indian Institute of Technology Guwahati
Guwahati-781039, Assam, INDIA

Mahanta

Prof. Pinakeswar Mahanta
Department of Mechanical Engineering
Indian Institute of Technology Guwahati
Guwahati-781039, Assam, INDIA

Acknowledgements

First and foremost, I would like I express my sincere gratitude to my supervisors Dr. Gaurav Trivedi and Prof. Pinakeswar Mahanta for their valuable guidance, constructive comments, motivation and support during my research work. I am thankful particularly to Dr. Gaurav Trivedi for providing research facilities and financial support for the construction of the experimental setups.

I would like to express my sincere gratitude to my Doctoral Committee members, Prof. Harshal B. Nemade, Prof. Vinayak Kulkarni and Dr. Pankaj Kalita for their valuable suggestions and encouragement during the period of my research work.

I am very much grateful to Mr. Dhiren Huzuri for his support by giving data logger and pyranometer for the experiment. I am grateful to all the faculty and supporting staff members at The Center for Energy for creating a friendly and helpful environment.

Since my research work required a lot of effort in the fabrication of the experimental setups, it would not have been so easy without the help of many people. I am very much thankful Mr. Gakul Das, Mr. Dilip Chetri, Mr. Gwmchar Baro, Mr. Jiten Basumatary, Mr. Gautam Gogoi, Mr. Santush Gogoi, Mr. Dipak Kr. Deka, Mr. Saiffuddin Ahmed, Mr. Minesh Ch. Mr. Medhi, Monoj Kr. Mr. Baishya, Mr. Mrinal Sarma, and Mr. Ganesh Nath for their constant help during the development of the experimental setup in the Central workshop of Mechanical Engineering Department, IIT Guwahati.

I would also like to thank Mr. Purna Chetri for his help during the materials purchase from the local market, development and practical test of the experimental setups.

Finally, my deepest gratitude goes to my family and my wife for their continuous love and support. Particularly, I would like to acknowledge the love and support given to me by my wife, who is my source of inspiration and strength.

Place: I.I.T Guwahati
Date: **Berihu Gebreyohannes Abreha**

Abstract

Renewable energy resources like solar and wind energy are intermittent in nature. Combining two or more renewable energy systems could improve the stability and reliability of power output significantly. Moreover, the efficiency of multi-energy generation system can be enhanced, if it is coupled with thermal energy storage (TES) system. Those hybrid energy generation systems can be used for various applications, such as, direct electricity generation and thermal energy production for cooking and space heating. The main objective of the present study is to design, develop and investigate the thermal performance of a suitable indoor solar hybrid cooking system using thermal energy storage materials. In order to achieve the intended goal, a PTSC and LHS units are designed and fabricated. The thermal performances of both systems are investigated experimentally and numerically. Furthermore, a hybrid PTSC and LHS system is proposed for solar cooking application and lab-scale experimental setup are coupled to test the performance of the hybrid system.

The performance of the fabricated PTSC system is investigated experimentally, analytically and numerically. The important parameters for all the methods are inlet temperature, beam radiation, mass flow rate. First, the thermal performance of PTSC is evaluated analytically by varying important parameters. The result indicates that the efficiency and useful heat decrease while inlet temperature increases keeping other parameters constant. On the other hand, the thermal efficiency is increased along with mass flow rate and solar radiations. Besides, the effect of the nanofluids on the thermal performance of PTSC is investigated numerically. The performance comparison study is conducted employing 5% Al_2O_3 nanoparticles and pure cooking waste oil (CWO). However, addition of nano-particles into the base fluid brought insignificant difference. Moreover, the performance PTSC based on cooking waste oil (CWO) HTF is compared with the Syltherm 800 (S-800). It is observed that the performance PTSC is better when CWO was used as a working fluid.

In the numerical study, extremely non-uniform temperature distribution along the bottom and top surface of the receiver pipe are observed due to variable heat flux input. The temperature profile also increases along flow direction from inlet to exit as expected. The experimental results indicate that the thermal performances of PTSC are better in the month of June as compare to October in the north east region of India. The maximum HTF outlet temperature recorded are 110.7 ^{0}C and 108 ^{0}C on June 15 and 22, respectively. Similarly, the maximum HTF outlet temperature recorded on October 13 and 18 are 89.9 ^{0}C and 86.8 ^{0}C, respectively. It is to mention that the analytical, numerical and experimental results are found in the good agreement.

Similarly, an experimental and numerical study of the lab-scale LHS unit is conducted. Erythritol ($C_4H_{10}O_4$) and cooking waste oil are employed as PCM and HTF, respectively. The performance of the LHS unit is tested experimentally during the charging process, whereas, both charging and discharging characteristics of the storage unit are studied during the numerical study. The performance of LHS is investigated with the help of charging time, liquid fraction, average transient temperature and stored energy parameters. During the charging process, both numerical as well as experimental tests are conducted at HTF volume flow rate of 75 LPM at 138 ^{0}C. For the discharging process, HTF inlet temperature is chosen to be at 87 ^{0}C keeping the volume flow rate same as that of the charging process. The optimal number of tubes and fins are decided after multiple investigations of different LHS models.

The effect of operating parameters on the performance of the storage unit is examined using both experimental and numerical analyses. The impact of the non-uniform flow rate of HTF on the melting of PCM is studied using three flow rates at the same inlet temperature. Similarly, for the constant volume flow rate, the study is performed at three different HTF inlet temperatures. It is observed that an increase in the flow rate of HTF and inlet temperature enhances the heat transferring rate of PCM and minimizes the charging time of the LHS unit. The experimental outcome of the storage unit is validated along with numerical results. The numerical analysis results exhibit very good similarity with the experimental data exhibiting a maximum deviation of 6.0%. The total time consumed in the complete melting and solidification of PCM inside LHS is estimated to be 175 min and 156 min, respectively. During the melting of PCM, the sensible heat, latent heat and total energy stored in LHS are found to be 9.3 MJ, 17.74 MJ and 27.03 MJ,

respectively. Similarly, the sensible heat, latent heat and total energy released during the solidification process are 4 MJ 17.6MJ and 21.6 MJ, respectively.

A comparison study of LHS unit with and without nanoparticles enhancement is also performed. Due to their stable thermal properties and availability, two different nanoparticles known as Al_2O_3 and CuO are considered for this study. In terms of the melting time of PCM, the immersions of nanoparticles into PCM bring considerable improvement. However, the thermal performance difference between the above mentioned LHS models based on the selected nanoparticles is insignificant. The reduction in melting time achieved by dispersing nanoparticles is about 4.6% as compared to the pure PCM, whereas, the stored energy of the pure PCM is higher than nano-PCM. On the other hand, the energy storage capacity of the storage unit is reduced by 23% when nanoparticles are included in PCM.

A hybrid lab-scale PTSC and auxiliary source of energy are proposed to power LHS developed for indoor cooking purposes. The experimental investigations of the coupled PTSC and LHS units, and the numerical investigation of the proposed LHS unit powered by PTSC and auxiliary energy source are evaluated. First, the performance of the LHS unit is examined using PTSC as a heat source, where the energy from the sun is generated in the receiver tube. The experimental test is conducted on a sunny day starting from 9:30 PM local time. The results indicate that the heat adding to the storage unit keeps increasing with solar radiation until 14:30. As the solar radiation intensity keeps falling down, the rate of heat generation in the absorber tube is also reduced. At 14:00, the average temperature of the LHS is 88 ^{0}C. Although the experimental test is conducted for more than five hours, the PTSC does not collect enough solar radiance for the complete charging of LHS. Therefore, an auxiliary energy source is required for the complete melting of PCM.

Numerical analysis of LHS powered by hybrid PTSC and auxiliary energy source is conducted for the estimation of its dynamic behavior. The rate of heat addition to the storage unit after 14:00 is minimal. The highest temperature (88 ^{0}C) achieved during the charging of LHS through PTSC alone is considered as a reference temperature of the numerical study of the solar hybrid system proposed for cooking application. The results indicate that the conduction heat transfer mechanism is dominant at the beginning of the charging process. It is observed that from 20 min – 70 min of charging time, the rate of temperature variation is almost steady.

Contents

Lists of Tables

Lists of Figures

Nomenclature

Notation

A_{Mush}	Mushy zone constant (Kg m^3s^{-1})
C_p	Heat capacity (J kg^{-1} K^{-1})
Q	Heat (J)
F	Body force (N m^{-3})
g	Acceleration due to gravity (m s^{-2})
L	Latent heat of fusion (J kg^{-1})
k	Thermal conductivity (W m^{-1} K^{-1})
P	Pressure (Pa)
S	Darcy law's source term
T	Temperature (K)
T_M	Phase change temperature (K)
V	Velocity (ms^{-1})
ΔH	Fusion latent heat (Jkg^{-1})
h	Specific enthalpy($kJkg^{-1}$)
$\bar{H}_o$	The daily monthly averages of extraterrestrial global solar radiation on a horizontal surface
I_o	Extera-terrestrial beam normal irradiance on a day in kW/m^2
I_s	Solar constant
N	Day of the year
K_T	Stochastic measure of these atmospheric effects
H_{tc}	Global solar insolation with atmospheric effects
E_{cap}	Energy storage capacity
$E_{req.}$	Total amount of energy required
A_c	Effective rea of the collector
a	Concentrator aperture
L	Concentrator length
D_{ro}	Receiver tube outer diameter

D_{ri}	Receiver tube inner diameter
(D_{go})	Glass envelope outer diameter
(D_{gi})	Glass envelope inner diameter
A_c	Collector area
CR	Concentration ratio
A_{ro}	Receiver outer surface area
$\dot{m}$	Mass flow rate
f	Focal length
$E_{sto.}$	Energy to be stored in the LHS
Q_u	Useful heat
Q_{loss}	Thermal losses
Q_u	Useful heat production
Q_{abs}	Solar irradiation absorbed
Q_s	Available solar irradiation
Q_{abs}	Absorbed solar energy
A_p	Aperture area
I_b	Direct beam radiation
$K(\theta)$	Incident angle modifier
F'	Collector efficiency factor
U_L	Overall loss coefficient
$h_{con,gco-amb}$	Convection HTC between the glass cover and ambient
$h_{rad,gco-sky}$	Radiation HTC between glass and the ambient
$h_{con,ab-HTF}$	Convection HTC between the absorber tube and HTF
$h_{cond,abo-abi}$	Conduction HTC between the outer and inner surface of the absorber tube
$h_{rad,abo-gci}$	Radiation HTC between outer surface of tube and inner surface of glass cover
$h_{con,abo-gci}$	Convection HTC between outer surface of tube and inner surface of glass cover
$h_{cond,gci-gco}$	Conduction HTC between inner and outer surface of the glass cover
D_g	Cover (glass) diameter
$h_{r,r-g}$	Radiation HTC between absorber tube and glass cover
T_g	Temperature of the glass

T_r	Temperature of the receiver
D_{ro}	Outer diameter of the receiver tube
U_O	Overall heat transfer coefficient
Nu	Nusselt number
Pr	Prandtl number
Re	Reynolds number
F_R	Heat removal factor of solar collector
F'	Collector efficiency factor
h_f	Heat transfer coefficient (HTC) to the fluid
η_{th}	Thermal efficiency
A_r,	Receiver pipe area, , and, respectively
A_a	Aperture area
T_{in}	Inlet fluid temperature
T_{out}	Exit fluid temperature
T_{am}	Ambient temperature
T_{fm}	Mean fluid temperature
S_{te}	Stefan number ()
f	Number of experimental data points
T_{exp}	Experimental transient temperature
T_{ave}	Average value of the multiple experimental temperatures
$\in_{abs}$	Absolute error
$\in_{exp}$	Experimental error
Q_{sen}	Stored sensible heat
Q_{lat}	Latent heat
Q_{tot}	Total heat stored
$Q_{sen,D}$	Released sensible heat
$Q_{lat,D}$	Released latent heat
$Q_{tot,D}$	Released total heat
S	Radiation heat flux
m	Mass of the storage material

Greek symbols

β	Thermal expansion coefficient (1/K)
ρ	Density (kg/m^3)
μ	Dynamic viscosity (Ns/m^2)
θ	Melt fraction
φ	Volume fraction of nanoparticles
ρ_{nf}	Density of nanoparticles
k_{nf}	Thermal conductivity of nanoparticles
c_{p-nf}	Specific heat capacity of nanoparticles
μ_{nf}	Dynamic viscosity of nanoparticles
ε_g	Emittance of glass
ε_r	Emittance of receiver
δ	Stefan Boltzman constant
ρ_a	Density
υ_a	Velocity
μ_a	Viscosity of air
θ_i	Incident angle
τ	Glass cover transmittivity for solar radiation
ρ	Specular reflectivity of the concentrator surface
α	Absorber tube emissivity/absorptivity
γ	Intercept factor
φ_r	Rim angle
η_{opt}	solar collector optical efficiency
ω	Hour angle
δ	Declination angel
φ	Latitude of the location
φ	Latitude of the location

Subscripts

Mush	Mushy zone constant (Kg $m^{-3}s^{-1}$)
ini	Initial
l	Liquid
s	Solid
C	Charging
D	Discharging
sen	Sensible
lat	Latent
tot	Total
ref	Reference
ave	Average
a	Air

Acronyms

LPM	Liter per minute
HTF	Heat transferring fluid
LHS	Latent heat storage
TES	Thermal energy storage
CWO	Cooking waste oil

Chapter -1

1 Introduction

1.1 Preface

Energy is a thermodynamic quantity that has the capability of doing work. It cannot be created and can be transformed from one form into another. We need energy to perform a job, to cook food and to move. As we know, cooking is one of the main requirements for all people because every human being has to take food for a living. In developing countries, the majority of the energy produced is consumed in cooking the food [1]. Generally, energy is an important resource that plays an imperative role in the economic development of every nation [2]. Due to rapid urbanization, population growth and economic development in undeveloped nations, the energy requirement is growing rapidly [3]. The majority of the current energy demand globally is supplied by non-renewable energy resources, such as coal, natural gas and crude oil. The predominantly dependence on non-renewable energy sources is closely connected with greenhouse gas emissions and climate change. This has created an immediate urge to transform the energy sector, mainly, from non-renewable to renewable sources and to use energy-efficient technologies. The world has faced big challenges due to the above-mentioned problems and using renewable energy sources is an effective strategic solution.

As shown in Fig.1.1 renewable energy resources have huge potential to fulfill the global energy demand. In addition, Fig.1.1 indicates that solar energy possesses the highest available green energy content. Solar energy has gained further attention due to the constant rise of greenhouse gas emissions and the rise in fuel prices. Solar energy has a high potential to meet global vital energy requirements, predominantly in developing nations. Usually, solar energy is used for cooking, water heating, space heating, air conditioning and drying purposes. Currently, solar

energy is employed in a modern standalone power generation system and coupled with other alternative sources of energy.

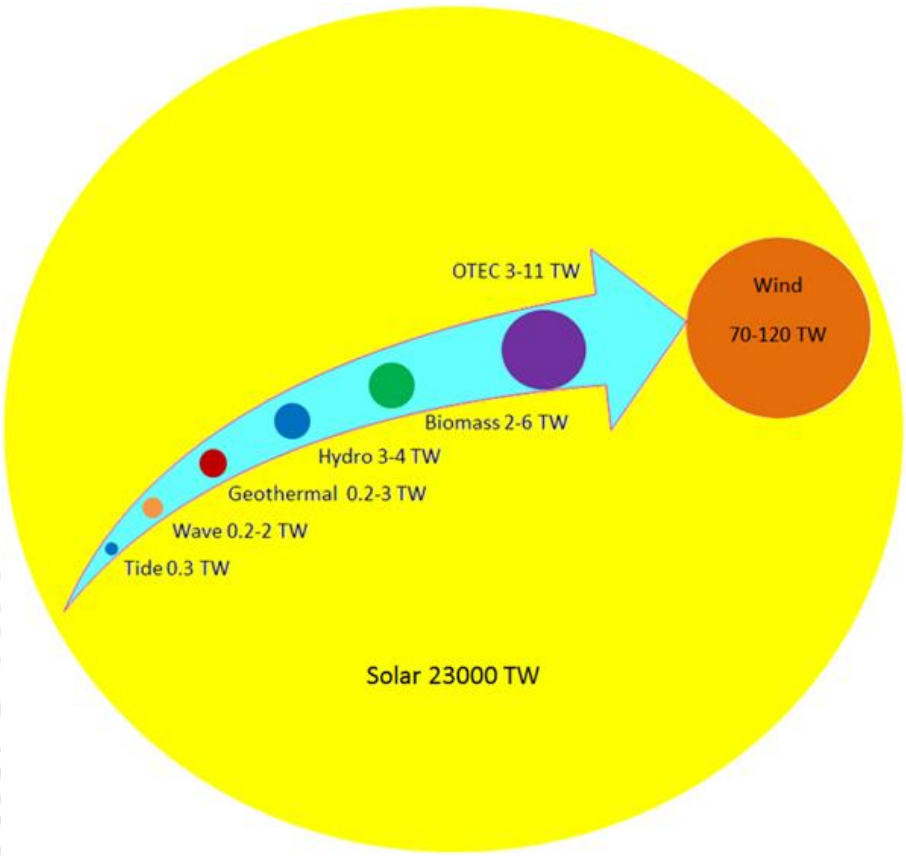

Fig. 1.1.Global potential for renewable energy resources [4]

In the modern era, solar energy can be converted into electrical energy by two methods, viz. directly using PV cells and indirectly by solar thermal systems employing concentrated solar collectors. In the direct solar energy conversion to electricity method, the photovoltaic converts sunlight into an electric current due to the photovoltaic effect. In the case of indirect conversion of solar energy to electricity, solar radiation is converted into thermal energy inside the boiler or receiver. Reflective mirrors and tracking systems are employed to focus the dispersed solar radiation into the receiver or boiler. The reflectors are designed with high quality and concentration ratios to generate huge energy that is enough to heat the working fluid. For the other thermal energy applications, for example, solar cooking, the thermal energy is directly utilized. Commonly, water or other synthetic oils are used as working fluid to convey the heat generated from the receiver or boiler into a desired place. However, solar energy is also suffered from inherent disadvantages due to its intermittent nature and non-uniform availability throughout the year. The mismatch

between demand and energy generation can be solved by coupling the solar collector unit with thermal energy storage (TES) systems. The section below, details about the different types of solar collectors and TES technologies.

1.2 Solar Collector

A solar collector is a device or medium, which is designed and developed to harvest the diluted solar radiation into a useful energy form. The solar radiation fall on the absorber surface is converted into heat for use directly or ultimately transferred into the working fluid or heat transferring fluid (HTF). In general, water, synthetic oil or air is used as a heat transferring fluid (HTF) of the system [4]. As we know, solar collectors are divided into two broad groups as non-tracking and tracking collectors [5]. The latter types of collectors are developed to follow the movement of the sun; as a result, the solar radiations and collectors are always normal to each other. On the other hand, non-tracking collectors are designed to be stationary regardless of the motion of the sun across the sky, which means they are kept at a fixed position. Furthermore, tracking solar collectors are categorized as single and dual axes tracking systems. As shown in Fig.1.2, the linear Fresnel reflector, parabolic trough solar collector (PTSC) and cylindrical trough collector are under the former classification. On the other hand, the parabolic dish reflector, circular Fresnel lens and central tower receiver fall under the category of dual axes tracking systems. The non-tracking solar collectors are also classified as evacuated tube, flat plate and compound parabolic solar collectors [6].

1.3 Solar Cookers

When the solar collector is used for cooking application by incorporating some important components, it is said to be a solar cooker. Amongst the different share of energy consumptions, energy for cooking purposes is the fundamental one and is being used majorly in most of the developing nations. Collecting solar energy requires an efficient and cost-effective type of solar collector. Several types of solar are available all around the world. The classification of solar cookers is a difficult task since there are multiple designs of solar cookers are employed worldwide. Based on the heat transfer mechanism to the cooking unit, solar cookers can be grouped into direct and indirect solar cookers. Additionally, solar cookers are also classified as with and without storage depending on the presence of energy storage. Fig.1.3 illustrates the classification of solar cookers and the difference among them is presented in the next sections.

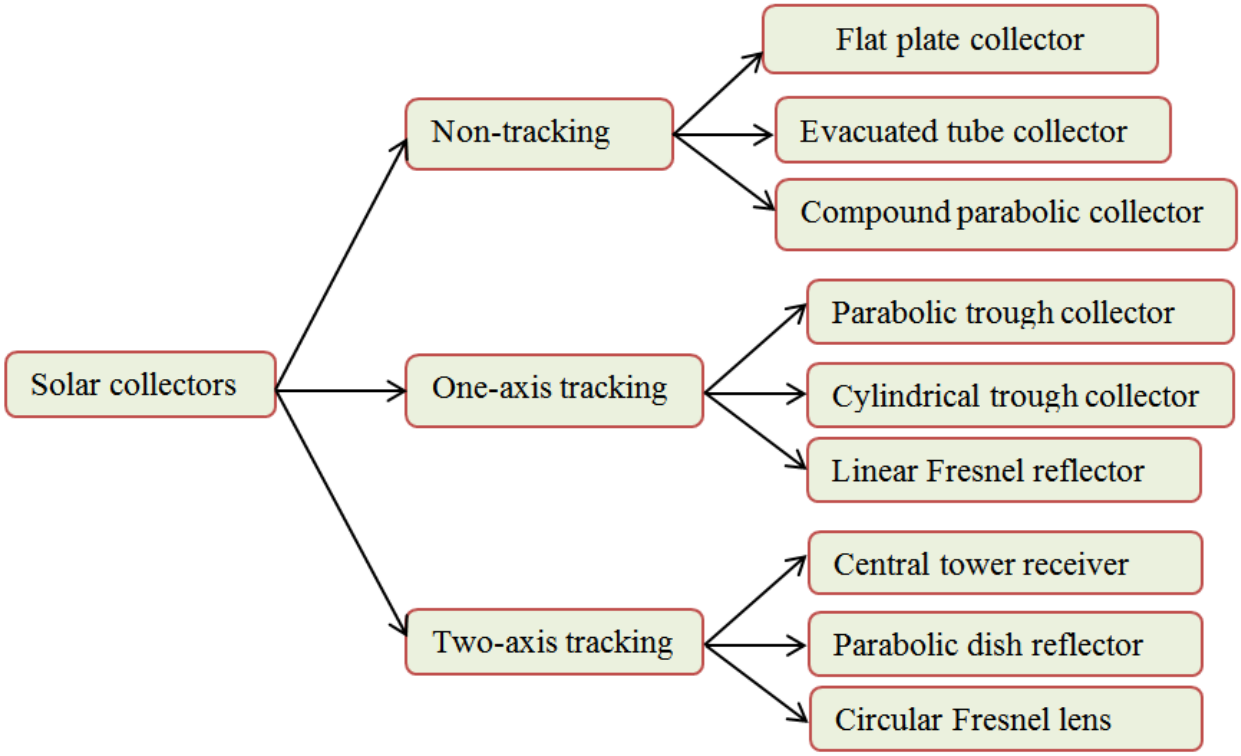

Fig. 1.2.Classification of solar collectors [7]

1.3.1 Direct type of solar cookers

In the case of direct types of solar cookers, solar radiation is directly applied to the cooking device. The solar cookers that commonly fall under this category are box type and concentrating solar cookers. Direct types of solar cookers are easily fabricated from low-cost materials; as a result, they are the most commonly used systems in general [7].

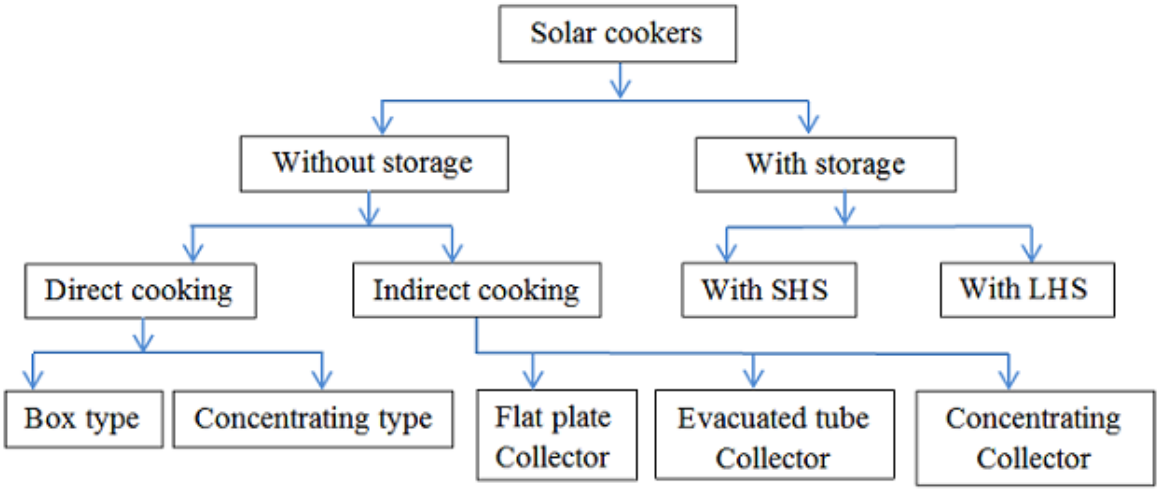

Fig. 1.3.Types of solar cookers [8]

1.3.1.1 Box type cooker

The box solar cooker is a container covered with either glass or plastic cover and the cover may be multiple or single. Similarly, the box types of solar cookers are considered the commonly available devices since they are simple in construction from easily available and low-cost materials. Due to the greenhouse effect, solar radiation arriving on to the cooker through transparent cover converts into thermal energy in the absorber plate. The black-colored absorber plate is placed to absorb the incoming solar energy and to transfer the heat energy into the cooking vessel. The box-type cooker is thermally insulated for minimal heat loss to the surrounding environment so that the better efficiency is obtained. [7],[8].

The advantage of a box-type solar cooker is simple, cheap, robust and simple to operate. These types of solar cookers are also more stable and they can maintain food staff warm for a long period. Box cookers are used to cook the food without danger of burning and flavors remain intact whether they are used for grilling, roasting, and [7].

Cooking using a box-type cooker has to be carried out outdoor and the slow cooking process due to low temperatures happens in sunlight for a long time. During intermittent solar radiation, the food remains partially cooked, therefore, it gets wasted. In the case of this type of cooker, there is no regulator over the rate of cooking. Even with the support of booster mirrors, box-type solar cookers have a low temperature up to 100 ^{0}C [8].

1.3.1.2 Concentrating type of solar cookers

Concentrating type cookers are capable of producing heat at a higher temperature and can be effectively used for different applications. These cookers primarily consist of a reflector to focus the incident solar irradiance on the cooking unit, a rotary system to keep the solar reflector facing toward the sun and cooking unit. The concentrating solar cooker is effective if it is built with a one or two-axis tracking system. The concentration ratio and temperature of these types of collectors reach up to 50 ^{0}C and 300 ^{0}C, respectively, which are suitable for cooking. The concentrating type of solar cooker is made from many-sided mirrors, parabolic concentrators or Fresnel lenses to achieve higher temperatures [5], [7].

The advantages of concentrating cookers consist of high cooking temperatures, capable of cooking any type of food within a short period of time. The drawbacks of concentrating cookers include high cost, the danger of fires and burns, and difficulty of handling and rotate the cookers as they require repeated directional rotation to track the sun and the food needs constant supervision [7].

1.3.2 Indirect type of solar cookers

In the case of indirect type solar cookers, heat transferring fluid (HTF) is employed to convey heat energy from solar collectors to physically displaced cooking devices [9]. This type of solar collector comprises of a central pipe containing a working fluid that is heated while it passes through the collector. The pipe is in turn connected with an insulated cooking unit that is kept inside the house or kitchen. Indirect solar cookers provide high thermal energy and temperatures even without following the sun and allow cooking in the shade. Commercially available cookers, such as flat plate collectors, evacuated tube collectors, and concentrating type collectors are placed under this group.

1.3.2.1 Flat-plate solar cooker

Flat-plate solar collectors are widely investigated systems in the scientific world for drying, space heating, water heating, and other applications. The solar radiation falls on an observer surface which is painted black. The heat generated by this cooker is transferred for the desired purpose using water or other types of liquid. The primary parts of the flat-plate solar collector are an absorber plate commonly made up of highly conductive metals; a transparent covering surface that passes solar radiation but protects heat losses, HTF internal channels and a structure that is used to contain other components [5], [10]. Cooking a large volume of foods within a short period of time inside the kitchen and regulation of heat flow in the pots are the advantages of this type of cooker. On the other hand, the flat-plate solar collector suffers from the problems of poor performance because of the reversed cycle during the absence of solar radiation. The primary drawback of this cooking device is due to the fixed pots, which is difficult for cleaning and dishing food.

1.3.2.2 Evacuated tube solar cooker

Evacuated tube type of solar collector system comprises of an evacuated tubular container with another pipe or tube filled partially with working fluid and coupled together with a heat exchanger via piping. The key component of the evacuated solar collector technology is the glass envelope, which is used to maintain a vacuum space between tubes and glass. The evacuated glass tubes are assembled in parallel. The outer part of the evacuated tube is transparent while the internal tube is coated with a selective material coating to maximize absorption of the incoming solar radiation [4]. Heat pipes are very suitable for this application since they transfer heat effectively from the solar collector to the hot plate with minimal temperature decrease [5]. The working fluid inside

these tubes heated up when the solar radiation reaches onto the evacuated tubes. As a result, the vaporized fluid rises direct toward the heat exchanger and transmits thermal energy. Evacuated tube types of solar collectors have more advantages as compared with concentrators or box type cookers. An evacuated solar cooking system delivers high temperatures thermal energy without tracking sun and capable for indoor cooking [7],[11].

1.3.2.3 Concentrating solar cookers

In the case of concentrating-type solar cookers, either spherical or parabolic shape is employed to concentrate the scattered solar radiation. A receiver that is connected with a heat exchanger through piping is provided on the focus line or point of the collector. Parabolic trough solar collector (PTSC) is the most mature solar energy harvesting device used for medium and hight temeperature delivery for various application besides to the good efficiency. The PTSC is a linear concentrating technolgy having a concentration ratio from 10 to 50 [12]. The HTF flowing inside the piping conveys energy from the receiver to the heat exchanger or cooking device.

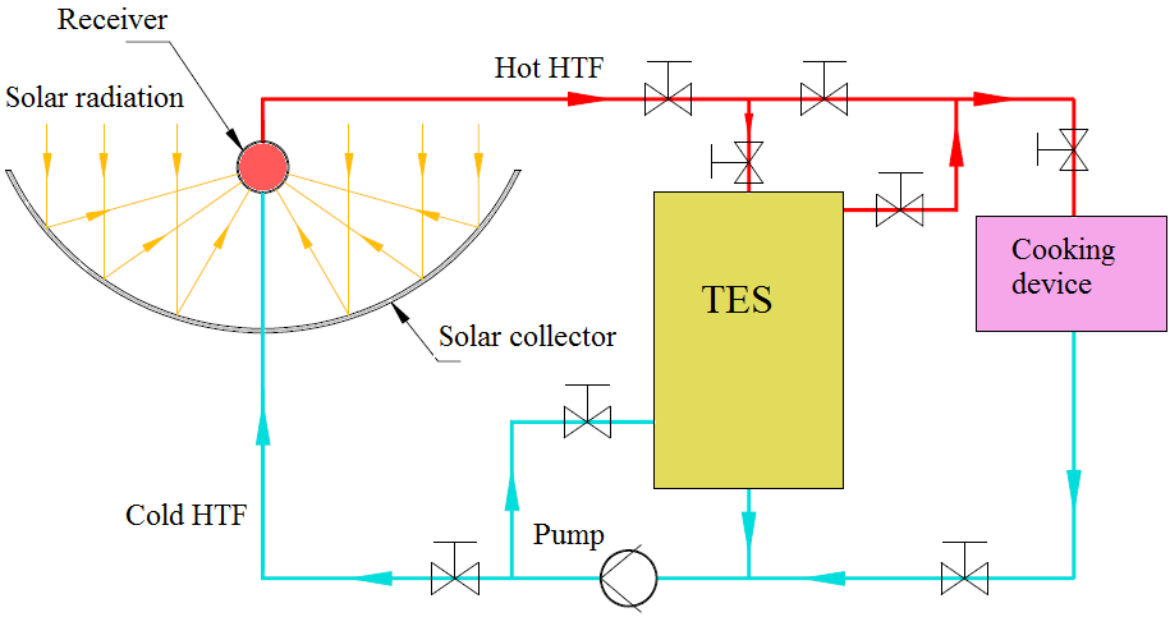

Fig. 1.4.Circuit diagram of solar and TES hybrid cooking device

1.3.3 Solar cookers with heat energy storage

The main problem of different types of many solar cookers is the incapability of cooking food in the absence of solar radiation or late evening hours and cooking outdoor efficiently. This problem can be improved by employing thermal energy storage (TES), and indoor cooking during the off

sun hours is possible [9]. Fig.1.4 illustrates a PTSC cooker coupled with TES. Thus, TES is fundamentally needed to increase the efficiency and reliability of cookers. There are three methods of storing thermal energy, viz. in the form of sensible heat, latent heat and in the form of heat of a reversible thermochemical reaction [13]. The details of these energy storage technologies are presented in the following section.

1.4 Thermal energy storage (TES)

Storing thermal energy is an important activity in several engineering processes. For instance, amongst the practical problems involved in the production of solar energy, there is a need for an effective technique by which the surplus heat energy collected during the sunshine period can be stored. Therefore, the preserved energy is released for utilization during the absence of solar radiation or late evening. There are several kinds of commercially available energy storage systems [14]. An efficient TES technology is required for heat recovery, utilization of solar energy and seasonal energy storage. TES systems are more helpful to bridge the mismatch between generation and energy consumption. Moreover, TES systems are capable of increasing the effective use of thermal energy equipment and can drive large scale switching easily. Any storable form of energy is stored in mechanical, electrical and thermal energy forms. The energy stored in the form of gravitational energy or pumped hydropower, compressed air and flywheels are mechanical energy storage systems. Electrical energy can be stored in batteries, where a reversible chemical reaction takes place. The TES stores heat as a change in the internal energy of a material as sensible heat, latent heat and reversible thermochemical reaction [13]. Hence, TES technologies can be classified into three kinds (see Fig.1.5): sensible heat storage (SHS), latent heat storage (LHS), and chemical heat storage (CHS).

The solar cookers should be built with heat storage material to store thermal energy for indoor cooking purposes and to cook food at any time of the day regardless of the clouds coverage during sunshine or at the night time [7],[15]. The characteristics of the three types of TES technologies are described in the following sections.

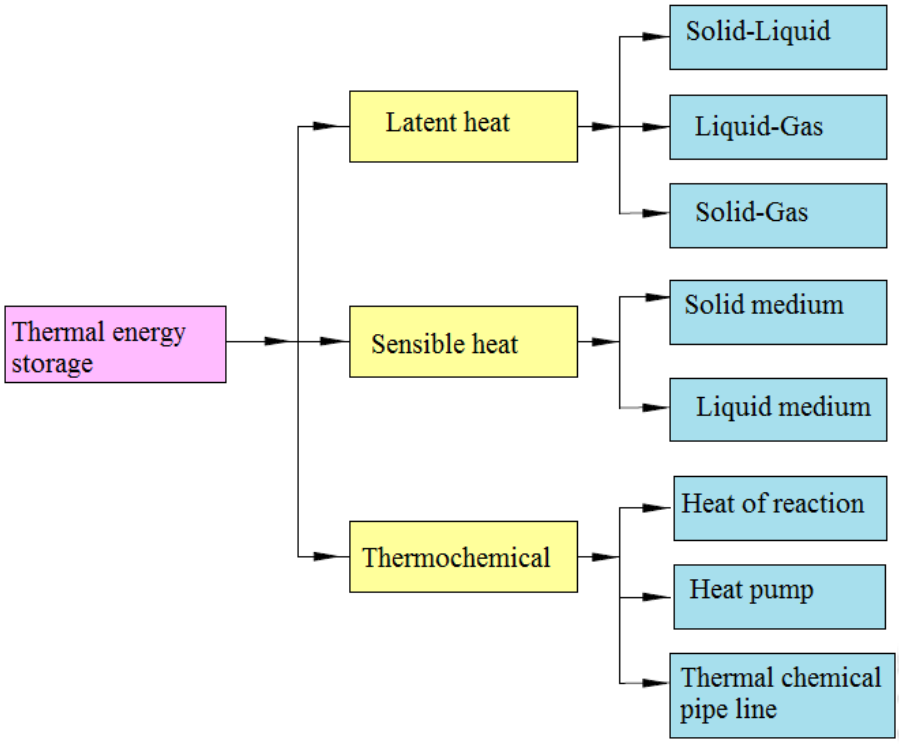

Fig. 1.5.Classification of thermal energy storage systems

1.4.1 Sensible heat storage

In the case of sensible heat storage (SHS), the energy is getting stored when the temperature of substances is kept rising. SHS can also store energy due to the density and specific heat of the storage material during the heat addition and releasing process. Hence, the quantity of heat energy getting stored depends on the thermal properties, mass and changes in the temperature of the medium. In general, the sensible heat storage materials should be chemically stable, easily available, low cost, and safe for operation. Rocks, iron, oil or water are common sensible heat storage materials [13]. The total amount of energy stored in the medium can be described as mentioned below.

$$Q = \int_{T_1}^{T_2} mc_p dT \ [J] \qquad (1.1)$$

where, Q, m, C_p T_1 and T_2 are the total amount of energy stored, mass, specific heat, initial temperature and final temperatures of the medium, respectively.

Sensible TES systems comprise a storage medium, a container (tank) and inlet/outlet devices. The tank must be robust and well insulated to preserve storage material and prevent thermal energy

losses. Hence, the properties of storage media, such as, high specific heat capacity, long term stability after repeated thermal cycling, compatibility with its container and low cost are primary desirable characteristics of the sensible storage medium. Based on the heat storage media, SHS can be classified as solid and liquid media storage depending on the type of material used for energy storage. [14].

1.4.1.1 Liquid media storage

Energy can be stored in liquid materials heat storage. It is to mention that most of the liquids are abundant and economically affordable. Water is one of the best storage media for low-temperature applications. Water obtains higher specific heat property than other liquid materials; furthermore, it is cheap in price and naturally abundant. For high-temperature applications, it requires costly insulation materials and pressure resisting container because of its high vapor pressure [14].

Underground natural aquifers have been preferred for large scale energy storage applications. Aquifers are geological formations that contain groundwater and can be offered a potential way of preserving heat energy for long periods. The storage capacity of the aquifer medium can range from hundreds to millions of cubic meters. For example, 105 m^3 of aquifer substances can store around 3 MJ of thermal energy for the change of 10 K temperature in each step [16].

Molten salts and petroleum-based oils are commonly used materials to replace water. But, the heat capacities of such materials are less than water. On the other hand, these alternatives materials have lower vapor pressure as compared to water and they are suitable for high-temperature operations [14]. Therminol and Caloria-HT are known as effective candidates of SHS oil materials. The working temperature of the oil is less than 350 ^{0}C because of stability and safety reasons [17]. For high temperatures application, molten mixtures of inorganic salts have been used. For instance, sodium hydroxide can store thermal energy up to 800 ^{0}C [14]. Liquid metals are also own high potential of SHS media. Most of the properties of liquid metal, petroleum-based oils and water are similar. However, liquid metals have low specific heat and a higher possibility of chemical reaction with its containment. On the other hand, the media possesses better thermal conductivity [14].

1.4.1.2 Solid media storage

Solid materials like metals, rocks, bricks and sand can be utilized for low as well as high-temperature thermal energy storage. The advantage of storing energy as sensible heat in solids materials can avoid the high vapor pressure problem of water and other limitations of liquids

substances. Cast iron has been considered as an effective SHS media among the list of solid materials. The cost of cast iron is expensive, due to this, rock piles or pebble beds are commonly used storage materials [14].

1.4.2 Chemical heat storage (CHS)

In CHS, thermal energy is stored by means of chemical reactions. The CHS systems depend on the amount of energy absorbed and released during the breaking and forming of molecular bonds in the reversible chemical reaction. The total heat energy stored in the medium depends on the endothermic heat of reaction, the volume of storage material and the degree of conversion [13]. The capability of storing energy for a long period, higher energy storage density and higher heat pumping rate are the common advantages of CHS systems. The total heat getting stored is given by the equation defined as per Eq. (1.2).

$$Q_r = A_r m \Delta h_r \tag{1.2}$$

where, m, A_r and h_r are the mass of heat storage, fraction reacted in medium and endothermic heat reaction, respectively.

1.4.3 Latent Heat Storage

Latent heat storage (LHS) preserves thermal energy during the phase transition of certain materials from solid state to liquid, solid state to gas and liquid state to gas or vice versa. The LHS materials are commonly known as phase change materials (PCMs) [15], [18]. In contrast to sensible storage materials, PCM charges and discharges heat at a constant temperature. PCM has the potential of storing 5–14 times more heat per unit volume than sensible storage materials like water, masonry, or rock [13], [19]. Although a number of PCMs can be melted due to the heat of fusion, some of them are utilized as an energy storage medium. For their utilization as LHS material, these substances must have certain necessary thermal, kinetic and chemical properties [20], [21]. The heat energy storage potential of a given storage media is explained by Eq. (1.3).

$$Q = \int_{T_1}^{T_m} mc_p dT + mH + \int_{T_m}^{T_2} mc_p dT \tag{1.3}$$

where, H is Heat of fusion per unit mass [J/kg].

Generally, the LHS system provides maximum energy storage density and has the capability to preserve heat as latent heat of fusion at a nearly constant temperature during phase transition temperature of PCMs. Due to these properties, LHS is preferred frequently [20].

A number of studies of TES based on the PCM have been reported. As it can be seen in Fig. 1.6, PCMs can be categorized based on organic and inorganic compounds. The former types of PCM include paraffin waxes, acids, esters and alcohols, whereas, materials that include salt hydrates inorganic salts inorganic metals and their eutectics are categorized under inorganic materials [13], [19]. Usually, organic compounds made from PCMs obtain a low melting point (T_m) and, can only be applied for room heating and low-temperature thermal storage systems. Molten salts are selected commonly for high-temperature thermal storage applications [22].

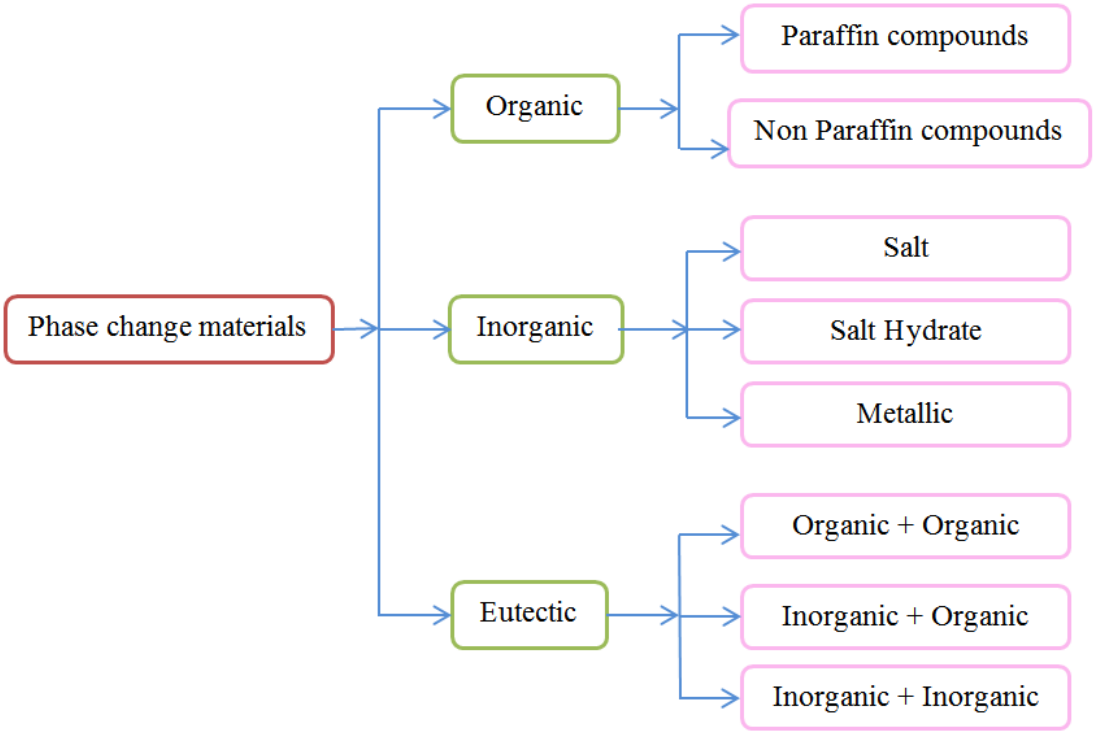

Fig. 1.6.Classification of PCMs [10]

From the perspective of melting temperature and latent heat of fusion properties, many organic and inorganic chemical materials can be identified as PCM. However, apart from the melting point property, the majority of PCMs do not fulfill the necessary criteria for appropriate energy storage media. For an ideal thermal storage media, there is not even a single material that fulfills all the required properties. The primary practical problems include poor thermal conductivity, density

variation, instability of properties under multiple cycling, phase segregation and sub-cooling of PCM [13].

1.4.4 Organic PCMs

Organic PCMs have a high latent heat capacity and are non-reactive with containment. These PCMs do not undertake phase segregation and supercooling with melt as well as solidification cycles and have better nucleation property. However, Organic PCMs have low phase change enthalpy, lower thermal conductivities and are inflammable in nature. Due to this, salt hydrates are preferred instead of organic compounds, though the former suffer from phase segregation and poor nucleation [18] [20], [23]. Organic materials melt and freeze multiple cycles without phase segregation and latent heat of fusion of such materials are easily degradable. This characteristic of organic materials is known as congruent melting [13].

1.4.5 Inorganic PCMs

The inorganic PCMs are either metals or salt hydrates. Salt hydrates are inorganic compounds that are formed by a combination of inorganic salt and water molecules. The linked water within the molecule is known as the water of hydration or water of crystallization. Metals that have a low melting point and metal eutectics are included in the category of metallic PCM. Due to their high weight, these metallic materials have not been completely considered yet for PCM technology. In contrast to organic PCMs, inorganic materials provide the advantages of higher latent heat storage capacity; non-flammability and sharp phase transitions but they are corrosive in nature. However, the majority of salt hydrates suffer from phase segregation and supercooling [20], [23].

1.4.6 Eutectic

The eutectic PCMs are a mixture of two or more compounds and these compounds may be either organic, inorganic or both. These materials are formed from two or more components which melt and freeze in a congruent manner. Eutectic almost melts and freezes constantly without segregation. Similarly, both components are liquefied simultaneously during melting without separation. A PCM made from a mixture of two or more salts has an advantage of lower melting temperature as compared to single salts. These mixed salts can exhibit similar thermal stability limits as well [24]–[26]. The major problem with these compounds is the cost, which are two or three times higher than inorganic or organic compounds [13], [19].

1.4.7 Melting point temperature of PCMs

From the perspective of working temperature, PCMs can be categorized as low temperature materials for melting points lower than 220 ^{0}C, as medium temperature materials with melting temperatures reach up to 420 ^{0}C and as high temperature materials with melting point above 420 ^{0}C. These high-temperature melting materials are suitable for concentric solar power (CSP) thermal storage [22], [27]. Therefore, all the above-mentioned phase change materials are employed for low-temperature applications. For high-temperature applications, such as CSP plant and high-temperature solar cooking, other PCMs with high melting points are required. Among all the above properties of PCM, heat capacity, melting point and, thermal performance during charging and discharging are the most important in designing and developing of LHS.

Three important factors that must be taken into consideration to designs a solar TES technology are environmental impact, cost-effectiveness and technical properties [28]. LHS with PCM has been drawn the attention of thermal energy researches for solar energy generation and other similar applications because of their high working temperature and phase transition enthalpy.

Identifying the most appropriate PCM for medium temperature cooking applications is the basic task. A comprehensive study of all commercially available PCMs has been conducted and commercial sugar alcohol known as Erythritol ($C_4H_{10}O_4$) has been selected as a suitable material to be utilized as PCM. Erythritol has a very promising medium melting temperature PCM for solar and other applications as LHS system. This is due to its excellent chemical stability after multiple phase change cycles, low cost, safe, high latent heat and wide-ranging transition temperature [29]. The melting point of the selected phase change PCM for the present storage application is in the range of 117-120 ^{0}C.

1.5 Motivation and objective of the study

The energy allocated for cooking in developing countries has a major share of the total energy consumption. Globally, above 2 billion people depend on traditional energy sources like firewood, cow dung, agricultural residue or charcoal for cooking and heating purposes. On the other hand, electricity is predominantly used in urban areas where a less population are living. This has been resulting adverse consequences for health, social impacts, economic livelihoods and the environment on local and global level [30]. As per the World Health Organization (WHO) nearly four million people are dying prematurely every year from illness resulted from household air

pollution due to the use of traditional solid fuels [31]. Solid fuel refers to the cheap biomass energy sources used for cooking or heating purposes such as firewood, crop residues, or cow dung.

Several studies have reported about the health impacts resulted from the collection and burning of the solid fuels. The impacts during the collection includes neck ache, backache, headache, and even wild animals and snake attacks. The use of biomass fuel leads additional harmful effects on health due to the emission because, the incomplete combustion of biomass fuels generates smoke containing of a large number of air pollutants. Because of social and cultural customs, in developing countries women and their young children are the main household members. Therefore, women and their children are frequently breathing such cooking smoke and they are disproportionately affected by the related health problems [30], [32].

There is consistent evidence that the intensive use of biomass fuel for household energy consumption increases the risk environmental degradation. Solid fuel dependency substantially increases deforestation and this causes soil erosion, pollution of streams and loss of biodiversity. The emissions produced by the combustion of solid fuels also have an adverse impact on the environment and contribute to global climate change [33]. In developing nations, million tons of biomass are burned every year and the emissions produced by the combustion also have a negative impact on the environment and contribute to global climate change.

Moreover, women and children share much of the burden during the collection of solid fuels and this contributes further to the social inequalities between men and women within the household. As a result, women are forced to walk several kilometers and spend significant time in the firewood collection. Hence, women are vulnerable for social inequalities because of an uneven distribution of responsibility.

Therefore, there is a need to search other alternative better solutions in order to alleviate problems associated with the use of biomass or solid fuels. It is imperative for the development of alternative, suitable, affordable methods of the cooking process in developing nations [34]. Cooking with solar energy is one of the promising solutions for achieving energy demands. Solar cooking is freely available, simple and environmentally friendly; hence, it is a better alternative for those who cook using firewood or cow dung cakes.

Solar based cooking has never been a strong competitor in the commercial market. It is not possible to cook using solar energy without storage in the absence of solar radiation. As we know, cooking is an activity that can be performed at any time of day and is not time-dependent. Safe and

comfortable cooking inside the kitchen is possible by heat transferring fluid (HTF). Heat is transported from the solar collector into the kitchen area using HTF. The use of sustainable solar energy for cooking and other services may face problems during the absence of solar irradiance. Thermal energy storage (TES) systems are used to minimize these problems. Thermal energy storage methods are used to perform cooking activity independent of the time. Hence, the primary objective of this study is to design, develop and evaluate the performance of PTSC and LHS systems for an indoor cooking application.

1.6 Organization of the thesis

The report of the thesis has been organized in seven chapters and the content of each chapter is described briefly in the following paragraphs.

Chapter 1 begins with the brief introduction of solar collectors and TES technologies. It discusses the classifications solar collectors, TES, PCMs and, the motivation and objectives of the proposed work.

Chapter 2 presents a detailed literature survey related to various aspects of solar collector and LHS systems, the effects of different parameters on the performance of PTSC and LHS, and the performance enhancement methods of LHS technologies. Moreover, the reviews on different numerical and experimental investigations performed in various operating conditions are presented. Finally, the research gaps which lead to define objectives of the thesis, are reported in this chapter.

Chapter 3 presents the sizing, fabrication and development procedure of the parabolic trough solar collector (PTSC) and latent heat storage (LHS) unit. Additionally, the experimental setup details, such as the determination of the thermal properties of the selected HTF and calibration measuring sensors are presented in this chapter.

Chapter 4 presents the analytical and numerical formulation of PTSC. Moreover, numerical and experimental results of the PTSC unit and the effects of operating parameters on the thermal performance of the storage unit and collector are discussed.

Chapter 5 deals with detail experimental and numerical analysis of LHS. The effect of operating parameters on the performance of the storage unit is investigated practically. Similarly, to investigate the performance of the LHS unit, a 3D numerical model is formulated and numerical

analysis of the LHS unit is presented in this chapter. Further, the effect of operating parameters on the thermal performance of the storage unit is discussed in detail.

Chapter 6 covers the performance evaluation of the proposed hybrid PTSC and LHS system for an indoor cooking application. The performance of the LHS unit based on the thermal energy generated by PTSC from direct solar irradiance is addressed in this chapter. Further, the outcome of the experimental investigation of coupled PTSC and LHS units and numerical investigation of the proposed LHS unit powered by PTSC and auxiliary energy sources are presented.

Chapter 7 presents the major conclusions that are drawn from experimental and numerical investigations. The scope for future work and recommendations are covered in this chapter.

Chapter - 2

2 State of the Art

2.1 Introduction

The global energy demand is increasing constantly from day to day. Consequently, fossil fuel resources have been used intensively to fulfill the growing demand. However, the exhaustive consumption of the depletable and pollutant energy resources have not only caused the global energy crisis but also deteriorated the environment. Moreover, the overall rise in fuel prices has brought another challenge for the society. In this regard, shifting from fossil fuel to other green alternative energy sources is an imperative step which not only reduces carbon dioxide emissions but also meets the increasing energy demand. However, renewable energy resources like solar and wind energy are intermittent in nature [35]. This has attracted the attention of the scientific community. As a result, several researchers across the globe are desperately searching for an alternative of the conventional sources and new renewable energy resources to generate clean and sustainable energy. Generally, the studies have been conducted on energy demand strategies, methods and technologies to secure sustainable energy supplies and to raise the energy productivity of power systems. Moreover, these studies are based on the development of new and renewable energy sources to supplement fossil fuels. For the attenuation of the associated energy crisis and environmental concerns, fossil fuel reduction by replacing more economically affordable renewable energy solutions becomes an acceptable solution. Solar energy is the cheapest, infinitely available, cleanest amongst other renewable energy sources.

Naturally, solar power is intermittent like other renewable energy resources, due to which it requires an efficient storage system to bridge the demand and supply of energy. Combining two or more renewable energy systems could improve the stability and reliability of power output significantly. Similarly, the inclusion of a thermal energy storage system (TES) system is essential

to stabilize the inconsistent daily supply of solar irradiance and the oscillations throughout the year [36]. As it is mentioned in section 1.4 tthermal energy can be stored as a change in internal of a material and they are classified in to three: SHS, CHS and LHS. Sensible and latent heat energy storage systems are the most used methods. The LHS technologies store the thermal energy in phase change material (PCM). In opposite to the sensible storage materials, PCM can be stored and release heat at a closely invariant temperature corresponding to the phase transition temperature of PCM. LHS systems can store large quantities of energy in relatively small volumes as compared to sensible storage. The use of LHS systems based on the solid-liquid transition have proved to be more efficient and economically attractive compared to the solid-gas and liquid-gas transformation. PCMs are accessible in wide range of operating temperature and geared for different applications [13], [20] [. Hence, significant amount of works related to LHS technologies are presented in the literature survey section.

The concentrating solar collectors are preferred for higher operating temperature requirements since the flat plate collectors cannot fulfill the medium and high temperature demand. The most common concentrating systems are the parabolic trough solar collector, linear Fresnel reflector, solar dish collector and solar towers. Amongst these, PTSC is the most fully fledged technology available in the modern era with an affordable price [37]. Similarly, literature reviews on performance investigation of solar collectors, mainly on PTSC are presented in this section

For the development of an efficient solar energy generation system coupled with LHS system, an optimization technique is helpful. The melting and solidification behavior of PCM is dealt with highly nonlinear equations and estimating the behaviour of such system during a phase change is difficult. Numerical modeling is helpful to overcome the analytical limitations to understand and investigate the charging and discharging process of PCM based LHS systems [38]. Performing numerical modeling and simulation of LHS systems is an acceptable solution to overcome the above-mentioned problems. Along with the numerical analysis of an energy generation system, an experimental analysis is also necessary to perform to validate the outcome of numerical analysis. Therefore, several researchers have designed, developed, and have conducted numerical and experimental performance evaluations of PTSC and LHS systems at different operating conditions presented in the following sections.

This chapter presents a detailed literature survey of numerical and experimental performance evaluations of PTSC and LHS techniques. Heat transfer enhancement techniques, the effects of

parametric variations on the operating conditions of LHS systems, the effects of natural convection on the melting and solidification of PCM are reported in the subsequent sections.

2.2 Review on performance evaluation of solar collectors

There are several studies that focus on the innovation and promotion of solar cookers for practical applications. Because of the global energy crisis, several researchers and academicians are investigating the design, fabrication and performance of numerous types of solar cookers. Solar cookers without thermal energy storage are categorized as either direct or indirect solar cookers based on the mode of heat transfer to the cooking device. In the case of direct type solar cookers, the solar radiation is employed directly for cooking. On the other hand, in indirect cookers, heat transfer fluids (HTF) are used to transport heat from the collector to the cooking unit. Different studies based on solar cookers without TES are also reviewed in this section.

Gallagher [39] designed, developed and tested a large-area Injera bread frying pan heated by solar radiation. The solar cooker consists of three primary parts, which are mirror, pan and mounts. The system was developed according to four primary principles which are efficient, affordable, robust and safe solar fryer to be used in developing countries. The sun radiation was directed toward the pan bottom by a mirror which was found beneath it. The heating power of the cooking system was found to be 640 W or with 60% efficiency as compared to the solar energy incident on the full mirror area. It was reported that the frying pan heated up to 180 ^{0}C with 15–20 min and was capable to cook four kilograms of bread within an hour.

Badran et al. [40] designed, developed and tested a mobile solar cooker and water heater using an ordinary satellite dish as a concentrator for solar radiation. Cooking food and heating water with different operating modes were performed using this system. Moreover, the former mode of operation was also validated by employing two approaches. The first operation was with the bare pot and the second one was putting the pot inside a glass box. The experimental results exhibit that 7 kg of water at 20 ^{0}C placed in the bare pot cooking test was brought into the boiling state in an hour. The time taken for boiling temperature reduced to 40 min when the pot was placed inside a glass box and the cooking power improved by 275%. In the case of water heating operation, 30 kg of water was heated from 20 ^{0}C to 50 ^{0}C in 2.5 hrs. and the maximum efficiency obtained was 77%.

Bellos et al. [41] investigated the performance of a PTC throughout the year in a location in Athens, Greece. A numerical model was developed to determine the daily performance of the collector. The numerical model was validated with the results reported in the literature. An input/output evaluation methodology was used to determine the thermal and exergetic daily performance of the system. It was reported that mean thermal efficiencies for December and in June are 37.1% and 68.7% respectively, while the mean exergetic efficiencies 2.0% and 8.5% respectively. In addition, they concluded that, the thermal and exergetic performance of the PTSC was the best during May, June, and July, whereas, November, December and January were found as unsuitable months for power generation using PTC.

Ozturk [42] designed, developed and tested a low-cost parabolic-type of solar cooker and experiments were conducted at Adana, Turkey. The results show that the daily average temperature of the water during the above-mentioned time was found to be 333 K. In order to determine the effectiveness of the cooker, the energy and exergy efficiencies were experimentally evaluated. As a result, the energy and exergy efficiencies of PTSC were found to be in the range of 2.8-15.7 and 0.4-1.25, respectively.

Petela [43] studied a theoretical exergy analysis of the solar cylindrical-parabolic cooker. The cylindrical cooking pot considered for the analysis was surrounded by a cylindrical-parabolic reflector and the pot was filled with water. The heat transfer equations for the cooking vessel, reflector and a proposed surface making up the system were formulated. It was shown that the energy efficiency system ranges from 6% to 19% which is low predominantly due to the loss of a significant quantity of insolation, because of the heat loss to the surrounding environment. While, the exergy efficiency is even lower than the energy efficiency by about 10 times.

Coccia et al.[44] designed, manufactured and tested a low-cost PTSC for industrial process heat applications. The PTSC prototype was built from fiberglass and extruded polystyrene, and the rim angle concentration ratio of the collector are 90^0 and 9.25, respectively. The above-mentioned materials were selected due to their cost, weight, resistance to atmospheric agents and simplicity of manufacturing. The thermal efficiency of the developed collector was determined using testbench performance based on ASHRAE Standard 93-2010 directives and soft water for temperatures up to 85 ^{0}C. It was reported that the results were comparable to other available collectors.

Forman et al. [45] performed an investigation of light concrete shells for the development of PTSC which was made from high strength concrete and was capable of replacing established steel structures. Aluminum sheets were attached directly onto the smooth concrete surface giving less deformation and maximum energy gains. They recommended that because of very brittle and weak in tension properties of concrete, the concrete shell should be made with highly accurate surfaces and few centimeters of thickness only to get structural stiffness and high optical efficiency.

Kumar et al. [11] developed a community solar pressure cooker with help of an evacuated tube solar collector. The cooking device is composed of components, such as an evacuated tube solar collector (ETSC) and a pressure cooker that were coupled with the heat exchanger. They conducted an experimental study on the solar pressure cooker. Moreover, they developed a numerical model to estimate the performance of the cooker by varying operating and climatic conditions. They concluded that the system based on ETSC generates higher temperature heat (120 ^{0}C) more than normal flat plate collector.

Harmim et al. [46] designed and prototyped a novel non-tracking box-type solar cooker in Adrar, Algerian Sahara. The system was developed from simple and locally available materials and was consisted of a fixed compound parabolic collector as a booster-reflector and an absorber-plate which could be fixed into the wall of the kitchen without facing any problem to get sunshine. Several experiments were conducted to evaluate the performance of innovative building-integrated and a non-movable compound parabolic concentrator. In the case of no-load operating conditions, the experimental temperature prediction of the cooker along with its reflector reached up to 165 ^{0}C and 166 ^{0}C in cold and hot seasons, respectively.

Shukla [47] presented a comparative study on community and domestic parabolic solar cookers using energy and exergy efficiencies as evaluation parameters. The study was conducted during the summer and winter seasons. The energy end exergy efficiencies of two different types of cookers were experimentally evaluated. The results indicated that the energy output of the community solar cooker varied between 2.73 W to 43.3 W. Similarly, the total heat generated in the case of domestic solar cooker varied from 7.77 W to 33.4 W. The exergy of the community solar cooker lied between 1.92 W and 2.58 W, whereas, it ranged from 0.65 W to 1.45 W for domestic solar cooker. In addition, the energy efficiency of the first solar cooker varied from 8.3% to 10.5%, whereas, the energy efficiency of the second ranged from 7.1% to 14.0%.

2.2.1 Thermal efficiency improvement methods of PTSC

Currently, PTSC are employed for different applications, such as, for solar cooking, electricity generation, solar cooling, industrial heating, desalination, refrigeration and chemical processes [48]–[50]. The efficiency of PTSC is the main factor that limits its feasibility and application. Hence, enhancing the performance of PTSC has become an important issue in the scientific community. The major constituents of PTSC are parabolic reflector and a receiver tube. The receiver tube also consists of a glass cover and a metallic absorber pipe, mostly made from copper or steel. The solar radiation that reaches on the wide area of the PTSC reflects into the receiver tube. The surface area of the receiver is too small as compared to the collector area. The concentrated reflected rays mainly focus on the receiver tube and generate high-temperature heat [51], [52] .

The generated high heat flux is captured by heat transferring fluid during its passage through the receiver tube. Thus, for safe and efficient operation of the PTSC system, the heat transferring rate between HTF and receiver tube should be increased. Regarding this, several techniques have been practiced for the advancement of heat transfer coefficient between two mediums (the absorber pipe and the working fluid). These techniques can be categorized into two main classifications; the use of nanofluids as HTF and modifying the geometry of absorber tube using inserts, such as, an extended surface like fins and porous plate [53]–[55].

In light of this, numerous scientific works have been carried out in order to enhance the efficiency of PTSC. Mwesigye et al. [8] assessed the thermal performance of PTSC by inserting a twisted tape using Syltherm 800 as a working fluid. It was reported that the inclusion of twisted tape resulted in 58% decrease in the entropy generation and 168% increase in the heat transfer coefficient. Similarly, Song et al. [56] employed a screw tape insert into the receiver tube and thermal oil Syltherm 800 was utilized as HTF. They reported that the thermal efficiency increased by 1%, whereas, the thermal losses got reduced by 15%. Furthermore, the heat transfer enhancement was found to be between 50 and 70%.

Bellos et al.[57] investigated the performance of PTSC using three different working fluid; pressurized water, thermal oil and thermal oil with nanoparticles. In addition to this, the collector system was tested using a dimpled receiver tube. They reported that the collector system operated with nanofluids and dimpled absorber tube enhanced its efficiency by 4.25% and 4.55%, respectively. Zadeh et al. [58] conducted an investigation to improve the efficiency of commercial

collector known as LS-2 PTC. It was operated with nanofluid as HTF, in which synthetic oil was used as the base fluid while Al_2O_3 was added as nanoparticles. It was reported that dispersing Al_2O_3 nanoparticles improved the collector efficiency by 10%. Similarly, Phelan [59] examined the usage of aluminum nanoparticles in the working fluid. Thermal oil was employed as a working fluid and they reported that the addition of nanoparticle improved efficiency by 5- 10%. Chen and Hans [60] conducted a performance comparative study of a PTSC with dimpled and smooth absorber tubes. They reported that the heat transfer coefficient of the dimpled tube was higher than the smooth one. Heat transfer improvement extended from 25% to 137% when the Reynolds number is set to be constant, and from 15% to 84% if the pumping power is maintained to be invariant.

Kumar and Reddy [61] investigated a 3D numerical investigation of the porous disc line receiver of PTSC. The collector receiver was built with porous discs to improve the heat transfer behavior of the receiver. Numerical investigation of solar parabolic trough collector was performed using different configurations of the porous disc in the circular receiver by varying boundary conditions. The impact of fluid properties, receiver design and intensity of solar radiation on total heat collection was examined. They concluded that the heat transfer rate was enhanced by 64.3% with respect to the Nusselt number whereas, pressures drop of 457 Pa was recorded against the receiver.

2.3 Review of LHS technologies development and performance analysis

The TES is essential to stabilize the inconsistent supply of solar flux the whole day and the oscillations throughout the year with the demand. Generally speaking, thermal energy storage systems are of three kinds: viz. sensible heat storage (SHS), latent heat storage (LHS) system and chemical heat storage (CHS) [15]. Due to higher storage density and nominal heat loss at a constant transition temperature, LHS received the attention of many researchers [62], [63].

Fornarelli et al. [64] presented a numerical analysis of melting process in a shell-and-tube latent heat storage. The numerical simulation was conducted on vertical shell and tube LHS device. A binary eutectic salt ($NaNO_3$–KNO_3) with a melting temperature of about 230 ^{0}C was selected as PCM and ‘‘Alusil TR 50”, a silicone thermal oil was selected as HTF. The results indicate that the enhanced heat flux formed due to natural convective flow increases the melting rate of the PCM. The PCM in LHS model with natural flow consideration melts completely three hours faster than the conductive only simulation. Lacroix [65] developed a 2D model to evaluate the transient

behavior of a shell-and-tube LHS system theoretically. Successive numerical experiments were conducted, and the results indicated that the geometric parameters must be carefully chosen for a selected PCM in order to enhance the performance of the storage.

Seddegh et al. [66] conducted a comparative study of the thermal behavior of a vertical and horizontal shell-and-tube energy storage using PCM. LHTES system consists of two concentric tubes with the PCM in the annulus and HTF in the tube. Its thermal behavior was studied and compared with a combined conduction and convection heat transfer model. During the charging process of horizontal orientation, convective heat transfer had a strong effect on the melting of the upper part of the solid PCM. On the other hand, convective heat transfer remained same during the entire charging process in vertical orientation. During the discharging process, the thermal behavior did not show any difference between horizontal and vertical systems. They concluded that the horizontal orientation had superior thermal performance during the charging process. The effect of HTF inlet temperature on the horizontal and vertical LHS models are also examined using three different temperature inlets: T = 343 K, 348 K and 353 K. It was reported that, the total melting time is decreased by 14% and 27% for former LHS unit and 12% and 27% latter one, respectively.

Esapour et al. [67] developed a 2D theoretical model to examine the effect of the number of HTF tubes in an LHS system during the charging process. Investigating the impact of the number of inner tubes as a geometrical parameter during the charging process was the main aim of this study. For this purpose four cases of MTHX LHS models are considered: the simple MTHX with single cental tube, 2, 3 and 4 inner tubes. A commercial RT 35 material was used as the PCM, and water was selected as HTF. The results exhibited that increasing the number of HTF tubes enhanced the melting of PCM. The total melting time of the MTHX models cases with one, two, three and four inner tubes are 56, 61, 71 and 79 minutes respectively. Moreover, the bottom section of the storage was influenced by an extra heat transfer which reduced the total melting time by about 29% for four tubes system.

Hakeem and Muthukumar [68] conducted a numerical experiments to evaluate the performance of latent heat storage (LHS) systems using PCM. Paraffin RT 50 was chosen as PCM and water were considered as heat transfer fluid (HTF). An effective heat capacity method was applied to study the latent heat of the PCM. Three cylindrical configurations of thermal storage models: pipe model,

cylinder model and shell-and-tube model were examined. The shell and tube configuration phase change model was influenced by the effect of convective heat transfer and it was reported that the complete melting time of the PCM in the first second and third LHS models are 4425 s, 2319 s and 1860 s, respectively. That means, the melting time of the shell-and-tube LHS model reduces by about 22.38 % and 59.32 % when compared with cylinder and pipe model.

2.3.1 Effects of natural convection and operating parameters on LHS

During the study of phase transition behavior of PCM, natural convection, which is the part of heat transfer mechanism was neglected and has been reported in several other studies. Sparrow et al. [69] performed the first study that indicates natural convection should not be ignored in the investigation of a phase change process. During melting or solidification process the density of PCM was not uniform and this induced buoyancy which caused convective motion within the liquid phase. Later many other researchers, such as Lacroix and Duong, Ezan et al. and Longeon et al. [70]–[72] performed experimental investigations and confirmed that the natural convection was the basic mode of heat transfer during the melting process and it influenced melting progress of PCM.

Tao et al. [73] performed a numerical analysis to study the effects of natural convection and PCM arrangement on the melting and solidification performance of LHS unit. Two shell-and-tube LHS numerical models were developed: with the PCM is placed in shell side in the first model and PCM tube side on the second one and their performance were investigated with and without natural convection. Neglecting the natural convection, the melting time of the LHS model with PCM arranged in tube side is reduced by 25.4% compared to the LHS model with PCM in the shell side. On the other hand, the melting time is reduced by 34.4% with PCM arranged in tube side when the natural convection is considered. It was reported that the natural convection had more substantial effects on melting performance than the solidification process. Similarly, Han et al. [74] performed a comparative study of different shell and tube type of LHS units. 3D numerical modeling and simulations were done for different cases of pipe and cylinder LHS units to investigate the impact of natural convection and different HTF inlets on the melting performance. The performance investigations were performed for horizontal and vertical orientations of the LHS models. They concluded that the heat addition rate of the horizontal cylinder model is higher than the horizontal pipe model and the complete melting time is decreased by 23.5%. Moreover, it was

reported that the natural convection could be the reason for the variable distribution of the solid-liquid interface.

In horizontally positioned shell and tube LHSS units, due to buoyancy the upper half melts quickly, while the bottom half remains in the solid state. To investigate this, several studies such as Tao and He and Cao et al. [75], [76] have been conducted. The result indicated that high temperature molten salt moved upward due to the effects of natural convection and this increased melting rate of the PCM in the upper half and decreased melting rate of the PCM in the lower half. Similarly, Zheng et al. [77] developed different shell and tube LHS models with different eccentricities to investigate melting and solidifying performance. They found that, moving the inner tube vertically downward from the center noticeably decreased the total melting time of PCM. The total charging-discharging time for the eccentric LHS models is decreased by 0.4–27% as compared with the concentric cases. Using a simplified front tracking method, Joybari et al. [78] performed a numerical investigation on pure conduction, joint conduction and natural convection model of PCM melting. They reported that the natural convection impacted predominantly in the melting process of PCM.

Mahdi et al. [79] reported a numerical study on the charging process in the triplex-tube type of LHS using longitudinal fins in the top and bottom halves. In order to study the effects of numbers and dimensions of fins in the lower and upper parts of the storage system, multiple cases of fin configuration were considered at different sections of the heat exchanger. Based on the outcome of the investigations, it was reported that considerable improvement could be attained by installing long fins at the lower section and few in number and relatively shorter in length fins at the upper section of the unit. In addition, the overall effects of natural convection on the upper and lower half of the storage unit are examined and it was reported that, the natural convection contribution is 1.7 times more than the contribution of conduction on the upper region. In the lower half of the LHS unit, the contribution of natural convection is 0.4 times more than the contribution of conduction does.

Kousha et al. [80] investigated the influence of inclination angle on the melting and solidification effectiveness of a shell and tube heat storage system both experimentally and numerically. Paraffin RT35 was selected as PCM and it was presented that the horizontally positioned LHS system had a higher rate of heat transfer during melting than the vertical one, but during the solidification process, the rate of heat transfer of the vertical unit was higher than the horizontal one.

Fornarelli et al. [81] conducted a numerical analysis of the melting process in shell-and-tube LHSS unit. The natural convection heat transfer effect versus the pure conductive heat transfer model was analyzed. The convective heat transfer in the PCM was driven by the buoyancy effects and to include this into their PCM, the Boussinesq approximation model was adopted. They reported that the heat flux to PCM increased due to convective motion and, as a result, charging time was reduced by around 30% of the total time required to melt PCM in the LHS unit.

Since the liquid PCM thermal conductivity is lower than the solid PCM, there is a smaller temperature difference reduction in the melting front of the PCM. Hence, this hinders the natural convection intensity and finally slows down the melting process of the whole LHS system [80] . Melting of PCM is dominated by natural convection heat transfer, whereas the solidification process is influenced by conduction. Incorporating fins with HTF tube enhances the natural convection during the melting of the PCM and conduction during the solidification process [82]. Furthermore, the available literature concludes that the natural convection plays a key role in the energy-storing process of PCM based LHS. Wang et al. [83] performed an experimental study on melting and solidification performance of shell and tube type of LHS using erythritol as PCM. They investigated the effect of HTF operating parameters: inlet temperature, mass flow rate and pressure on the thermal performance of the storage unit. It was reported that increasing the parameters in the charging process noticeably augmented the effectiveness of the storage system. The total melting time is reduced decreased by 15.9%, 25.9%,,and 33.7%, when the in let tempreature is raised from 150 ^{0}C to 155 ^{0}C, 160 ^{0}C, and 165 ^{0}C, respectively.

2.3.2 Thermal performance enhancement techniques of LHS

LHS based on PCM store or release energy, when a material experiences a phase transition from solid state to liquid state or vice versa [84] . However, PCM suffers from inherent low thermal conductivity and this is one of the critical problems that result low melting and affects the solidification rate of PCM. Improving the thermal conductivity of the PCM is an imperative step to develop an effective LHS unit. In order to alleviate the low thermal conductivity issue of PCM, many effective techniques have been practiced. Generally, thermal conductivity enhancement techniques can be categorized into two parts, i.e., by enlarging the surface area of the hot walls and adding high thermal conductivity materials, for example, metallic nanoparticles in PCM.

Mahdi and Nsofor [85], [86] conducted a numerical study of latent heat TES system using nanoparticles and fins based PCM melting enhancement method. It is important to mention that

three enhancement techniques: nanoparticles alone, fins alone, and nanoparticle fin combination were used in this study. The results showed that the melting rate of the LHS unit could be enhanced more using fins than using nanoparticles alone or the combination of the two methods (use of fins as well as nanoparticles together). They concluded that the melting time can be reduced from 75 min to 66 min when the same volume fraction of fins is added instead of nanoparticles. The heat transferring process between energy-storing material (PCM) and HTF could be considerably boosted using multiple embedded HTF tubes and fins. However, the proper arrangement of the fins with respect to the PCM is necessary to develop an efficient LHSS unit.

Bhagat et al. [87] performed a numerical estimation of finned shell and tube-based latent heat thermal energy storage. A numerical model was developed to study the thermal performance and design optimization of multi-tube storage unit. The effects of geometric parameters, such as, the width and thickness of the fin, and the number of fins on the thermal performance of the storage unit were studied. The results indicated that the above-mentioned parameters significantly affected the performance of LHS unit. The thermal conductivity enhancement of longitudinal fin on the PCM is examined by monitoring the outlet temperature of the HTF. It was reported that the presence of longitudinal fins improves the performance of the LHS. After 1800 s, charging period liquid fraction of the PCM is 0.7 and 0.553 in the case of fins and no fins, respectively. Additionally, the HTF outlet temperature can be reduced by 4.5 ^{0}C when the longitudinal fins are applied. Similarly, Hosseini et al., Pakrouh et al. and Sciacovelli et al. [88]–[90] conducted and presented a numerical optimization study of fin parameters that could influence the phase change melting process. They concluded that adding an optimized number of fins, fins height and fins thickness could bring a noteworthy enhancement in the performance of the LHS system.

Yuan et al. [91] performed a numerical investigation of employing Lauric acid as PCM in the phase change process. For studying melting characteristics of latent heat thermal energy storage, PCM was placed in the annular and two fins were considered by varying the installation angle of the fins. The results stated that the melting rate of LHS unit, in which the fins were installed vertically straight (at $\theta=0^{0}$), was maximum and at the end of the melting process, 60-min the PCM in the unit with fins installed in vertical postion melts faster. Similarly, Liu and Groulx [92] conducted an experimental study of finned horizontal cylindrical LHTES using dodecanoic acid as PCM. It was reported that the time taken for the complete melting of PCM in the case of angled fins was slightly less as compared to the case when straight fins were employed. The thermal

performance of thermal energy storage systems during melting and solidification could be improved by installing longitudinal fins on the HTF tubes [82],[29].

Several methods have been practiced to improve the performance of LHS systems. Adding certain volume fraction of nanoparticles into PCM enhances the thermal efficiency of a storage unit. The most commonly employed nanoparticles are Al, Al_2O_3, Cu, CuO, Au, ZnO, SiO_2, Fe and Fe_2O_3. The dispersed nano-fluids into the base fluid enhance thermal properties as compared to the corresponding base fluid [93], [94]. It is important to note that the volume fraction should not exceed 5% [95]. The major thermal properties that influence the performance of LHS system are density, specific heat capacity, thermal conductivity and dynamic viscosity. The thermal properties of nano PCM (a mixture of PCM and nanoparticles) are derived from the respective base fluid and volume fraction of nanoparticle considering the theoretical mixing [96], [97].

2.4 Review of solar cookers integrated with LHS

Furthermore, two or more renewable energy resources can be coupled together to supplement each other. The energy storage units can store energy when the resource is present in abundance and retrieve when demand peaks [98]. As explained previously, the efficiency of multi-energy generation system can be enhanced, if it is coupled with TES system [99]. The hybrid energy generation systems can be employed for various applications, such as direct electricity generation and thermal energy production for cooking and space heating. The cooking process is conducted inside a kitchen independent of time without any restriction in terms of the presence of solar energy. Hence, solar cookers must be built with a heat storage unit for storing thermal energy in order to resolve the issue of cooking when solar radiance is not available. In this section, studies conducted by different researchers based on the types of solar cookers which use latent heat storage units are summarized.

Haileselassie et al.[100] claimed that Injera cooking was possible in the absence of sun using PCM solar thermal energy-storing materials. Heat storage system using phase change material was developed and tested. In this work, solar salt was used as thermal energy storage material. The developed energy storage prototype was loaded with two kg of solar salt (a mixture of 60% $NaNO_3$ and 40% KNO_3). The storage system was powered by an average heat of 650 W and completely melted after 4.5 hours. The melting behavior of solar salt and its possibility for Injera baking was studied using experimentally as well as numerically. It was reported that the PCM thermal energy

storage system was tested for indoor night cooking by frying egg that took approximately 32 minutes.

Mussard and Nydal [101] studied high temperatures heat storage for cooking purposes by charging heat storage combined with a low-cost small-scale PTSC. The system was fabricated with solar collection and sun-tracking units, self-circulation loop, heat storage and insulations. The self-circulation loop functionality was based on the thermosiphon principle, in which a heat transferring oil circulates inside the loop. The storage was integrated with a self-circulating PTSC filled with thermal oil, which transferred heat from the solar collector to thermal energy storage. The cylinders were filled by nitrate salts (KNO_3–$NaNO_3$) to preserve energy as latent heat. The results exhibited that the storage unit could preserve over 200 ^{0}C heat energy and could be used for cooking and frying.

Prasanna and Umanand [102] modelled and designed a hybrid solar and Liquefied Petroleum Gas (LPG) cooking system. The heat obtained from solar radiation was brought to the kitchen using a circulating fluid. The transfer of solar energy was two-stage process, where energy from the collector was conveyed to a transitional energy storage buffer and later the energy was released from the buffer to a cooking device. Three parameters were used to control the maximum heat transfer from collector to cooking load, which are fluid flow rate from solar collector to buffer, from the buffer to cooking load and the diameter of fluid transferring tubes. The additional energy required for the solar load was provided by auxiliary energy sources, such as LPG and electrical energy. The whole system model was based on the bond graph approach using seamless integration of power flow. The experimental results were validated by simulating the modelled system.

Kumaresan et al.[103] studied the performance estimation of a noble double-walled cooking vessel (tava type) appropriate for an indoor solar cooking purpose coupled with the TES system. The system was made up of PTSC, double-walled cooking unit, TES tank and pump. The PCM stored solar energy from PTSC by virtue of HTF that circulated in a closed-loop. A special bowl type cooking device (tava) was developed for a cooking purpose that permitted HTF to circulate from the collector, TES tank and cooking vessel. The experiment was performed using a known amount of edible oil that was placed in an inner bowl, which got heated due to the circulation of hot HTF. The overall heat balance of the system was estimated, which indicated that the average rate of heat gained by oil was merely 0.25 kW out of 2.45 kW supplied by the TES tank. It was reported that

the overall efficiency of the system and cooking unit efficiency were 10.2% and 73.5%, respectively.

Sharma [104] investigated the performance of a solar cooker using an evacuated tube solar collector (ETSC) coupled with a PCM storage system. The storage unit was made employing two hollow aluminum cylinders to preserve solar energy during sunshine hours so that food could be cooked in the late evening or night. The gap between the two cylinders was contained by 45 kg commercial-grade erythritol as PCM. They performed several cooking experiments with the ETSC and PCM storage unit with and without load. The results indicated that the LHS unit stored an adequate amount of heat which enabled cooking during the day as well as in the night. Although ETSC system was expensive, it was helpful for community applications and PCM stored heat at high temperatures i.e., up to 130 ^{0}C without a tracking system and helped indoor cooking during non-sunshine hours.

Kumaresan et al.[105] performed an experimental investigation to study the performance of a PTSC connected with a TES system. The experimental setup includes a PTSC, TES tank which contains Therminol 55 as HTF and a pump circulating the fluid. It was reported that, a maximum temperature of 212 ^{0}C was attained around noon during stagnation test. When mass flow rate of 0.1 kg/s of HTF pass throgh the receievr tube the maximum temperature achieved is only 116 ^{0}C at outlet of the PTSC.Additionally, the instantaneous efficiency of the PTSC depended on the beam radiation and heat gain. Moreover, the collector efficiency increased significantly during 8.00 AM - 9.00 AM, whereas, the peak instantaneous efficiency of PTC was recorded at 62.5% by noon. The heat losses increased due to the reduction of the insolation rate beyond 12.00 PM. The use of PTC after 02.00 PM was not recommended because the energy loss was more than the energy gained and, as a result, the average temperature of HTF kept in the storage tank decreased.

2.5 Literature closure and objectives of the present study

Extensive reviews on the development and performance investigation of various types of solar collectors and LHS technologies have been conducted. The literature review is focused on the development, experimental and numerical performance evaluation of different types of solar collectors and LHS technologies. Besides, the literature review covers the thermal performance enhancement techniques of PTSC and LHS systems. In addition to this, the literature review discusses the performance analysis of solar cookers integrated with available thermal energy storage technology for late evening indoor and outdoor cooking.

I. Several researchers performed performance analysis of PTSC experimentally, numerically, analytically or in the combination either of the above two. However, the performance comparison study of PTSC using the above mentioned three methods is not yet reported.

II. The charging and discharging behavior of LHS systems employing different PCMs are reported by several researchers. However, most of the studies deal with a simple geometrical structure, such as rectangular in shape and shell-and-tube heat exchanger type with a single pipe. There is not enough research work done on the heat transfer improvement of shell-and tube LHS unit employing many finned HTF tubes.

III. Several researchers evaluated the performance of LHS and PTSC using synthetic or petroleum based oil as working fluid. Environment friendly and cheap working fluid is necessary to harvest solar energy. A profound experimental and numerical analysis of PTSC and LHS systems using cooking waste oil as a working fluid is required.

IV. Although many research works have been concluded on solar cookers with TES units in recent years to address the issues experienced with solar cookers without TES, the solar cooking system has limitations in terms of cooking time and cost. The solar cooking device is not preferred as compared to conventional fuels in rural areas. Similarly, LPG, kerosene, electricity and coal are being utilized in the urban areas for cooking purposes. In order to increase the acceptability of solar cookers, it should perform better as compared to other types of cooking systems not only in terms of cost but also in terms of cooking time and cooking quality.

V. Despite the fact that solar cookers are built with TES technologies, there is no guarantee about consistent and existence of solar energy availability during day time because of cloud coverage. Therefore, in order to make use of the available solar energy for cooking applications efficiently and reliably, it is essential to design and develop a suitable solar cooking system with TES in a combination of other energy sources, such as fuel and electricity. The current literature indicates that no such work has been reported so far. From the survey, almost all of the researchers had tried to improve the performance of LHS or solar collector independently, and a few of them tried to couple solar collectors with LHS. Additionally, some of the researchers had designed solar cookers but none of them has tried to combine solar energy with other types of available energies. Therefore, combining stored solar energy with other sources of energy helps in minimizing the time taken for cooking, the

cost of energy and the quality of food. Thus, the objective of the present study is to design, develop and investigate the thermal performance of a suitable indoor solar hybrid cooking system using thermal energy storage materials.

2.5.1 Research objectives

Based on the above points the following objectives are proposed to be investigated.

i. Design and develop lab-scale LHS and PTSC units for solar cooking purposes.
ii. To conduct a performance investigation of PTSC experimentally, numerically and analytically.
iii. To perform an extensive numerical study to optimize the numbers of tubes and fins orientations in order to select the most effective LHS unit.
iv. To investigate the charging and discharging characteristics of multi-tube shell and tube type LHS unit based on erythritol as PCM and using food waste oil as HTF.
v. To carry out an experimental study of the LHS unit to evaluate its thermal performance by varying operating parameters.
vi. To integrate solar-powered cooking assisted by energy storage materials with electrical and/or biomass energy and evaluate the overall performance of the system.
vii. To validate the numerical analysis of the LHS unit with the experimental data.

Chapter - 3

3 Experimental setup sizing and fabrication

3.1 Introduction

In this section, sizing and fabrication of the lab-scale experimental setups processes are presented. The major experimental setups discussed in this chapter include the PTSC and LHS systems. A detailed description of the design of individual components and their fabrication is also presented. The PTSC system is used to concentrate the incoming scattered solar radiation and convert into heat energy. The LHS unit is employed to store thermal energy generated by PTSC. The total thermal energy required to be stored is 32 MJ and a storage tank is sized based on the energy requirement. Similarly, the size and parameters of the solar collector system are decided after the incident solar energy estimation. The energy flow diagram using an experimental setup is demonstrated in Fig.3.1. Based on the design and specifications, the required components are fabricated. Data measuring instruments and auxiliary materials are procured through a commercial market-place, and finally, the experimental setup is assembled and tested on the rooftop of the Electronics and Electrical Engineering Department to get maximum solar radiance.

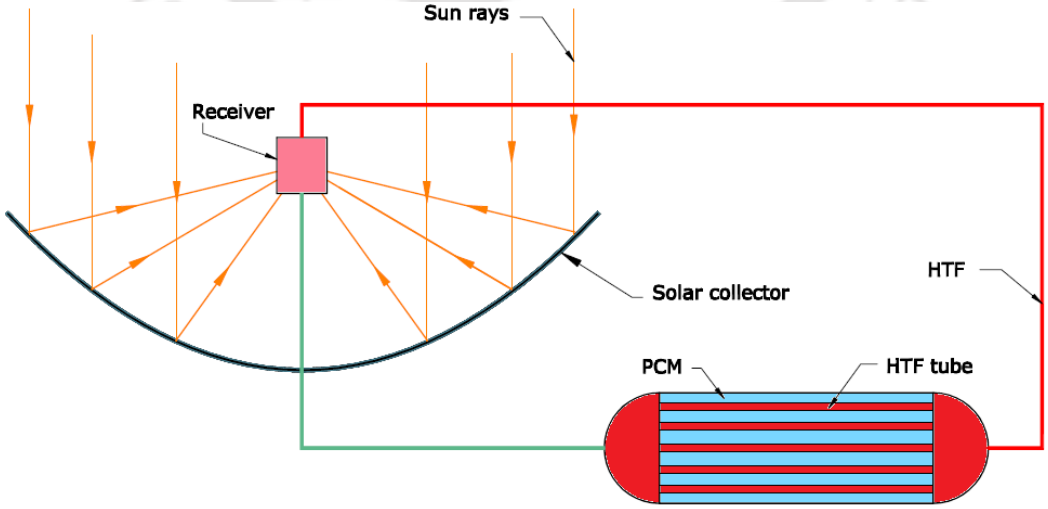

Fig. 3.1.Energy flow diagram of the fabricated experimental setup

Heat is transported from the solar collector into the kitchen area using HTF. As we know, the use of sustainable solar energy for cooking and other services may face a problem because of the absence of solar irradiance. Thermal energy storage (TES) systems are used to minimize such type of problems. Thermal energy storage methods are employed to perform cooking activity inside the kitchen independent of the time. This chapter describes the explanation of PTSC and LHS systems.

3.2 Sizing and fabrication of lab scale PTSC

The lab-scaled PTSC system is shown in Fig.3.2 and consists of a reflector, receiver, supporting structure and manually tracking device. The focus of this section is to estimate the availability of solar energy and, designing and development of the above mentioned parts of the collector.

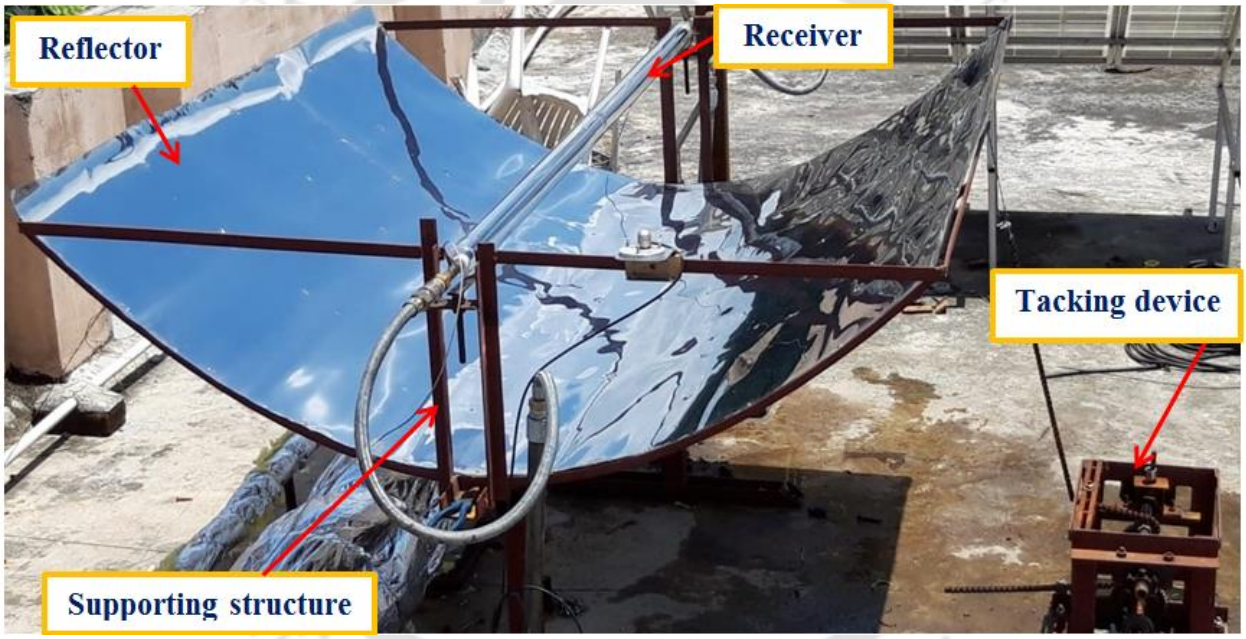

Fig. 3.2.Pictorial view of the PTSC system

3.2.1 Solar insolation Estimation

The amount of solar insolation available on the collector affects the thermal performance of solar cooking system directly. The quantity of solar energy being received at a specific location is a function of various parameters like day, time of the day, latitude of the location and atmosphere. The daily monthly average of extraterrestrial global solar radiation on a horizontal surface (H_o) at any location is given by Eq. (3.1).

$$\bar{H}_o = \frac{24}{\pi} \times I_o \left[\frac{\pi}{180}\omega_s \times \sin(\varphi)\sin(\delta) + \cos(\varphi)\cos(\delta)sin(\omega_s)\right](Wh/m^2) \quad (3.1)$$

where I_o, $\omega_s, \delta, \varphi$ are extra-terrestrial beam normal radiation on a day in kW/m^2, hour angle, declination angle and latitude of the location, respectively.

$$I_{o=}I_{sc}\left[1 + 0.033cos\left(\frac{2\pi N}{365}\right)\right] \quad (3.2)$$

where, I_s is solar constant, which is 1360 W/m^2 and N is a day of the year.

Declination angle in degree $$\delta = 23.45sin\left[\frac{2\pi(N-80)}{365}\right] \quad (3.3)$$

Hour angle at the sunrise or sunset $$\omega_s = cos^{-1}(-\tan(\varphi)\tan(\delta)) \quad (3.4)$$

The solar radiation becomes maximum in the north horizon during the month of June as the apparent movement of the sun tends towards the North. As shown in Fig A.4 (appendix section) the declination angle of sun is 23.45 on June 21st in the north hemisphere. Sizing of the PTSC was done for a randomly chosen day close to maximum solar radiation and June 11 was selected in order to build cost effective PTSC. Guwahati is located at a latitude and longitude of 26.1445°N and 91.7362°E, respectively. The daily averages of extraterrestrial global solar radiation on a horizontal surface H_o on June 11 can be calculated as follow.

φ=latitude of the location (degree) =26.2^0.

For June 11 the day of the year (N) = 162.

$$\delta = 24.45sin\left[\frac{2\pi(162-80)}{365}\right] = 23.153^0$$

$$I_o = 1360\left[1 + 0.033 * cos\left(\frac{2\pi * 162}{365}\right)\right] = 1317.89\ W/m^2$$

$$\omega_s = cos^{-1}(-\tan(26.2)\tan(23.153)) = 102.15^0$$

Substituting the above values in to equation Eq.3.1, the global solar radiation on a horizontal surface is determined and its value described below.

$$\bar{H}_o = 11{,}240\ Wh/m^2$$

Atmospheric effects like water vapour should be considered in order to determine solar insolation available on a horizontal surface. Clearness index K_T is a stochastic measure of these atmospheric effects and the global solar insolation with atmospheric effects (H_{tc}) is obtained as below.

$$H_{tc} = K_T \times H_o \tag{3.5}$$

The value of clearness index K_T is 0.6 [106]. The total solar thermal energy gathered from the collector can be expressed as

$$H_{tc} = 0.6 \times H_o = 0.6 * 11{,}240 \ \frac{Wh}{m^2} = 6744 \ Wh/m^2$$

3.2.2 Sizing of the PTSC

The knowledge of exact quantity of heat required for cooking and the availability of solar energy is essential to design solar concentrator [107]. The heat transfer fluid in this system is heated up by the solar thermal collector. The energy demand for a specified cooking should be determined a first in order to estimate the size of the collector. As it is mentioned in the next section 3.3.1, the LHS unit is charged using PTSC and the energy storage capacity (E_{cap}) of the unit is 32 MJ (8888.89 Wh). The total amount of energy required ($E_{req.}$) for one cycle charging of LHS unit is estimated as 32 MJ (8888.89 Wh). Considering 60% of heat losses of the total collected solar energy incurs in the receiver, piping circuit and TES tank and the overall efficiency (η) of PTSC is estimated to be 0.4 [108]. As a result, the effective area of the collector (A_c) in m^2 can be calculated using Eq. (3.6).

$$A_c = \frac{E_{req.}}{\eta H_{tc}} \tag{3.6}$$

Thus, employing the above relation, the effective area of PTSC is calculated as 3.28 m^2.

This is to mention that the heat loss in the receiver to the atmosphere should be minimized; therefore, the absorber tube should be enclosed inside a glass envelope. Hence, 60 mm diameter glass cover (D_g) is required for this purpose. The effective area of the collector in terms of the glass cover is mentioned below.

$$A_c = L * (a - D_g) \tag{3.7}$$

where, L is the length of the collector and the glass tube. It is set to be at 2 m, while *a* is the aperture of the collector and is of 1.7 m, which is obtained from the above relation.

$$3.28 \ m^2 = 2 \ m * (a - 0.06 \ m)$$

Hence, the principal dimensions of the collector are the aperture (a) and length which are considered as 1.7 and 2 m, respectively.

3.2.2.1 Parabolic profile

The parameters that are commonly used to determine form and size of a parabolic trough are trough length (L), focal length (f), aperture width (a) and rim angle (φ_r). The equation of the parabola, in terms of the coordinate system, is given below and the plot of this equation illustrates the curve shown in Fig.3.3. Solar radiations incident on the solar parabolic mirrors are concentrated into the receiver, from which it reflects radiations on the focal point. Focal length (f) is the distance between focal point and the vertex of a parabola. It is a decision parameter that determines the parabola completely and given by Eq. (3.8) and (3.9) [109].

$$y = \frac{x^2}{4 \times f} \tag{3.8}$$

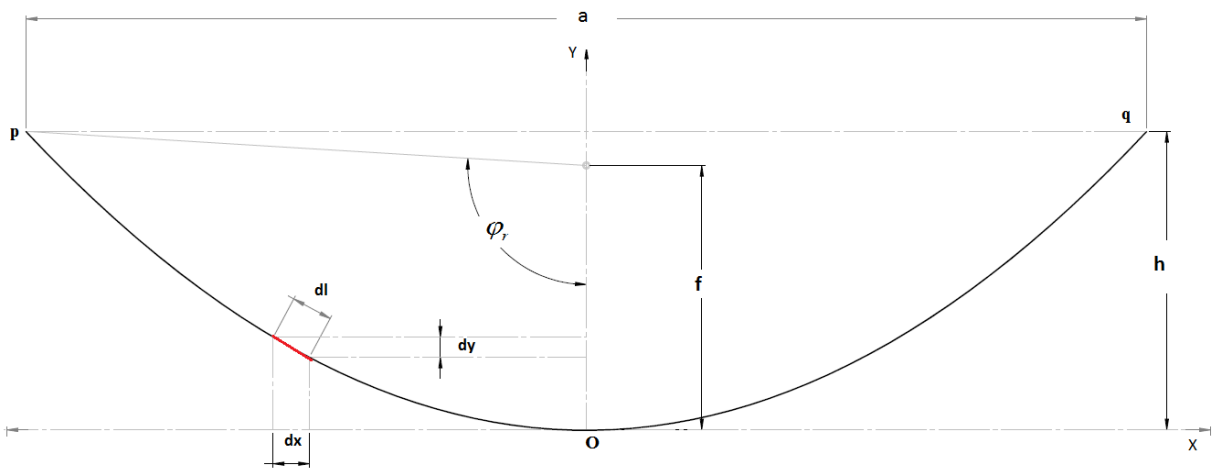

Fig. 3.3.Section of a linear parabolic concentrator showing major dimensions

$$f = \frac{a^2}{16h} \tag{3.9}$$

The curvilinear length $\widehat{pq}$ of a parabolic trough is determined by integrating the parabolic curve. An elemental *dl* length as described in Fig. 3.3 is taken from the curve and is integrated between $-\frac{a}{2}$ and $\frac{a}{2}$ to calculate curvilinear length.

$$dl = \sqrt{(dx^2 + dy^2)} \tag{3.10}$$

And Eq. 3.10 can be expressed as

$$dl = \left(\sqrt{(1 + \left(\frac{dy}{dx}\right)^2} \right) dx \tag{3.11}$$

Rewriting Eq. (3.8)

$$\frac{dy}{dx} = \frac{d}{dx}\left(\frac{x^2}{4f}\right) = \frac{x}{2f} \tag{3.12}$$

Eq. (3.12) can be explained as:

$$dl = \left(\sqrt{(1 + \left(\frac{x}{2f}\right)^2}\right) dx \tag{3.13}$$

Then the curvilinear length $\widehat{pq}(l)$ can be expressed as

$$l = \int_{-a/2}^{a/2} \left(\sqrt{(1 + \left(\frac{x}{2f}\right)^2}\right) dx \tag{3.14}$$

After integration and simplification of Eq. (3.14), the parabolic curvilinear length is described asper Eq. (3.15)

$$l = 2f\left(\frac{a}{4f}\sqrt{(1 + \left(\frac{a}{4f}\right)^2} + \frac{1}{2} ln \frac{\sqrt{1 + \left(\frac{a}{4f}\right)^2} + \frac{a}{4f}}{\sqrt{1 + \left(\frac{a}{4f}\right)^2} - \frac{a}{4f}}\right) \tag{3.15}$$

3.2.2.2 Area of the receiver (Ar)

As mentioned earlier, each the collector and glass tube length is of 2 m. Similarly, the receiver is a two meter long (L) and 22 mm diameter copper tube (D_r) covered by a 60 mm evacuated tube and the area is calculated as follows.

$$A_r = \pi . D_r . L \tag{3.16}$$

3.2.2.3 Concentration ratio

The concentration ratio (CR) is the term used to explain the amount of radiation concentration attained by the combination of a collector and receiver. The CR is explained as the ratio of the aperture area to the receiver pipe. It gives a practical estimate of the factor by which radiation flux on the energy-absorbing surface is increased. Which means it is a geometric ratio in that the collector aperture area (A_c) is divided by the surface area (A_r) of the receiver:

Where A_a is the paraboloid aperture area, A_r is the receiver area, D_c is the paraboloid diameter and D_r the diameter of the receiver.

$$CR = \frac{A_c}{A_r} \tag{3.17}$$

3.2.2.4 Rim angle

The rim angle (φ_r) (see Fig. 3.3) is defined as the angle measured at the focus from the axis to the rim of the solar parabolic truncated. The rim angle affects the solar radiation that reaches the collector and PTSC [110]. The rim angle has remarkable features that alone determine cross-sectional shape of PTSC. The rim angle is described as Eq. (3.18).

$$\varphi_r = 2tan^{-1}(\frac{a}{4f}) \tag{3.18}$$

Technical specifications of the parabolic solar collector are given in Table 3.1 for the ready reference.

Table 3.1

Technical specifications of parabolic solar collector

Name	Symbol	value
concentrator aperture	a	1.7 m
concentrator length	L	2 m
Receiver tube outer diameter	D_{ro}	0.022 m
Receiver tube inner diameter	D_{ri}	0.018 m
Glass envelope outer diameter	(D_{go})	0.06 m
Glass envelope inner diameter	(D_{gi})	0.054 m
Collector area	A_c	3.28 m^2
Concentration ratio	CR	23
Glass cover transmittivity for solar radiation	τ	0.89
Specular reflectivity of the concentrator surface	ρ	0.88
Absorber tube emissivity/absorptivity	α	0.94
Intercept factor	γ	0.95
Mass flow rate of water	m	0.2 kg/sec.
Focal length	f	0.4 m
Rim angle	φ_r	93.5^0

3.2.3 PTSC structure

PTSC is susceptible to high aerodynamics forces and its own weight. As a result, PTSC structure should be rigid and strong enough to withstand these effects [111]. Considering the above factors, structure of collector is made up of steel materials, such as rectangular hollow section (RHS), U-channel, flat and angle steel. The stand of the PTSC is constructed employing strong U-channel and RHS bar steel in order to withstand hard weather conditions. The stand of the collector is fixed on a concrete ground using anchor bolts. In order to develop high performance PTSC, its profile should be perfect and smooth. Due to this reason, metallic frames are included on the back surface of the sheet. In order to keep the parabolic curve, the frames are cut as perfectly as possible from 8 mm thickness mild steel plate using automated lather cutting machine.

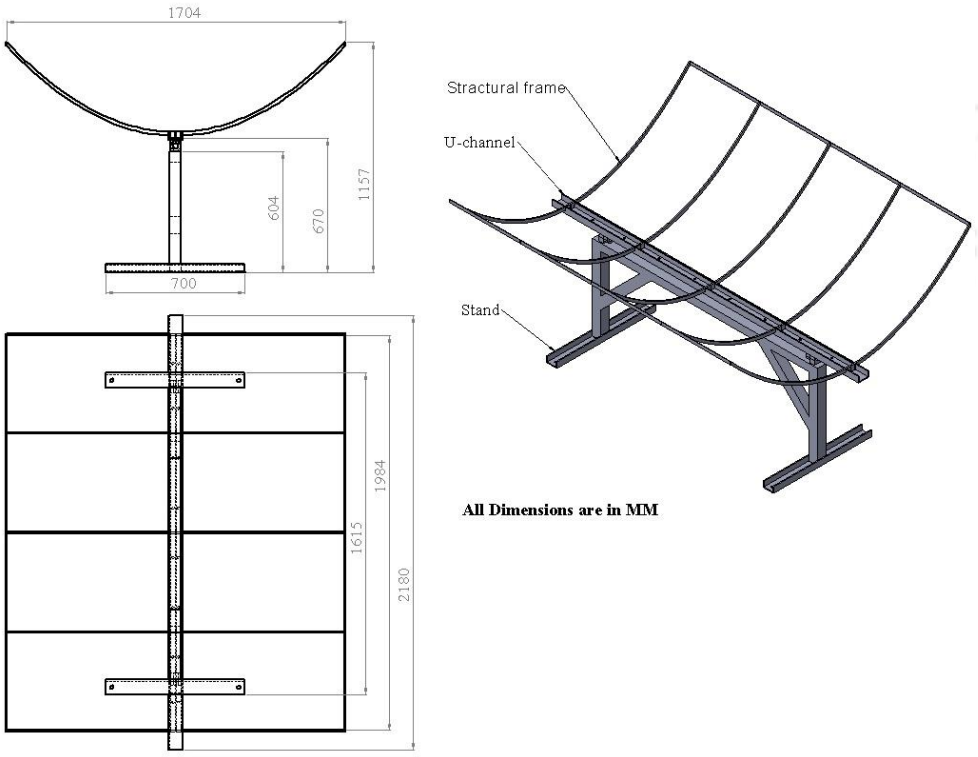

Fig. 3.4.Principal dimensions of the PTSC

The frames are welded on U – shaped mild steel. The distance between consecutive frames is kept as 500 mm and is shown in Fig.3.4. Opposite ends of the frames are connected by a flat steel bar. The aperture area of the reflecting surface is 3.4 m^2 and very high shinny steel sheet is used as a

reflected surface. The reflective mirror made from stainless steel sheet is bolted with the metallic frames as shown in Fig. 3.5.

The shape of the parabola may not have been perfect due to issues during construction, such as imperfect alignment among metal guiding frames and imperfect laminating of the reflecting material. This could affect the quantity of solar radiation on the absorber system and the amount of heat transferred to working fluid, which circulates through absorber tube collector.

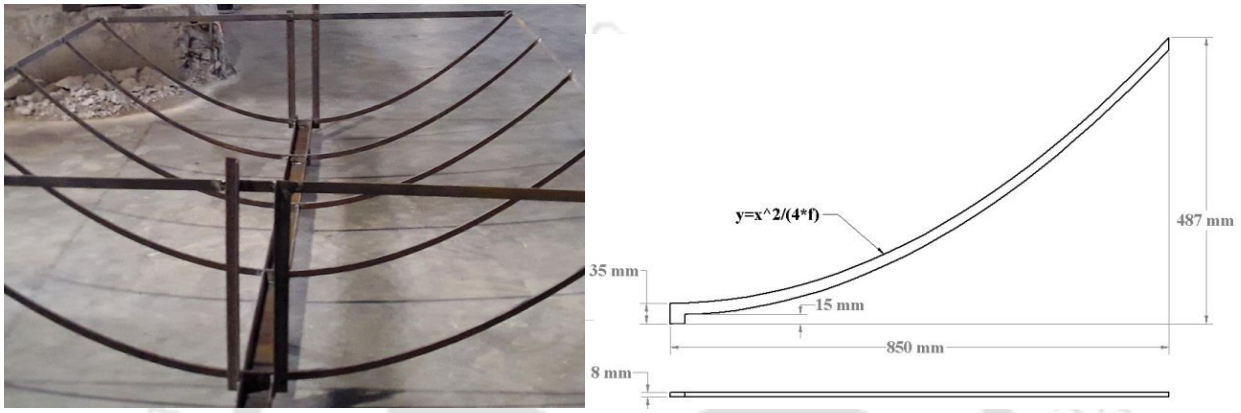

(a) (b)

Fig. 3.5. Pictorial view of PTSC during construction (a) and profile of the steel frame (b)

3.2.4 The Reflecting Assembly

For the collection of the solar energy, the PTSC commonly employs a mirror, aluminum foil or stainless steel sheet in the shape of a parabolic cylinder [108]. The sun radiation is reflected and concentrated towards a receiver pipe located at the focus line of the collector. The receiver absorbs the incoming radiations and transforms them into thermal energy. The energy is being transported and collected by HTF circulating within the receiver tube. The reflecting material here in this study is made up of stainless steel sheet having 0.4 mm of thickness. Due to good reflectivity, non-corrosive and easily to bend stainless steel is selected.

3.2.5 Solar Absorption System

The solar radiation incident on the surface of PTSC is reflected back to the receiver (absorption) system. Hence, the receiver is an important element of PTSC, in which solar radiation is converted in the form of thermal energy. As shown in Fig.3.6, PTSC absorption system comprises of a glass tube shield, receiver tube, support device and bushing. Absorber tubes are commonly built from high conductive metal pipes. Similarly, in this study the absorber tubes are manufactured from

copper pipes. The absorber tube is painted by black coating materials to improve solar absorption ability as well as low emittance coefficient [112]. Therefore, minimal losses eventually result to maximize thermal efficiency. The absorber system is placed at the focus line, i.e., the central axis of the absorption system placement coincides with the focal line of PTSC. The copper pipe external diameter (D_r) and internal diameter (d_r) is set to be 22 mm and 18 mm, respectively. For minimal heat losses, the absorption tube has to be enclosed in a concentric glass tube. The external diameter (D_g) and inter diameter (d_g) of glass envelope tube are 60 mm and 54 mm, respectively. The effective length of the glass envelope and receiver tube is equal to the length of PTSC, i.e., 2000 mm.

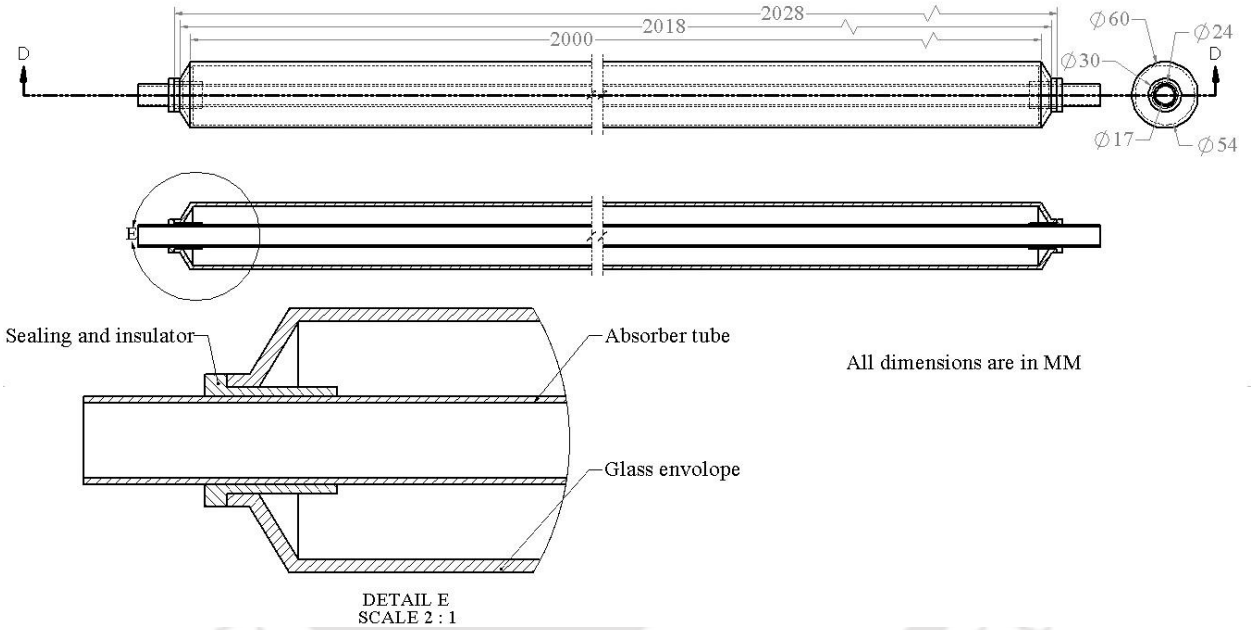

Fig. 3.6.CAD view of the solar receiver system

3.2.6 PTSC Orientation

In order to obtain maximum utilization of the solar radiation received, the position of the sun needs to be tracked. The strength of solar radiation varies during the day and with seasons as well [113]. In general, the tracking collectors can be categorized into two groups; single-axis tracking and double-axes tracking collectors. A PTSC can be orientated along with its long axis in either east-west or north-south direction and its aperture is tilted straight towards the equator at an angle, which equals to the local latitude. In the north-south direction orientation, the collector must follow the sun from east to west by rotating its axis in order to face sun continuously. On the other hand, PTSC can be installed in the east-west orientation tracking the sun from north to south [114].

During a year, a horizontal north-south alignment collects slightly more energy than a horizontal east-west one. As a result, the PTSC designed by us is oriented in a north-south orientation and the sun is tracked manually from east to west direction. For this reason, a manually driven PTSC tacking device is developed in the Mechanical Central Workshop at IIT Guwahati and, the principal and pictorial view of the device is shown in Fig.3.7.

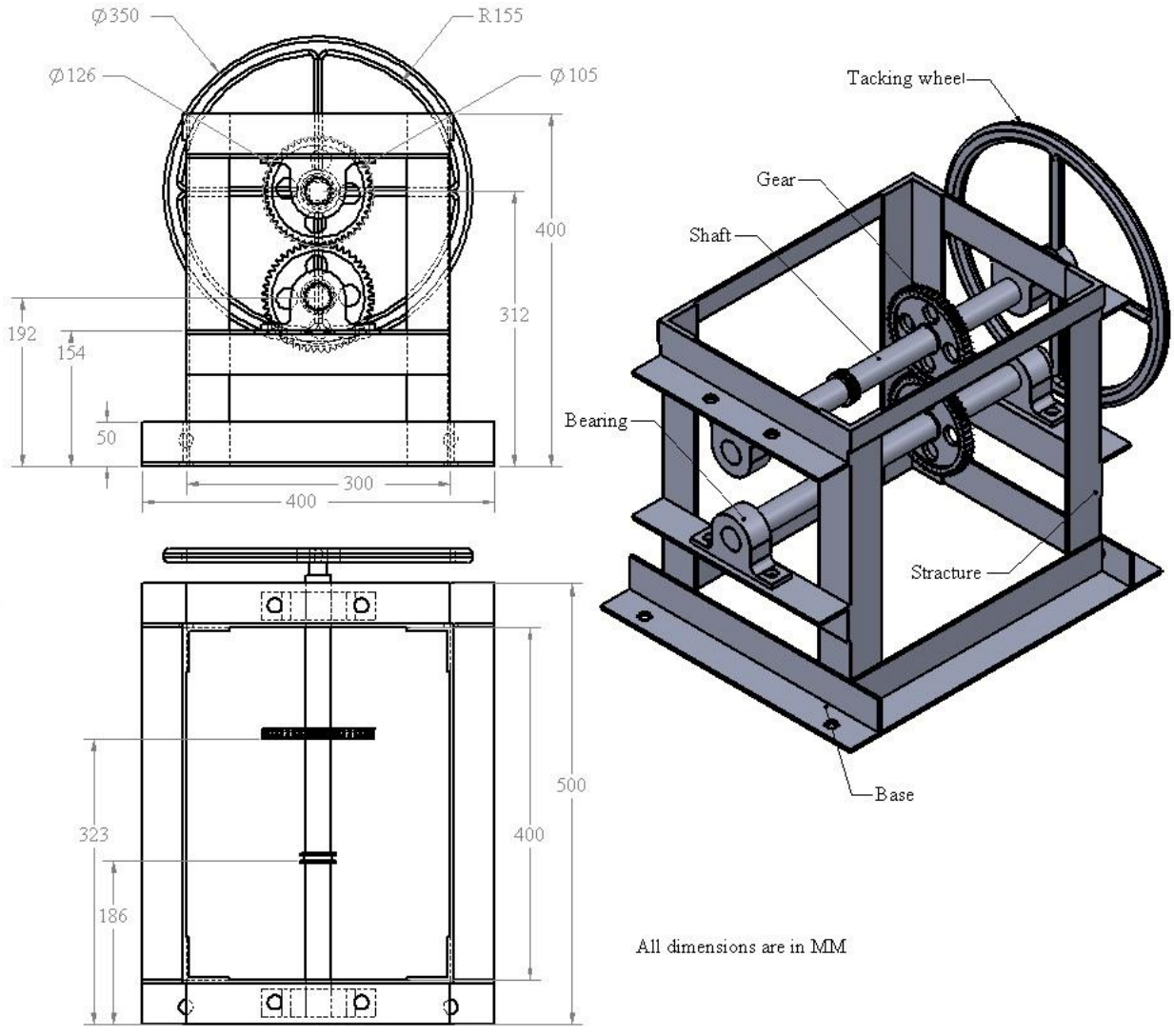

Fig. 3.7.Principal and pictorial representation of the tracking device

3.3 Lab-scale LHS unit sizing and fabrication

The overall design of thermal energy storage (TES) is presented in this section. Details of three basic components (storage tanker, HTF tubes (pipes) and fins) are presented in detail.

3.3.1 Sizing of LHS unit

In the case of latent heat storage, the amount of heat getting stored depends on the mass and the latent heat fusion of the PCM. The material used for this type of application is called phase change materials (PCM). Due to the existence of two phases, handling this type of system becomes very complex, although latent heat storage is an isothermal phenomenal. As explained earlier, TES technologies based on PCM store energy in sensible and latent heat forms. SHS can also store energy due to the density and specific heat of the storage material during the process of melting and solidification. Hence, the amount of heat stored depends on the specific heat of the medium, change of temperature, amount of storage material and latent heat of fusion. The energy stored in a sensible form is described by Eq. (3.19).

$$Q = \int_{T_l}^{T_m} mc_p dT + mL + \int_{T_m}^{T_l} mc_{lp} dT \tag{3.19}$$

where Q is the total amount of energy stored [J]; m is the mass of the medium [kg]; C_p is the specific heat of the medium that depends on temperature [J/kgK].

Three important factors must be taken into consideration to designs a solar TES system, which are technical properties, cost-effectiveness and environmental impact [28]. As we know, latent heat storage with PCM have drawn attention of thermal energy researches for solar power generation and other applications due to their high phase transition enthalpy and high working temperature.

Identifying the most preferred PCM for medium temperature cooking applications is an important issue to be addressed. A medium melting temperature PCM is required for solar cooking [28]. A detailed study of all the commercially available PCMs is conducted and a commercial sugar alcohol used sweetener in the food industry known as Erythritol ($C_4H_{10}O_4$) is selected as a suitable material to be used as PCM because of its superior thermo-physical properties. Erythritol has excellent chemical stability after multiple phase change cycles, low cost, safe, high latent heat, wide-range transition temperature of latent heat of fusion, a suitable phase change temperature and higher decomposition temperature. Erythritol is a very promising medium melting temperature PCM for solar and other applications as a TES system. The phase change temperature of PCM is in the range of 116-120 ^{0}C is selected for the proposed storage application. Around 100 ^{0}C temperature heat is sufficient to cook most of the food items.

Heat storing container preserves solar energy in the form of heat by altering solid phase of the material into the liquid phase. This stored energy is released for cooking during the absence or lower intensity of sunlight. The size of the tank is designed depending on the maximum quantity of heat needed to be stored and the thermal properties of the fluid used for circulation. In order to determine the size of TES, the total amount of energy required for daily cooking should be determined first. It is important to mention that the daily total thermal energy required ($E_{req.}$) of a household for all cooking purposes is approximately 22 MJ.

The size of the tank directly depends on the maximum quantity of energy that needs to be stored and the physical properties of the circulating HTF. Hence, considering the efficiency of the storage tank (η_{sto}), the energy to be preserved in the tank can be calculated employing Eq. (3.20).

$$E_{sto.} = \frac{E_{req.}}{\eta_{sto.}} \tag{3.20}$$

Considering the charging/discharging efficiency of the storage unit as 70 %, Eq. (3.20) is determined as follows.

$$E_{sto.} = \frac{22\ MJ}{0.7} \approx 32\ MJ$$

The total heat of PCM is calculated using the equations below.

$$E_{storage} = \int_{T_i}^{T_m} mc_p\, dT + ma_m \Delta h_m + \int_{T_m}^{T_f} mc_p\, dT = m\left[c_p(T_m - T_i) + a_m \Delta h_m + c_{lp}(T_f - T_m)\right] \tag{3.21}$$

where, A_m =Fraction melted

Δh_m=Heat of fusion per unit mass [J/kg]

m =Mass of heat storage medium [kg]

C_{lp}= Average specific heat between T_m and T_f [J/kg K]

$$C_p\left(\frac{kJ}{kg \times C^0}\right) = \begin{cases} 1.68 & for\ T \le 118\ C^0 \\ 2.66 & for\ T \le 118\ C^0 \end{cases} \tag{3.22}$$

From the above equation, we can estimate mass (m) of the required PCM as follows.

$$m_{PCM} = \frac{E_{sto.}}{C_p(T_m - T_i) + a_m h_m + C_p(T_f - T_m)} = 58\ kg$$

$$V_{PCM.} = \frac{m_{PCM}}{\rho_{PCM}} = \frac{58kg}{1450\ kg/m^3} = 0.04\ m^3$$

where $m_{storage}$ is the mass of the storage tank; $V_{storage}$ is the volume of the tank and ρ is the density of the PCM.

There are different problems that PCM must overcome to be deployed for effective application. Low thermal conductivity is one of the critical problems of PCMs and can be improved using effective techniques. The inclusion of extended surfaces into PCM is one of the most common methods employed to improve the thermal conductivity of an energy storage system. In the present study, a shell and tube type of LHS with multiple finned HTF tubes is designed. For the maximum heat transfer from the heat source to the PCM, employing fins is a commonly practiced and efficient technique [115]. Petroleum-based HTF is commonly utilized to study the performance of charging and discharging of LHS system having high and medium melting temperatures. The total number of HTF tubes (N_t) is determined to be 19 by virtue of the optimization method and four longitudinal fins are welded in every tube as indicated in Fig.3.16. The total number of fins (N_{fins}) is 76. A detailed analysis of the optimization process is presented in section 5.7.1. The width and thickness of the fins are 12 mm and 2 mm, respectively. Similarly, the external diameter and thickness of the copper tube are 20 mm and 2 mm, respectively.

A tank with a diameter *D* and height *l*, and volume *V* is considered for the study. The volume of the tank is expressed by Eq. (3.23). The enclosure of the regenerative shell and tube type heat exchanger is fabricated using a 3 mm thick stainless steel plate to protect from rust and corrosion. Similarly, because of the excellent thermal conductivity property, copper is utilized for HTF tube and fins. It is to mention that the storage system is 1000 mm long and the internal diameter of the shell is 240 mm.

The volume of PCM can be related with the gross volume of storage shell, HTF tube and fins as indicated in Eq. (3.23) [86].

$$\begin{aligned} V_{PCM} &= V_{shell} - V_{tubes} - V_{fins} \\ &= l * \left[\frac{\pi}{4}(D^2 - n_t d_o^2) - n_{fins} \times t \times h\right] \end{aligned} \tag{3.23}$$

Except for *l* and *D*, all the terms in the above equation are known and two parameters are assumed to be related according to the following relationship.

$$l = 4 \times D \tag{3.24}$$

From the above equations, the diameter and length of the shell are estimated as 0.24 m and 01 m, respectively.

$$0.04 = 4D \times \left(\pi\left(\frac{D^2 - 19 \times 0.02^2}{4}\right) - 76 \times 0.002 \times 0.012\right)$$

$$l = 4 \times 0.24\ m \approx 1\ m$$

Table 3.2

Thermo-physical properties of the PCM

Chemical property of PCM	Erythritol
Melting Point	118 ^{0}C
Latent heat of fusion (L_{HF})	354.7 kJ/kg
Density (ρ) at melting point	1450 kg/m^3
Thermal conductivity	0.73 W/(m.K)

The material properties of the selected PCM and HTF are depicted in Table 3.2. Erythritol retains good thermal stability after multiple thermal cycles and its latent heat starts displaying slow degradation after 500 thermal cycles [116], [117]. Important information about the dimensions of TES is presented in Table 3.3.

Table 3.3

Principal dimensions of TES

Item	Height(H)(m)	Diameter (m)		Width(w)(m)	Thickness(t)(m)	Vol.(m^3)	Qty.
		External	Internal				
TES tanker	0.96	0.246	0.24		0.003	0.04345	1
Tube	0.96	0.018	0.0156		0.002	0.004643	19
Fin	0.96			0.012	0.0015	0.001313	76

3.3.2 LHS unit manufacturing

In this section, various components of LHS unit development process are discussed. The materials required for the fabrications of the components were collected from the local market and manufactured at the IIT Guwahati's Central Workshop indigenously. The overall design and sizing of LHS thermal energy storage are discussed in section 3.3.1. The assembled CAD multi-view of LHS unit is shown in Fig.3.8 and it consists of two major components, the shell and bundles of finned HTF tubes. The shell includes the tank (Fig.3.9), front header and rear header (Fig.3.10). Furthermore, the storage unit consists of data monitoring instruments, such as temperature sensors and pressure gauge. The HTF carries heat from the solar collector and passes it through HTF tube transferring solar thermal energy to the PCM.

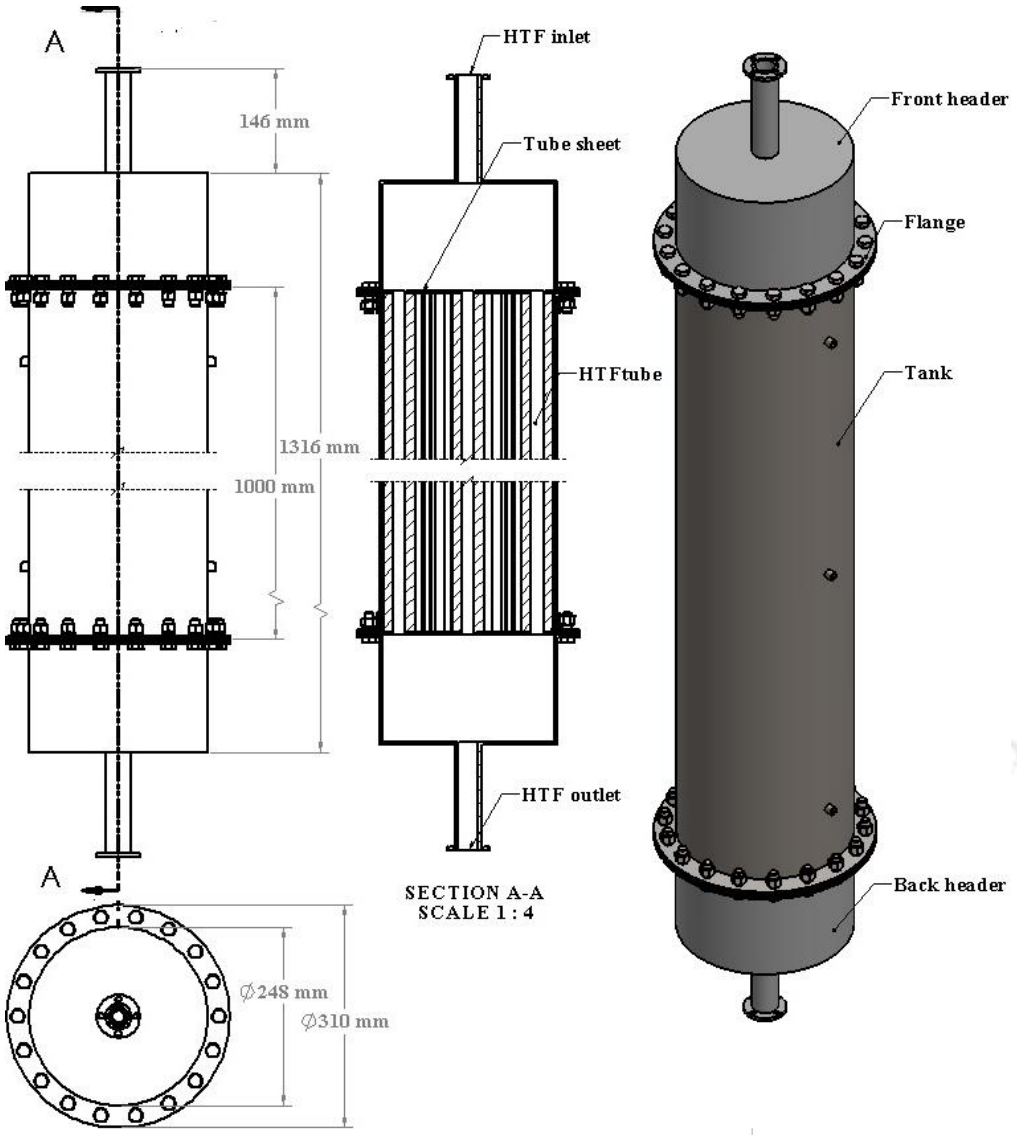

Fig. 3.8.Principal and pictorial view of LHS unit

3.3.2.1 Storage tank

Fig.3.9 displays the front and side views of the storage tank. The PCM is placed in the annulus between the tank and bundle of tubes. The internal diameter and length of the tank are 240 mm and 1000 mm, respectively. The storage tank is manufactured using 3 mm thick stainless steel plate. The storage tank is coupled with other components to form an enclosure and for this purpose, flanges are provided at both ends of the tank.

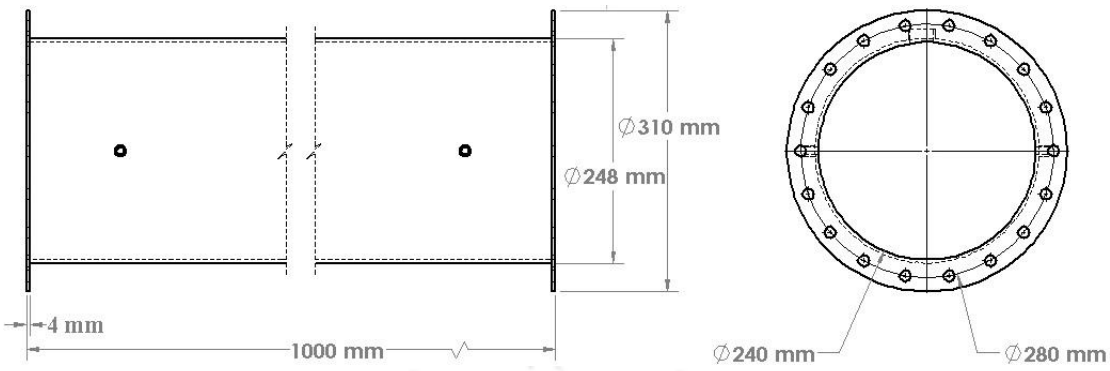

(a)

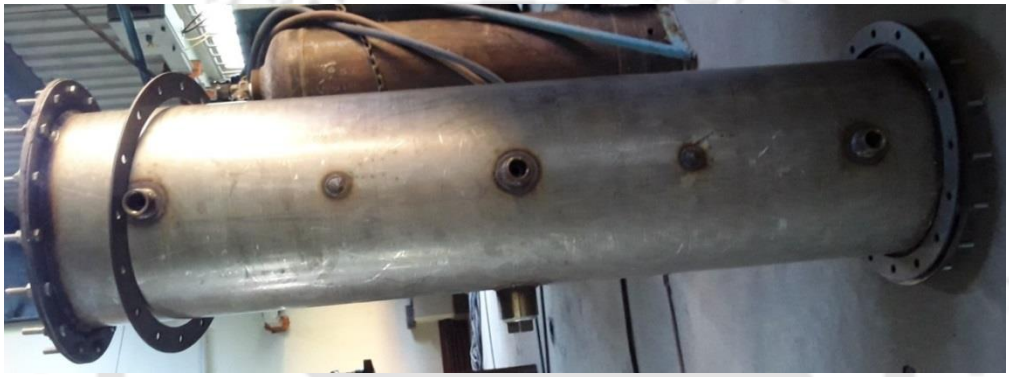

(b)

Fig. 3.9.The principal (a) and photographic (b) view of storage tank

3.3.2.2 Front and back header

Fig. 3.10 illustrates the CAD view of the front and back header of the storage unit, and both the components are identical. HTF enters into the tube side of the storage unit through front header. On the other hand, the rear header is employed to discharge HTF out of the storage unit and both headers are used as a diffuser to stabilize the HTF flow. Similar to the storage tank, the front and back header are crafted using the same thickness stainless steel material.

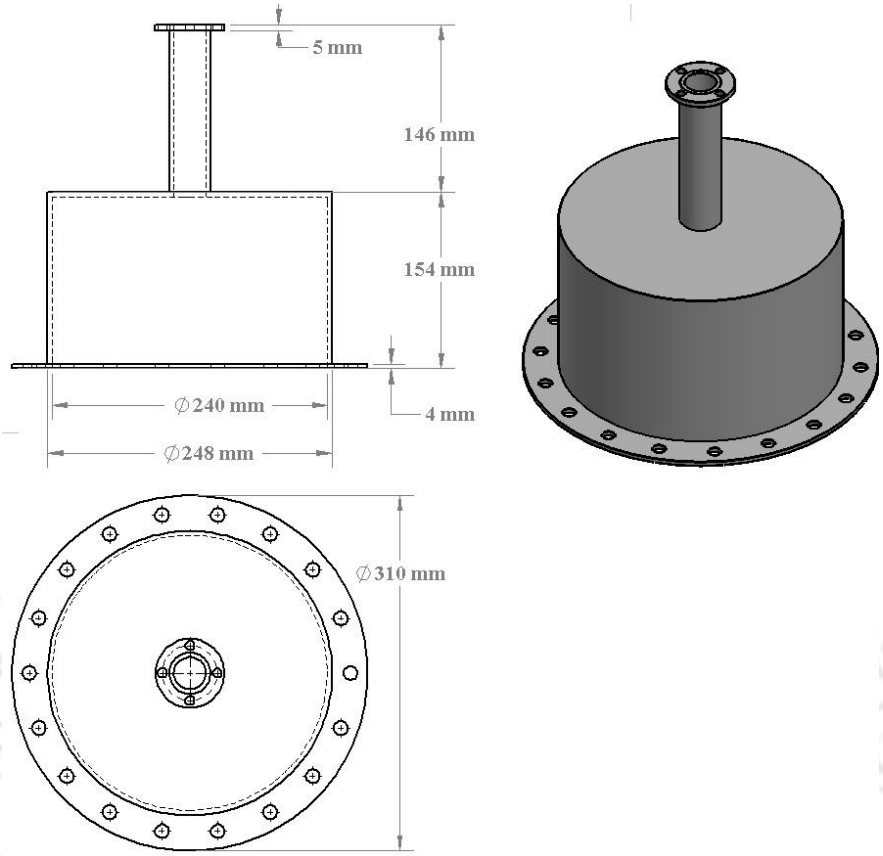

Fig. 3.10.Multi-view of the front and back header

3.3.2.3 Finned HTF tubes

As mentioned in the previous section, LHS unit comprises of the shell, 19 tubes and 76 fins. In order to enhance transfer of heat from heat carrying fluid to the PCM, each HTF tube is welded with four fins. The HTF tubes and fins are fabricated using copper tubes and copper sheets, respectively. Copper is selected because of its superior heat conductivity property. For the integration of each copper tube with respective fins, continuous welding is mandatory. If there is a discontinuity between the copper tube and fins, the heat transferring rate from tubes to the fins would be hindered. However, continuous welding tends to melt the metal and create holes or crack that may result in leakage. Therefore, in order to deter such consequences, welding is performed very carefully using low temperature melting and good conductor silver filler material. Finned HTF tubes are shown in Fig. 3.11.

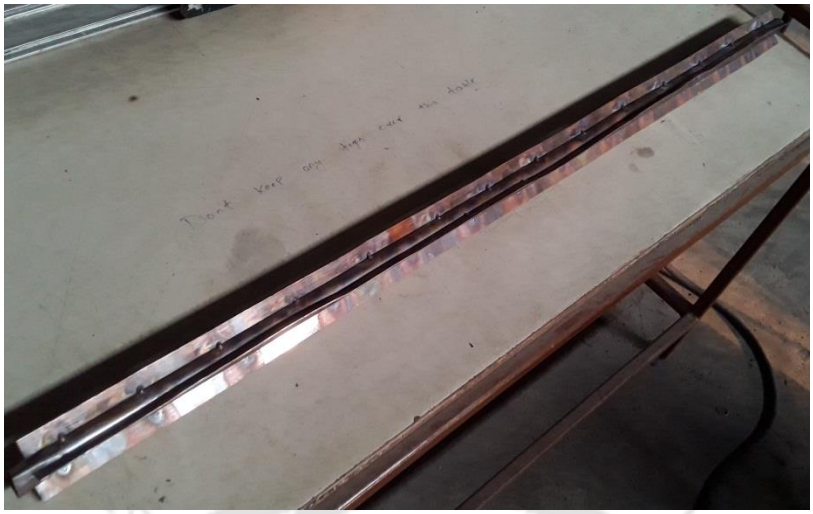

(a) Photograph of finned tube

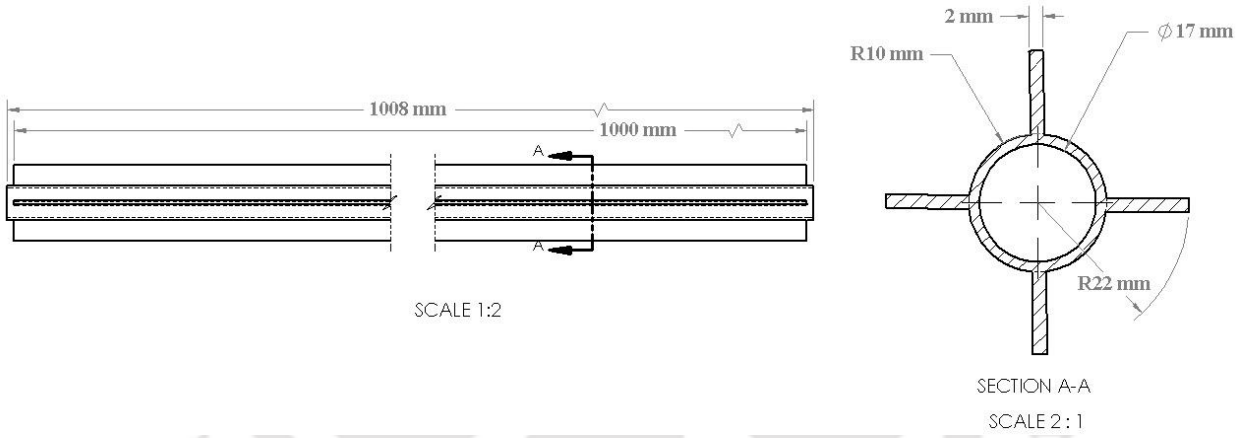

(b)

Fig. 3.11.Finned HTF tubes (a) photographic pictorial view and (b) multi view

3.3.2.4 Tube sheet

The storage system comprises of the front and back side tube sheet (plate). The CAD and photographic view of the tube sheet are shown in Fig 3.12. Similarly, the tube sheet is made using 4 mm thick copper plate. The tube sheets are used to separate tubes and distribute them uniformly across the LHS system. Both the front and back side of the tube sheets are drilled with 19 holes so that the working fluid is confined to move from the front toward the back header via copper tubes. Hence, the ends of tubes pass through the holes of the front and back side tube sheets, and are joined by welding. The finned HTF bundles and tube sheets form a cage structure. This structure is inserted into the tank and is covered at both sides by the front and back headers. Later it is bolted altogether through the flanges provided. The principal dimensions of the designed shell and tube

heat exchanger type of storage are the internal diameter of the shell and its length, whose values are 240 mm and 1000 mm, respectively.

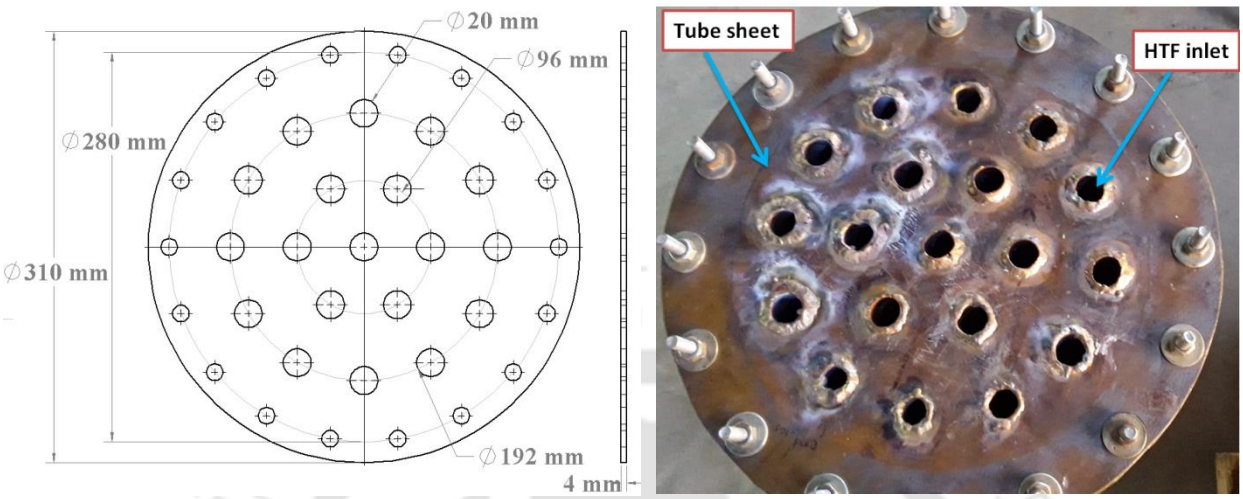

(a) (b)

Fig. 3.12.CAD view (a) and photographic view of the copper tube sheet (plate) (b)

3.4 Experimental setup layout

The photographic view of the assembled experimental setup applied for the proposed study is shown in Fig 3.13. PTSC is used to convert solar radiation into thermal energy and a receiver is placed at the focal line of PTSC. The solar radiation fall on the collector is reflected back to the receiver. The developed storage system is a shell and tube type version of heat exchanger designed for latent heat storage purposes. The PCM is filled in the vacant space between the shell and tubes and HTF supplies or releases heat to the PCM during its passage through tubes. The principal dimensions of LHS unit components are indicated in Fig. 3.8. The LHS unit is heated /cooled during the charging /discharging employing waste cooking oil as HTF. The working fluid passes through HTF tubes of the LHS unit to transfer thermal energy and stored it in the form of sensible and latent heat. A gear pump is utilized to pump HTF through the receiver of PTSC and feed it back into the energy storage system. Furthermore, several accessories and measuring instruments are employed along with the above-mentioned items. Some measuring instruments are presented in the next section.

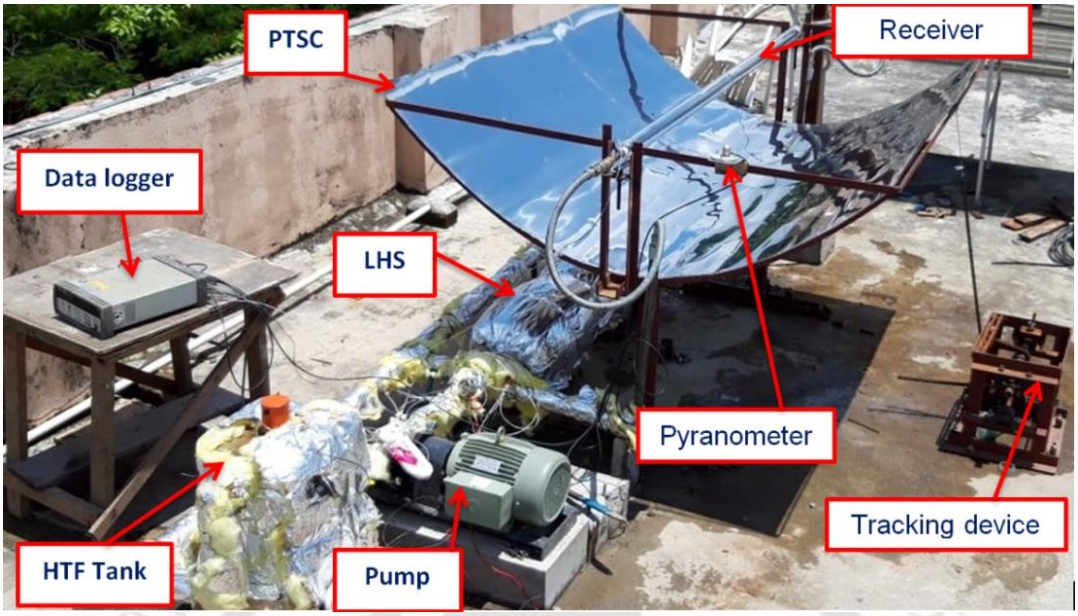

Fig. 3.13.Photographic view of the experimental setup

3.5 Measuring instruments

The experimental and metrological data are collected using the respective instruments. This is to mention that all measuring instruments are fixed at the right positions. Hence, the major measuring instruments that are used during experimentation are described below.

i) **Pyranometer**: It is used to measure the solar radiation strength incident on the surface of the reflector. The pyranometer made by Apogee bearing model number SP-101 is employed during experimentation.

ii) **Data logger**: Data logger (Agilent 34972A), which is developed by Agilent Technologies, is utilized to monitor and store transient temperature and solar radiation intensity values. The data logger is equipped with a 20-channel multiplexer, through which the thermocouple and pyranometer are connected to it.

iii) **KD2 PRO thermal properties analyzer**: This instrument is employed to determine the thermal conductivity of cooking waste oil, which is used as a working fluid.

iv) **Rheometer**: The dynamic viscosity of the selected HTF is tested using a Rheometer testing machine.

v) **Digital anemometer**: The velocity of wind on the surface of the collector is measured with a digital anemometer shown in Fig 3.14 (g).

vi) **Thermocouple**: The temperature from different locations of the PTS and LHS units is recorded using thermocouples. The temperature sensors applied for PTS and LHS are metal-sheathed K- type thermocouples.

vii) **Infrared thermometer**: The surface temperature at different locations, such as, at the surface of the PTSC and LHS unit are determined using an infrared thermometer.

viii) **Circulating pump**: The working fluid placed in the oil tank is circulated through LHS and PTSC using a gear pump. The pump is capable to operate under high temperature conditions and its discharge rate is 75 LPM.

(a) (b) (c) (d)

(e) (f) (g) (h)

Fig. 3.14.Data measuring instruments

3.6 Summary

In this section, the sizing and fabrications process of PTSC, LHS unit and other supporting devices are summarized. The PTSC system designed in the proposed work consists of several parts and, its aperture and length is 1.7 m and 2 m, respectively. The reflective part of the collector is made using a stainless steel sheet. The LHS unit consists of an enclosure, PCM and 19 finned HTF tubes. Based on the amount of thermal energy required to cook food items of a single household, the size of the storage unit is estimated. Erythritol is selected as PCM and is found to be a very promising medium melting temperature PCM for solar and other applications as TES. The HTF tubes and fins are designed using copper tubes and copper sheets, respectively. The storage system is 1000 mm long and the internal diameter of the shell is 240 mm. The storage tank is designed using a 3 mm thick stainless steel plate. The width and thickness of the fins are 12 mm and 2 mm, respectively. Similarly, the external diameter and thickness of the copper tube are 20 mm and 2 mm, respectively.

Chapter - 4

4 PTSC performance investigation

In this chapter, detailed description of designing a parabolic trough solar collector (PTSC) is presented for solar cooking application using thermal energy storage system. This chapter details theoretical and numerical formulation, analytical and numerical results, solar data input calculation and experimental results of the PTSC developed during fabrication of solar cooker.

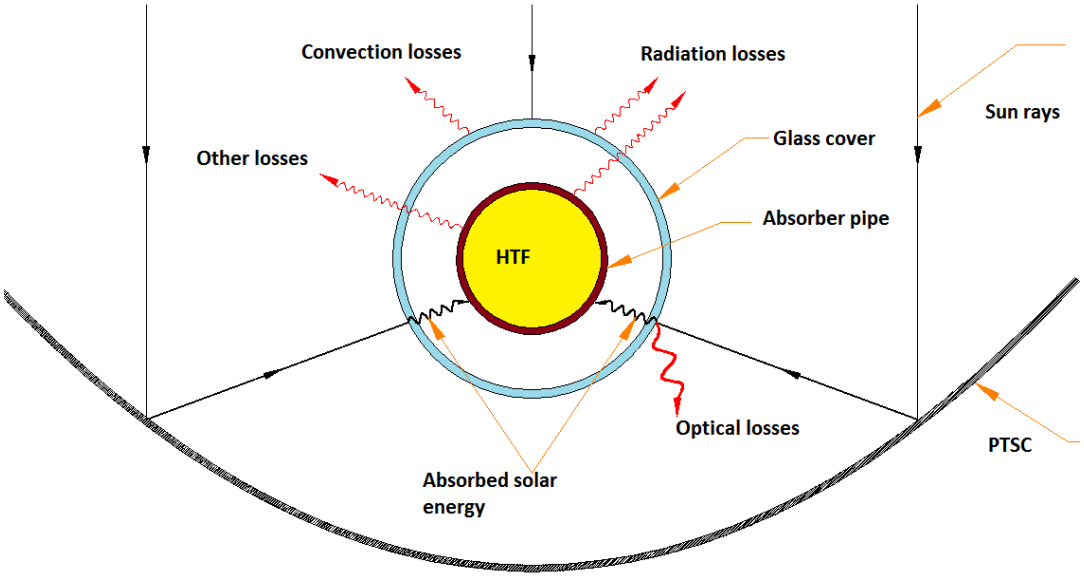

Fig. 4.1.Schematic representation of the cross section of PTSC and solar energy balance

4.1 Optical and thermal modeling of PTSC

Fig.4.1 displays the solar energy absorbed by HTF and energy disperses to the surrounding environment. The performance of PTSC is evaluated considering the optical and thermal parameters. In practice, the concentrator cannot reflect 100% of incident solar energy, which means that a fraction of solar radiation is absorbed by the receiver tube. This is resulted due to the optical losses which hinder the perfect reflection of solar radiation towards receiver. The factors which are responsible to the losses, are accuracy of tracking mechanism, material and shape of the reflector [118].

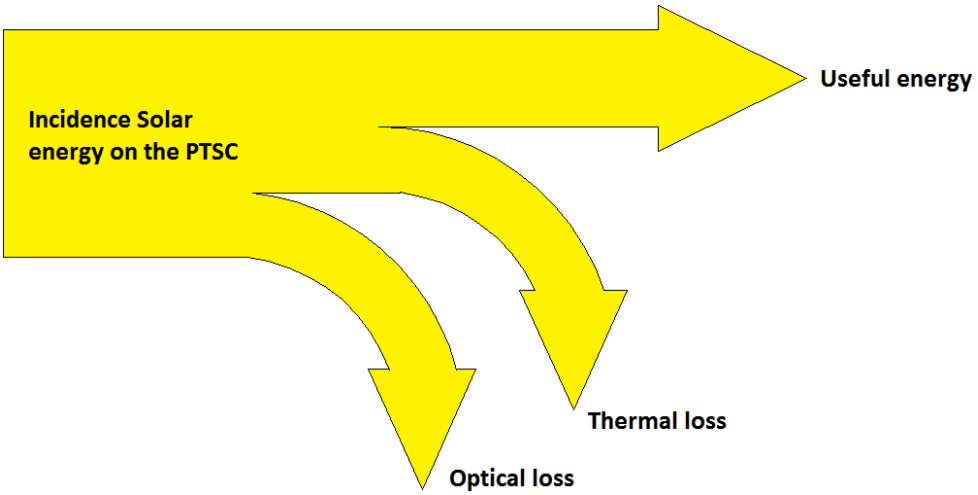

Fig. 4.2.Heat balance of the PTSC system

Considering the heat balance of the system (Fig 4.2), the solar irradiation absorbed (Q_{abs}) by an absorber tube is divided into useful heat (Q_u) and thermal losses (Q_{loss}) as shown in Eq. (4.1). The useful heat generation (Q_u) is an instant magnitude of thermal energy absorbed by HTF, when its pass through the receiver tube [119].

$$Q_{abs} = Q_u + Q_{loss} \tag{4.1}$$

The absorbed solar energy (Q_{abs}) can be estimated based on the solar collector optical efficiency (η_{opt}) and the available solar irradiation (Q_s) [119].

.

$$Q_{abs} = \eta_{opt}.Q_s \tag{4.2}$$

The solar radiation falls onto the PTSC aperture is defined as the product of the direct beam radiation (I_b) and aperture area (A_p).

$$Q_s = A_p.I_b \tag{4.3}$$

The factors which influence optical efficiency of the solar collector system are technical failure tracking error and geometric error. The optical efficiency varies with the solar flux incident angle and it can be formulated with the help of incident angle modifier $K(\theta)$

$$\eta_{opt} = \rho.\gamma.\tau.\alpha.K(\theta) \tag{4.4}$$

An incidence angle modifier is used to estimate incidence angle deviation from the normal incidence radiation on the aperture. Hence, it is related with geaometric features of the PTSC and

the incident angle (θ) [120]. Therefore, the mathematical expression for an incidence angle modifier is represented by Eq. (4.5).

$$K(\theta) = \cos(\theta) - \frac{f}{L}.\left(1 + \frac{W^2}{48.f^2}\right).sin(\theta) \tag{4.5}$$

Fig. 4.3 shows the sectional view of the receiver system and the thermal resistance network. The heat transfer processes in the PTSC receiver system consist of the solar energy absorption on the receiver pipe and the glass cover. The second process is the convection mode of heat transfer from the receiver to the HTF and from the glass cover to the environment. The next heat transfer is radiation, which flows from the receiver pipe to the glass cover and then to the ambient. Another heat transfer process is the conduction heat transfer between the glass tube and absorber pipe [121].

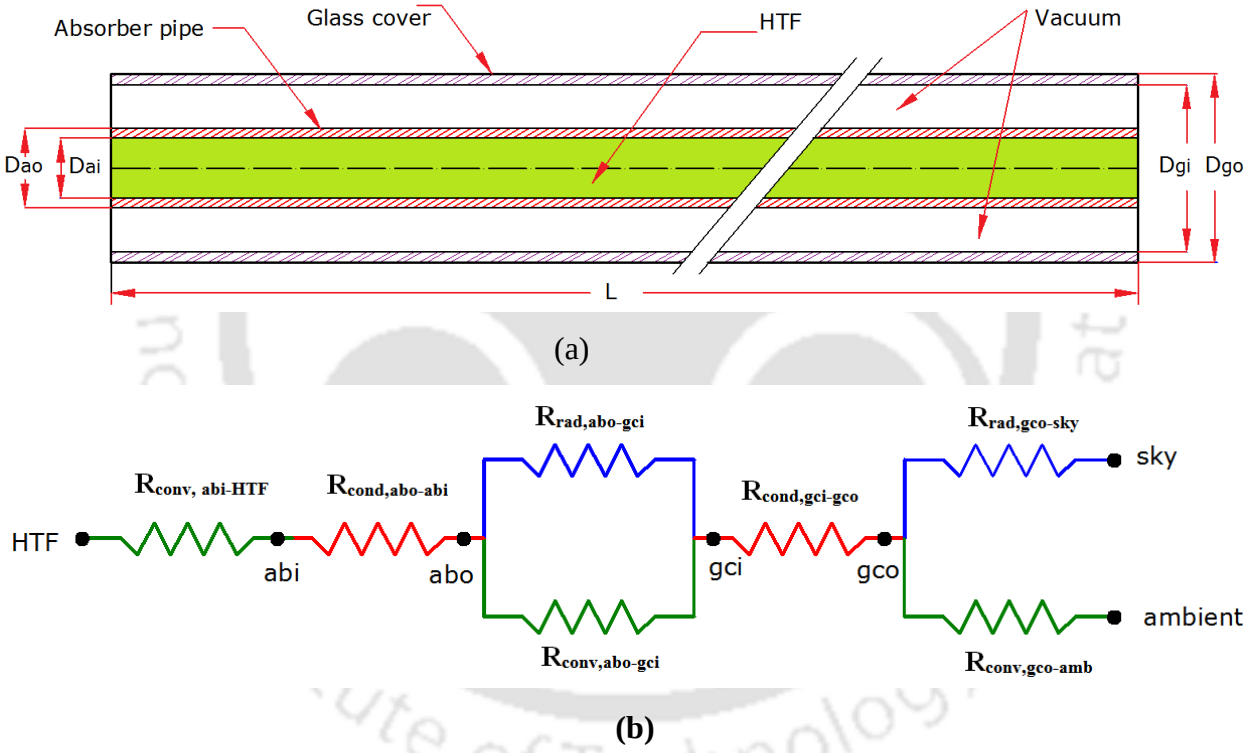

Fig. 4.3.Sectional view (a) and thermal resistance network (b) of a receive pipe

The performance of solar collector is affected by two major parameters; (1) parameters which are related with the design of the collector, (2) the parameters which have a significant role in the operating conditions. The heat removal factor (F_R), collector efficiency factor (F'), heat loss coefficient (U_L) and optical efficiency are design parameters, whereas, solar flux, ambient temperature, inlet HTF temperature are the parameters having an impact on the operating

conditions. The working fluid or HTF is directed to flow inside the absorber tube to extract solar thermal energy from receiver.

The collector efficiency factor (F') is a constant defined as the ratio of actual useful energy extracted to the useful energy gain resulting when the temperature of the whole collector absorber surface and local mean fluid temperature remains same.

$$F' = \frac{U_o}{U_L} \tag{4.6}$$

All thermal losses are combined into single coefficient called overall loss coefficient (U_L) and it is one of the most imperative parameters. Assuming the air placed between the glass and absorber tube is in a standstill condition, the overall loss coefficient can be estimated as follows.

$$U_L = \left[\frac{A_{ro}}{A_g\left(h_{c,g-amb+}h_{r,g-amb}\right)} + \frac{1}{h_{r,r-g}}\right]^{-1} \tag{4.7}$$

In the above equation, $h_{c,g\text{-}amb}$ is the convection HTC between glass cover and the ambient that is occurred due to the flow of wind, and is explained as [122].

$$h_w = h_{c,g-amb} = \frac{Nu_a \times k_a}{D_g} \tag{4.8}$$

The Nusselt number for air flow over the absorber tube is estimated using the following equations [121].

$$Nu = 0.4 + 0.54Re_a^{0.53}\ for\ 0.1 < Re_a < 1000$$
$$Nu = 0.3Re_a^{0.6}\ for\ 1000 < Re_a < 50{,}000 \tag{4.9}$$

It is also important to define the equation of Reynolds number and it is determined by internal flow conditions.

$$Re_a = \frac{\rho_a V_a D_g}{\mu_a} \tag{4.10}$$

where k_a, ρ_a, μ_a and υ_a are thermal conductivity, density, dynamic viscosity and velocity of air, respectively and D_g is the cover diameter.

$h_{r,g\text{-}amb}$ is the radiation HTC between glass and the ambient, which defined as Eq. (4.11).

$$h_{r,g-amb} = \varepsilon_g \sigma\left(T_g + T_{amb}\right)\left(T_g^2 + T_{amb}^2\right) \tag{4.11}$$

$h_{r,r\text{-}g}$ represents the radiation HTC between the absorber tube and glass cover and defined as follows.

$$h_{r,r-g} = \frac{\sigma\left(T_r + T_g\right)\left(T_r^2 + T_g^2\right)}{\frac{1}{\varepsilon_r} + \frac{A_r}{A_g}\left(\frac{1}{\varepsilon_g} - 1\right)} \tag{4.12}$$

where T_g, T_r, ε_g, ε_r and δ are temperature of the glass, temperature of the receiver, emittance of glass, the emittance of the receiver and Stefan Boltzman constant, respectively.

U_O stands for the overall heat transfer coefficient. It represents heat transfer from an environment to HTF, and is related with the outer diameter of receiver tube D_{ro}, which is expressed by equation depicted below [121].

$$U_O = \left[\frac{1}{U_L} + \frac{D_{ro}}{h_f D_{ri}} + \frac{D_{ro} \times ln\left(\frac{D_{ro}}{D_{ri}}\right)}{2k}\right]^{-1} \tag{4.13}$$

where, k is the material thermal conductivity of absorber pipe and h_f is the heat transfer coefficient (HTC) of the fluid which is evaluated using Nusselt number as mentioned below.

$$h_f = \frac{Nu_f \times k_f}{D_{ri}} \tag{4.14}$$

Similarly, the Nusselt number in the above equation is estimated using flow conditions of the HTF. For laminar flow, when Reynolds number is lower than 2300, the Nusselt number is utilized. For internal flow in the circular tubes, Nusselt number (*Nu*) can be evaluated employing the equation mentioned below.

For the laminar flow,

$$Nu = 3.66 + \frac{0.0667ReP \times r \times D_{ri}/L}{1 + 0.04 * \left(Re * Pr * \frac{D_{ri}}{L}\right)^{2/3}} \tag{4.15}$$

For the turbulent flow,

$$Nu = 0.023 \times Re^{0.8} \times Pr^{0.4} \tag{4.16}$$

Similarly, Prandtl number (Pr) is defined as

$$Pr = \frac{\mu \times C_P}{k} \tag{4.17}$$

For turbulent flow condition, i.e., Reynolds number greater than 4000, Nusselt Number is used.

It is also important to define the equation of Reynolds number and is determined by employing internal flow conditions.

$$Re = \frac{4\dot{m}}{\pi \times D_{ri} \times \mu} \tag{4.18}$$

The energy losses (Q_{loss}) from absorber to the glass cover are radiation thermal losses, because convection loss is neglected due to the space between the absorber tube and glass cover considered as vacuum [123] and is described according to Eq.(4.19).

$$Q_{loss} = h_{r,r-g}\, A_{ro}\left(T_r - T_g\right) = \frac{A_{ro}\sigma\left(T_r^4 - T_g^4\right)}{\frac{1}{\varepsilon_r} + \frac{A_r}{A_g}\left(\frac{1}{\varepsilon_g} - 1\right)} \tag{4.19}$$

Similarly, the thermal losses from glass to the ambient are both convection and radiation thermal losses and can be estimated as follows.

$$Q_{loss} = h_{c,g-amb}A_{go}\left(T_g - T_{amb}\right) + h_{r,g-amb}A_{go}\left(T_g - T_{amb}\right) \tag{4.20}$$

$$Q_{loss} = A_{go}h_w\left(T_g - T_{am}\right) + \varepsilon_g . A_{go} . \sigma . \left(T_g^4 - T_{amb}^4\right) \tag{4.21}$$

Considering the steady state conditions, thermal losses from absorber to the glass cover (Q_{loss}) and from the cover to the ambient are equal. Furthermore, thermal losses of PTSC can be related with the outer surface area (A_r) and average temperature (T_r) of the absorber tube as well as the thermal loss coefficient (U_L) and is estimated by Eq. (4.22).

$$Q_{loss} = A_r U_L (T_r - T_{amb}) \tag{4.22}$$

The heat removal factor (FR)

The heat removal factor of solar collector (F_R) varies between $0<F_R<1$ and it is used for the estimation of total useful heat gain. The F_R can be defined as the ratio of actual energy to the useful energy that would be collected if the whole collector surface remains at working fluid inlet temperature. The F_R is a convenient measure of the efficiency when absorber tube is considered as a heat exchanger. The F_R depends on HTF flow rate, thermal properties of the working fluid, absorber tube material and can be described by Eq. (4.23).

$$F_R = \frac{\dot{m}C_P\left(T_{fo} - T_{fi}\right)}{A_C\left[S - U_L\left(T_{fi} - T_a\right)\right]} \tag{4.23}$$

The collector heat removal factor can be also rewritten as:

$$F_R = \frac{\dot{m}C_P}{A_C U_L}\left[1 - exp\left(\frac{A_C U_L F'}{\dot{m}C_P}\right)\right] \quad (4.24)$$

Another parameter is the collector flow factor and it is defined as the ration F_R to the collector efficiency factor (F'). Flow factor is commonly applied in the analysis of collectors and it is represented as.

$$F'' = \frac{F_R}{F'} = \frac{\dot{m}C_P}{A_C U_L F'}\left[1 - exp\left(\frac{A_C U_L F'}{\dot{m}C_P}\right)\right] \quad (4.25)$$

Thermal Efficiency of a PTSC

Comparing to the other PTSC parameters thermal efficiency is the most important quantity and it is explained as the ratio of useful heat to the solar direct beam irradiance.

$$\eta_{th} = \frac{Q_u}{Q_s} \quad (4.26)$$

The useful energy gained of a PTSC can be calculated according to the heat balance on the fluid volume of HTF. Depending, the reference temperature taken from the collector the useful energy can (Q_u) can be estimated in to two different ways.

The first one is calculated using the energy balance on the HTF volume.

$$Q_u = \dot{m}C_p(T_{out} - T_{in}) \quad (4.27)$$

If the receiver surface temperature is not known, it is appropriate to express the Q_u in terms of the inlet working fluid temperature by means of heat removal factor F_R as follows.

$$Q_u = A_p F_R\left[S - \frac{U_L(T_{in} - T_{amb})}{CR}\right] \quad (4.28)$$

From Eq. (4.3), (4.27) and (4.28), the thermal efficiency of the collector can now be re-arranged as per Eq. (4.29).

$$\eta_{th} = F_R\left[\eta_o - \frac{U_L(T_{in} - T_{amb})}{I_b * CR}\right] \quad (4.29)$$

The above variables A_a, A_r, T_{in}, T_{out} and T_{amb} represent the aperture area, receiver pipe area, inlet fluid, exit fluid and ambient temperatures, respectively.

Considering the heat transfer between receiver tube and HTF fluid, the useful heat can also be calculated in another way. Convection is the heat transfer mechanism between working fluid and absorber tube, which is formulated using heat transfer coefficient (h) and is presented below.

$$Q_u = hA_{ri}(T_r - T_{fm}) \tag{4.30}$$

where, T_{fm} is the mean fluid temperature that can be estimated as the average of inlet (T_{in}) and outlet (T_{out}) fluid temperatures.

$$T_{fm} = \frac{T_{in} + T_{out}}{2} \tag{4.31}$$

4.1.1 Modified Thermophysical properties Nanoparticles /Nano fluids

Several methods have been practiced to improve the performance of solar collectors. Adding volume fraction of nanoparticles into base heat transferring fluid (HTF) enhances the thermal efficiency of collector system. The dispersed nano-fluids into base fluid enhance thermal properties as compared to the corresponding base fluid [124]. It is important to note that the volume fraction should not exceed 5% [95]. The most common employed nanoparticles are TiO_2, SiO_2, Al, Al_2O_3, Cu, CuO, Au, ZnO, Fe and Fe_2O_3. The major thermal properties that influence the performance of solar collector are density, specific heat capacity, thermal conductivity and dynamic viscosity. The thermal properties of nano-fluid are derived from the respective base fluid and volume fraction of nanoparticle [125] in the following manner.

$$\rho_{nf} = \rho(1-\varphi) + \rho_{np} \times \varphi \tag{4.32}$$

$$c_{p-nf} = \rho(1-\varphi)c_p + \frac{\rho_{np}\varphi c_{p-np}}{\rho_{nf}} \tag{4.33}$$

$$k_{nf} = k\frac{\left(k_{np} + 2k + 2\varphi(k_{np} - k)\right)}{k_{np} + 2k - \varphi(k_{np} - k)} \tag{4.34}$$

$$\mu_{nf} = \frac{\mu}{(1-\varphi)^{0.25}} \tag{4.35}$$

where, φ is the volume fraction of nanoparticles and, ρ_{nf}, k_{nf}, c_{p-nf} and μ_{nf} are density, thermal conductivity, specific heat capacity and dynamic viscosity, respectively.

4.2 Solar data input calculation

For designing and performance evaluation of solar collector systems, it is important to know about the characteristics and nature of solar radiation falling on the surface of earth. Hence, the extent solar radiation incident on the PTSC and position of the sun with reference to the location of the solar collector should be known. Therefore, the position of the sun with respect to the solar collector for every day in a year and time of the day can be related using incidence angle. Knowing latitude angle (φ), hour angle (ω), declination angle (δ), the incident angle is determined using Eq. (A.7). The latitude of the site is 26.19^0 and, declination and hour angles are estimated using Eq. (A.5) and (A.6), respectively.

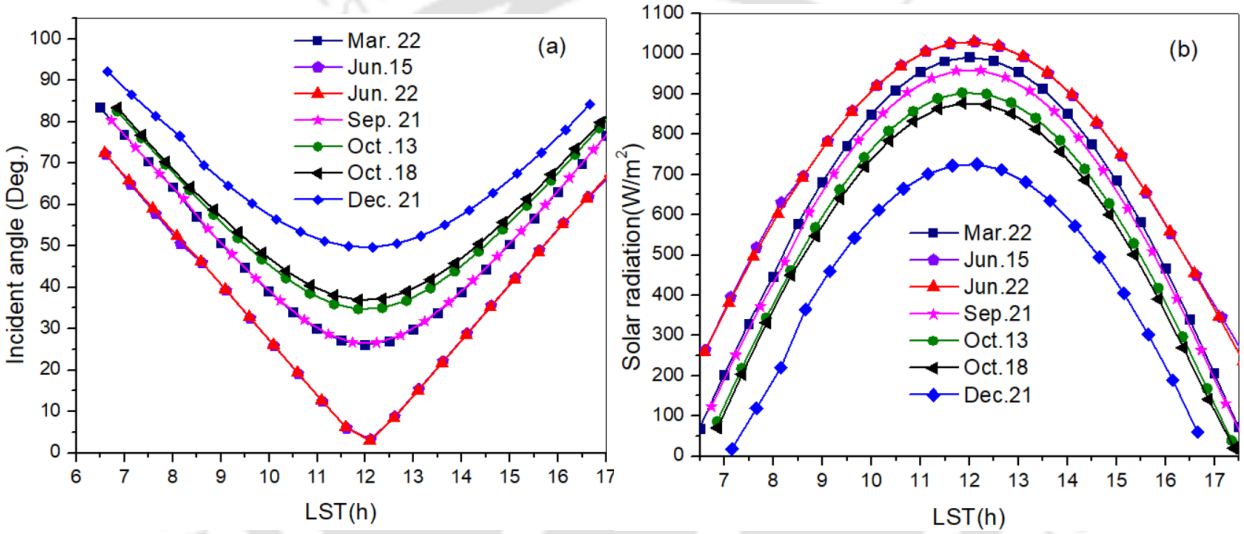

Fig. 4.4.Variation of solar incidence angle (a) and radiation (b) versus solar time of four days

The declination angle variation throughout the year is presented in Fig.A.4 of the Appendix A. The value for June 15 and June 22, and also October 13 and October 18 are -8.482^0, -10.691^0, 23.3140^0, and 23.448^0, respectively. Similarly, incidence angle variation against the solar time on March 22, June 15, June 22, September 21, October 13, October 18 and December 21 are illustrated in the Fig.4.4 (a). When sun is directly overhead of a location point P on a horizontal surface, the incidence angle is zero and the point P gets maximum solar irradiance at this instant.

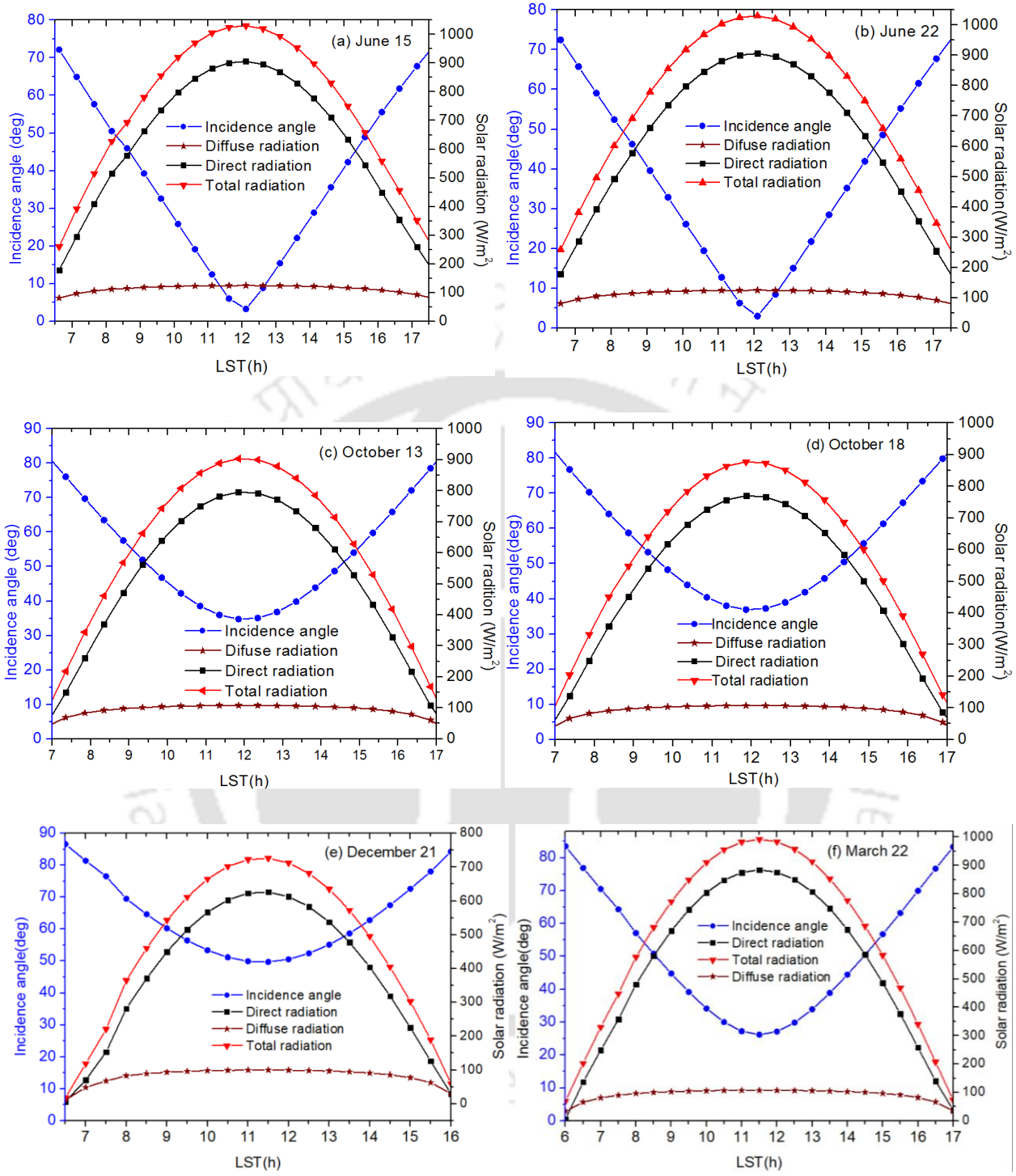

Fig. 4.5.Diffuse radiation, beam radiation, total solar radiation and incidence angle variation versus LST

It can be observed from Fig. 4.4(a) that the incidence angles of June 15 and June 22 decreases more rapidly from morning to solar noon, and increases faster as compare to the incidence angles

recorded on the other days. It means that the total solar radiation falling on PTSC is higher during the month of June and is clearly seen in Fig.4.4 (b). The hourly diffuse, beam and total radiations on June 15, June 22, October 13, October 18, December 21 as well as March 22 are estimated using incidence angle and solar constant, and are presented in Fig. 4.5 (a), (b), (c), (d), (e) and (f), respectively. As it is expected, the radiation is maximum for the days of June 15, June 22 and March 22. The experimental test was conducted on June 15, June 22, October 13 and October 18. As a result, the next analytical, numerical and experimental result discussions are focused on these mentioned four days.

4.3 Analytical and Numerical results

In this section, the results of analytical, numerical and experimental performance evaluation of PTSC are discussed. The effects of various parameters on the thermal performance of PTSC are examined in the analytical study. The same parameters and inputs are employed for all the studies. Several practical experiments are conducted in the months of June and October, and results of four selected days (June 15 and June 22, and October 13 and October 18) are presented in this section.

4.3.1 Analytical performance evaluation of the PTSC

Based on the mathematical equations which are presented in section 4.1, thermal modeling of PTSC is developed using Engineering Equation Solver (EES). The mathematical model is employed to study the thermal performances of the collector by varying important parameters, such as inlet temperature, beam radiation, mass flow rate and mixing nanoparticles with HTF. The thermal model developed in this proposed work is solved multiple times by varying input parameters. Therefore, the following section describes about the effects of above-mentioned parameters on the performance of PTSC. The dimensions of PTSC which is considered for this study, are listed in Table 3.1.

The developed analytical model of the current study is validated using an experimental data found in the literature. These data reported by Dudley et al.[126] are used in order to check if the developed analytical model provides reasonable results. The selected HTF is Syltherm 800, and its properties are listed in Table 4.2. The model is tested for different operating conditions of the PTSC and the results are given in Table 4.1. The outlet temperature of the HTF is considered as decision variable and the average deviation is found to be 0.19%

Table 4.1

Validation of the presented analytical model with experimental results from literature

Cases	I_b	T_{am}	u_{wind}	Vol.	T_{in}	T_{out}(K)		Deviation
	W/m^2	K	m/s	l/min	K	Model	Exp. [126]	%
1	933.7	294.35	2.6	47.7	375.35	397.00	397.15	0.04
2	968.2	295.55	3.7	47.8	424.15	445.90	446.45	0.12
3	982.3	297.45	2.5	49.1	470.65	491.90	492.69	0.16
4	909.5	299.45	3.3	54.7	523.85	541.60	542.55	0.18
5	937.9	299.35	1.0	55.5	570.95	588.58	589.55	0.16
6	880.6	301.95	2.9	55.6	572.15	588.90	590.35	0.25
7	920.9	304.25	4.2	56.8	652.65	669.20	671.15	0.29
8	903.2	300.65	2.6	56.3	629.05	645.33	647.15	0.28
Average								0.19

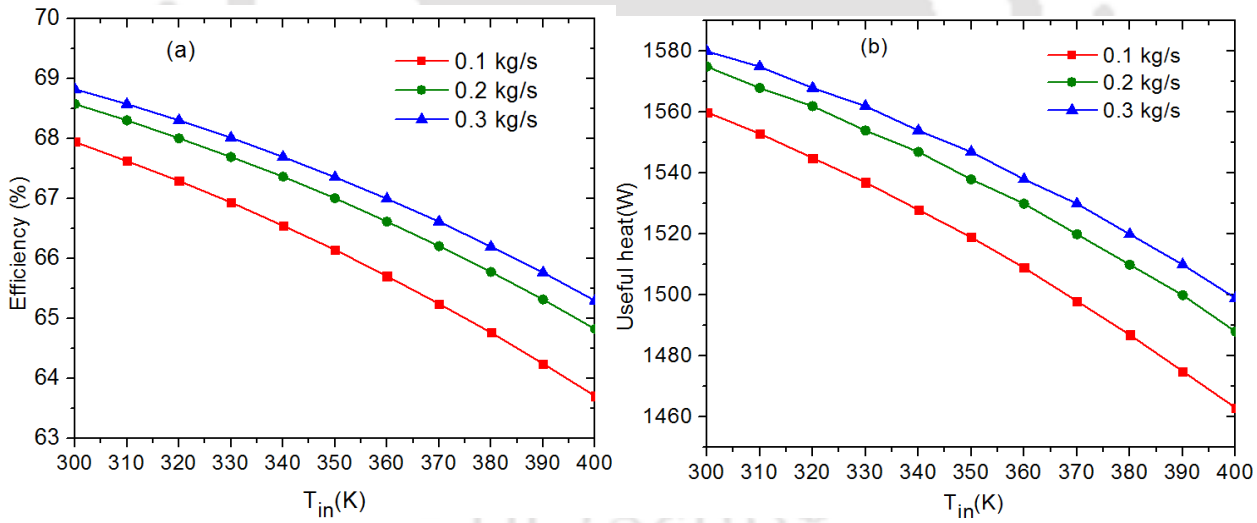

Fig. 4.6.Effects of inlet temperature on the efficiency (a) and useful heat generated (b)

In the analytical performance evaluation of PTSC, ambient conditions are treated as constant in order to emphasize investigations of the thermal improvement. The performance of PTSC is evaluated using useful heat and thermal efficiency by varying inlet temperature while keeping other parameters constant. Fig.4.6 illustrates the variation of HTF inlet temperature with respect to useful heat generated and the efficiency at three different mass flow rates. The solar radiation is maintained at a constant value of 700 W/m^2 and both Fig.4.6 (a) and (b) present that rising HTF

inlet temperature leads to reduce efficiency and useful heat, respectively. The results of this study exhibit similarity with other literature results. For instance, Bellos and Tzivanidis [12] conducted an analytical study to examine the effects of various thermal improvement techniques on the PTSC. They concluded that the thermal efficiency of the PTSC is reduced when the flow rate and inlet temperature are increasing. As a result, the current study delivers logical and acceptable results.

The influence of increasing mass flow rate on the HTF outlet temperature and receiver temperature is illustrated in Fig.4.7 (a) and (b). In this case, the HTF inlet temperature is kept constant at 360K. Both figures exhibit that outlet and receiver temperatures decrease while the mass flow rate increases. This is resulted because the lower mass flow rate of HTF takes longer time to pass through the absorber tube and attains a high temperature. Moreover, the graph indicates that the HTF outlet and receiver tube temperature increases when solar radiation becomes higher. The increase in solar radiation results into the heat gain of HTF proportionally.

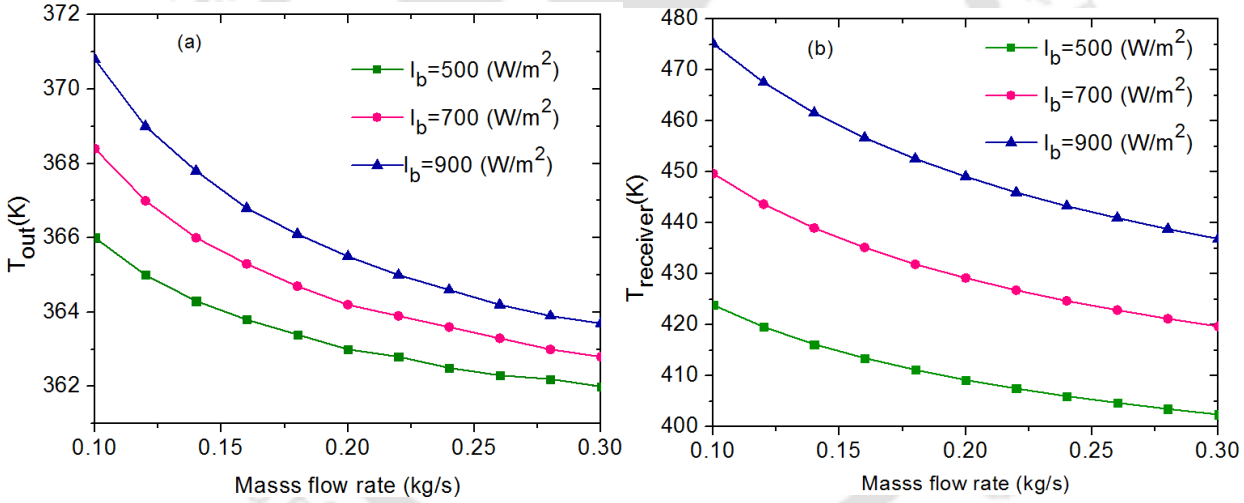

Fig. 4.7.Effects of mass flow rate variation on the HTF outlet (a) and receiver wall temperature (b)

The effects of increasing HTF mass flow rate with respect to thermal efficiency is shown explicitly in Fig.4.8 (a) and (b). Both figures validate that increasing HTF mass flow rate enhances the thermal efficiency of PTSC system, keeping HTF inlet temperature and beam solar radiation constant at 360 K and 700 W/m^2, respectively. Moreover, it is to mention that the thermal efficiency increases slightly with the rise in HTF inlet temperature. Further, the efficiency increases with an increase in the beam radiations.

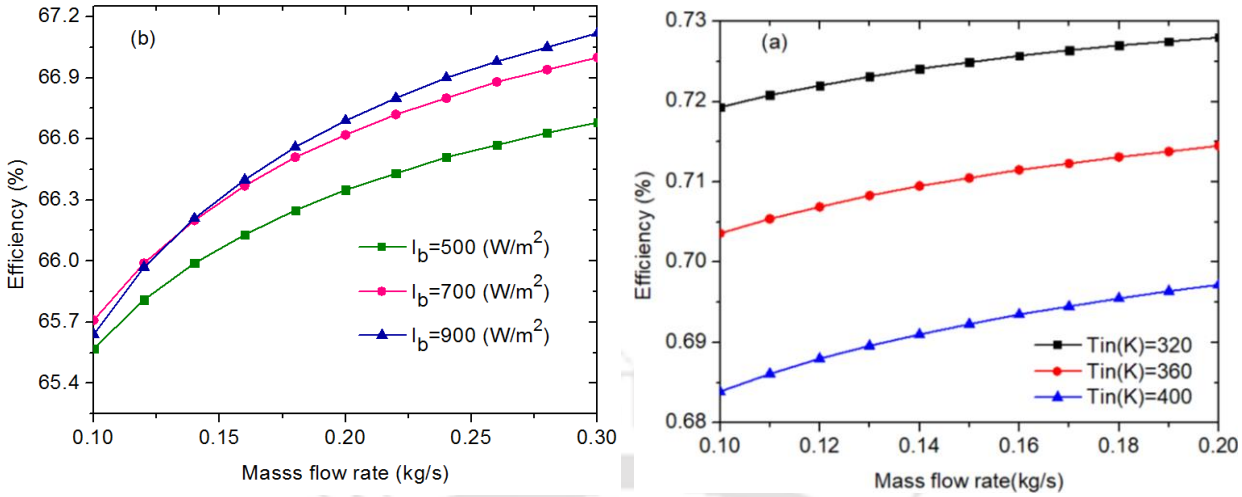

Fig. 4.8.Effects of mass flow rate variation versus thermal efficiency

Similarly, the effect of nanofluids on the thermal performance PTSC is investigated numerically. The performance comparison is performed using 5% Al_2O_3 nanoparticles and base fluid HTF (CWO). Numerical analysis of this study is presented in the following section. Al_2O_3 is selected because of its stable thermal properties [127], [128]. The thermal properties of various materials are listed in Table 4.2. The properties of Al_2O_3 are derived using Eq. (4.32) -(4.35) as mentioned in section 4.1.1.

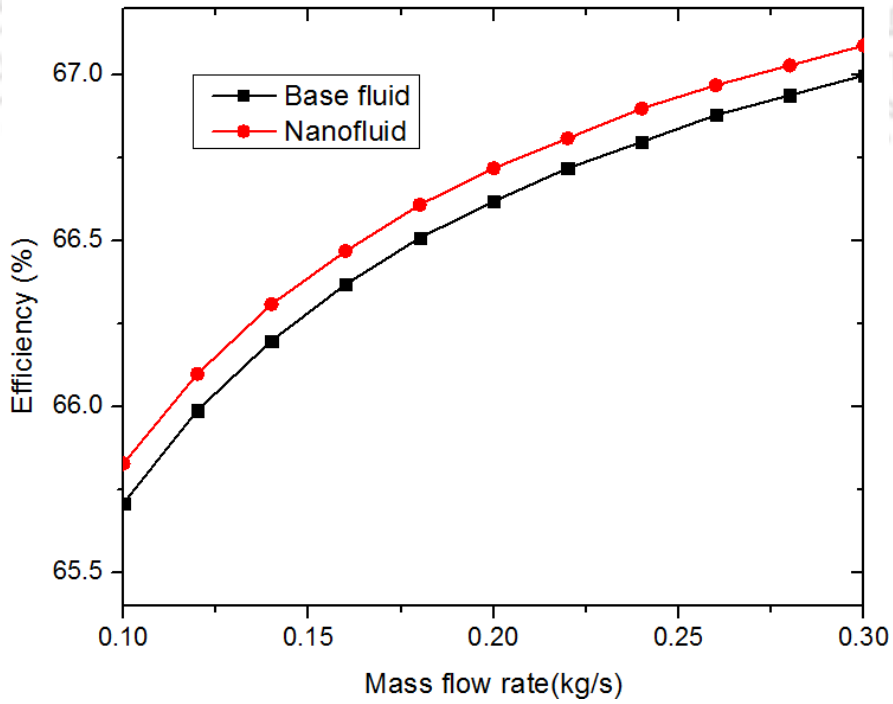

Fig. 4.9. Thermal efficiency variation against flow rate for the base fluid and Nano fluid

Fig.4.9 depicts thermal efficiency variation of the base fluid and nano fluid with respect to mass flow rate which ranges from 0.1 to 0.3k g/s. It is to mention that the immersion of nano particles into the base fluid improves thermal conductivity of the mixture, which further enhances the thermal efficiency [37]. The presence of nanoparticle improves the thermal conductivity of the base fluid and this depicted in Fig. 4.9. However, adding a 5% volume concentration of nano particles into the base fluid brings insignificant difference as it is indicated in the figure. Mixing more than 5% nanoparticle with base fluid is not recommended since the Reynolds number of the HTF is also raised that leads to the increase of pumping power. In addition, the presence of high concentration nanoparticle is no easy to handle during operation because of the formation agglomeration which is formed due the partial settlement of the particles. Therefore, nanofluid is not considered during the practical performance study of the PTSC.

The performance PTSC based on cooking waste oil (CWO) HTF is compared with the commonly used HTF, which is called Syltherm 800 (S-800) in this section. The thermal properties of S-800 under different inlet temperatures are listed in Table 4.2. The parameters, such as useful heat, heat transfer coefficient, heat loss, and HTF flow rate and inlet temperature are used to compare both HTFs.

Table 4.2

Thermal properties of Syltherm 800 HTF at a temperature of 360 K

Property	Inlet Temperature(^{0}C)					
	70	80	87	90	100	110
Specific heat capacity (Cp) [J/kg K]	1694	1711	1723	1728	1745	1762
Density($\boldsymbol{\rho}$)[kg/m3]	890.5	881.68	875.5	872.9	864.1	855.2
Thermal conductivity(k) [W/m K]	0.1256	0.1237	0.1224	0.1218	0.12	0.1181
Viscosity ($\boldsymbol{\mu}$) [Pa. s]	0.00443	0.00386	0.00353	0.00339	0.00299	0.00265

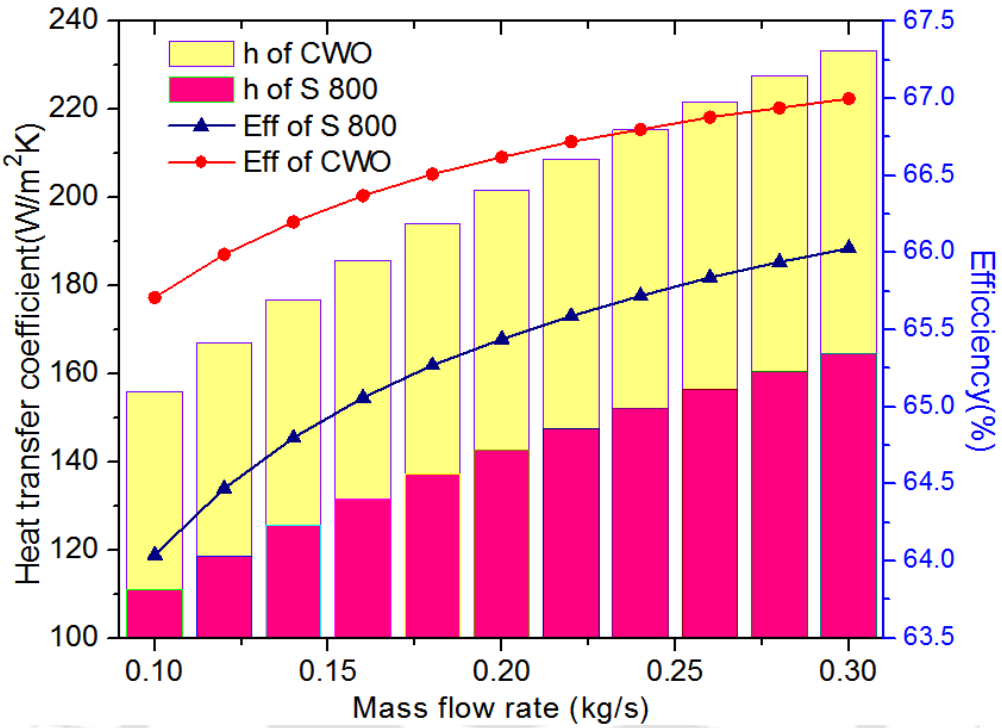

Fig. 4.10.Thermal performance comparison of CWO and S 800

Fig.4.10 exhibits thermal efficiency and heat transfer coefficient of CWO and S-800 considering them as working fluids. In this case, the HTF inlet temperature and solar radiation are kept constant at 360 K and is 700 W/m^2, respectively. It can be observed in this figure that the efficiency and heat transfer coefficient of CWO acting as HTF increase more than S-800 at the same mass flow rate variation. For CWO, the highest thermal efficiency and heat transfer coefficient obtained at mass flow rate of 0.3 kg/s are 67% and 233.4 W/m^{2}K, respectively. On the other hand, for S-800 the thermal efficiency and heat transfer coefficient recorded at 0.3 kg/s mass flow rate, are 66% and 164.5 W/m^{2}K, respectively.

Furthermore, the effect of HTF inlet temperature on the thermal efficiency and heat loss of these two HTFs are exhibited in Fig.4.11. The mass flow rate and solar radiation are kept invariable at 0.2 kg/s and 700 W/m^2, respectively, with respect to the other parameters. The figure indicates that the thermal efficiency of CWO is higher than S-800. Moreover, it is clearly noticed that the heat loss of CWO is lower than S-800. In general, the higher the inlet temperature and the more the energy loss.

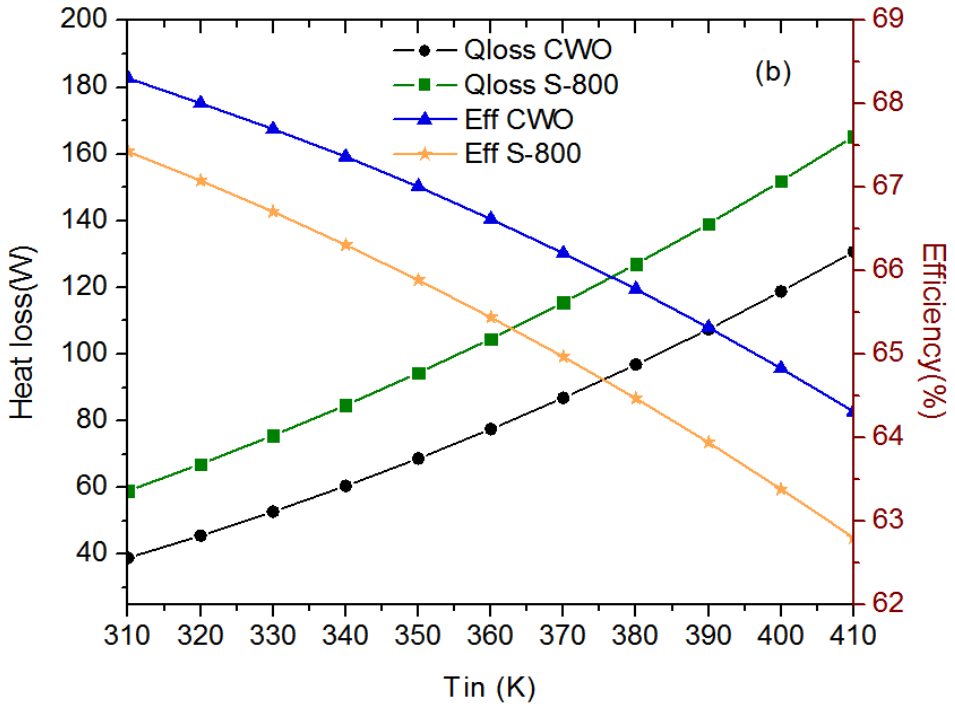

Fig. 4.11.Effects of HTF inlet temperature against efficiency and Heat loss of CWO and S 800

4.3.2 Numerical Analysis of PTSC

The equations presented in section 4.1 are capable to evaluate the performance of PTSC analytically. However, uniform wall temperature profile is considered to evaluate the performance of absorber tube wall [129]. Furthermore, in order to study the thermal performance of PTSC receiver, a numerical modeling and simulation are performed. Hence, governing equations are formulated; the boundary conditions are presented and the numerical modeling approaches to solve the problem are discussed in the next subsections.

4.3.2.1 Numerical modeling for the receiver of PTSC

The dimensions employed for the physical modeling of numerical study are same as that of the actual dimensions used for the fabrication of PTSC to conduct a practical experiment. The main parameters that are utilized to model a PTSC receiver system are the outer and inner diameters of the glass envelope and absorber pipe, respectively, and the length of the glass envelope and absorber pipe. These parameters are listed in section 3.3.2, in Table 3.1.

Table 4.3.

Thermophysical properties of HTF, glass, copper, nanoparticle and air

Material	$\rho(kg/m^3)$	$C_p(J/kgK)$	k(W/m.K)	$\mu(kg/ms)$
HTF	889.1	1800 [130]	0.205	8.84×10^{-3}
Copper [131]	8978	381	387.6	
Glass	2220	910	1.75	
Al_2O_3	3970	765	40	
Air (at T=40^0C)	1.127	1007	0.02662	1.918×10^{-5}

4.3.2.2 Geometrical modeling and meshing of the PTSC receiver

The PTSC computational domain mainly consists of four domains, namely, two solid and two liquid domains. The solid domains contain an absorber tube and a glass cover, whereas, two fluid domains comprise of HTF (fluid domain) and air contained in the annular space between receiver pipe and the glass envelope. Absorber tube is manufactured from copper pipe and is coated with black paint to increase energy absorptivity. The fluid domain acted as HTF is the cooking waste oil. The thermophysical properties of HTF and copper are listed in Table 4.3. The computational domain modeling and meshing are performed using ANSYS CFD software and the proposed CFD model of the PTSC system is shown in Fig.4.12.

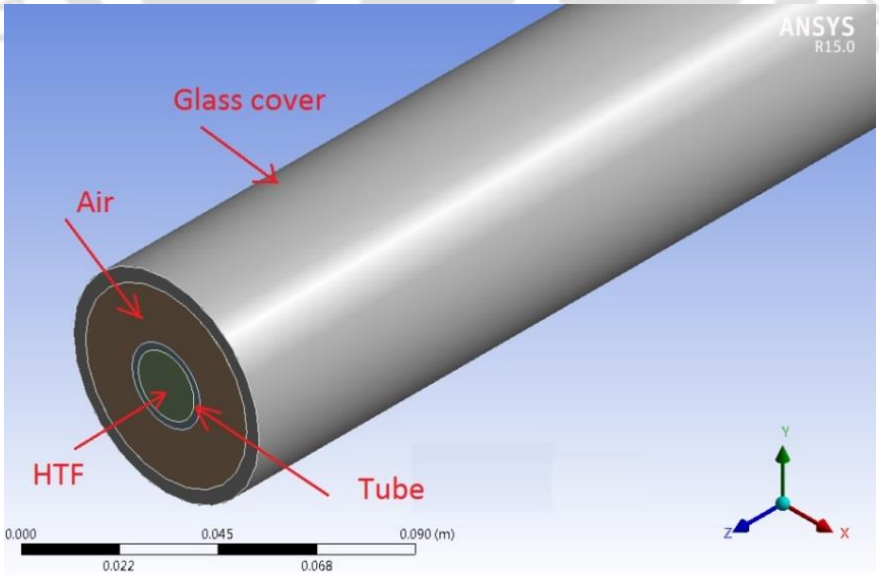

Fig. 4.12. Physical model of the receiver system

To ensure the accuracy of the numerical computations, a grid independence test is performed, where the inlet velocity of HTF is 0.9 m/s, inlet temperature is 305 K and direct beam radiation is 600 W/m^2. Increasing the number of grid elements progressively from 317,820 to 482966 and keeping all other parameters constant, the temperature increment of HTF from inlet to outlet dT**,** is estimated for each grid size and selected elements are listed in Table 4.4. It can be seen that there is no significance change in the outlet temperature of HTF with the variation of grid number. Considering the computation accuracy and time, the grid of 382,295 elements is employed in the following calculations.

Table 4.4

Grid independent test

S.No	No of Elements	Tin(K)	Tout(K)	dT
1	317520	305	309.934	4.934
2	345400	305	310.237	5.237
3	**382295**	**305**	**310.809**	**5.809**
4	482966	305	310.860	5.860

4.3.2.3 Governing equations

The governing equations used for numerical evaluation of PTSC are implemented based on the following assumptions. No-slip velocity boundary conditions are considered and the fluid is incompressible and continuous. The mass flow rate is uniform along PTSC and thermo-physical properties of all domains are independent of temperature. The air pressure, which is placed in the annular gap between glass envelope and copper absorber tube is low and is treated as vacuum. Hence, only radiation heat losses from absorber tube to the glass cover are considered.

The solar flux falls onto PTSC reflector and glass envelope uniformly. Majority of solar radiation incident on PTSC reflects back to the receiver tube and glass cover. The intensity flux density is variable around circumferential direction of the absorber tube and glass cover.

The heat transfer from solar energy into HTF passes the following steps. The total solar irradiance falls on the PTSC reflector area uniformly, except the small portion below glass envelope due to its shading. Major part of solar radiation incident on PTSC reflects back to the receiver tube passing through glass cover. Small fraction of the solar radiation is refracted, diffused and absorbed by the glass envelope and a larger amount reaches on the outer wall of absorber.

Similarly, some part of the energy arrived at outer wall of the receiver pipe reflects back, while the remaining is transferred into HTF.

In general, the heat transfer processes in the PTSC receiver system consist of solar energy absorption in the receiver pipe and on the glass cover. The convection mode of heat transfers from the receiver to HTF and from the glass cover to the environment. The radiation heat transfers from the absorber to the glass envelope and then to the ambient. The conduction heat transfer occurs between envelope and the absorber pipe. The governing equations includes energy equation for solid and fluid domains and, continuity and momentum equations for fluid domain.

Continuity equation:

$$\frac{\partial u}{\partial x}+\frac{\partial v}{\partial y}+\frac{\partial w}{\partial z}=0 \tag{4.36}$$

Momentum equation:

$$\frac{\partial v}{\partial t}+(v.\nabla)v=\frac{1}{\rho}(-\nabla \mathrm{P}+\mu\nabla^2\mathrm{v}+\mathrm{F}+\mathrm{S}) \tag{4.37}$$

Energy equation for the fluid domain:

$$\rho C_p u\frac{\partial u}{\partial x}+\rho C_p v\frac{\partial v}{\partial y}+\rho C_p w\frac{\partial w}{\partial z}=k\left[\frac{\partial^2 T}{\partial x^2}+\frac{\partial^2 T}{\partial y^2}+\frac{\partial^2 T}{\partial z^2}\right] \tag{4.38}$$

Energy equation for the solid domain:

$$\frac{\partial^2 T}{\partial x^2}+\frac{\partial^2 T}{\partial y^2}+\frac{\partial^2 T}{\partial z^2}=0 \tag{4.39}$$

The governing equations that represent domains are numerically modeled and solved using ANSYS Fluent environment, in which finite volume method (FVM) is applied to analyze the equations. Coupled algorithm is employed for numerical pressure-velocity coupling. The Body Force Weighted scheme is implemented to solve pressure correction equation. The momentum and energy equations are discretized using second-order wind differencing scheme.

To minimize heat loss, the absorber tube is enclosed by a glass tube. The major mode of heat transfer through evacuated annulus space between absorber tube and glass cover is radiation heat transfer. The surface-to-surface radiation model in ANSYS Fluent [132] is employed to account for the radiation exchange between receiver pipe and glass envelope. The glass cover is assumed to be gray and diffuse, and evaluate energy exchange between them; the view-factors of the

participating zone are computed. In addition to this, the glass cover is treated as opaque to the radiation within infrared energy spectrum.

The input parameters for the numerical study are HTF velocity inlet, HTF temperature inlet, non-uniform solar radiation at the wall of the absorber pipe, and ambient temperature. Pressure outlet boundary conditions are selected appropriately. In reality, the heat flux distribution in the absorber tube is not uniform and there are significant variations around the circumference of the tube. In this study, direct non-concentrated solar radiation is applied on the external wall of glass cover and top external surface of the absorber pipe. On the other hand, the concentrated solar flux is applied at the bottom external wall of the absorber pipe. The direct beam radiation is multiplied with the CR of PTSC to determine the input for the bottom part.

4.3.2.4 Numerical Simulation Results

In this section, the numerical simulation results of PTSC receiver system presented in Fig 4.12 are discussed. The input parameters to the numerical model, HTF inlet temperature and mass flow rate is fixed at 305 K and 0.2 kg/s, respectively. The initial temperature of all the domains is 300 K and direct solar radiation is considered as 650 W/m^2.

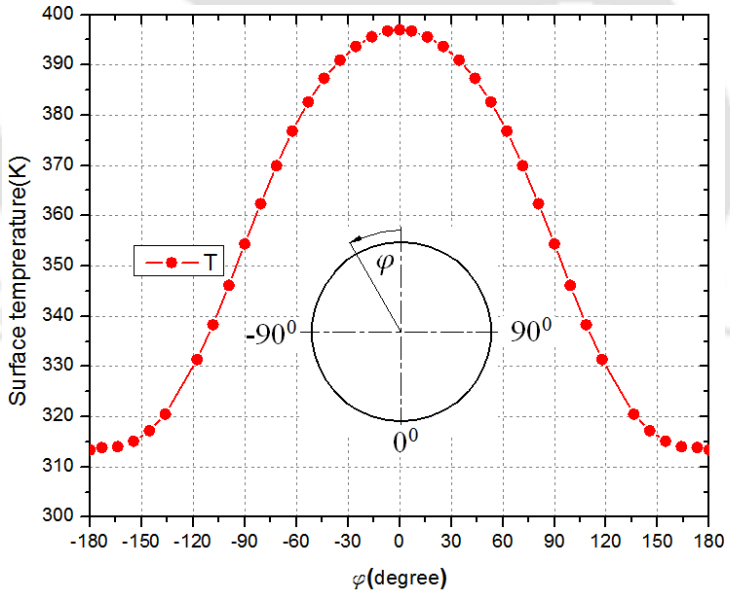

Fig. 4.13.Circumferential temperature distribution of glass cover

As it is mentioned in the above section, non-uniform heat flux is applied onto the external surface of absorber tube and glass cover. Concentrated solar heat flux is applied on the bottom wall of the absorber tube and the direct solar radiation falls on the top surfaces of the absorber and glass

envelope. The non-uniform heat flux distribution results into temperature gradients on the wall of the receiver pipe and glass envelope.

Hence, the simulation results of circumferential temperature distributions on the walls of the glass cover and absorber tube are illustrated in Fig 4.13 and Fig.4.14, respectively. The extremely non-uniform temperature distribution is the reflection of variable solar flux into the absorber system. Moreover, cross sectional temperature distribution along longitudinal axis of the receiver pipe is not uniform and can be observed in Fig.4.14. It can also be stated that the temperature of exit section is larger than the temperature of the middle section. Additionally, it can be noticed from both the figures that the temperature of absorber pipe is higher than the glass envelope.

Similarly, due to non-uniform heat flux, the temperature profile at the bottom section of receiver tube and glass envelope is larger than the upper parts. Furthermore, the temperature of the receiver and envelope pipes also increases along the flow direction from HTF inlet to exit. Besides, the outer wall temperature of the receiver pipe is higher than the inner one, and the reverse is true for the glass envelope.

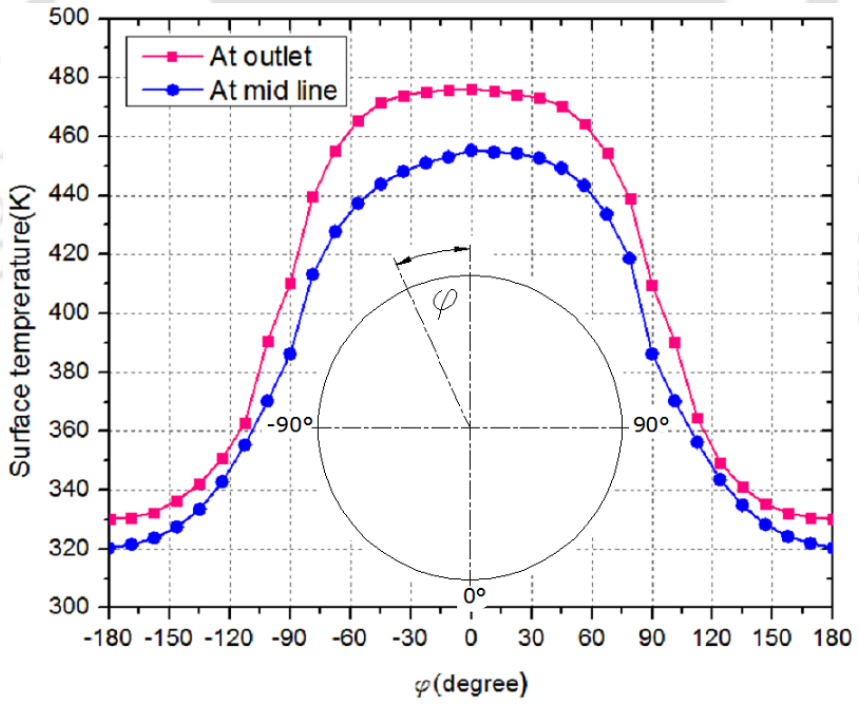

Fig. 4.14.Circumferential temperature distribution of absorber pipe

Fig.4.15 presents temperature distributions on three different cross-sections of the receiver tube along the axial direction; at the HTF inlet section (z=0), middle section (z=1m) and exit section

(z=2m). Since it is expected that the HTF temperature rises when it passes from inlet to outlet and the temperature of the bottom HTF domain is higher than the top section. This is self-evident that the HTF temperature found near to the bottom wall of the receiver pipe is larger than the rest because of the low thermal conductivity of HTF.

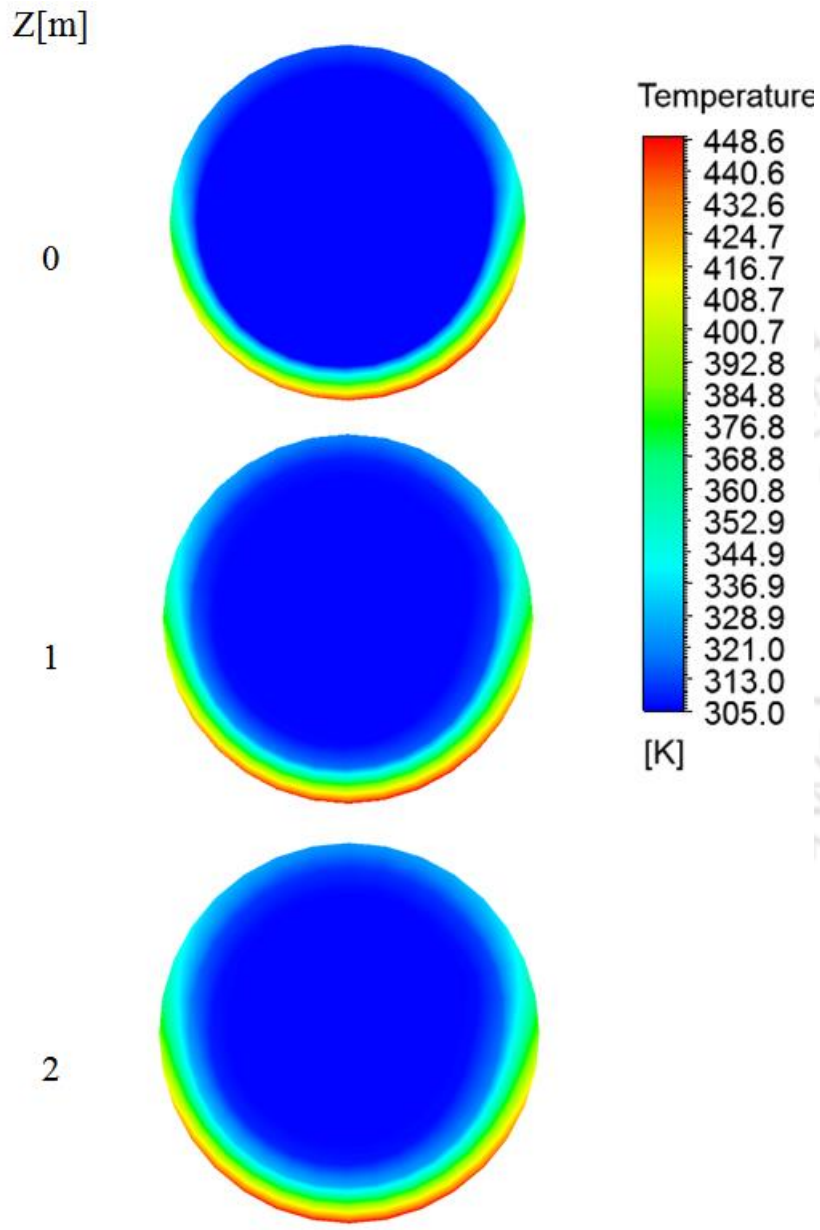

Fig. 4.15.Cross-sectional view of temperature profile at inlet, middle section and exit absorber pipe

4.4 Experimental Results

4.4.1 Experimental setup procedure of PTSC

The PTSC experimental is fabricated at the Central Workshop of, Indian Institute of Technology Guwahati (IITG) and is installed on the roof top of EEE department, IITG. The location (latitude and longitude) of IITG is **26.1879^0N** and **91.6916^0E**. The PTSC is positioned in the north-south direction and rotates in the east-west direction. Fig.3.13 depicts the schematic of the experimental setup fabricated in this study. The solar collector system comprises of the reflector, glass cover, absorber pipe and accessories. The accessories are circulating pump, data logger, storage tank, pyranometer and thermocouples. Two thermocouples are mounted on the absorber tube, one each at the inlet and outlet. The PTSC is used to concentrate dispersed solar radiation towards receiver. The absorber tube is placed across the focal line of the PTSC and converts solar radiation into thermal energy.

The performance of TES system is estimated using the major important parameters viz. HTF volume flow rate, initial temperature of the system and inlet, and solar irradiance. These parameters are gathered from experimental setup having a data acquisition system. The practical experiments are conducted on selected days of the months of June and October. The results of analytical estimation, numerical simulation and experimental evaluation of the PTSC system are discussed in this section. The experiments are performed when there are no clouds, during bright sunny day and data is recorded at every five min. The PTSC unit manually tracks movement of the sun in every 15 min.

In this section, the experimental thermal performance study of the PTSC is presented. The results are obtained from experimental tests on the selected days in the month of June and October. Important parameters like useful heat, thermal efficiency, and HTF outlet temperature and heat loss are employed to evaluate performance of the collector. Moreover, analytical and numerical outlet temperature results of the selected days are presented and compared with experimental results. The experiment tests are performed from 9:00 AM till noon. The HTF inlet temperature and mass flow rate and solar radiation are the inputs for the experimental analysis. In the experiments, initial temperature of the working fluid is started at the ambient value. The outlet and inlet temperature of HTF are measured using two thermocouples installed at each point.

4.4.2 Experimental test results

Fig.4.16 (a), (b), (c) and (d) indicate the HTF outlet temperature resulted in the analytical, numerical and experimental analysis methods on June 15 and 22, and October 13 and 18 respectively. The results exhibit that the experimental outlet temperature is lower than the temperature found analytically and numerically. This is due to the heat loss, which is neglected during the numerical and analytical evaluations. It is to mention that the total solar radiation on each day becomes high before noon just around 11:30 AM. The maximum beam radiation obtained on June 15, June 22, October 13 and October 18 are 905 W/m^2, 906 W/m^2, 776 W/m^2 and 770W/m^2, respectively. The maximum HTF outlet temperature is achieved after 2:00PM in all the cases and the maximum generated experimental outlet temperature on June 15 and 22 are 110.7^{0}C and 108 ^{0}C, respectively. Similarly, the maximum HTF outlet temperature obtained on October 13 and October 18 are 89.9 ^{0}C and 86.8 ^{0}C, respectively. As it is expected, the HTF outlet temperature is higher in the month of June as compared to the month of October. Because, the solar radiation in the month of June is higher than October. The outlet temperature starts to fall down after 3:00 PM local time in the month of June, whereas, after 2:30 PM in October.

Fig.4.17. (a), (b), (c) and (d) illustrates useful heat (Q_u), heat loss (Q_{loss}) and thermal efficiency with respect to day hours on June 15, June 22, October 13 and October 18, respectively. The useful heat increases with time in the beginning of the experiment and, after 12:00PM, the useful heat starts falling down rapidly. In the same manner, the thermal efficiency rises with time i.e., from the start of the experiment till noon with some discontinuities. However, similar to the useful heat, thermal efficiency decreases quickly after 12:00PM. This may be resulted because of two reasons. First, the solar radiation becomes weaker after 12:00PM on all days and the heat gained from the collector is also minimized. Second, it may happen due to increasing HTF inlet temperature. As it is pointed out while describing analytical results in section 4.4.1 and Fig.4.6, the useful heat and thermal efficiency of PTSC decrease as HTF inlet temperature increases. Moreover, it can be observed from Fig.4.17, the useful heat in month of June is significantly higher than October due to the higher solar radiations

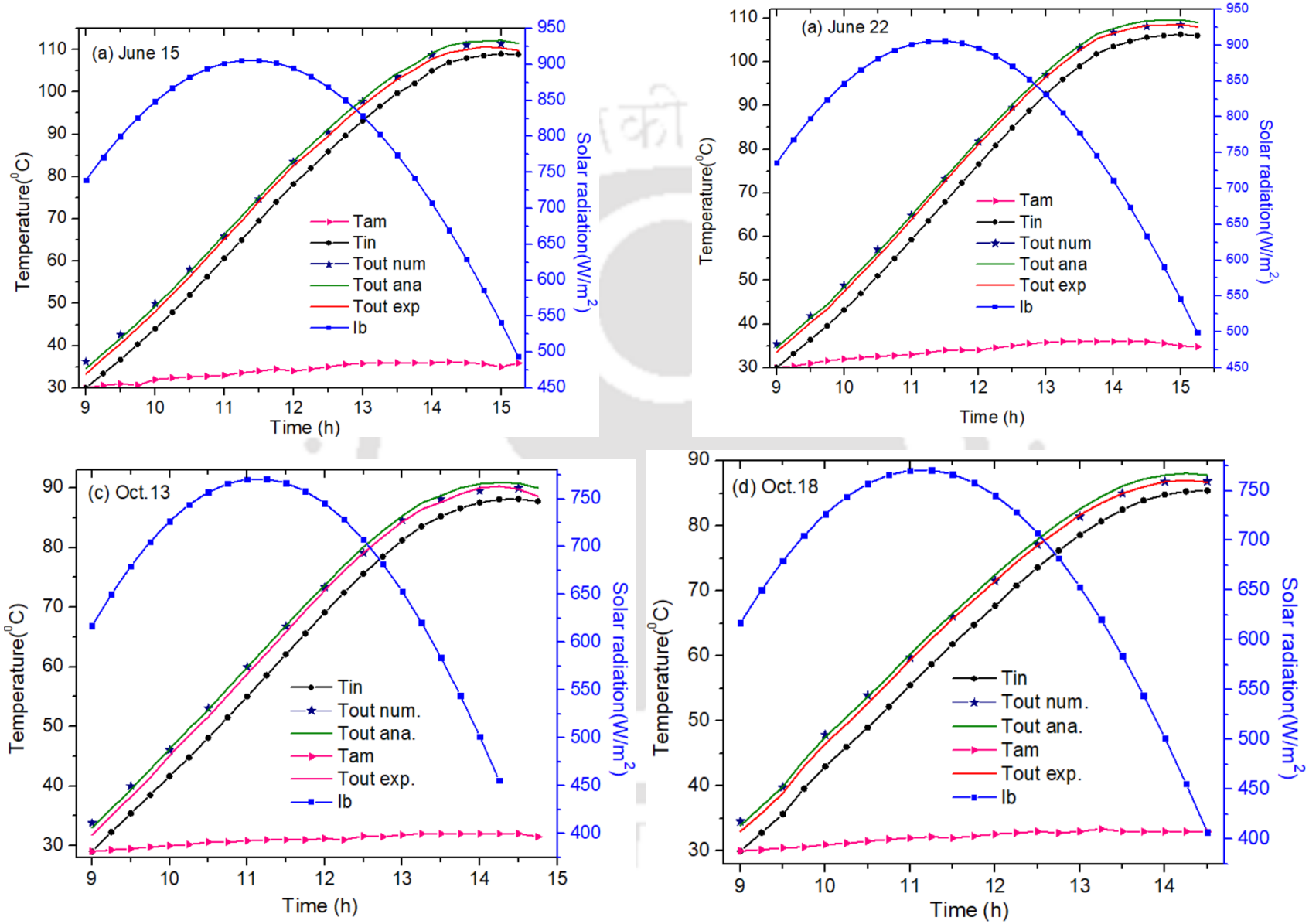

Fig. 4.16.Variation of experimental, analytical and numerical outlet temperature versus daytime for June 15(a) Jun.22 (b), Oct.13(c) Oct.18 (d)

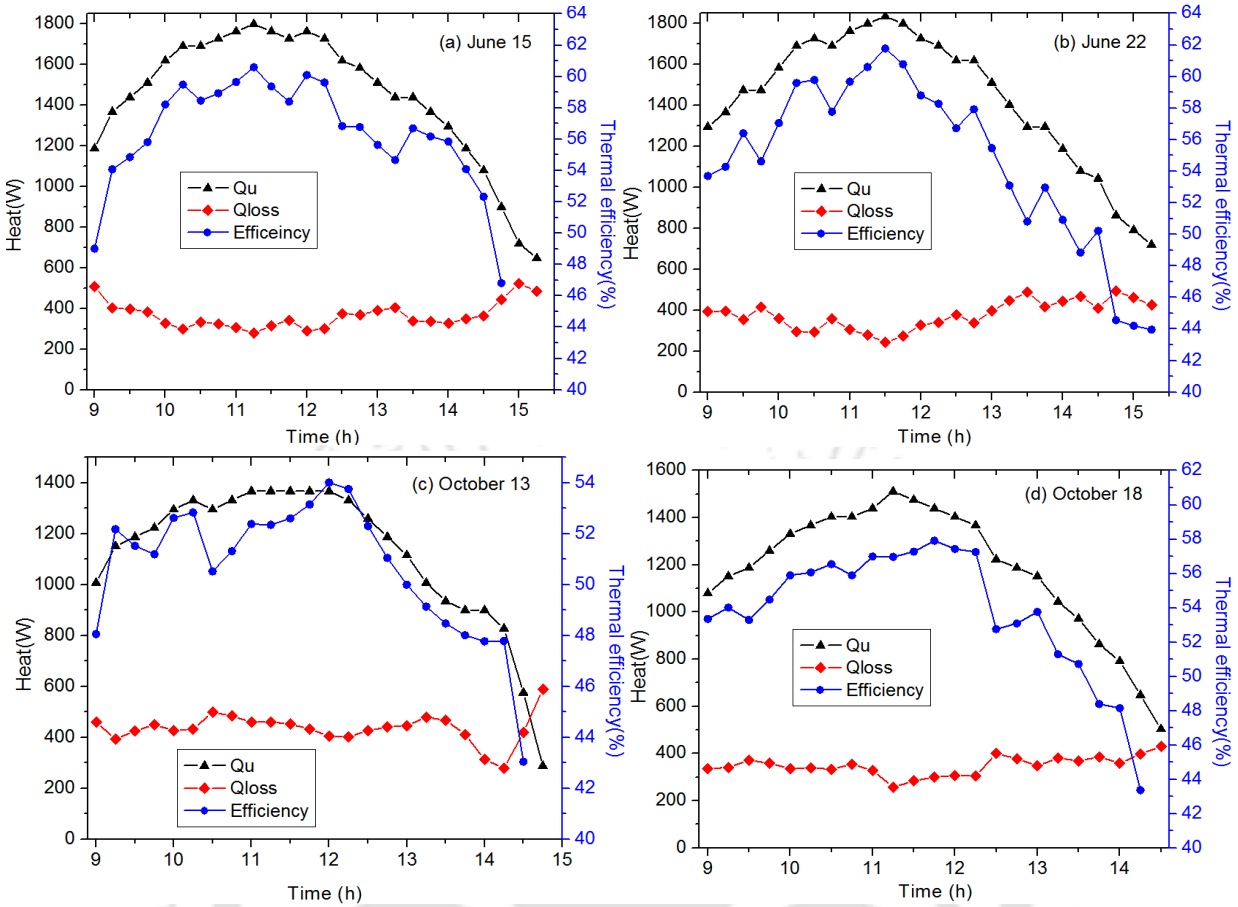

Fig. 4.17.Variation of useful heat, heat loss and thermal efficiency against day time for the days of June 15(a) and 22(b) and for October 13 (c) and 18(d)

4.4.1 Performance Curve of the PTSC based on ASHRE standard

The thermal efficiency of PTSC can be expressed using ASHRAE standard [133]. Fig.4.18 shows the experimental (on June 15) thermal efficiency of the collector with respect to the parameter $(T_{in}-T_{am})/I_b$. A straight line that fits best to the curve is derived. The intercept of the straight line is the value of the constant $F_R \times \eta_O$ and its slope is $F_R U_L/C$. The thermal efficiency of the collector is related with inlet temperature of HTF, solar irradiance and the ambient temperature. Hence the thermal efficiency Eq. (4.29) can be rewritten as,

$$\eta_{th} = F_R\eta_o - \frac{F_R U_L}{C}\left(\frac{T_{in}-T_{am}}{I_b}\right) \tag{4.40}$$

where, $F_R\eta_o$ stands for intercept and $\frac{F_R U_L}{C}$ is for slope of the fitted line.

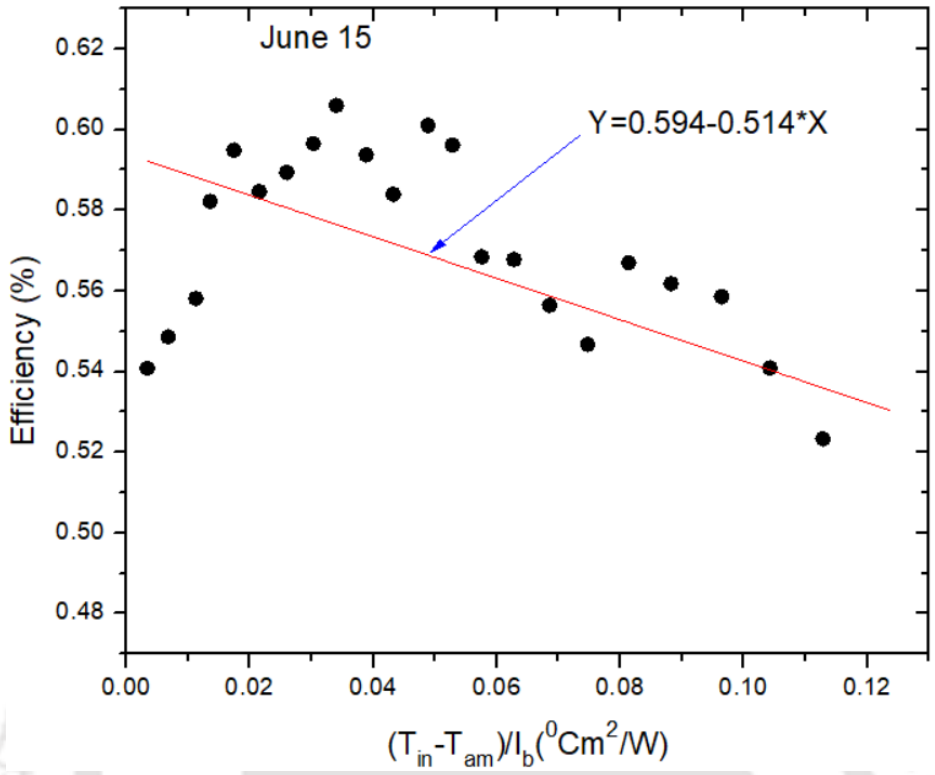

Fig. 4.18. Performance Curve of the PTSC based on ASHRE standard

Using equation of the line, value of $F_R\eta_o$ is estimated to be 0.594 and ($U_L F_R$ /CR) equals 0.5387. The optical efficiency is 0.7 as it is listed in Table 3.1 and CR is 23. Hence, the value of F_R and U_L can be determined as follows.

$$F_R = \frac{Intercept}{\eta_o} = \frac{0.594}{0.7} = 0.85$$

$$U_L = \frac{slope * CR}{F_R} = \frac{0.514 * 23}{0.85} = 13.9$$

4.5 Summary

The PTSC experimental setup sizing and fabrication procedures are discussed in this chapter. The thermal performance of PTSC is evaluated by varying the important parameters, such as inlet temperature, beam radiation, mass flow rate. The result indicates that the efficiency and useful heat is reduced while inlet temperature is increased keeping the other parameters constant. On the other hand, thermal efficiency increases when mass flow rate and solar radiations surges. The performance comparison study is performed using 5% Al_2O_3 nanoparticles and pure cooking waste oil (CWO). However, addition of nano-particles into the base fluid brings negligible difference.

Moreover, the performance of PTSC based on cooking waste oil (CWO) HTF is compared with the commonly used Syltherm 800 (S-800) HTF. It is found that the performance of PTSC improvises when CWO is utilized as HTF.

The input parameters to the numerical model are HTF inlet temperature, mass flow and direct solar radiation. Extremely non-uniform temperature distribution along the bottom and top surface of the receiver pipe are observed due to the variable heat flux input. The temperature also increases along the flow direction from inlet to exit as anticipated. The experimental results indicate that the thermal performance of PTSC is better in June as compared to October. It is also found that the analytical, numerical and experimental results have good agreement among themselves which verifies correctness and reliability of the proposed system.

Chapter - 5

5 LHS unit performance investigation

5.1 Introduction

For practical applications, it is important to test effectiveness of the storage unit. The LHS unit sizing and development procedure is discussed in the Chapter 3. Moreover, the thermal performance of the proposed LHS is studied experimentally as well as numerically. The number of HTF tubes, fins connected on each tube and the configurations of the finned tubes embedded inside PCM are determined using an optimization technique. For the performance analysis of LHS, decision parameters, such as liquid fraction, temperature and stored energy are employed. The performance of the storage unit, when Al_2O_3 is added into PCM, is also studied in this chapter.

5.2 Experimental Result Analysis

A PCM with medium melting temperature is required for a solar cooking purpose [28]. Erythritol is a very promising as PCM for solar and other applications which utilize TES systems. This is due to its excellent chemical stability even after multiple phase change cycles, low cost, safe, high latent heat and wide-ranging transition temperature. For enhancing the heat transfer from heat source, the PCM with heat exchanger with fins have been investigated and found to be more efficient technique [115]. In the present study, a shell and tube type of LHS with multiple finned HTF tubes are developed. Petroleum-based HTF is commonly employed in the study of LHS having PCM with a high or medium melting temperature. Hence, there is a need to search for other easily available and eco-friendly HTF materials such as cooking waste oil (CWO). To the best of the knowledge of the authors, no study has been presented either experimentally or through numerical analysis of a finned multi-tube LHS storage for solar cooking having erythritol as PCM and CWO as HTF. As a result, the thermal performance of the finned multi tube shell and tube

type LHS unit is evaluated based on the above-mentioned PCM and HTF. In order to achieve the goal, an investigation is performed both analytically as well as experimentally using a lab-scale experimental setup. The effect of operating parameters on the performance of the storage unit is examined. For verifying the experimental results of the storage unit, a 3D LHS computational model that replicates the actual unit is developed using ANSYS-Fluent. Moreover, multiple investigations of different LHS models are carried out to select the optimal number of HTF tubes and fins for the optimal performance of LHS. Average temperature, liquid fraction, melting time and stored energy parameters are considered as thermal performance measuring variables. The experimental and numerical results reported in this study can be used as guideline by system designers and technologists for the design and development of thermal energy storage systems.

5.2.1 Materials preparation

The selected energy storage material (PCM) for this study is a commercial sugar alcohol utilized as sweetener in the food industry and known as Erythritol ($C_4H_{10}O_4$) with a purity of 98.0%. Its thermal properties are tabulated in Table 5.1. The phase transition point of the selected PCM is approximately 118 ^{0}C. The major thermo-physical properties of HTF like thermal conductivity, density, specific heat capacity, and dynamic viscosity play vital role in the analysis of TES systems. As explained earlier, economically cheap and easily available cooking waste oil is considered as HTF for this study. To understand the thermal properties of HTF, a sample of the selected HTF is taken and a series of thermo-physical tests are performed before conducting the actual experiment on the TES. It is to be noted that the specific heat capacity of the working fluid is obtained from the literature. The properties of the HTF obtained in laboratory tests and literature are indicated in Table 5.1. The magnitude of transient temperature during the phase transition period is monitored and recorded to study the performance of the LHS unit. Due to this, ten thermocouples are implanted inside the PCM at different places. The locations of these temperature sensors are clearly indicated in Fig.5.1.

Table 5.1

Thermophysical properties of Erythritol, HTF and copper [17, 28, 31, 32]

Material	$\rho(\mathbf{kg/m^3})$	$\mathbf{C_p(J/kgK)}$	k(W/m.K)	L(kJ/kg)	$T_m(^0C)$	$\mu(\mathbf{kg/ms})$	$\beta(\mathbf{K^{-1}})$
Erythritol	1450(solid)	1680	0.73	354.7	118	$1.6x10^{-2}$	$2.94x10^{-5}$
	1280(liquid)	2660	0.33				
HTF	889.1	1800	0.205			$8.84\ x10^{-3}$	
Copper	8978	381	387.6				

5.2.2 Geometric details of the LHS unit

In this section, experimental and numerical study of a lab-scale shell and tube type LHS configuration is discussed. The aforementioned type of LHS unit is fabricated in the Central Workshop at IIT Guwahati. Prior to the LHS system manufacturing process, all the components of the LHS unit are predominantly designed, analyzed and optimized through numerical modeling tools. Fig.5.1 illustrates the physical modeling diagram of the LHS unit that has been considered for this study. The storage unit consists of a storage tank, finned HTF tubes, working fluid or HTF and the PCM. The energy storage media is packed in the vacant space between the casing of storage tank and HTF tubes, while the HTF that conveys heat energy from the source of heat to the LHS storage unit passes through the HTF tubes. The enclosure of the regenerative shell and tube type heat exchanger is made up of a 3 mm thick stainless steel plate to avoid corrosion. Similarly, because of the excellent thermal conductivity property, copper material is employed for HTF tubes and fins. The storage system is 1000 mm long and the internal diameter of the shell is 240 mm. Similarly, the external diameter and thickness of the copper tube are 20 mm and 2 mm, respectively. The number of HTF tubes is determined to be 19 by virtue of optimization method (see section 5.7.1) and four longitudinal fins are welded in every tube as indicated in Fig.5.1 (a). The width and thickness of the fins are 12 mm and 2 mm, respectively.

300

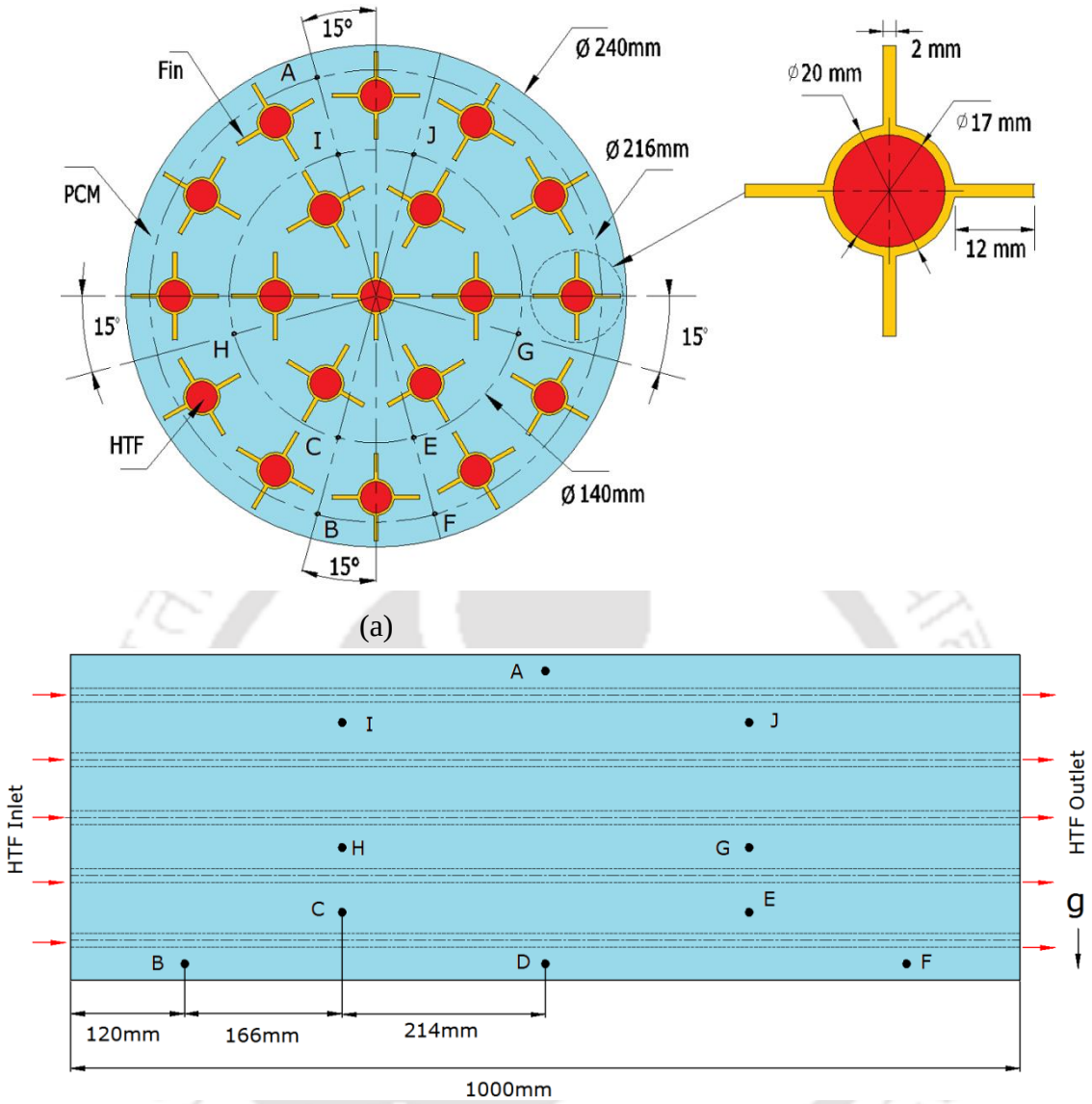

Fig. 5.1.Physical modeling representation of the LHS unit and thermocouples locations (a) front (b) side view.

5.2.3 Experimental Procedure

The HTF inlet temperature is selected based on the requirement to get the selected PCM melted. For the experimental and numerical evaluation of the LHS, the HTF inlet temperature should remain the same. For this reason, the HTF is heated using an electrical heater and the temperature is maintained to be 138 ^{0}C constantly with the help of a temperature controller. Fig.5.2 depicts the schematic representation of the experimental setup employed in this study. The experimental setup mainly consists of the PCM storage unit, HTF reservoir tank, gear pump, pressure gauge, and data acquisition system (DAS). The DAS composed of a data logger, K-type thermocouples, and a

computer for temperature reading and recording of the LHS system. All the thermocouples are calibrated in the laboratory, the error is less than $\pm 2\%$ which is considered to be negligible. A leakage test is done to ensure that was no leakage in the whole piping system. Before the beginning of the experiment, 50 kg mass of the selected PCM is melted using an electric furnace. During the melting of the PCM, the maximum operating temperature of the furnace is maintained at 150 ^{0}C which is below the decomposition temperature range [136]. The liquid PCM is filled into the annulus of the shell of the heat exchanger (the space between the shell and HTF tubes). The PCM is not filled fully inside the shell to avoid high-pressure during the heating process of PCM in the LHS.

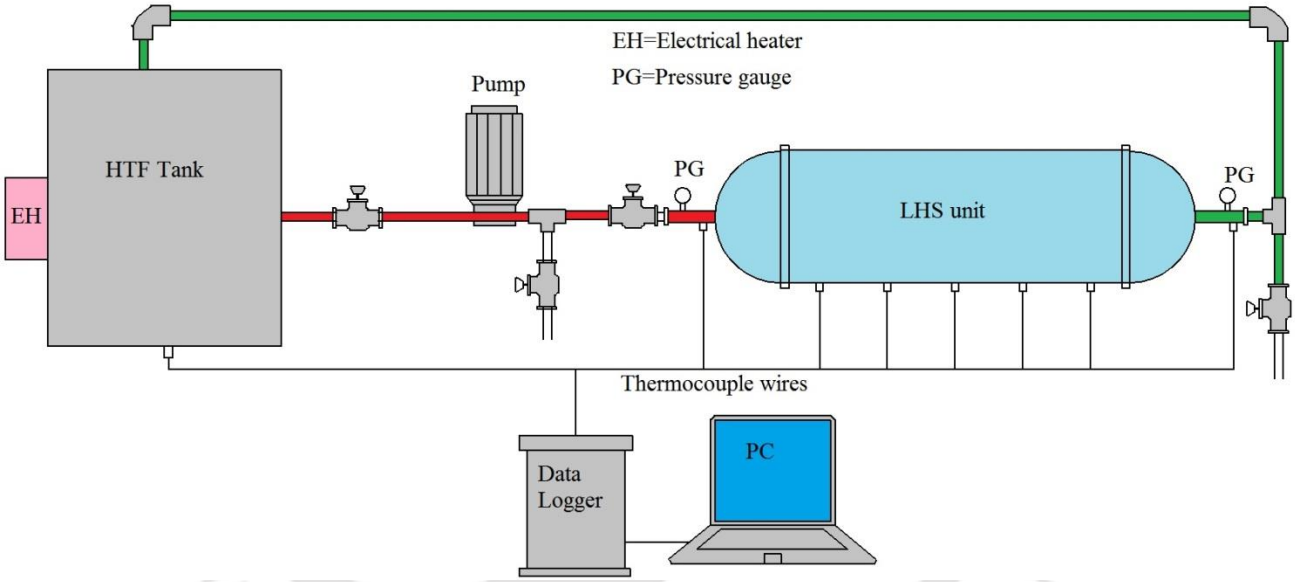

Fig. 5.2.Schematic representation of the experiment setup

The performance of the TES system is estimated using important parameters, such as HTF volume flow rate, the initial temperature of the system and, inlet and outlet temperature of the HTF. These parameters are gathered from the experimental setup using the data acquisition system. For this purpose, several thermocouples are mounted at different locations of the experimental setup. Two thermocouples are placed in each of the LHS unit inlet and exit, and one thermocouple is immersed into the HTF which is contained inside the oil tank. The remaining thermocouples are placed in the LHS system at different axial and radial directions as displayed in Fig.5.1. The thermocouples placed inside the PCM are annotated by alphabets from A to J. The experimental setup together with the piping system is insulated with 50 mm thick glass wool insulation material. Initially, the whole experimental setup is maintained at thermal equilibrium with its environment.

Subsequently, the melting process elevates as the heated HTF is pumped into the inner part of the LHS unit. The inlet HTF temperature is kept constant at 138 ^{0}C and circulates via HTF tubes. The pictorial view of the LHS unit prototype during the experiment is shown in Fig. 5.3.

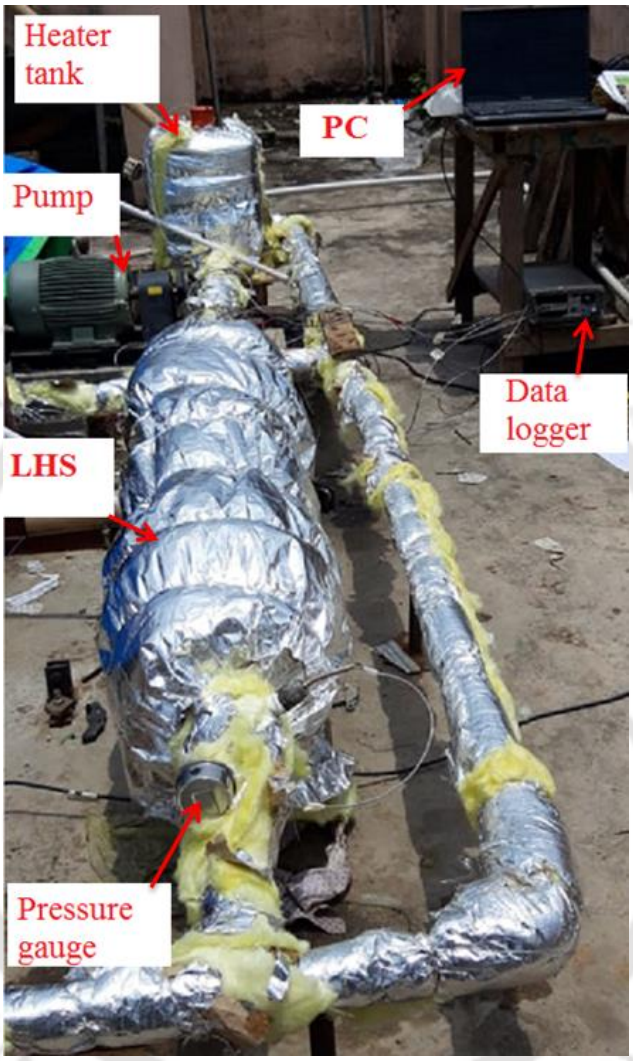

Fig. 5.3.Scheme of the insulated experimental setup of LHS system

The Reynolds number needs be estimated first and it can be determined using Eq. (5.1) to determine type of flow.

$$R_e = \frac{\rho V D}{\mu} \tag{5.1}$$

It is found that the Reynolds number lies in the laminar flow regime, therefore, the flow of HTF through the whole system is considered laminar.

Similarly, the magnitude of the mass flow rate is estimated using Eq. (5.2).

$$\dot{m} = \rho \dot{V} \tag{5.2}$$

Heat is transferred from the HTF towards PCM via the hot walls of HTF tubes together with fins and the heat transferred to PCM can be evaluated using Eq. (5.3).

$$\dot{Q}_{HTF} = \dot{m} C_p \Delta T \tag{5.3}$$

Stefan number (S_{te}) is a dimensionless parameter that indicates the portion of sensible heat compared to the latent heat and quantifies the intensity of driving force during the melting process is defined by Eq. (5.4).

$$S_{te} = \frac{C_p(T_{hot} - T_m)}{L} \tag{5.4}$$

The inlet temperature is HTF is maintained constant at 138 ^{0}C in the range that can be generated by a solar collector fabricated for this purpose.

5.2.4 Experimental error

Experimental error is certain to happen in conducting a practical test and taking the measurement of various parameters. The most common cause of experimental error measurement is calibration, observation, reading, sensitivity and drift. For evaluating the gathered actual experimental data the experiment repeatability and experimental error have to be determined first and this is achieved by explaining temperature absolute error ($\in_{abs}$) explained by Eq. (5.5).

$$\in_{abs} = \left|T_{exp} - T_{ave}\right| \tag{5.5}$$

where, T_{exp} represents the experimental transient temperature value and T_{ave} stands for the average value of the multiple experimental temperatures' readings. Besides, the average error of experimental error ($\in_{exp}$) can be estimated as per Eq. (5.6)

$$\in_{exp} = \frac{\sum_{i=1}^{n}\left|T_{exp} - T_{ave}\right|}{f} \text{ x } 100 \tag{5.6}$$

where, f is the value that represents the number of experimental data points.

It is to be noted that multiple PCM melting experiments are carried out at the same operating parameters. The experiments are performed using the same input values as mentioned previously. The experimental results report the maximum absolute error of 2.3 ^{0}C and absolute average error

of 1.2 ^{0}C. In addition, the temperature measurement error bars of the LHS are exhibited in Fig. 5.4 together with temperature of the at two representative points (A and D).

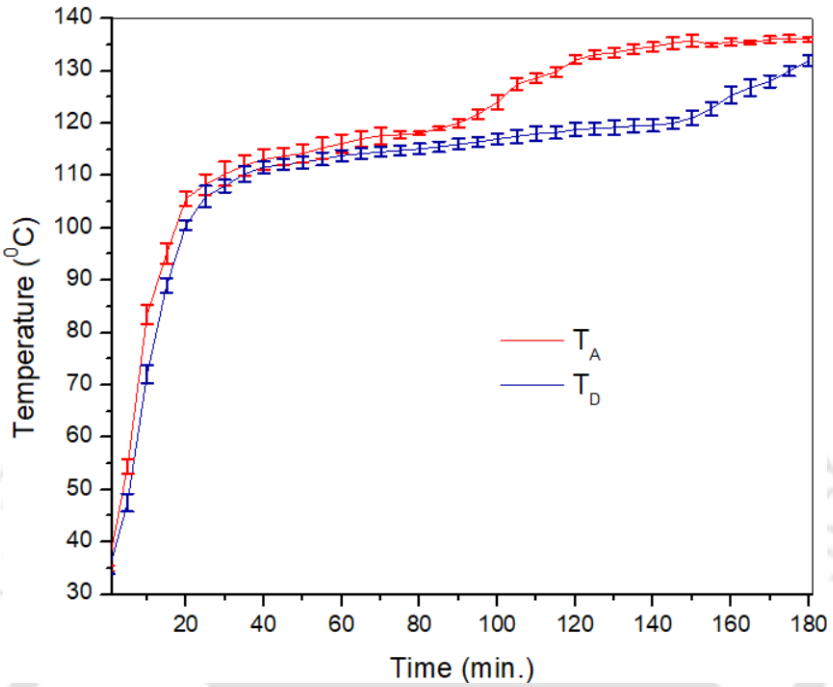

Fig. 5.4.Average transient temperature with error bars of the PCM at points A and B

5.2.5 Experimental temperature evaluation

Fig.5.5 illustrates the temperature evaluation at the selected monitoring points (A to J) during the chagrining process. The thermocouples embedded in the PCM are also used to monitor the temperature variation across the radial and axial direction of the storage unit. At the initial stage of the process, the temperature at all measuring points under consideration increases rapidly with the slight increment. This could be due to the conduction heat mechanism in the beginning. Later the transient temperature of some thermocouples increases differently as compared to other thermocouples. The rate of temperature augmentation varies in the radial and axial direction of the LHS unit.

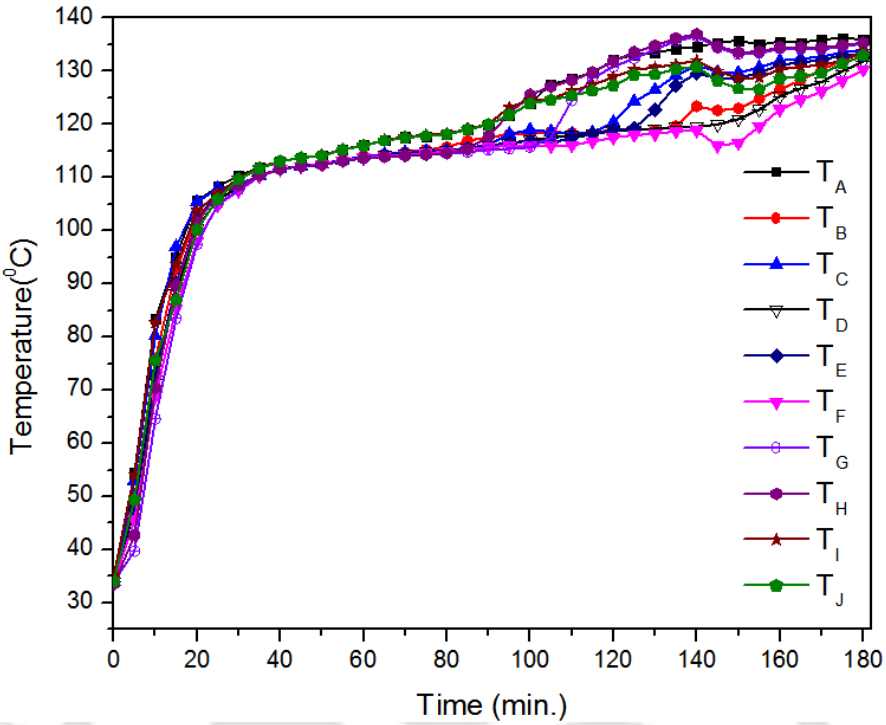

Fig. 5.5.Experimental temperature evaluation during the charging process at a flow rate of 75 LPM and 138 ^{0}C inlet temperature

For an in-depth understanding of the heat transfer characteristics of the PCM in all direction, the temperature variation of selected points is examined carefully. For the investigation the temperature variation along the radial direction, four points (A, C, D and H) are selected and the transient temperature is shown in Fig.5.6 (a). As clearly displayed in Fig.5.1, points A and D are situated at the same radial distance, but point A is placed at the top section of the storage and point D is at the bottom section. Likewise, the thermocouple positions of C and H are at the same distance from the inlet side of the storage unit, but point C is near the bottom section while point H is located above C. However, the transient temperature curve of a thermocouple located at point A remains above that of point D throughout the entire process. Similarly, the temperature curves of C and H indicate similar trends. This is due to the presence of natural convection in the liquid erythritol. In other words, due to the density difference, the solid phase fraction of the PCM is squeezed towards the lower portion of the storage unit, while the liquid part floats in the upper section. As a result, the presence of liquid phase PCM in the upper portion of storage enhances the melting in that region. Conversely, due to the unbalanced quantity of solid PCM on the bottom section decreases the melting rate.

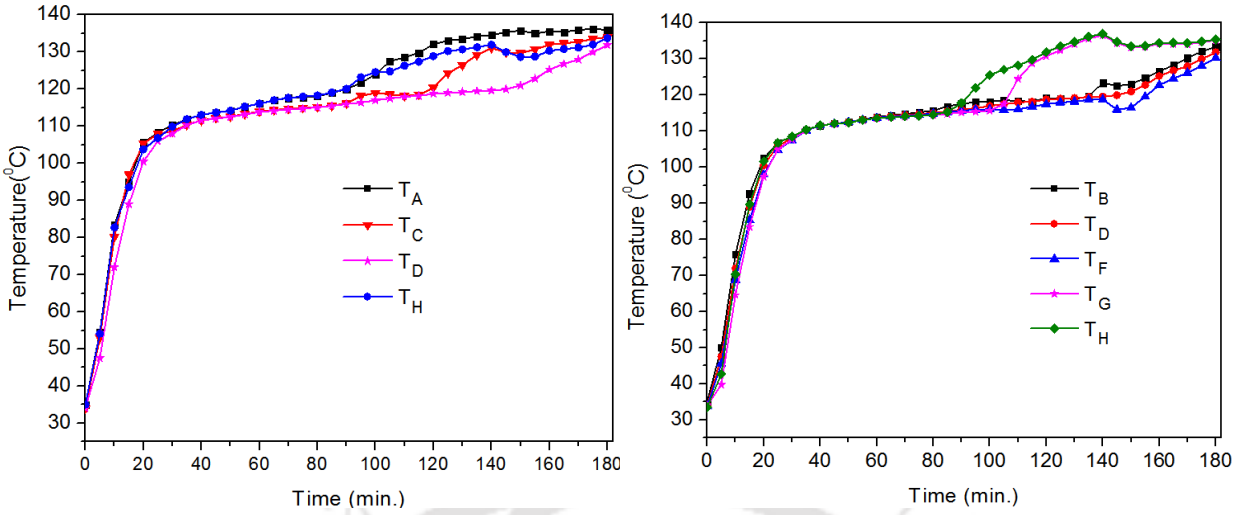

Fig. 5.6.Radial (a) and axial (b) transient temperature distribution at selected monitoring points

For examining the effect of gradient temperature along the longitudinal axis, five points (B, D, F, H and G) are selected. Points B, D and F are positioned at the same radial distance from the center of the storage unit but at a different axial distance; the former one is near to the inlet of the HTF, the second one is in the middle of the storage unit, whereas, the third one is situated near to the outlet of the HTF. Therefore, as it is displayed in the transient temperature curve of Fig. 5.6 (b) the temperature evolution at point B is slightly higher than that of point D and F due to the temperature gradient across the horizontal axis of the LHS unit. The variation in the heat transfer between these points is due to point B is being adjacent to the inlet of HTF. Similarly, the timewise temperature curves dissimilarity of the other points located at the same radial distance but at a different axial distance, like points C and E, points H and G and points I and J are justified using a similar explanation.

5.2.6 HTF volume flow rate effect

Fig.5.7 displays the transient average temperatures comparison of the storage unit at four thermocouples locations (A, B, C and F) using three different total volume flow rates of the HTF viz. 75 LPM, 65 LPM, and 55 LPM. It can be seen that increasing the volume flow rate introduces minor temperature differences as the time elapses. However, in the early and intermediate heat addition process, the rate of temperature increase with the corresponding working fluid flow rate variation is insignificant in all measuring points. Generally, the effect of this non-uniform flow

rate exhibits visible change on the melting progress variation of the PCM as indicated in all graphs (Fig.5.7 (a)-(d)).

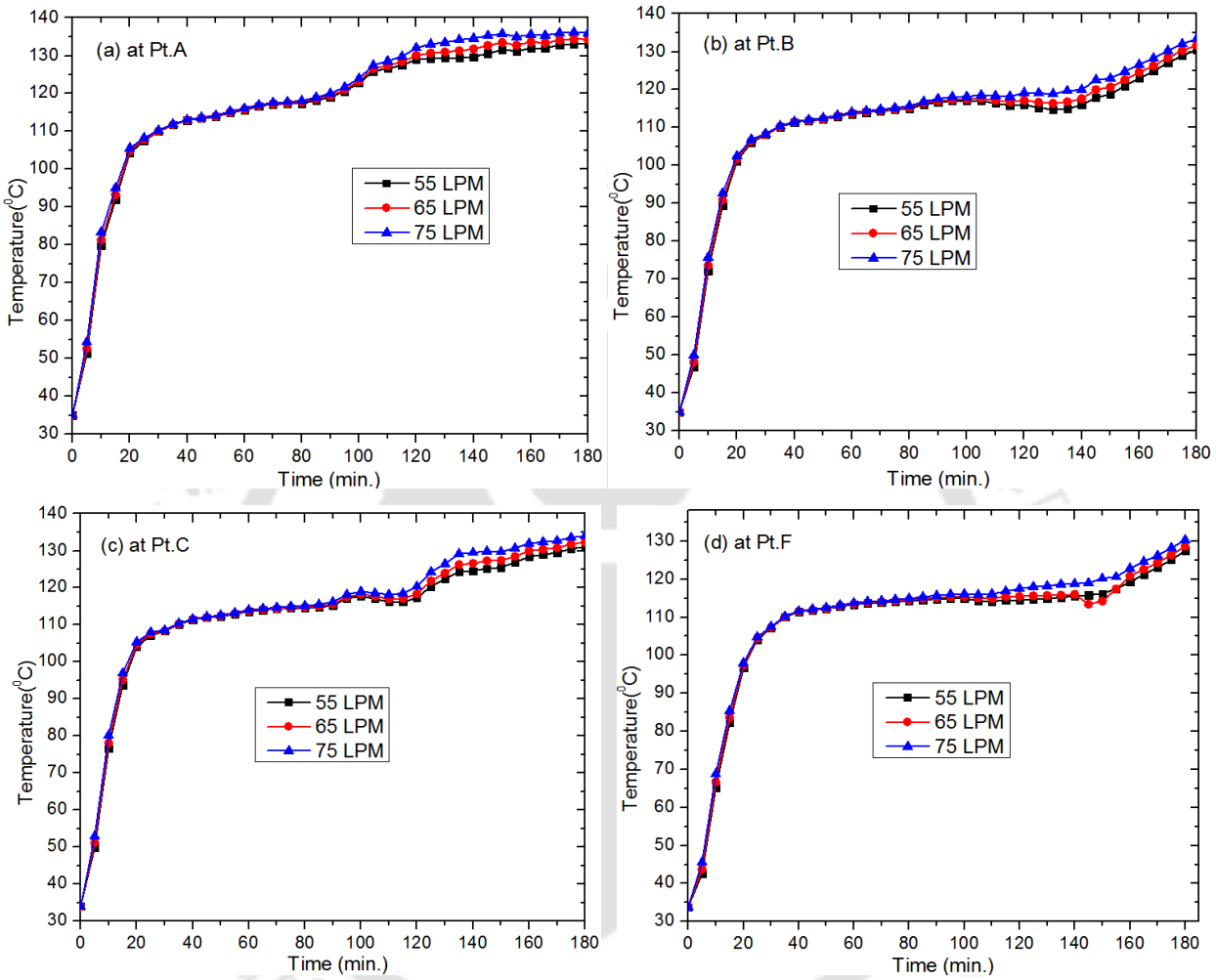

Fig. 5.7.HTF inlet speed effect on the transient temperatures of the LHS unit at selected positions

5.2.7 Effect of HTF inlet temperature

Adding external heat to PCM stores sensible heat only until the temperature of the system reaches over its melting point. Hence, increasing the inlet temperature of the fluid leads to store the intended quantity of energy within a shorter time. Fig.5.8 illustrates the comparisons of transient liquid fraction curves for the LHS unit under study at three HTF inlet temperatures of 133 ^{0}C, 138 ^{0}C and 143 ^{0}C during the heat-storing process. It can be observed from the graph that the HTF inlet temperature affected heat storage progress and the higher the inlet temperature resulted in a shorter melting time of PCM.

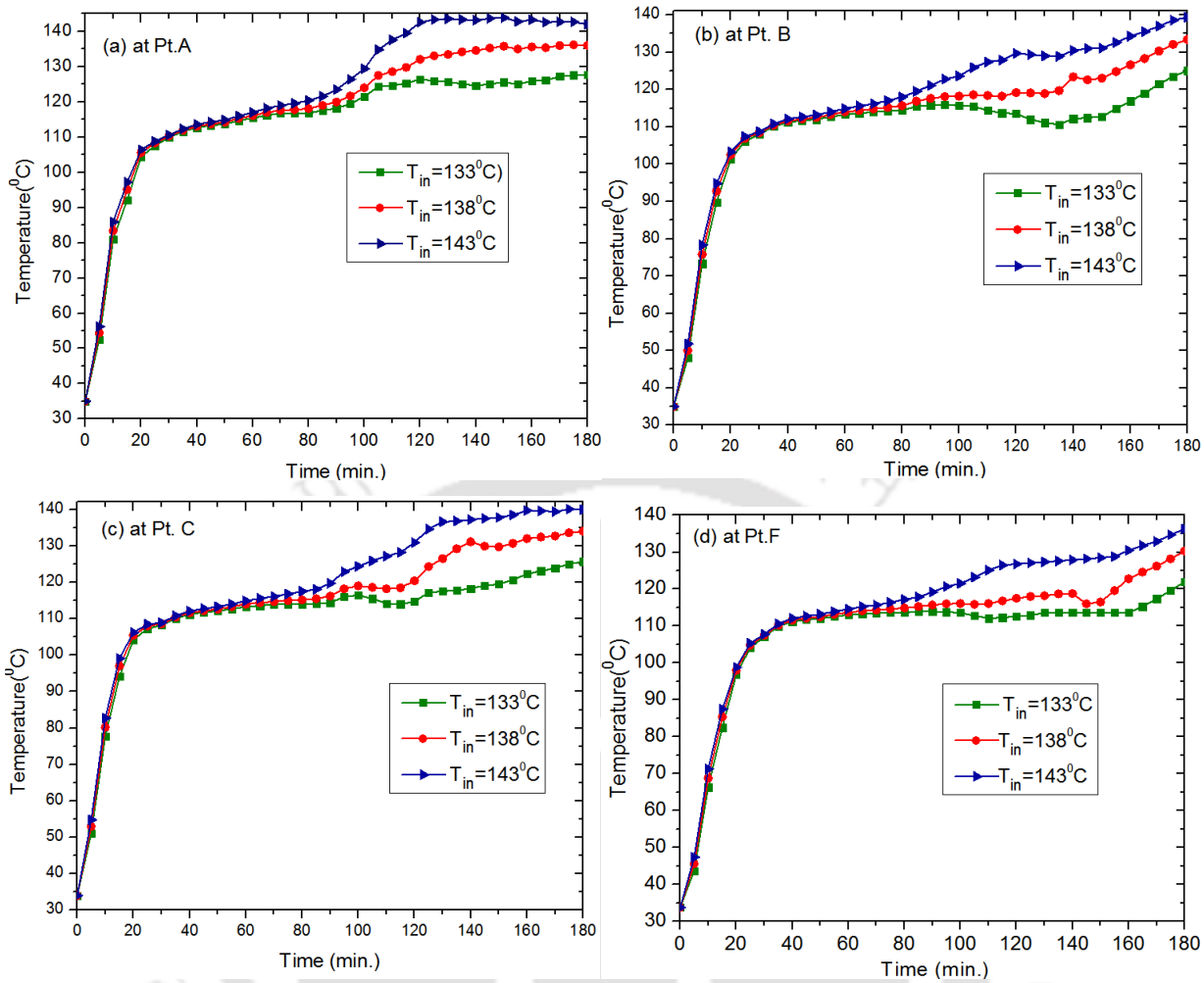

Fig. 5.8.HTF inlet temperature effect of the LHS unit at selected points

5.2.8 Outlet temperature variation

The variation of HTF outlet temperature with error bars versus time is depicted in Fig.5.9. In addition, the figure depicts the time-wise inlet and outlet temperature difference (dT) of the working fluid. The HTF outlet temperature is directly affected by PCM and the heat transfer mechanisms of HTF. At the beginning of the heat addition process, the outlet temperature is increasing rapidly and this is attributed to the higher heat transfer rate at the early stage. Near to the beginning of the process, the higher inlet temperature conveyed by HTF is mostly absorbed by the PCM because the temperature of HTF is higher as compared to the PCM. We can observe from the graph that the rate of outlet temperature gets reduced after the PCM in the storage unit absorbed the required amount of heat. The difference in temperature between inlet and outlet reaches around 0 at the time of 180 min.

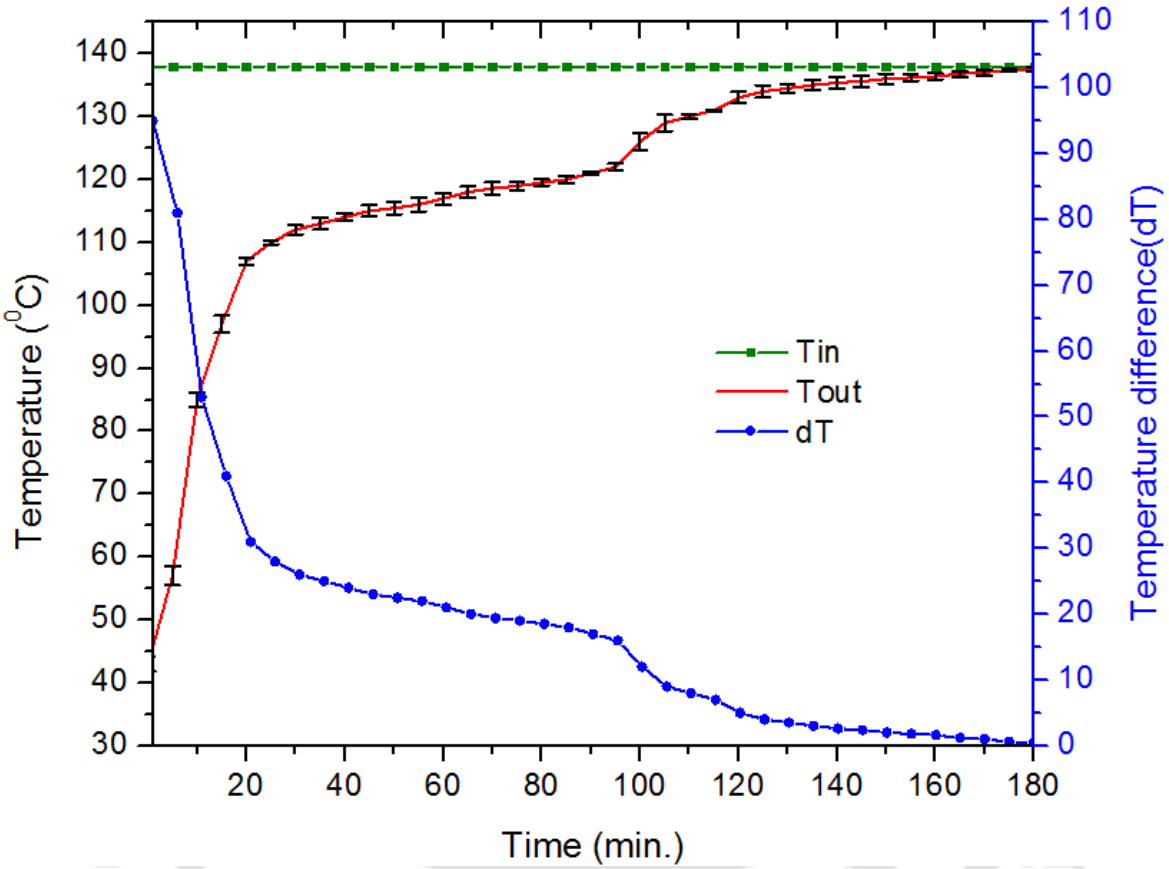

Fig. 5.9. HTF outlet and inlet and outlet temperature change (dT) variation

5.3 Numerical results

For the design of the effective TES system optimization technique is commonly used and this method is a difficult task. The melting and solidification behavior of PCM is dealt with highly non-linear equations and predicting the property of such a system during the phase change is difficult. Numerical modeling tools are helpful to overcome the analytical limitations to understand and investigate the charging and discharging process of PCM based LHS systems [38]. Performing numerical modeling and simulation of LHSS systems is the best solution to alleviate the above problem.

In section 5.2, thermal performance of the developed shell and tube LHS unit is studied experimentally. For comparison of the experimental results of the storage unit, a 3D LHS computational model that replicates the actual unit is developed using ANSYS-Fluent. Moreover, multiple investigations of different LHS models are carried out to select the optimal number of HTF tubes and fins for the optimal performance of LHS. Average temperature, liquid fraction, melting time and stored energy parameters are considered as thermal performance measuring

variables. The experimental results reported in this paper can be used as a guideline by system designers and technologists for the design and development of thermal energy storage systems.

5.4 Numerical formulation

In this section, we present a numerical analysis of LHS and its component in detail. The assumptions, equations involved for analyzing the melting process of the PCM and corresponding initial and boundary conditions, and numerical procedures are discussed in this section. It is to be noted that the shape of the storage unit is circular and symmetric. Therefore, for minimizing computational time, a quarter of the LHS model is chosen as the computational domain for the numerical analysis and is shown in Fig.5.10 for completeness.

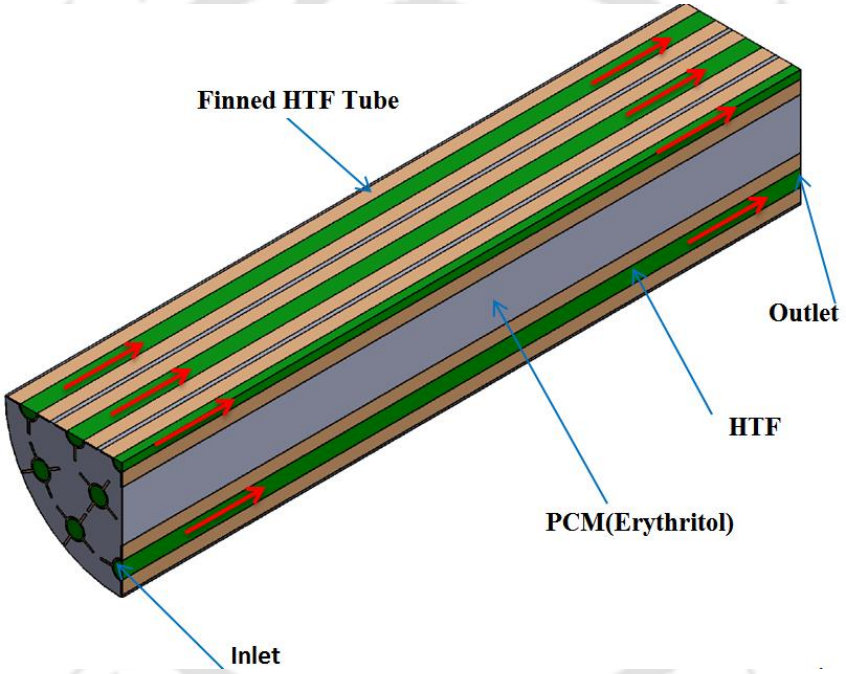

Fig. 5.10.Isometric sectional pictorial drawing of the LHS model

The performance of the TES system is estimated using the major important parameter viz. HTF flow rate, the initial temperature of the system and inlet and the HTF outlet temperature. These parameters were gathered from the experimental set up using the data acquisition system. For this reason, several thermocouples are fixed in different locations of the Experimental setup. Two thermocouples are placed one in each of the HTF storage tank, LHS unit inlet and outlet and the remaining temperature sensors are mounted in the LHS system at different axial and radial directions as displayed in Fig. 5.1. The thermocouples mounted inside the PCM are annotated by alphabets from A to J as indicted. During the charging process, the hot HTF was directed into the

LHS unit and heat conveyed into the PCM. The inlet temperature is HTF is maintained constant at 138 ^{0}C in the range that can be generated by the solar collector fabricated for this purpose.

5.4.1 Numerical analysis of governing equations

For the numerical investigation of the LHS unit, a 3D numerical model is developed. The following assumptions are taken into account to develop a thermal model of PCM. The flow was presumed to be laminar, unsteady, and incompressible Newtonian fluid flow and three dimensional. The PCM and HTF tubes have uniform initial temperature across all points, phase transition occurred in a temperature interval, it is isotropic and homogeneous and thermal loss toward the external wall of the storage unit is presumed to be zero. The combination of both convection and conduction heat transfer model was adapted to examine natural convection [33]. In several studies, it has been mentioned that neglecting the natural convection involvement in the phase transition process of the PCM is not recommended. Since the natural convection affects the melting and solidification of the PCM. The Boussinesq approximation method is adopted to consider the natural convection in the numerical model. The selected method is used to take care of the small density variations that account only for buoyancy force otherwise it is assumed that the fluid density remains invariable in all terms [66]. In the charging and discharging of the PCM, the natural convection is handled by including the buoyancy effect of the liquid PCM [131]. In this regard, the third term in the right-hand side of Eq. (5.8) stands for this purpose. As per the above-mentioned assumptions, the Eq. (5.7), (5.8) and (5.9) are employed for the transient analyses of the PCM melting process and HTF flow.

Continuity equation

$$\frac{\partial \rho}{\partial t} = \nabla.(\rho \vec{V}) \tag{5.7}$$

Momentum equation

$$\rho \frac{\partial \vec{V}}{\partial t} + \rho \vec{V}.(\nabla.\vec{V}) = -\nabla \mathrm{P} + \mu \nabla^2 \vec{V} + \rho \beta \vec{g}(T - T_{ref}) + \vec{S} \tag{5.8}$$

Energy conservation equation

$$\frac{\partial}{\partial t}(\rho h) + \nabla.(\rho.\vec{V}h) = \nabla(\mathrm{k}\nabla \mathrm{T}) \tag{5.9}$$

The momentum equation's source term is valid only for the PCM domain and it is not considered for the analysis of HTF [137]. The external surface of each HTF tube is with the direct contact of

the longitudinal fins and the thermal resistance between contact surfaces is minimal. On the interface of working fluid and HTF tubes' walls, the conjugate heat transfer is expressed by Eq. (5.10) [138].

$$k_{tube}\frac{\partial T_{tube}}{\partial n} = k_{HTF}\frac{\partial T_{HTF}}{\partial n} \tag{5.10}$$

The thermal diffusivities in the fins and PCM are not uniform as a result an interface is created. The interfaces between those two domains are evaluated using conjugate heat transfer as per Eq. (5.11) [139].

$$k_{PCM}\frac{\partial T_{PCM}}{\partial n} = k_{fin}\frac{\partial T_{fin}}{\partial n} \tag{5.11}$$

where, 'n' denotes the vector normal to the interface in the direction from fin to PCM and vice versa.

The entire enthalpy (H) Eq. (5.12) of energy storage media is the summation of the sensible enthalpy (h) Eq. (5.13) and the latent heat (ΔH) Eq. (5.14) which is caused due to phase change.

$$H = h + \Delta H \tag{5.12}$$

where,

$$h = h_{ref} + \int_{T_{ref}}^{T} C_p dT \tag{5.13}$$

$$\Delta H = \theta L \tag{5.14}$$

The numerical analysis of phase change stages such as melting and solidification of PCM are modelled as moving boundary conditions [140]. The moving boundary does not develop smoothly from one stage to the next one in a logical order and predicting the phase transition is challenging. For modelling moving solid/liquid interfaces of the PCM numerically, the commonly used enthalpy-porosity technique is applied which represents co-occurrence of both liquid and solid phases simultaneously. The enthalpy-porosity method traces movement of the mushy region of PCM indirectly via liquid fraction parameter. For a particular cell in the PCM, the liquid fraction (θ) of that cell is equal to its porosity. The solid part of PCM is represented by zero value of liquid fraction and the porosity or liquid fraction of the liquid part is equal to unity [141], [142]. The melting fraction (θ) can be estimated based on Eq. (5.15):

$$\theta = \frac{\Delta H}{L} = \begin{cases} 0 & if\ T < T_s \\ \dfrac{T - T_s}{T_l - T_s} & if\ T_s < T < T_l \\ 1 & if\ T > T_l \end{cases} \quad (5.15)$$

Hence, the source term $\vec{S}$ which is part of the momentum conservation equation is represented by Eq. (5.16).

$$\vec{S} = \frac{(1-\theta)^2}{(\theta^3 + \varepsilon)} A_{Mush} \vec{V} \quad (5.16)$$

Mushy region constant is an imperative parameter for the entire model of PCM and its value ranges between 10^4 and 10^7 (kg m^{-3} s^{-1}). The value for this study is chosen as 10^5 [143]. Here, ε is a trivial quantity (10^{-3}) employed to avoid division by zero. During the heat addition process, PCM remains solid until temperature of the LHS reaches phase transition point and energy is stored in the form of sensible heat during this period. Later heat gets stored as latent heat at steady temperature until PCM melts completely. The liquid PCM continues the heat addition process in the form of sensible heat till the process keeps going on. The stored sensible heat (Q_{sen}), latent heat (Q_{lat}) and whole heat stored (Q_{tot}) in the storage unit can be calculated as per Eq. (5.17), (5.18) and (5.19).

$$Q_{sen} = mC_p(T - T_{ini}) \quad (5.17)$$

$$Q_{lat} = mL\theta \quad (5.18)$$

$$Q_{tot} = mC_p(T - T_{ini}) + mL\theta \quad (5.19)$$

During the heat releasing process heat is discharged from the PCM to the working fluid. The quantity of released sensible heat ($Q_{sen,D}$), latent heat ($Q_{lat,D}$) and their summation ($Q_{tot,D}$) are estimated using the following equation.

$$Q_{sen,D} = mC_p(T_{ini} - T) \quad (5.20)$$

$$Q_{lat,D} = mL(1 - \theta) \quad (5.21)$$

$$Q_{tot,D} = mC_p(T_{ini} - T) + mL(1 - \theta) \quad (5.22)$$

5.5 Boundary conditions

For the melting process, the initial and boundary conditions numerical modeling were kept similar to that of the experimental study. Initially (t=0), the reference temperature of the whole computational domain (PCM, HTF tubes and HTF) was set to be at constant room temperature (27 ^{0}C). Besides the HTF domain was assumed zero velocity to treat this no-slip boundary was applied. Then after (t>0), HTF is pumped into the LHS unit with a volume flow rate of 75 LPM and temperature of 138 ^{0}C. Similar to the experiments study, multiple simulations are conducted by varying inlet HTF temperature and volume flow rate values; the HTF inlet temperature varies from 133 ^{0}C to 143 ^{0}C because heating the PCM over the above limit can cause non-uniform heat distribution [28]. To protect heat loss, the outside walls are thermally insulated. During the period of the solidification process, the LHS system was maintained to start from 138 ^{0}C and the value of the HTF volume flow rate is the same as the charging process, whereas the HTF inlet temperature is 87 ^{0}C.

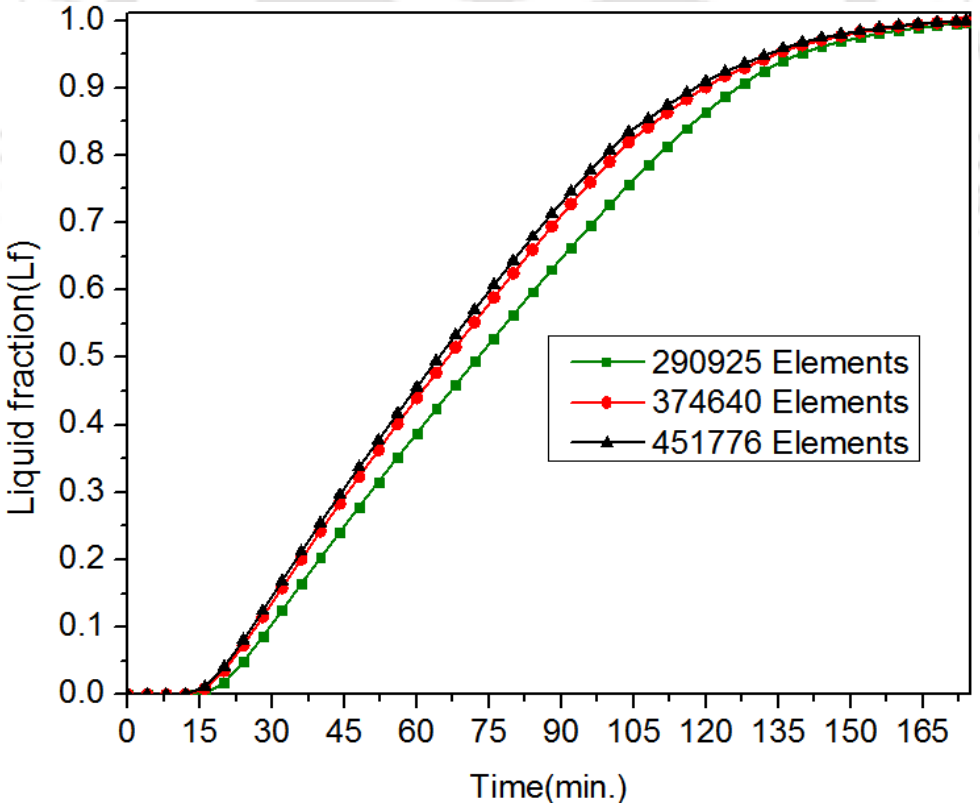

Fig. 5.11.Effects of the grid element size on the timewise average liquid fraction

5.6 Numerical procedure

As explained in the above section the governing equations that represent the PCM and HTF were numerically modeled and solved using ANSYS Fluent environment. The governing equations that represent PCM, HTF and finned HTF tubes, are numerically modeled and are analyzed using ANSYS Fluent environment. For the numerical pressure-velocity coupling, semi-implicit pressure-linked equation (SIMPLE) is applied. The PRESTO scheme is implemented to treat the pressure correction equation. The momentum and energy equations are discretized with a second-order wind differencing scheme. The numerical results could be affected by the considered element mesh and time step size. For ensuring an accurate numerical solution, the grid size and time step size should be selected appropriately. Accordingly, the LHS model is tested for multiple possible meshes and time step sizes. Three different grid elements sizes of 290925, 374640 and 451766 are presented here for comparison and examined carefully. Similarly, three different time step size of 2s, 1s, and 0.5s are selected for the analysis.

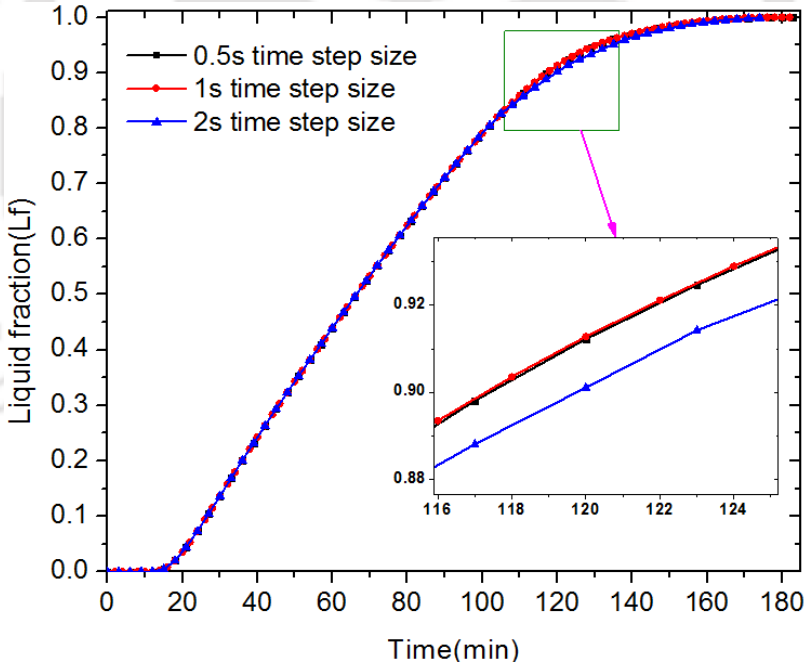

Fig. 5.12. Effects of the time step size on the timewise average liquid fraction

The transient liquid fraction parameter is considered to perform the independence tests for both grid and time step sizes as shown in Fig.5.11 and Fig. 5.12. It can be noted from the graph, the estimated liquid fraction graph for 451,776 and 374,640 grid elements are very close. Similarly, the liquid fraction curves of the corresponding three different grid elements coincide with each other for different time steps sizes. Hence, considering the computational time and accuracy the

entire simulation was performed with 374640 total number of grid elements and 1s time step size. The values for under-relaxation factors for energy, liquid fraction, momentum and pressure are set at 1, 0.9, 0.7 and 0.3, respectively.

Moreover, to ensure the reliability of the developed numerical CFD code, numerical simulation was conducted and compared against the practical results of Agyenim et al.[29]. The same properties of PCM, similar initial and boundary conditions as the experimental study were used for validation. The timewise average temperature parameter during the charging process was used for the comparison of the two studies. Fig.5.13 depicts the present numerical and practical results and a good agreement observed.

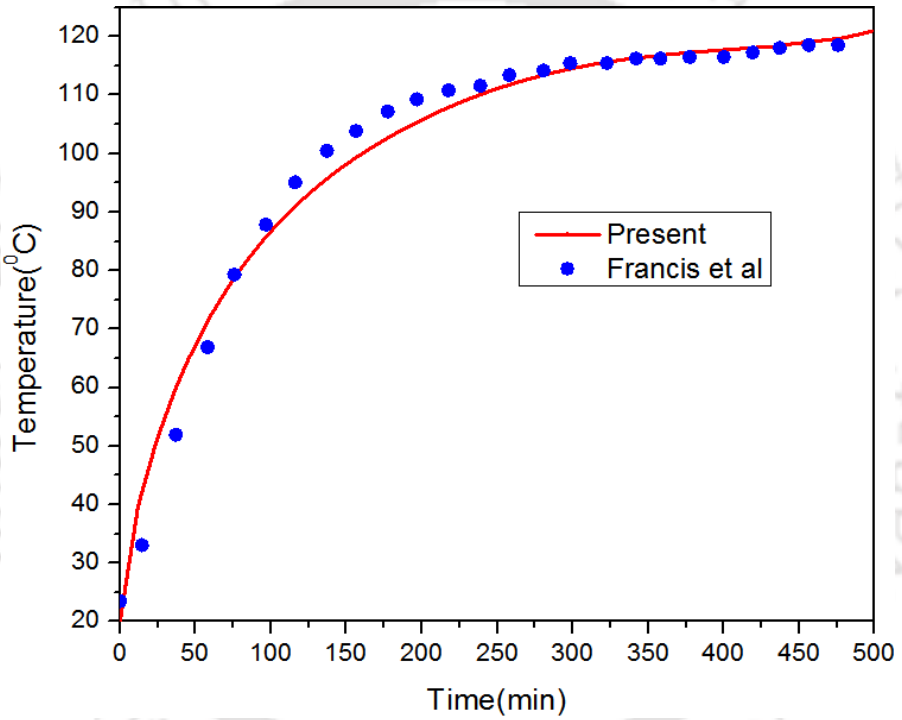

Fig. 5.13.Transient temperature numerical result comparison vs. the experimental results by Agyenim et al [29]

5.7 Numerical Analysis

In this section we present and result and subsequent numerical and experimental analysis of LHS.

5.7.1 Optimization of the numbers of HTF tubes and fins

Several techniques are presented in the literature to improve the low thermal conductivity of PCM. Among these methods embedding multiple finned HTF tubes in the PCM is the most effective and common practice to enhance the thermal transportation inside the storage unit. Hence, the optimum numbers of HTF tube and fins which are connected on the external surface of each tube should be

determined. In this section, a two-dimensional numerical model is developed to determine optimal number of HTF tubes and optimal number of the fins on each tube. Therefore, to optimize the numbers of HTF tubes, four cases of LHS models with 15, 17, 19 and 21 HTF tubes are proposed as shown in Fig. 5.14. Furthermore, to decide the numbers of fins in a single HTF tube, three LHS models with 2, 4 and 6 numbers of fins are considered as shown in Fig. 5.15.

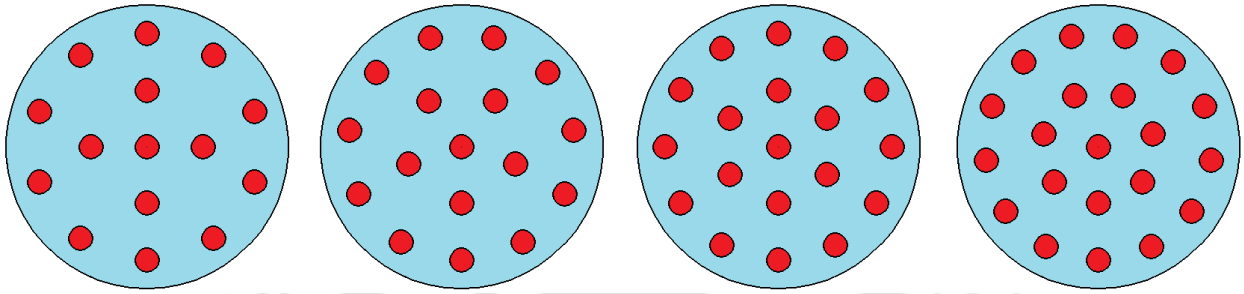

(a) (b) (c) (d)

Fig. 5.14.Determination of number HTF tubes (a) 15 tubes (b) 17 tubes (c) 19 tubes and (d) 21 tubes

Fig.5.14 illustrates four LHS models considered for the optimization process. These models are differentiated from each other based on the numbers of HTF tubes. Moreover, Fig. 5.15 also demonstrates three LHS models with different numbers of fins configurations. The internal shell diameter of every LHS model is appropriately selected so that the amount of PCM contained in the annulus is same for each case. The dimensions of the internal diameter of the proposed LHS models along with their melting times are indicated in Table 5.2. It can be seen from Table 5.2 that increasing the number of HTF tubes from 15 to 19 results to a noteworthy reduction in melting time. Briefly, while comparing the 15 and 17 HTF tubes, it can be observed that the reduction in melting time is 9 %. On the other hand, it is compared to the 17 tubes with 19 tubes, the decrease in melting time is 8.4 %. However, comparing the total time taken to complete the melting of PCM in the last two LHS models (with 19 and 21 HTF tubes), there is not any significant change. Increasing the numbers of tubes brings an insignificant effect on the melting time by reducing it by 2.1 %, therefore, the optimum numbers of HTF tubes are selected as 19.

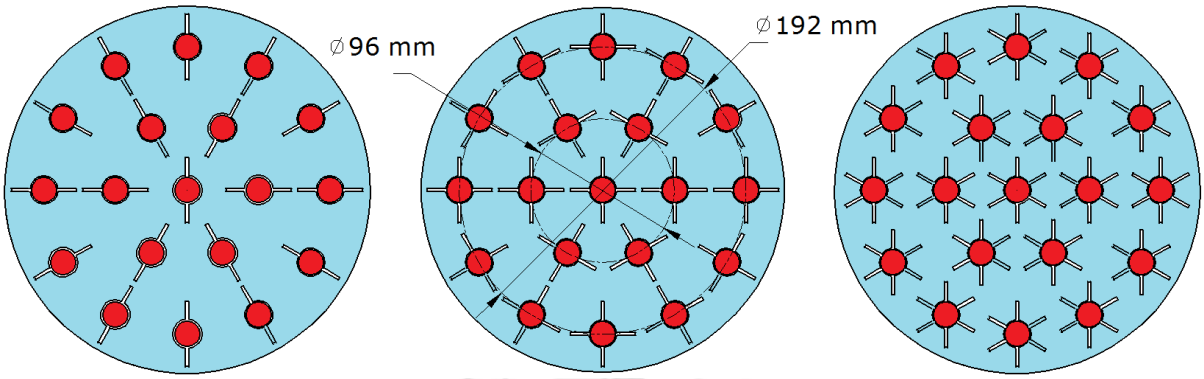

(a) (b) (c)

Fig. 5.15.Determination of number of fins (a) 2 fins tubes (b) 4 fins and (c) 6 fins

Likewise, three kinds of LHS models, with 2, 4 and 6 fins connected with each HTF tubes are examined to find the optimum numbers of fins connected with each tube. From the above discussion, the optimum LHS model has 19 HTF tubes and this is considered for the optimization of fins. The numerical result of each case is listed in Table 2 and the melting rate is enhanced as the numbers of inserted fins are increased. It can be observed that the time taken to complete the melting of the LHS model with two fins is reduced by 30.8 % as compared to the unfinned optimum LHS model mention in Fig. 5.14 (c). Similarly, there is a 34.9 % reduction in melting time when four fins model is compared with the 2 fins LHS. Generally, increasing the number of fins improves the melting rate of the PCM, however, the reduction in melting time is only 8.3 % comparing the six fins versus the four fins LHS model. Therefore, the LHS unit consists of 19 HTF tubes in which four fins are connected on the external surface of each tube is found to be the best option.

Table 5.2

Number of HTF tube and fins optimizations

Numbers of HTF tubes	Inner shell diameter (mm)	Melting time(min.)	Numbers of fins	Inner shell diameter (mm)	Melting time(min.)
15	236	288	2	237.7	166
17	238	262	4	240	108
19	240	240	6	242.5	99
21	242	235			

In this section, the effective fins presence and their configuration with respect to the HTF tube and PCM have been discussed and the optimum fins configurations are recommended. To achieve this, three different LHS models are considered and the thermal performance of each model is compared. To optimize the configuration of HTF tubes and fins with in the PCM, 2D thermal model is developed for the selected four LHS models and solved using the developed governing equations Eq. (5.7) - (5.16). Fig.5.16 illustrates the various models considered for optimization and out of the selected LHS models. In the other three models, each HTF tube is supported by four fins. The dimensions of the fins in all the three LHS models are same and the only difference among them is the way how the fins are oriented with respect to the HTF tube and PCM.

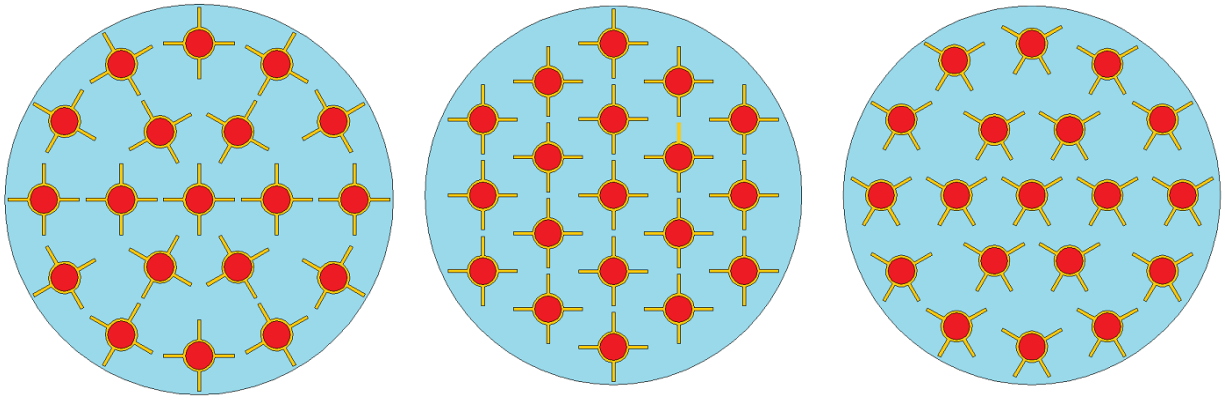

(a) (b) (c)

Fig. 5.16..Optimizations fins Configuration models

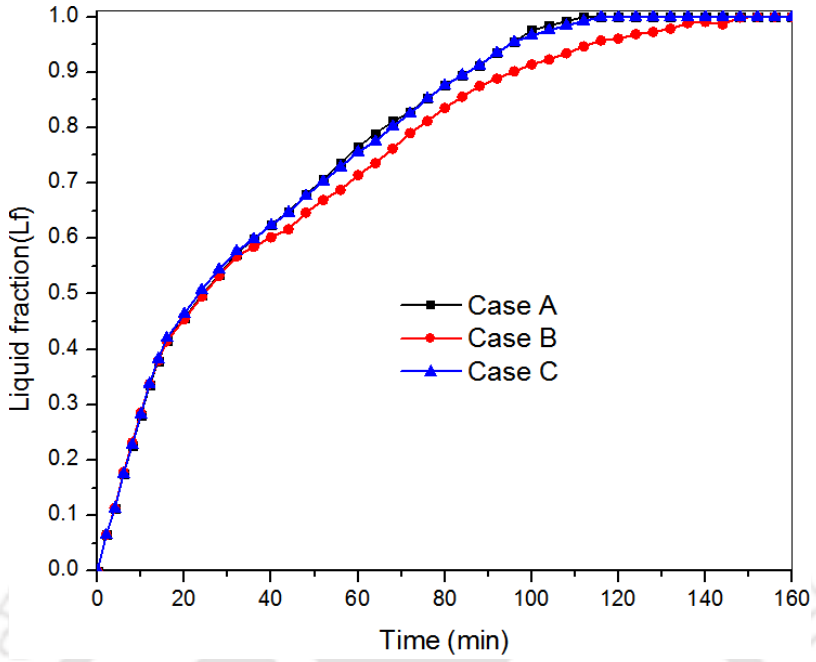

Fig. 5.17.Comparison of three LHS models at different fins configurations

The main differences among the finned LHS models are clearly indicated in the Fig.5.16. The optimization is done based on the charging time and using liquid fraction as performance measurement parameter. The liquid fraction variation comparison as a function of time for all LHS units is indicated in Fig. 5.17. It can be seen from figures that, there is no marked difference in the melting progress among the finned LHS models about the beginning of charging process. This could be resulted due to the dominant conduction heat transfer mechanism in the presence of fins. After 40 min melting, time the LHS model in case B starts to slow down and the complete melting time is higher as compared to the others. The total time taken to complete the melting of LHS models case A and case C are 108 and 110 min, respectively. As a result, the LHS unit represented in model A is found the optimized configuration and it is also simple in construction.

5.7.2 Temperature evaluation

The temporal average temperature of the LHS model at selected six points (B, C, D, E, F, and H) during the time of charging processes are illustrated in Fig.5.18. To estimate the performance of LHS unit experimentally thermocouples were mounted at different points of the TES system and the above-mentioned points are considered to investigate the radial and axial temperature gradient. Almost all curves are ascending in a parallel way and with an insignificant difference up to 35 minutes. The rate of temperature augmentation slows down after that. As clearly displayed in Fig.

5.1, points B, D and F are placed at the equal radial distance from the central axis of the LHS unit. Point B is at the front of the radial axis and D is at the middle point whereas F is at the back. However, as it is displayed in the transient temperature curve the temperature evolution at point B is slightly higher than that of point D and the value of point D is more than point F and this reason was resulted due to the temperature gradient across the longitudinal axis of the LHS unit.

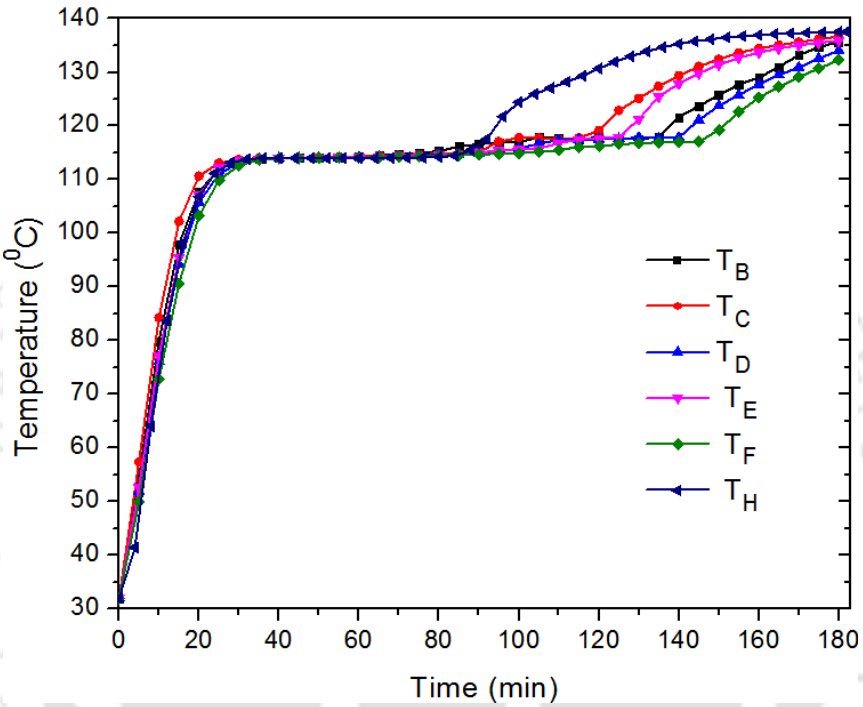

Fig. 5.18.Temperature curves of LHS unit at selected points at volume flow rate of 75 LPM

5.7.3 Charging/discharging average temperature

Fig.5.19 illustrates the transient temperature during the heat storing and solidification processes. Similarly, the temperature is expressed as a volumetric average temperature of each grid element of the numerically represented model. The rate of heat addition and removal is so high at the beginning of the melting and solidification process respectively. During the charging process rate of heat, addition starts to slow down after a time of 24 min; this could be resulted due to natural convection formation. The average temperature of the LHS model reaches 136.5 ^{0}C at the time of 180 min. The rate of heat removal during the solidification process is getting slowdown after a 15 min period.

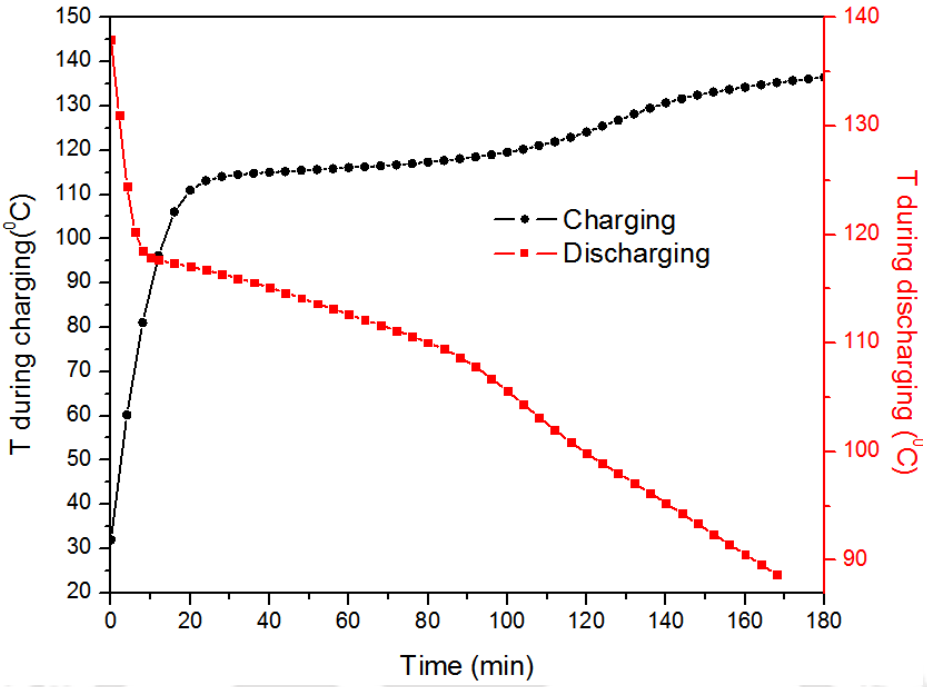

Fig. 5.19.Average temperature during melting and solidification process at flow rate of 75LPM

5.7.4 Convective flow analysis

For an in-depth understanding of the heat transfer characteristics of the system under consideration, including additional timewise decision parameters are required. Fig.5.20 presents the numerically predicted temperature and velocity streamlines distribution at four different time instances. The colored temperature contours that indicate heat transfer characteristics are drawn in the left hand of the symmetric line, whereas, convective flow is shown toward the right side of the line. Since the HTF tubes and fins are made from high thermally conductive material, the fins wall temperature is almost equal to the inlet hot working fluid temperature. The temperature contour presented in the figure reveals that the heat transferred from HTF to the tubes and the fins is higher. Even during early stage of the process, PCM near the fins is getting melted early since the presence of fins promotes the heat flux expansion. With time, because of the heat expansion, liquid part of the PCM increases and due to the slight temperature difference between the layers of the liquid region, the relative density difference is produced. The non-uniform density drives the liquid PCM to flow, developing natural convection. The relatively hotter liquid PCM ascends upward and hence, enhancing melting in the upper section. While the cooler liquid PCM descends downward and hinders melting in the lower part. This process directly induces vortexes as illustrated in Fig.5.20 on the right half-section. The movement of liquid PCM is shown through streamlines.

Near the beginning of the process, there are very sparse convective flows and this could be attributed to the influence of conduction heat transfer. It is evident from the velocity streams graph that the effect of natural convection is enhanced after heat is supplied to the LHS for one hour. Thus, as the time elapses, more flow fields are developed which originate from the hot walls toward the outer surface of the storage unit.

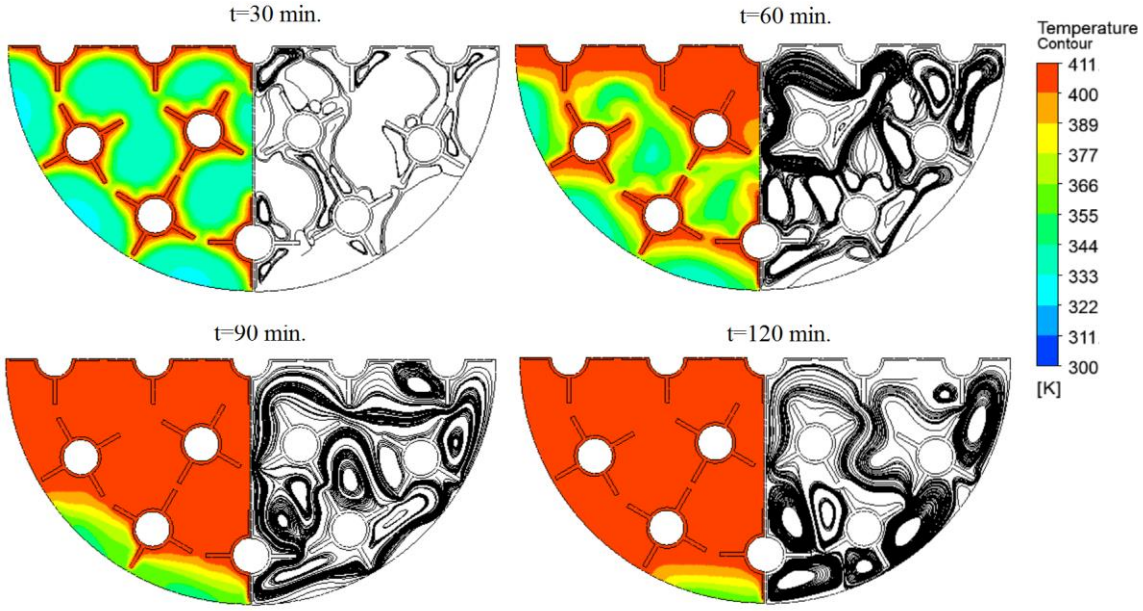

Fig. 5.20. Temperature distribution (left) and velocity streamlines (right) in the middle section (z=0.5m) four different periods

5.7.5 Liquid fraction evaluation

The liquid fraction is another dimensionless parameter that helps to evaluate the performance of LHS and the value varies from zero to one. The melting fraction indicates the comparison amount PCM either it is liquid or solid-state. If the PCM is completely solid, the liquid fraction is zero (0), whereas, if the PCM exists in a liquid state the melting fraction is one. When the PCM remains in the mushy condition the liquid fraction value varies from zero and one. The solid-liquid phase interface is indicated in Fig.5.21 and the blue color stands for the PCM in the solid-state while, red color represents the PCM in the liquid phase. Any color other than red and blue represents mushy condition of the PCM.

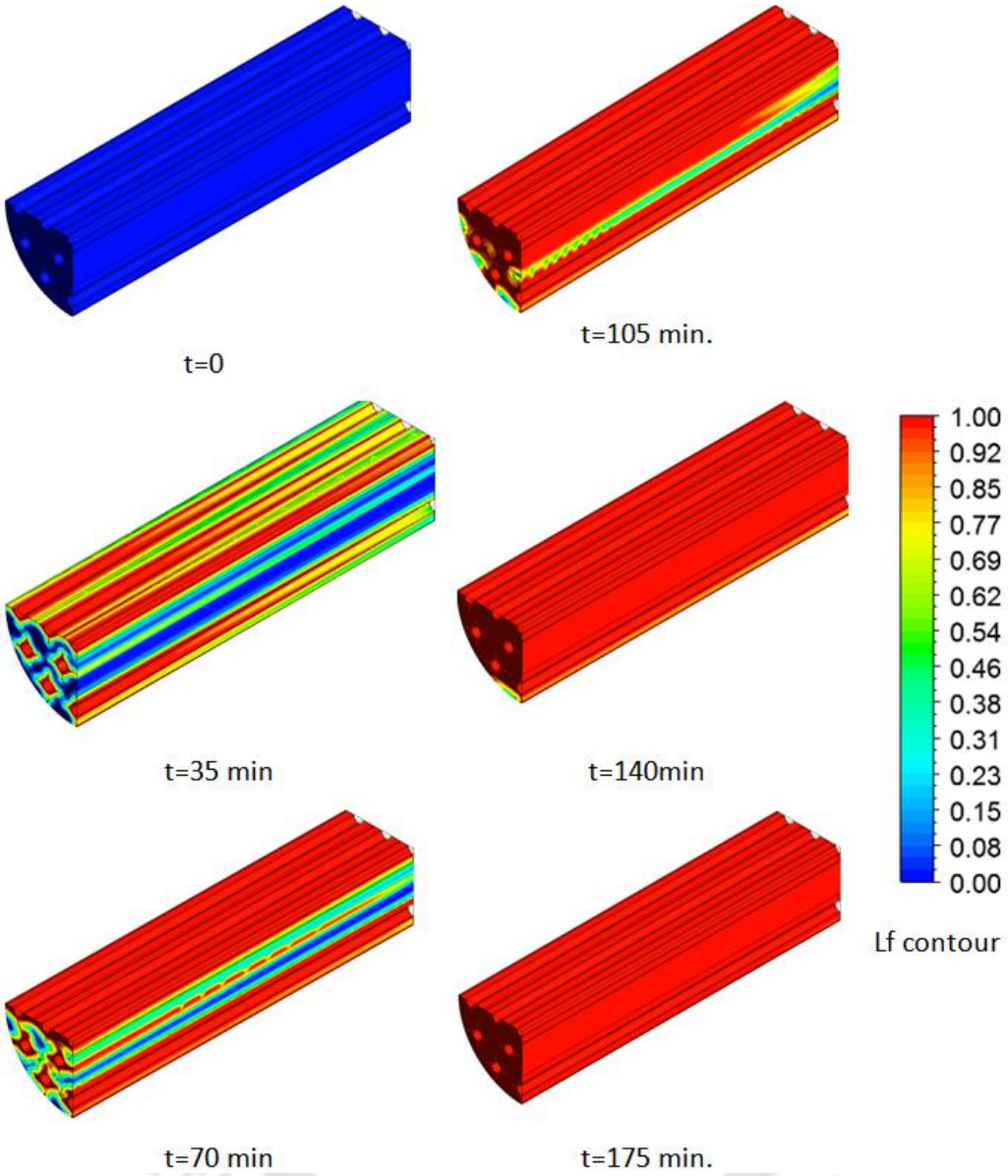

Fig. 5.21. Average melt fraction contours during the charging process

The figure illustrates that the melting of the storage system at the beginning of the process is fast and more than 50 % of the PCM melts with less than 70 mins. This is because of the minimum influence of natural convection at that time. However, as the melting of PCM increases, the effect of natural convection becomes stronger, which slows down the melting of the remaining solid PCM placed at the bottom section of the storage unit. In other words, the liquid PCM starts forming relatively hot and cold temperature layers and buoyancy is developed as a result of the variable density between cold and hot liquid PCM. Thus, the relatively hot and less dense liquid flows to the upper section and enhances the melting process in the upper section. On the other hand, the

relatively low-temperature liquid PCM flows downwards and delays the melting process. Relating to this Yuan et al. [91] investigated the effects of installation angle of fins on melting behavior of the LHS system and they have reported similar findings. Because of this, the total time taken for the complete melting of energy storage material is 175 min. This means that less than 50% of the PCM consumes more than 105 mins, which is 60% of the overall melting time.

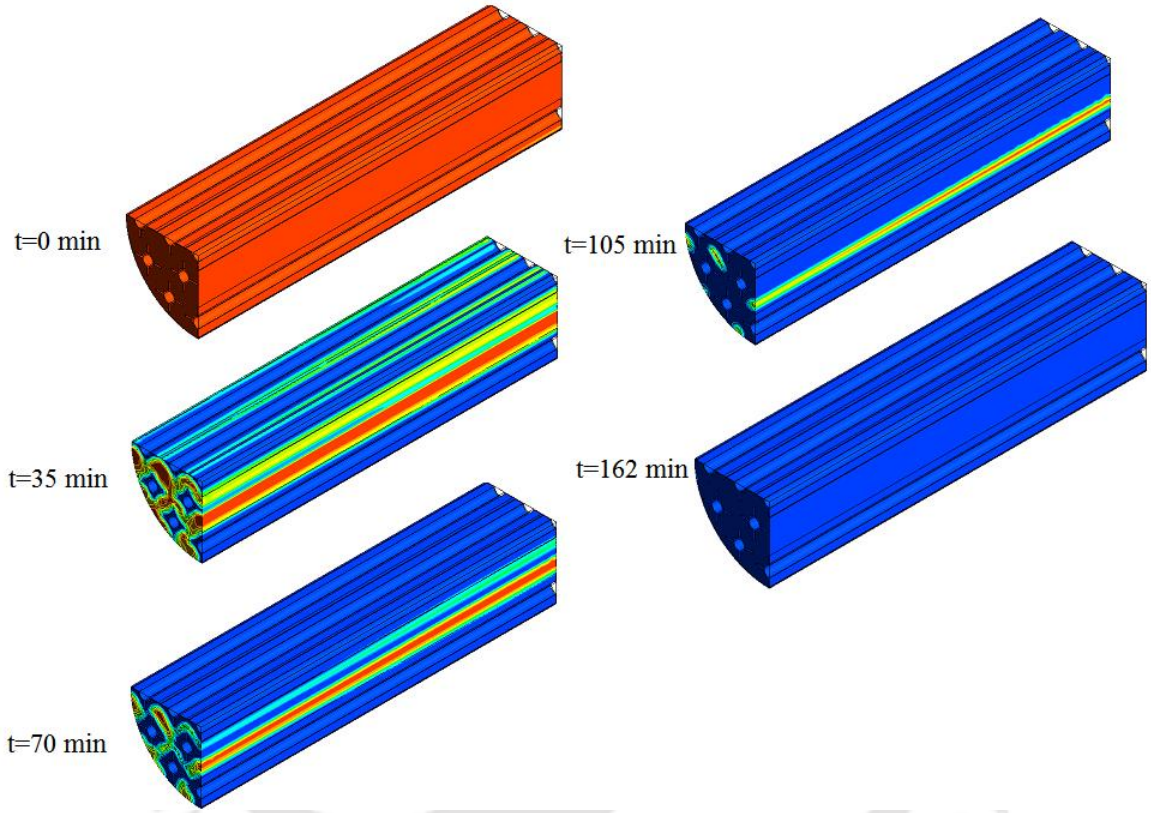

Fig. 5.22. Average melt fraction contours during the discharging process

Fig.5.22 presents the solid-liquid outlines of the liquid fraction of the 3D LHS model in the period discharging process. As it can be observed from the picture the rate of solidification process during the early period is fast. More than 50% of the liquid PCM is transformed into solid state within 35 min. However, the LHS unit consumes 162 min for the complete solidification process.

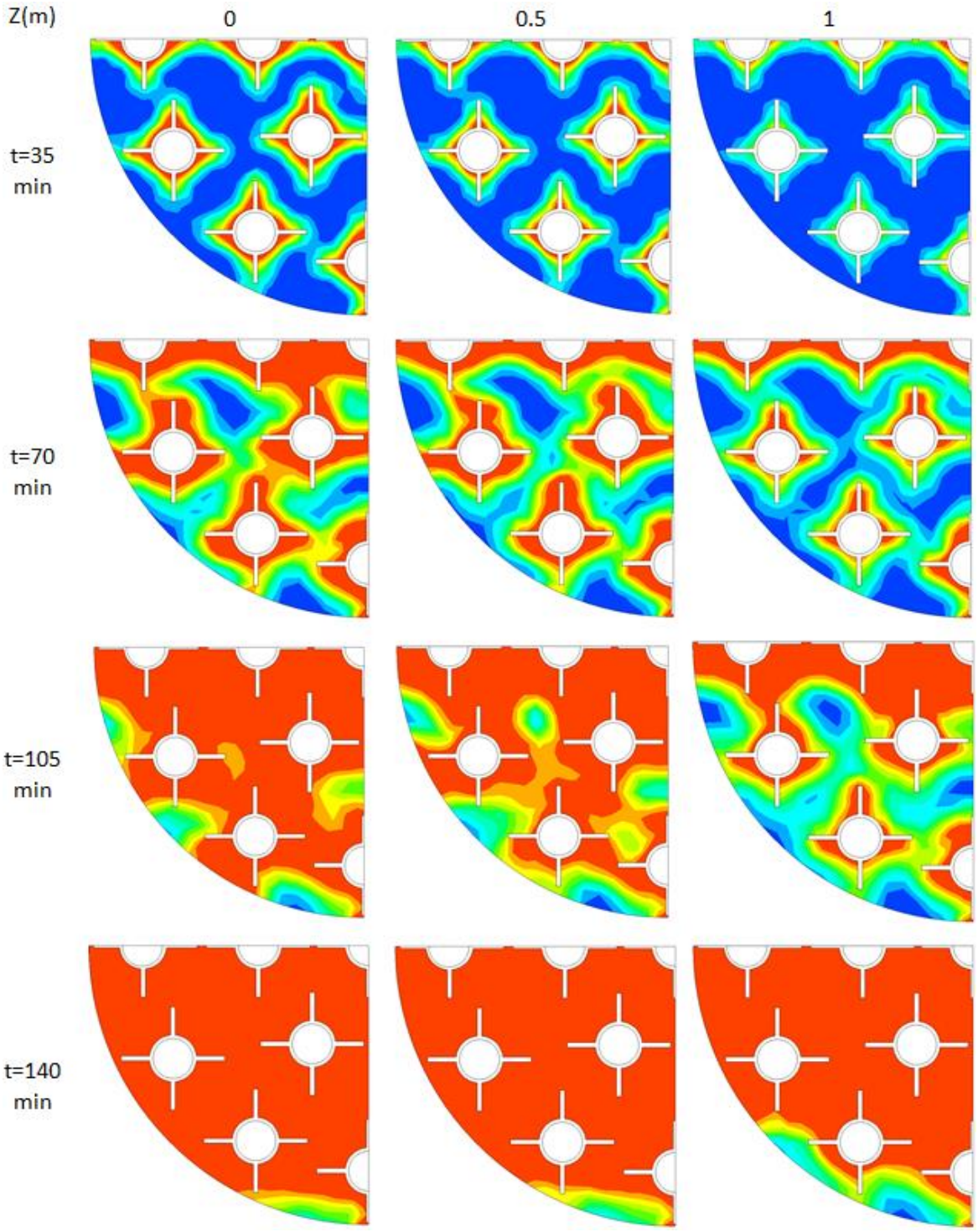

Fig. 5.23. 2D average melts fraction contours at the three different planes

In order to observe the effect of melting progress along the axial direction 2D melting fraction analysis at three different planes were considered: at entry portion (z=0), middle plane (z=0.5 m) and exit portion (z=1 m). Fig. 5.23 depicts the 2D average melt fraction contours at the three

different planes and four-time period. As can be noted from the figure the melting fractions contours are not uniform even at the same time due to the effect axial temperature gradient. The two-dimensional volume average liquid fraction of LHS model at the three selected planes was compared. As can be noted from the figure the liquid fractions contours of the PCM at the entry portion have increased relatively as compared with the middle and exit portion. In general, the liquid fraction of LHS across the axial direction is not uniform even at the same time due to the effect axial temperature gradient. This axial temperature gradient could result as a result of the large temperature discrepancy between the inlet HTF and PCM. Another important parameter that aids to evaluate the thermal storage performance is charging time and it is described as the time taken for the TES to accumulate energy. As explained earlier, the liquid fraction is a decisive parameter. Therefore, the variations in charging time with respect to melting fraction can be represented in terms of the graph of melting fraction.

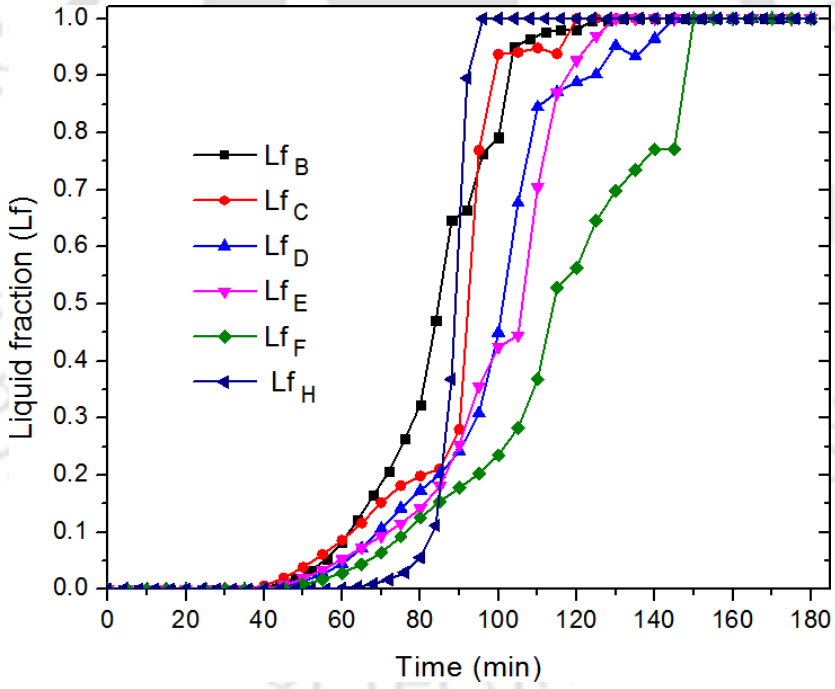

Fig. 5.24.Liquid fraction curves of LHS unit at selected points at volume flow rate of 75 LPM

Fig.5.24 also displays the temporal numerical average liquid fraction at seven monitoring points (B to H). Initially, the average liquid fractions at the selected points are zero. Near the beginning of the heat addition process, the average liquid fraction rate of points G and H are delayed compared to the other points. This is because of the early natural convection formation around the center of the LHS unit that decelerate melting rate around points G and H. After the melting period,

at t=80 mins, both G and H start accelerating more than other points and complete melting ahead of the other points at t= 94 mins. and t=110 mins. for point H and G, respectively. It can be observed that the melting rate of points B and F reduces in the last stage of charging time. It is due to the solid PCM is pushed toward the lower section of the LHS and hinders the melting progress of the PCM around points B and F. Although the thermocouples B and F are located at the same axis, there is a visible difference in the melting rate between them because of the axial temperature gradient from the front toward the backside of the storage system. This difference is clearly visible in the other points placed on the same axis (C and E; H and G).

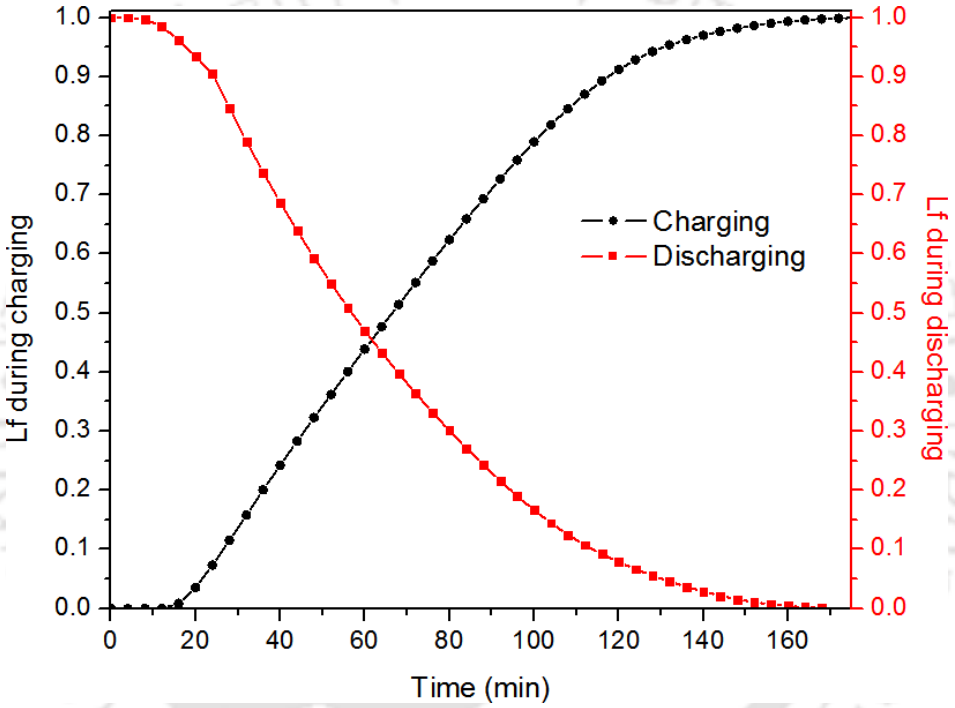

Fig. 5.25.Average liquid fraction during melting and solidification process at flow rate of 75LPM

5.7.6 Charging/discharging liquid fraction variation curve

Charging/discharging time is one of the main parameters of thermal storage that is explained as the time taken for the TES to accumulate/retrieve energy. The variations charging/ discharging time versus transient melting fraction can be explained in terms of the graph of melting fraction as depicted in Fig.5.25. The average liquid fraction can be expressed as a volumetric average liquid fraction of each grid element of the numerically represented model. Near the beginning of the melting process, the average liquid fraction of the LHS model is zero as long as the melting point is above the initial temperature of PCM. The phase transition to a liquid state starts at the time while the melting temperature is equivalent to the PCM temperature.

It is clearly indicated in the graph that the average melting progress of the PCM rising at high rate starting from 15 to 120 min charging period. In this time duration more than 90 % part of the PCM was found in liquid state. Later, the PCM rate of melting started to slow down as the effects natural convection intensifying. Briefly, due to the effect of buoyancy the liquid PCM forms relatively hot temperature zone on the top part of the PCM and relatively cold temperature zones in lower portion. Hence, the higher temperature liquid PCM enhance the melting speed of the PCM in the upper section, whereas the relatively lower temperature liquid PCM slowed down the melting of solid PCM which found in the lower part. During the solidification process, the phase transition progress is slow until 20 min period and begins to accelerate till the time of 96 min. After that the rate discharging starts to slowdown and the complete solidification process with in 160 min.

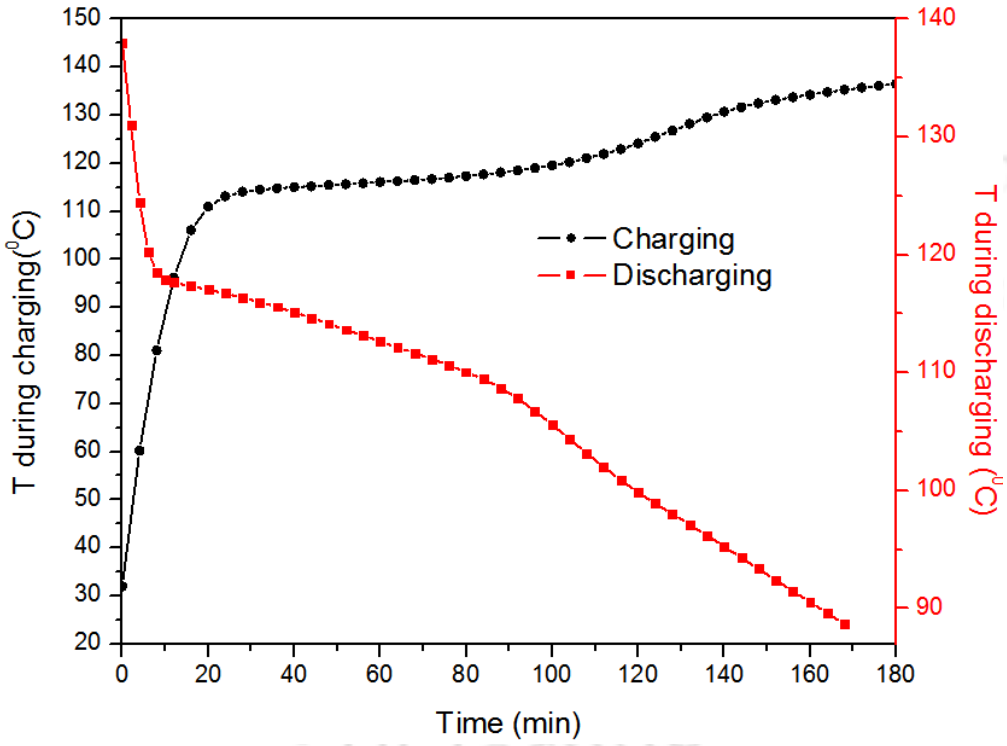

Fig. 5.26.Average temperature during melting and solidification process at a flow rate of 75 LPM

Furthermore, Fig.5.26 illustrates the transient temperature during the heat-storing and solidification processes. Similarly, the temperature is expressed as a volumetric average temperature of each grid element of the numerically represented model. The rate of heat addition and removal is so high at the beginning of the melting and solidification process respectively. During the charging process rate of heat, addition starts to slow down after a time of 24 min; this

could be resulted due to natural convection formation. The average temperature of the LHS model reaches 136.5 ^{0}C at the time of 180 min. The rate of heat removal during the solidification process is getting slowdown after a 15 min period.

5.7.7 HTF volume flow rate effect

The impact of HTF flow rate variation on the melting progress of the PCM was investigated. To perform this test, three flow rate values 75 LPM, 65 LPM, and 55 LPM at the same inlet temperature of 138 ^{0}C were selected. Therefore, the transient average liquid fraction and temperatures comparison curves obtained from the numerical results of the three numerical predictions are displayed in Fig.5.27 (a) and Fig.5.27 (b), respectively. Wang et al. [30] reported that the rise of HTF speed considerably decreases the melting time. At the initial and final stage of the melting process, the flow rate variation does not bring significant change on the heat transferring rate of the PCM as noted from Fig.5.27 (a). However, the effect of the non-uniform HTF volume flow rate brought visible change during the middle stage of the heat addition process. It means increasing the volume flow rate increases the melting progress of PCM.

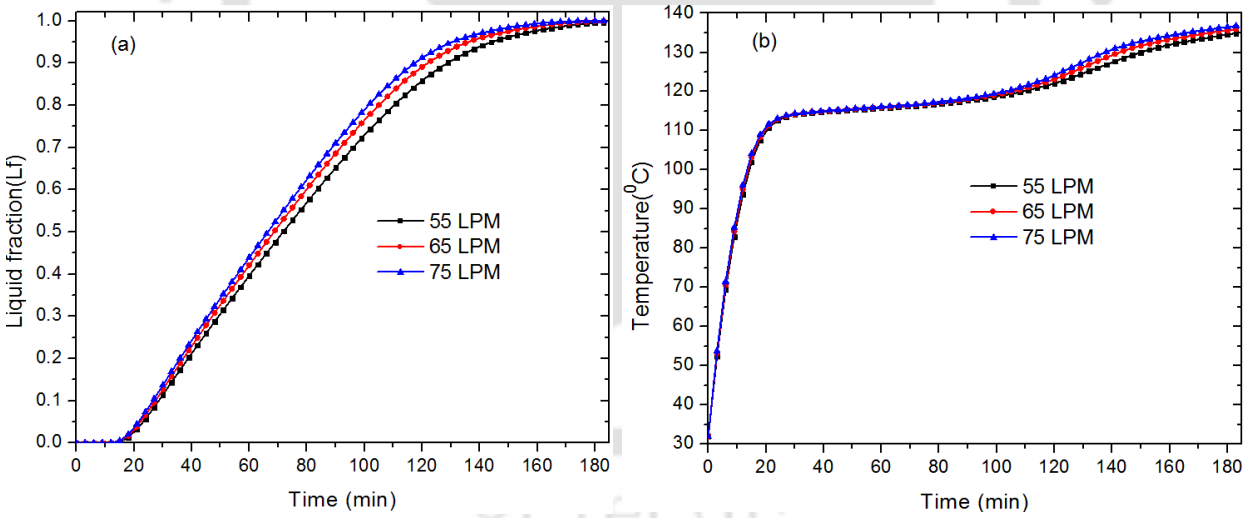

Fig. 5.27. Liquid fraction (a) and temperature (b) at three different flow inputs

Besides, the effect of increasing the HTF volume flow rate on the transient temperature of PCM is indicated in Fig.5.27 (b). Likewise, it can easily be noted from the figure that raising the volume flow rate value brought minor temperature differences in the early and last moments of the melting process. This might have occurred due to the conduction-dominant heat transfer process close to

the initial moment of the process. However, in the intermediate of the heat addition process, the rate of temperature increase with the corresponding HTF flow rate variation is visible.

5.7.8 HTF inlet temperature effect

Adding external heat to PCM stores sensible heat only until the temperature of the system reaches over its melting limit. Hence increasing the value of HTF inlet temperature leads to store the intended quantity of energy within a shorter period. Fig. 5.28 illustrates the comparisons of transient liquid fraction and temperature curves for the LHS unit understudy at three HTF inlet temperatures of 133 ^{0}C, 138 ^{0}C and 143 ^{0}C during heat storage. We can note from the figures that the HTF inlet temperature affected heat storage progress and the higher the inlet temperature resulted in a shorter melting time of PCM.

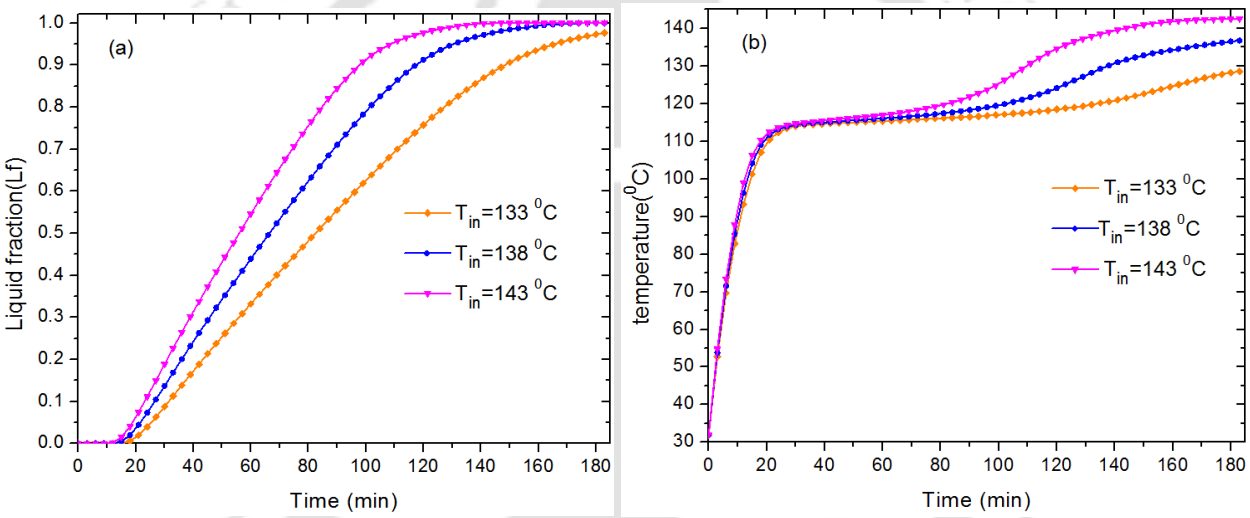

Fig. 5.28.Average liquid fraction (a) and temperature (b) at three different inlet temperatures input

5.7.9 Stored/discharged energy

The total magnitude of stored/discharged thermal energy depends on three parameters of the energy storage media: the PCM mass, temperature, and latent heat and heat capacity of PCM. 50 kg mass of erythritol PCM was considered for the numerical evaluation of the LHS model. Fig. 5.29 (a) and (b) show the rate of heat addition and removal variation versus time of the LHS unit under the process of charging and heat releasing. The HTF is pumped into the storage unit at the flow rate of 75 LPM for both process and inlet temperature of 138 ^{0}C for melting and 87 ^{0}C for the solidification process. The quantity of thermal heat gets stored/ removed during the time of the

charging/discharging process for the considered parameters are calculated by the help of Eqs. (9) – (14).

As can be visibly indicated in Fig.5.29 (a and b), in the early step of the charging/discharging period the heat gets added/discharged predominantly as sensible heat form as compared to the latent heat. This is resulted due to the supremacy of conduction heat transfer of the PCM at the beginning of the process. Gradually, the rate of latent heat addition process starts to overcome sensible heat as the effect natural convection is growing continuously and after a period of 60 min melting process, the sensible heat remains almost steady. After the conclusion of charging process, it is estimated that the sensible heat, latent heat and total stored energy are 9,429 kJ, 17,735 kJ and 27,164 kJ, respectively. For the solidification process the released sensible, latent heat and total energy at the time of 156 min are 4 MJ, 17.6 MJ, and 21.6 MJ, respectively.

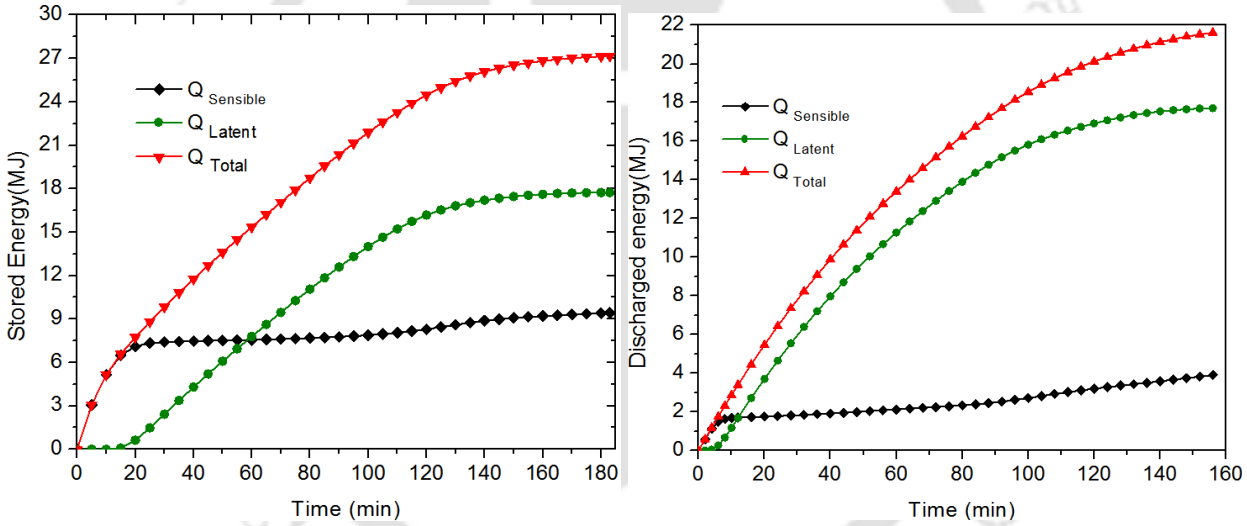

(a) (b)

Fig. 5.29.Energy storage/removal rate during heat storing/solidification process

Fig.5.30 (a) and (b) illustrate the influence of increasing the inlet HTF speed and temperature on the total stored energy. The figures indicated that both parameters affected the amount of total stored heat. In brief the higher HTF inlet temperature, the shorter energy storing time. At the moment when the HTF inlet temperature is 143 ^{0}C, the LHS unit stored total energy of 27 MJ within a period of 160 min charging time. On the other way, the LHS system stored total energy of 25.3 MJ and 26.5 MJ in 180 min period of charging if the HTF inlet temperature was considered

to be 133 ^{0}C and 138 ^{0}C, respectively. In the case of HTF flow rate variation, the rate of stored energy is influenced reasonably when the flow rate value is increasing.

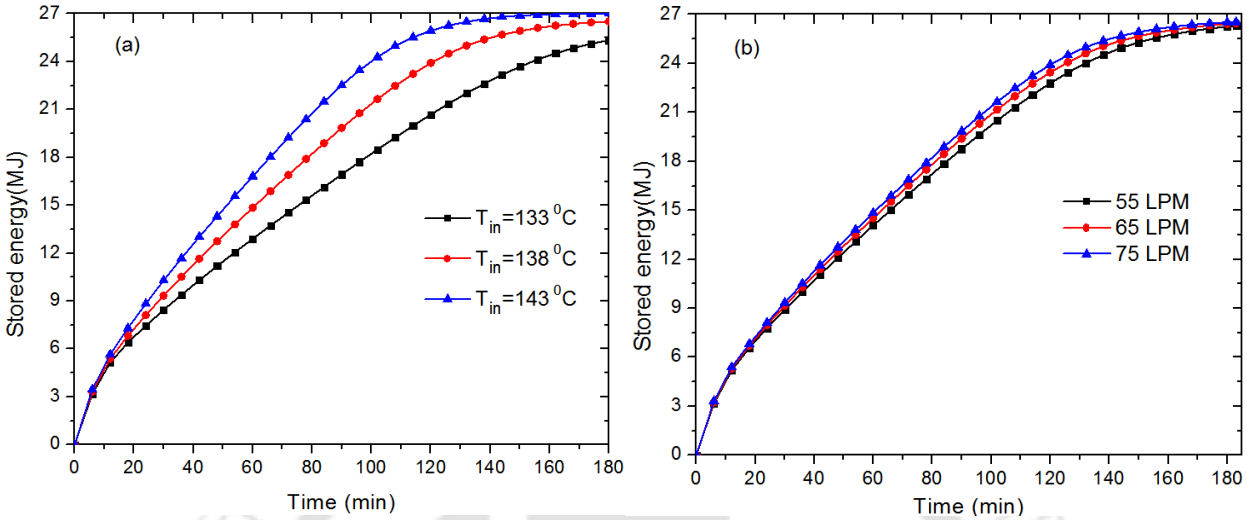

Fig. 5.30.Total stored energy at three different HTF flow rate (a) and inlet temperatures (b)

5.7.10 Experimental and numerical results comparison

In order to attest the real-time experimental results reliability, validating against an equivalent numerical solution is helpful. For this reason, the numerical results of the developed 3D LHS model are compared with the practical results. The geometrical dimensions that are used to fabricate the experimental setup are also applied for numerical modeling. For experimental and numerical results comparison, five points (B, C, E, F and H) are selected inside LHS. These identified points are analogous to the location of the thermocouples implanted on the practical setup. Fig.5.31 exhibits the experimental and numerical temperature predictions at five different locations during the charging process. The comparison of both studies was performed in terms of transient temperature for the spell of the charging process. Both simulation and the experimental tests are conducted by putting the same volume flow rate of 75 LPM and 138 ^{0}C inlet temperature. The solid and open marks on the lines represent experimental and numerical results respectively. In both the studies (numerical and experimental), transient temperature rate of point H ascends more than the others. At the beginning of the energy-storing phase, the temperature at all points increase at a similar rate, however, as time elapse, the temperature augmentation in each point tends to vary. This occurs as a result of the influence of natural convection on the liquid part of the PCM and temperature gradient across the radial distance.

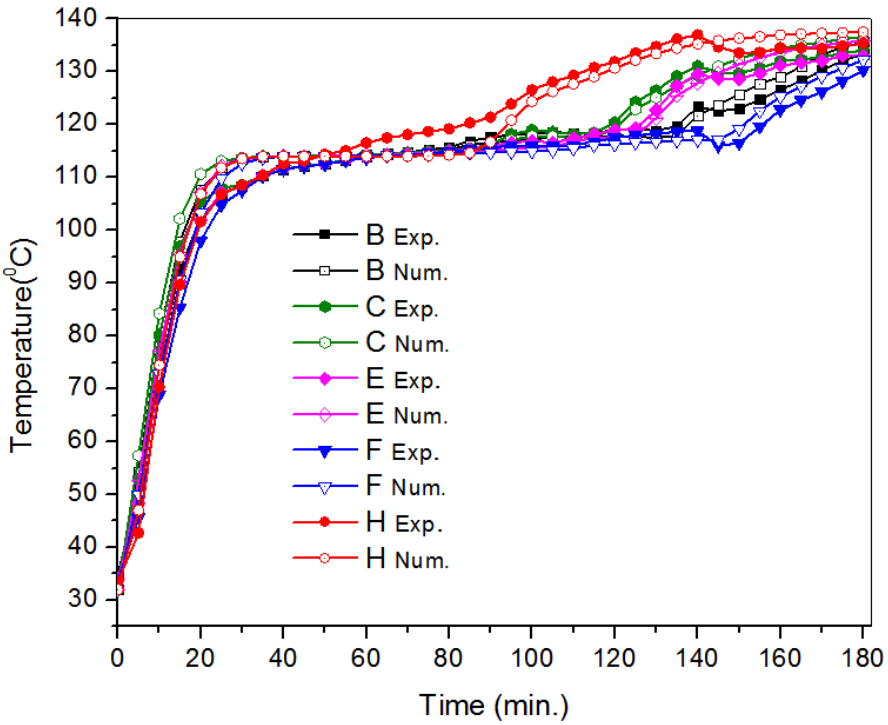

Fig. 5.31.Comparison of the experimental and numerical temperature evaluation at selected points

It can be concluded from Fig.5.31 that the numerical results have reasonably good similarity with the experimental results showcasing a maximum deviation of about 6.0%. Furthermore, the temporal temperature profiles of both the studies exhibit a similar trend. The performance of LHS is analyzed numerically using essential parameters viz. energy storage, melting fraction charging time and average temperature. The outcome of this analysis is discussed in the next section.

Fig. 5.32 shows both the experimental and the numerical predictions of the specific heat storage rate at selected points (B, C, E, F and H) located inside the PCM. The timewise heat storage rate of each point is obtained from the summation of sensible heat and latent heat. As mentioned previously, the heat gets stored primarily in the form of sensible heat during the beginning of the process. During this period, there is no significant difference in the rate of heat addition in all the points and both methods of evaluation. After 45 minutes of melting period, the heat storage profile variations among the selected monitoring points are considerable. This is because of the non-uniform natural convection everywhere. Based on our analysis, it can be concluded that the numerically and experimentally predicted specific heat storage rates errors at the selected measuring points are within the acceptable norms.

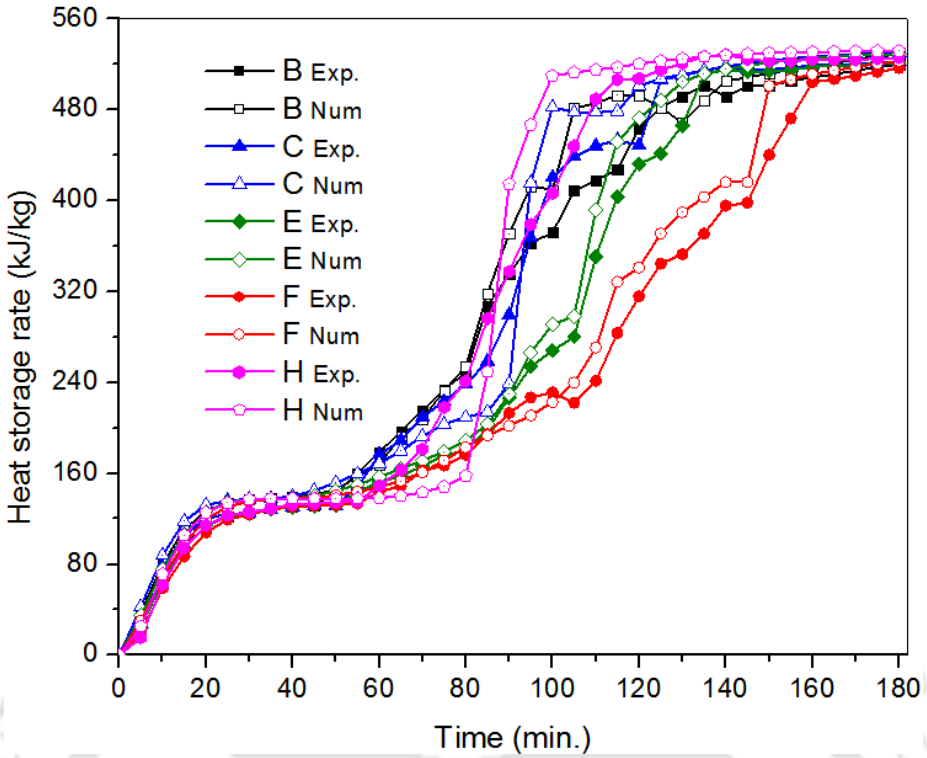

Fig. 5.32.Comparison of the specific energy profile at selected points obtained from experimental and numerical predictions

5.8 Thermal performance enhancement of LHS system using nanoparticles additives

In addition to use fins, dispersing nanoparticles into PCM is one of the methods that help to enhance the performance of the storage systems. The presence of highly conductive nanoparticles inside PCM decreases thermal resistance. Obviously, increasing concentration of nanoparticles enhances thermal conductivity of the PCM. However, mixing higher concentration of nanoparticles with PCM results more particle agglomeration. As a result, the volume fraction does not exceed 5% [95]. Due to their stable thermal properties and availability, two different nanoparticles known as Al_2O_3 and CuO are considered for this study [127], [128]. The performance comparison study is performed by mixing 5% Al_2O_3 and CuO nanoparticles into PCM as well as using only PCM. The major thermal properties which influence the performance of LHS system are density, specific heat capacity, thermal conductivity and dynamic viscosity. The thermal properties of the selected nanoparticles (Al_2O_3 and Cu) and PCM are listed in Table 5.3. While the thermal properties of the nano-PCM (mixture of PCM and nanoparticle) are derived from the respective base fluid and volume fraction of nanoparticle, considering the theoretical mixing [96], [97] using Eq.(5.23) - (5.28).

Density
$$\rho_{n,PCM} = \varphi_n \rho_{np} + (1 - \varphi_n)\rho_{PCM} \quad (5.23)$$

Specific heat capacity
$$C_{P,npcm} = \frac{\varphi_n(\rho_{np} C_{P,np}) + (1 - \varphi_n)(C_P \rho)_{PCM}}{\rho_{n,PCM}} \quad (5.24)$$

Latent heat
$$L_{n,PCM} = \frac{(1 - \varphi_n)(\rho L)_{PCM}}{\rho_{n,PCM}} \quad (5.25)$$

Thermal expansion coefficient
$$\beta_{n,PCM} = \frac{\varphi_n(\rho\beta)_{np} + (1 - \varphi_n)(\beta\rho)_{PCM}}{\rho_{n,PCM}} \quad (5.26)$$

The effective dynamic viscosity of nano-PCM can be calculated as following [144].

$$\mu_{n,PCM} = 0.983 e^{(12.959\varphi_n)} \mu_{PCM} \quad (5.27)$$

The effective thermal conductivity of the nanoPCM is written using the model developed by Maxwell's theory and Brownian motion [145].

$$k_{n,PCM} = \frac{k_{np} + 2k_{PCM} - 2 * \varphi_n(k_{PCM} - k_{np})}{k_{np} + 2k + \varphi_n(k_{PCM} - k_{np})} k_{PCM} \quad (5.28)$$

Table 5.3

Thermophysical properties of HTF, Erythritol, copper and nanoparticles [130], [131], [134], [135]

Material	$\boldsymbol{\rho}(\mathbf{kg/m^3})$	$\mathbf{C_p}(\mathbf{J/kgK})$	k(W/m.K)	L(kJ/kg)	$T_m(^0C)$	$\boldsymbol{\mu}(\mathbf{kg/ms})$	$\boldsymbol{\beta}(\mathbf{K^{-1}})$
Erythritol	1450	1680	0.73	354.7	118	$1.6x10^{-2}$	$2.94x10^{-5}$
Copper	8978	381	387.6				
Al_2O_3	3600	765	36				
CuO	6510	540	18				

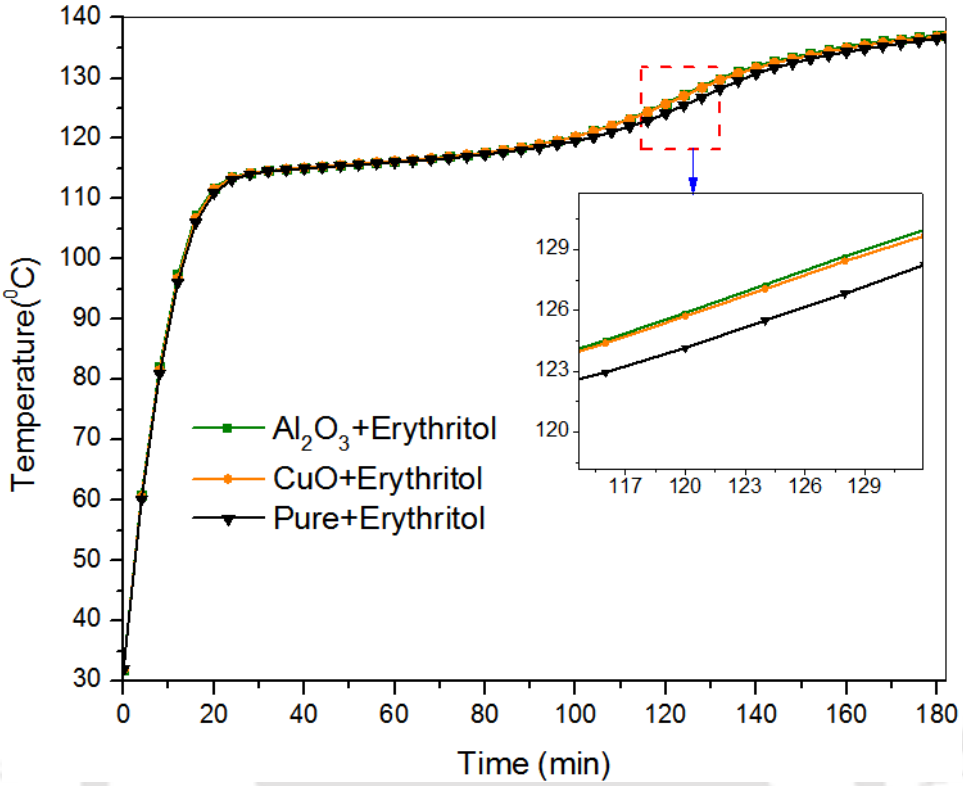

Fig. 5.33.Transient temperature curves of the nano-PCM and pure PCM

The transient temperature and liquid fraction curves of the nano-PCM and pure PCM are represented in Fig 5.33 and 5.34 respectively. As it can be seen, the immersion of nanoparticles into PCM brings considerable improvement, since the presence of nanoparticle provide better heat transfer throughout the entire PCM. However, the thermal performance difference between the two LHS models based on the selected nanoparticles is insignificant. As a result, the next discussion deals about the performance analysis of the LHS unit based on pure PCM and nano-PCM dispersed with Al_2O_3 nanoparticles.

Reducing charging/discharging time should not be considered as the only parameter to choose the best storage system. In addition to this, the amount of energy storage capacity criteria must be included. The total mass of storage material considered in both storage units are equal. In the first LHS model only 50 kg of pure PCM is considered. In the second LHS model, 95% of the effective volume of the storage unit is contained by Erythritol and the remaining part is replaced by the selected nanoparticle. Hence, the transient energy storage of the two LHS models (based on pure PCM and nano-PCM) is estimated. The comparison of the stored energy for the pure PCM and nano-PCM for 5% values of volume fraction is presented in Fig. 5.35. It is observed in both cases

that the quantity of stored energy increases with time. Initially, the storage unit is stocked with solid PCM and, when the hot HTF is sent in the tubes, heat is transferred to PCM via the hot walls of the tube and fins. In the beginning of the process, heat is getting stored mainly in the form of sensible heat.

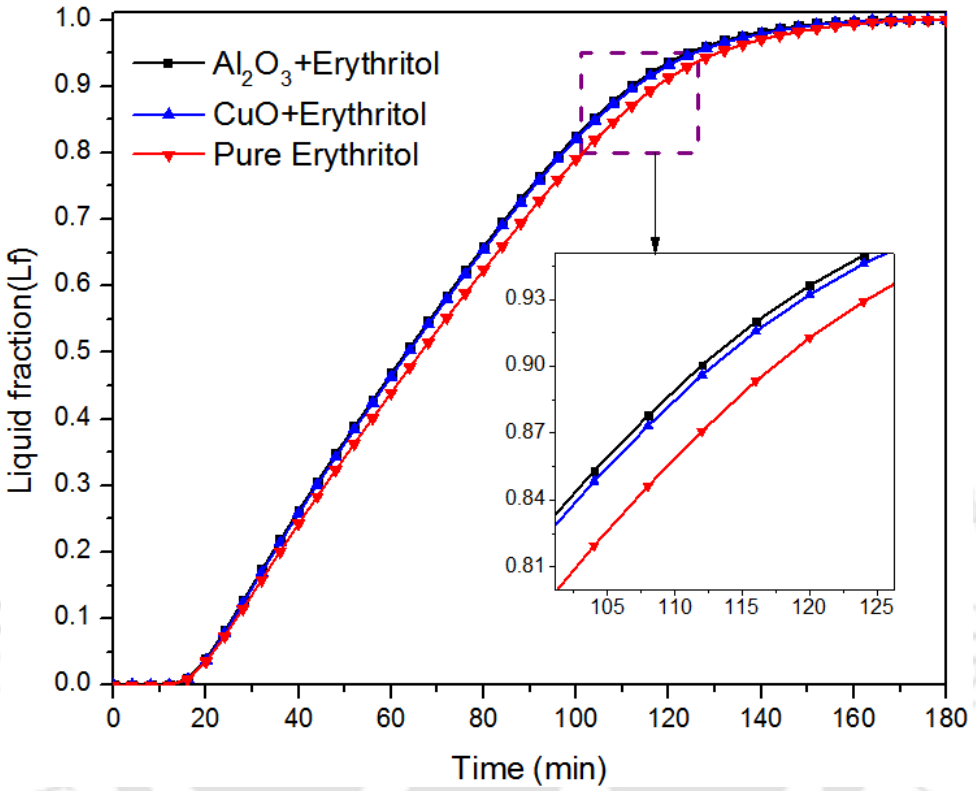

Fig. 5.34. Transient liquid fraction curves of the nano-PCM and pure PCM

Later, the convection heat transfer becomes dominant and energy is stored in the form of latent heat. It can be observed from Fig. 5.35 that the variation of the sensible heat storage rate between pure PCM and nao-PCM is insignificant. However, the energy stored in the latent heat form is higher for the pure PCM as compared to nano-PCM. Certain volume of the PCM is occupied by the presence of nanoparticles and this decreases the latent heat storage capacity of the storage unit. In general, inserting nanoparticles minimize the total stored energy, since the most of the energy is stored in the form of latent heat. As a result, unlike the temperature and liquid fraction versus time curves, the transient stored energy of the storage unit based on pure PCM is higher than the nano-PCM based storage unit. It is validated since a fraction volume of the PCM is replaced by the inclusion of nanoparticles. The reduction in melting time achieved by dispersing nanoparticle

is about 4.6% as compared to the pure PCM. On the other hand, the energy storage capacity of the storage unit is reduced by about 23%, when nanoparticles are included in the PCM.

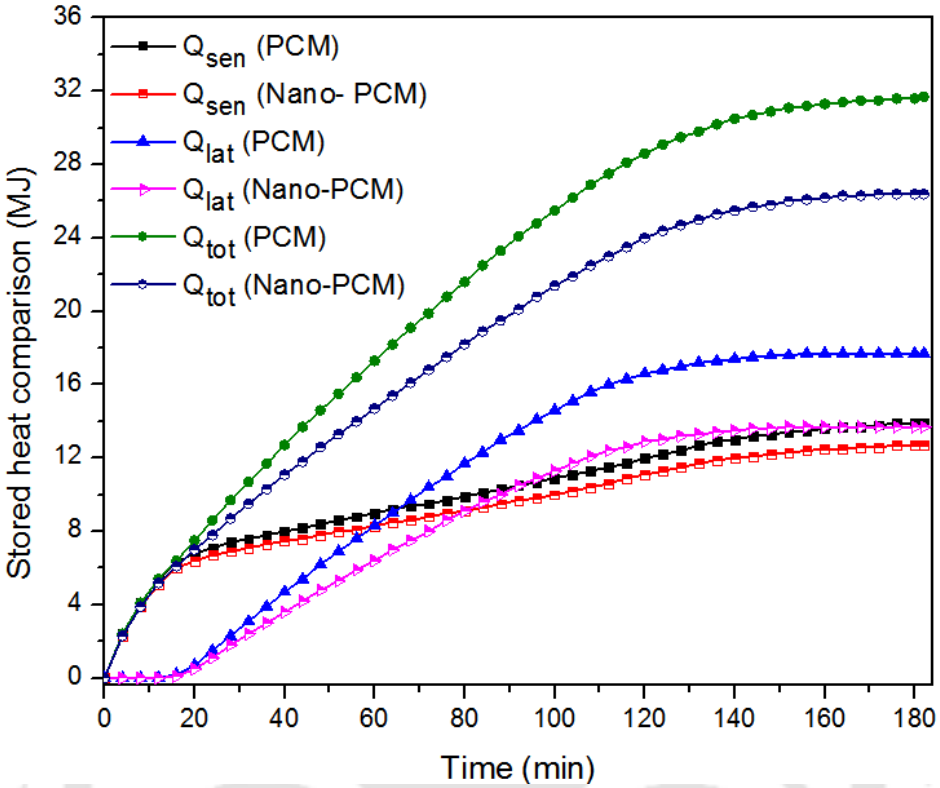

Fig. 5.35. Stored energy comparison of the LHS unit based on pure PCM and nano-PCM

5.9 Summary

TES technologies are commonly used to bridge the gap between energy generation and demand. Due to this, TES based on phase changing materials (PCM) has attracted scientific community worldwide because of its higher energy storage density. As we know, PCM has poor thermal conductivity and this inherent property is the main challenge of LHS systems to be utilized in commercial applications. Consequently, several effective thermal conductivity enhancement techniques have been presented in literature. In the current study, shell and tube type LHS with multiple finned HTF tubes is designed, employing Erythritol ($C_4H_{10}O_4$) as energy storage media and cooking waste oil as HTF. Experimental and analytical thermal performance of LHS is studied in detail using parameters, such as charging time, liquid fraction, average transient temperature and stored energy. Both numerically as well as experimentally, various tests are conducted with HTF volume flow rate of 75 LPM at 138^0C. The numerical analysis results exhibit very good

similarity with the experimental data showing a maximum deviation of 6.0%. The impact of HTF mass flow rate and temperature variation on the melting behaviour of the storage is examined in depth. It is observed that the higher flow rate and higher inlet temperature enhance melting performance. The total time necessary for the complete melting and solidification of PCM inside LHS is estimated to be 175min and 156 min, respectively. During the melting of PCM, the sensible heat, latent heat and total energy stored in LHS are found to be 9.3 MJ, 17.74 MJ and 27.03 MJ, respectively. Similarly, the sensible heat, latent heat and total energy released during the solidification process are 4 MJ 17.6MJ and 21.6 MJ, respectively.

Comparison study of the LHS unit with and without nanoparticles is also performed. Due to their stable thermal properties and availability, two different nanoparticles known as Al_2O_3 and CuO are considered for this study. In terms of melting time of the PCM, the mixing of nanoparticles into PCM bring considerable improvement, since the presences of nanoparticles provide better heat transfer throughout the entire PCM. It is observed, the thermal performance difference between the two LHS models based on the selected nanoparticles is insignificant. The reduction in melting time achieved by dispersing nanoparticle is about 4.6% as compared to the pure PCM. However, the stored energy for the pure PCM is higher as compared to the nano-PCM based storage. On the other hand, the energy storage capacity of the storage unit is reduced approximately by 23% when nanoparticles are included in the PCM.

Chapter- 6

6 Performance investigation of the LHS unit powered by hybrid PTSC and auxiliary energy sources

6.1 Introduction

The performance of the storage unit developed in the proposed work is presented in Chapter 5 experimentally and numerically, where an electrical energy is applied as a heat source for the melting of PCM. The working fluid inlet temperature is maintained at a constant value using temperature controller.

However, solar energy generation and storage systems are operated under variable weather conditions. When energy generation systems operate with fluctuating inputs, their performance gets badly affected. In this chapter, the performance of a LHS unit is studied based on the thermal energy generated by PTSC using direct solar irradiance. Moreover, the experimental investigation of the coupled PTSC and LHS unit, and numerical investigation of the proposed LHS unit powered by PTSC and auxiliary energy source are also presented.

6.2 Advantage of hybrid energy systems

Renewable energy resources like solar and wind energy are intermittent in nature. Combining two or more renewable energy systems could improve the stability and reliability of power output significantly [36]. Moreover, the efficiency of the multi-energy generation system can be enhanced if it is coupled with thermal energy storage system [99]. These hybrid energy generation systems can be used for various applications, including thermal energy production for cooking.

Different aspects of hybrid energy systems have been investigated by scientific community, none of these studies reported on the performance evaluation of LHS unit coupled with hybrid solar and other auxiliary energy resources. In the proposed study, a lab scale PTSC and electric heater is combined together to power a LHS developed for indoor cooking purpose. The goal of this study is to evaluate the performance of the LHS unit powered by solar and other auxiliary energy sources.

Energy supply that is powered by solar energy is less reliable as the energy generated depend on weather conditions and time of the day. Therefore, the incorporating solar energy with other auxiliary energy sources is necessary to provide reliable power without any interruption and to increase overall efficiency of the system. In order to achieve the above mentioned objective, lab scale PTSC and LHS units are developed. A PTSC is employed as a heat source for the charging of storage unit and, biogas fuel is proposed as an auxiliary power source to provide power continuously. However electrical heater is utilized in place of biogas cylinder and, experimental and numerical performance study of the storage unit is performed.

For safety reasons, usually, cooking activity is performed inside the kitchen and it can be done at any time of the day. Moreover, the total time consumed for cooking using nonconventional resources should compete with conventional cooking methods. Hence, solar based cooking technology should be supported by other auxiliary source, such as biogas or electrical heater. The objective of this study is to evaluate the performance of the LHS unit powered by hybrid renewable energy resources. Parabolic trough solar collector (PTSC) and electric heater are employed to heat the HTF fluid.

6.3 Description and experimental setup procedure

This study is the part of an indoor hybrid solar cooking system. The photograph in Fig.3.13 shows the entire integrated experimental setup. The system consists of a LHS unit, PTSC, electric heater, pump, pressure gauges, and thermocouples. The LHS unit is heated /cooled during charging /discharging using cooking waste oil as HTF. Experimental temperature measurements are taken at HTF inlet and outlet, and at different positions of the LHS system. For this purpose, multiple K-type thermocouples are mounted on the inlet and outlet of the storage system and at different positions. The thermocouples are distributed across storage unit to measure the radial and axial temperature gradient. The positions of the thermocouples are indicated in Fig 5.1.

The schematic diagram of the practical setup is illustrated in Fig.6.1. To convert solar radiation in to thermal energy, PTSC is utilized. The collector is manually rotated in east–west direction to follow the movement of the sun. For harvesting the solar energy, a receiver is placed at focal line of the PTSC and solar radiation fall on the collector is reflected back to the receiver. The receiver consists of absorber tube made from copper pipe, and glass enclosure to minimize heat loss. Cooking waste oil is circulated through the receiver and absorbs concentrated solar energy. The

working fluid passes through HTF tubes of the LHS unit to transfer thermal energy which is stored in the form of sensible and latent heat.

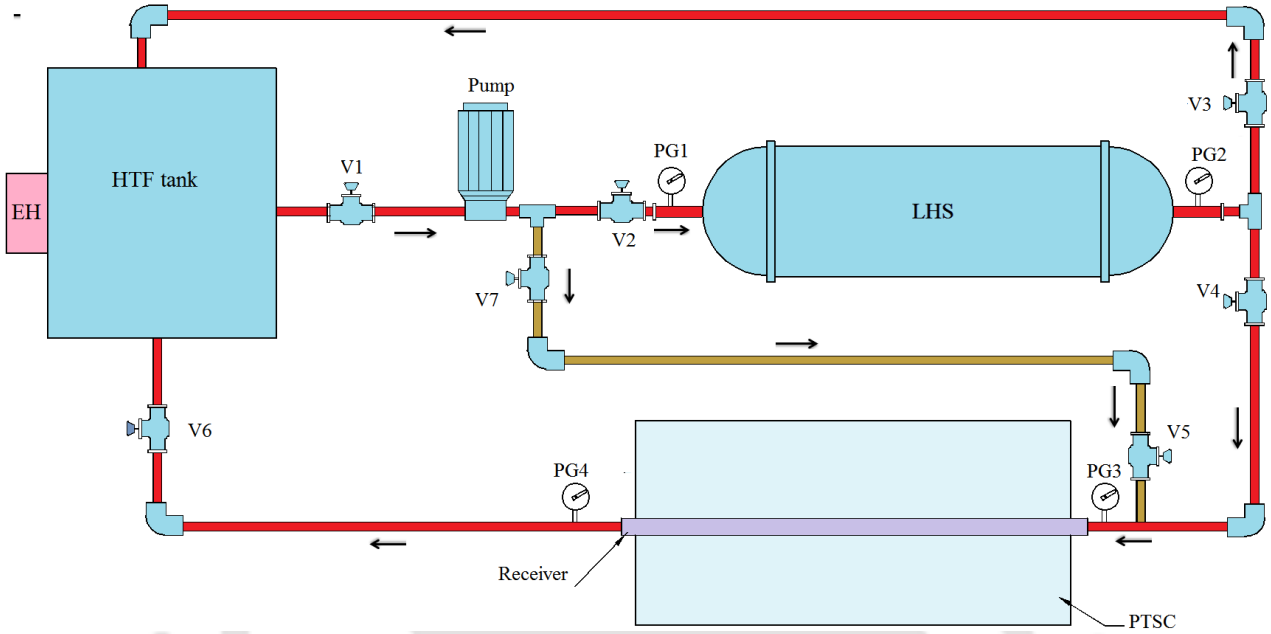

Fig. 6.1.Block diagram of the intended practical setup

6.4 Charging performance of the LHS based on the PTSC system

In this section, the performance of LHS unit is tested using PTSC as heat source. The HTF is circulated from oil tank to PTSC and LHS units at the flow rate of 0.2 kg/s. The HTF is heated during its passage through receiver tube. The LHS unit stores thermal energy, when hot working fluid passes via finned HTF tubes embedded in the PCM. A gear pump is utilized to pump HTF through receiver and put back into the energy storage system. The temperature and pressure parameters are monitored by placing temperature sensors at different location of the LHS unit and pressure gauge at the inlet and outlet of LHS and PTSC. As mentioned earlier, ten thermocouples are embedded inside the LHS unit and a thermocouple is mounted at each inlet and outlet of the PTSC absorber tube. The experimental test is conducted on a sunny day of June 21, 2019 on the roof top of EEE Dept. IITG starting at 9:30 PM local time.

Fig.6.2 presents the transient average temperature of PCM, inlet and outlet temperature of the absorber tube and direct solar radiation. The average temperature of PCM is estimated from the temperature history of ten thermocouples. The plot exhibits that the solar radiation reaches at its

peak before noon, just around 11:30 AM. It can be observed that all the temperature curves increase till 14:30 PM. As the solar radiation intensity keeps falling down, the rate of heat generation in the absorber tube is also reduced. As a result, the outlet and inlet temperature are almost equal after 15:00 PM. At this moment, the rate of heat charging of LHS becomes steady and the rate of temperature increase is recorded minimal. At 14:00 PM, the average temperature of LHS is 88 ^{0}C. It should be noted that the melting point of PCM inside storage unit is 118 ^{0}C. Even though the experimental test is conducted for more than five hours, PTSC input is not enough to charge LHS completely. Therefore, an auxiliary energy source is required for the complete melting of PCM.

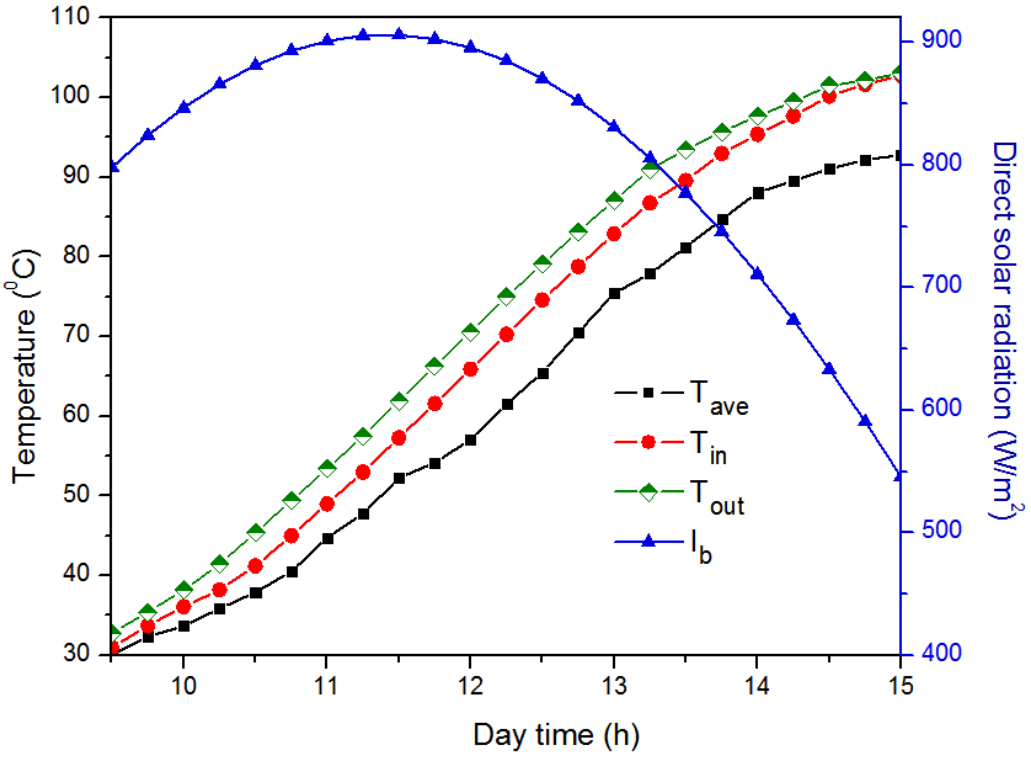

Fig. 6.2.Solar radiation and temperature profile of the HTF at inlet and outlet of the PTSC and average of the LHS unit

6.5 Numerical evaluation of the proposed LHS unit powered by PTSC and auxiliary Energy sources

In this section, performance of LHS unit powered by PTSC and auxiliary energy source is evaluated numerically. This numerical analysis is proposed in order to estimate the dynamic behavior of the LHS unit coupled with hybrid PTSC and other energy sources. For this purpose,

the results of charging process of LHS unit using PTSC system is considered as an initial condition to the numerical analysis. As mentioned in the above section, the rate of heat addition to the storage unit after 14:00 PM is minimal. At this instant, the average temperature of PCM is 88 ^{0}C and is considered as a reference temperature for the numerical study of solar hybrid system proposed for cooking application. Similar boundary conditions employed in Chapter 5 are also applied here in this study i.e., the HTF inlet flow rate and temperature are 75 LPM and 138 ^{0}C, respectively. It is important to note that the numerical model developed in Chapter 5 is also applied for this analysis. Moreover, the same assumptions and numerical procedures are also utilized.

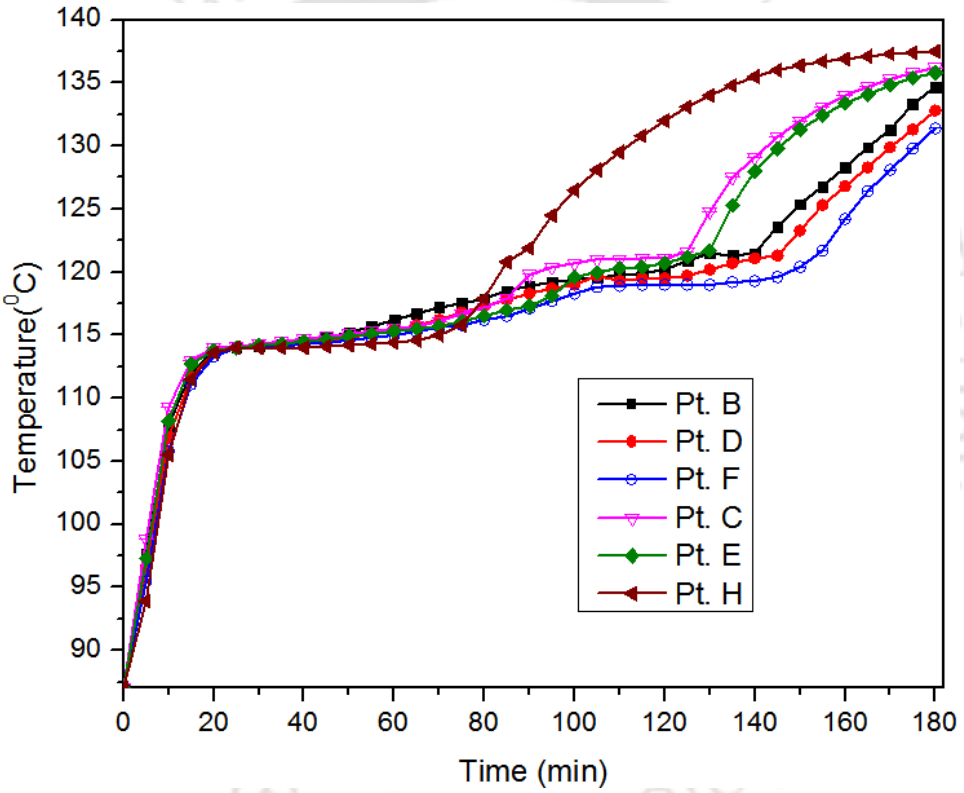

Fig. 6.3.Temperature variation of the LHS powered by PTSC and auxiliary energy sources

Fig.6.3 illustrates temperature variation of PCM at selected monitoring points. Similarly, six (B, C, D, E, F and H) points are considered for the temperature measurement and these points represent thermocouple probe locations. In the beginning of the charging process, the rate of heat addition is fast and the variation is insignificant among all the points. This is resulted due to dominant conduction heat transfer mechanism at an early stage of the process. From 20 min to 70 min of charging time, the rate of temperature variation in all the points is almost steady. This is attributed

to the phase transition of PCM at constant temperature. After this period, the storage unit experiences an extended period of slow heating until the end of the process. All the temperature curves increase with the melting time after 70 min. However, the temperature increment of point H is highest as compared to rest of the points. This is resulted due to the effect of natural convection which facilitates melting of PCM on the upper section and slows down the melting of PCM placed at the bottom of storage unit.

To conclude, the PTSC developed in the proposed work seems incapable to melt PCM placed inside the storage unit on its own. Therefore, it is imperative for the PTSC to get assisted with other auxiliary energy sources or another PTSC should be installed in parallel to power LHS unit.

6.6 Summary

The inclusion of thermal energy storage system (TES) system is an important measure to stabilize an inconsistent daily supply of solar irradiance and the oscillations throughout the year. In this chapter, performance of LHS unit is presented, based on the thermal energy generated by PTSC from direct solar irradiance. Moreover, the experimental investigation of the coupled PTSC and LHS unit, and numerical investigation of the proposed LHS unit powered by PTSC and auxiliary energy source are also depicted in this chapter. The results indicate that the PTSC developed in the proposed work needs to be integrated with other auxiliary energy sources or similar PTSC units in parallel to sufficiently power LHS unit.

Chapter- 7

7 Conclusion and Future Scope

The main objective of the present study is to design, develop and investigate the thermal performance a suitable indoor solar hybrid cooking system using thermal energy storage materials. In order to achieve the intended goal, a PTSC and LHS units are designed and fabricated. The thermal performances of both systems are investigated experimentally and numerically. Therefore, the main conclusions drawn from the study of LHS and PTSC units are discussed in this chapter. Furthermore, a hybrid PTSC and LHS system is proposed for solar cooking application and lab-scale experimental setups are developed and coupled with each other to test the performance of proposed hybrid system.

7.1 PTSC system

The designed PTSC for this study was manufactured in the Central Mechanical workshop using domestically available materials. The reflector and receiver are the most important components of PTSC system. The aperture and length of the reflector are 1.7 m and 2 m, respectively. The reflective part of the collector is made from stainless steel sheet. An experimental, analytical and numerical investigation is carried out to study performance of the fabricated PTSC system is conducted. For the analytical study of the PTSC, the governing equations described in section 4.1 are solved using Engineering Equation Solver (EES). The performance of the collector is evaluated using variable important parameters: inlet temperature, beam radiation, mass flow rate and mixing nanoparticles with HTF. The result indicates reduction in the efficiency and useful heat when inlet temperature is increased, and other parameters are kept constant. On the other hand, the thermal efficiency improves with the change in mass flow rate and solar radiations. The effect of the nanofluids on the thermal performance of PTSC is also investigated numerically. The performance comparison is performed using 5% Al_2O_3 nanoparticles and pure cooking waste oil (CWO) but mixing nanoparticles into the base fluid brings insignificant improvement in the performance of the system. Moreover, the performance of PTSC based on cooking waste oil (CWO) HTF is compared against the commonly used HTF Syltherm 800 (S-800) and CWO is found better.

Therefore, the numerical and experimental study of the PTSC is performed using CWO as HTF medium.

Thermal modelling of the absorber tube is performed for numerical performance study of the PTSC, and the equations are solved using ANSYS Fluent environment. For the consideration of radiation exchange between receiver pipe and glass envelope the surface-to-surface radiation model in is employed. Likewise, the input parameters in the numerical modeling of PTSC are HTF inlet temperature, mass flow and direct solar radiation. A non-uniform temperature distribution along the bottom and top surfaces of the receiver pipe is observed due to the variable heat flux input. The experimental results of selected four days of the June and October months are presented. Important parameters, viz., useful heat, thermal efficiency, and HTF outlet temperature and heat loss are applied for the performance evaluation of the collector. The experimental results indicate that the thermal performance of PTSC is better June than October. The maximum obtained HTF outlet temperature is 110.7 ^{0}C and 108 ^{0}C on June 15 and June 22, respectively, whereas the maximum obtained HTF outlet temperature on October 13 and October 18 are 89.9 ^{0}C and 86.8 ^{0}C, respectively. Additionally, the HTF temperature outlets of the three evaluation methods are compared employing the same input parameters. It is observed that the analytical, numerical and experimental results are found to be in good agreement.

7.2 LHS unit

An experimental and numerical study of the shell and tube LHS unit developed in the proposed work is presented in this thesis. For improving the overall heat transfer rate, multiple HTF tubes connected with fins are embedded in the PCM. The numbers of HTF tubes and fins are determined using an optimization method. Regarding this, 2D numerical study is performed to find the optimum numbers of HTF tubes and fins prior to the 3D numerical investigation of the LHS. The Boussinesq approximation method is employed to consider the natural convection for both the 2D and 3D studies. For this purpose, combined convection and conduction heat transfer model was adapted. Based on the optimization study and energy requirement, the size of LHS unit is decided and it consists of a shell and 19 HTF tubes in which four fins are integrated each tube. The HTF tubes and fins are made from copper tubes and copper sheets, respectively. The width and thickness of the fins are 12 mm and 2 mm, respectively. The storage system is 1000 mm long and its shell internal diameter is 240 mm. The storage tank is designed using a 3 mm thick stainless steel plate.

Erythritol ($C_4H_{10}O_4$) and cooking waste oil are employed as PCM and HTF, respectively. The performance of the LHS unit is validated experimentally during charging process. Experimental and analytical thermal performance of LHS is studied in detail by varying parameters, such as charging time, liquid fraction, average transient temperature and stored energy. During the charging process, both numerical as well as experimental tests are conducted with HTF volume flow rate of 75 LPM at 138 ^{0}C. For the discharging process, the HTF inlet temperature is chosen to be at 87 ^{0}C and the volume flow rate remains same as that of the charging process. For the numerical study of the storage unit, a 3D LHS computational model emulating the actual unit is developed using ANSYS-Fluent.

The effect of operating parameters on the performance of the storage unit is examined using both experimental and numerical analysis methods. The impact of the non-uniform flow rate of HTF on the melting of PCM is studied using three flow rates at the same inlet temperature. Similarly, for the constant volume flow rate, the numerical study is performed at three different HTF inlet temperatures. It is observed that an increase in the flow rate of HTF and inlet temperature enhances the heat transferring rate of PCM and minimizes charging time of the LHS unit. The experimental outcome of the storage unit is validated with numerical results. The numerical analysis results exhibit a very good similarity with the experimental data exhibiting a maximum deviation of 6.0% only which is acceptable for real life applications.

The total time necessary for complete melting and solidification of PCM inside LHS is estimated to be 175min and 156 min, respectively. During the melting of PCM, the sensible heat, latent heat and total energy stored in LHS are found to be 9.3 MJ, 17.74 MJ and 27.03 MJ, respectively. Similarly, the sensible heat, latent heat and total energy released during the solidification process are 4 MJ 17.6MJ and 21.6 MJ, respectively. Further, it can be concluded that erythritol as PCM and cooking waste oil as HTF are found as promising materials for an efficient LHS design.

Furthermore, the comparison study of LHS unit with and without nanoparticles is also performed. Two different nanoparticles known as Al_2O_3 and CuO are employed for the proposed study. The melting time of the PCM improves due to nanoparticles with PCM and it also enhances heat transfer throughout the entire PCM. The reduction in melting time achieved by employing nanoparticle is about 4.6% as compared to the pure PCM. However, the stored energy in the pure

PCM is higher as compared to the nano-PCM. It is observed that the energy storage capacity of the storage unit is reduced approximately by 23% when nanoparticles are mixed with PCM.

7.3 PTSC and LHS Hybrid system

The lab scale PTSC and an electric heater is coupled together to design a hybrid LHS. The performance of the LHS unit is studied based on the thermal energy generated by the PTSC using direct solar irradiance. Moreover, the experimental study of the coupled PTSC and LHS unit and numerical analysis of the proposed LHS unit are performed.

The performance of LHS unit is measured using PTSC as heat source. The HTF is circulated from an oil tank to PTSC and LHS unit at the flow rate of 0.2 kg/s. The results indicate that the heat addition to the storage unit increases with solar radiation till 2:30 PM. When the solar radiation intensity falls down, the rate of heat generation in the absorber tube also reduces. This validates that an auxiliary energy source is required for the complete melting of PCM. Therefore, PTSC has to be assisted by other auxiliary energy sources or extra PTSCs should be installed in parallel to supply sufficient power to the LHS unit. Numerical analysis of the LHS powered by hybrid PTSC and auxiliary energy source is performed to examine its dynamic behavior.

7.4 Future Scope

The lab-scale PTSC and LHS units have been developed and their performances are tested at different operating conditions. As a result, the predicted results indicate that both prototypes are promising. However, there are several scopes for further research for the improvement of the fabricated experimental setups. Some of the future scope and suggestions for further studies are as follow:

- To investigate the solidification process of the developed LHS unit experimentally.
- To determine exergy and energy efficiency of the PTSC and LHS units.
- Design and manufacture of a solar cooking utensil and couple with PTSC and LHS units.
- To conduct heat transfer analysis of solar cooking utensil.
- To perform economical and cost analysis of the developed experimental setups.

References

[1] S. D. Pohekar, D. Kumar, and M. Ramachandran, "Dissemination of cooking energy alternatives in India — a review," vol. 9, pp. 379–393, 2005, doi: 10.1016/j.rser.2004.05.001.

[2] E. Tang, C. Peng, and Y. Xu, "Changes of energy consumption with economic development when an economy becomes more productive," *J. Clean. Prod.*, vol. 196, pp. 788–795, 2018, doi: 10.1016/j.jclepro.2018.06.101.

[3] P. Nejat, F. Jomehzadeh, M. Mahdi, and M. Gohari, "A global review of energy consumption , CO 2 emissions and policy in the residential sector (with an overview of the top ten CO 2 emitting countries)," *Renew. Sustain. Energy Rev.*, vol. 43, pp. 843–862, 2015, doi: 10.1016/j.rser.2014.11.066.

[4] M. J. Muhammad, I. A. Muhammad, N. Azwadi, C. Sidik, M. Noor, and W. Muhammad, "Thermal performance enhancement of fl at-plate and evacuated tube solar collectors using nano fl uid : A review ☆," vol. 76, pp. 6–15, 2016, doi: 10.1016/j.icheatmasstransfer.2016.05.009.

[5] L. Evangelisti, R. D. L. Vollaro, and F. Asdrubali, "Latest advances on solar thermal collectors : A comprehensive review," *Renew. Sustain. Energy Rev.*, vol. 114, no. August, p. 109318, 2019, doi: 10.1016/j.rser.2019.109318.

[6] S. Suman, M. Kaleem, and M. Pathak, "Performance enhancement of solar collectors - A review," *Renew. Sustain. Energy Rev.*, vol. 49, pp. 192–210, 2015, doi: 10.1016/j.rser.2015.04.087.

[7] R. M. Muthusivagami, R. Velraj, and R. Sethumadhavan, "Solar cookers with and without thermal storage — A review," vol. 14, pp. 691–701, 2010, doi: 10.1016/j.rser.2008.08.018.

[8] E. Cuce and P. M. Cuce, "A comprehensive review on solar cookers," *Appl. Energy*, vol. 102, pp. 1399–1421, 2013, doi: 10.1016/j.apenergy.2012.09.002.

[9] H. M. S. Hussein, H. H. El-ghetany, and S. A. Nada, "Experimental investigation of novel

indirect solar cooker with indoor PCM thermal storage and cooking unit," vol. 49, pp. 2237–2246, 2008, doi: 10.1016/j.enconman.2008.01.026.

[10] K. Schwarzer and M. Eugenia, "Solar cooking system with or without heat storage for families and institutions ˆ," vol. 75, pp. 35–41, 2003.

[11] R. Kumar, R. S. Adhikari, H. P. Garg, and A. Kumar, "Thermal performance of a solar pressure cooker based on evacuated tube solar collector," vol. 21, pp. 1699–1706, 2001.

[12] E. Bellos and C. Tzivanidis, "Assessment of the thermal enhancement methods in parabolic trough collectors," *Int. J. Energy Environ. Eng.*, pp. 59–70, 2018.

[13] A. Sharma, V. V. Tyagi, C. R. Chen, and D. Buddhi, "Review on thermal energy storage with phase change materials and applications," *Renew. Sustain. Energy Rev.*, vol. 13, no. 2, pp. 318–345, 2009, doi: 10.1016/j.rser.2007.10.005.

[14] S. M. Hasnain, "Review on sustainable thermal energy storage technologies , part ii : cool thermal storage," vol. 39, no. 11, pp. 1139–1153, 1998.

[15] Antoni Gil, Marc Medrano, Ingrid Martorell, Ana La´zaro , Pablo Dolado , Bele´n Zalba, Luisa F. Cabeza, "State of the art on high temperature thermal energy storage for power generation. Part 1-Concepts, materials and modellization," *Renew. Sustain. Energy Rev.*, vol. 14, no. 1, pp. 31–55, 2010, doi: 10.1016/j.rser.2009.07.035.

[16] M. T. Kangas and P. D. Lund, "Modeling and simulation of aquifer storage energy systems" no. 3, pp. 237–247, 1994.

[17] W. A. Duffie, J.A. and Beckman, "Solar energy thermal processes," *Univ. Wisconsin-Madison, Sol. Energy Lab.*, 1974.

[18] B. Zalba, J. M. Marín, L. F. Cabeza, and H. Mehling, *Review on thermal energy storage with phase change: Materials, heat transfer analysis and applications*, vol. 23, no. 3. 2003.

[19] M. K. Rathod and J. Banerjee, "Thermal stability of phase change materials used in latent heat energy storage systems : A review," *Renew. Sustain. Energy Rev.*, vol. 18, pp. 246–258, 2013, doi: 10.1016/j.rser.2012.10.022.

[20] S. S. Chandel and T. Agarwal, "Review of current state of research on energy storage , toxicity , health hazards and commercialization of phase changing materials," *Renew. Sustain. Energy Rev.*, vol. 67, pp. 581–596, 2017, doi: 10.1016/j.rser.2016.09.070.

[21] M. M. Farid, A. M. Khudhair, S. Ali, and K. Razack, "A review on phase change energy

storage : materials and applications," vol. 45, pp. 1597–1615, 2004, doi: 10.1016/j.enconman.2003.09.015.

[22] B. Xu, P. Li, and C. Chan, "Application of phase change materials for thermal energy storage in concentrated solar thermal power plants : A review to recent developments," *Appl. Energy*, vol. 160, pp. 286–307, 2015, doi: 10.1016/j.apenergy.2015.09.016.

[23] J. Pereira and P. Eames, "Thermal energy storage for low and medium temperature applications using phase change materials – A review," *Appl. Energy*, vol. 177, pp. 227–238, 2016, doi: 10.1016/j.apenergy.2016.05.097.

[24] S. Bauer, Thomas and Pfleger, Nicole and Laing, Doerte and Steinmann, Wolf-Dieter and Eck, Markus and Kaesche, "High-temperature molten salts for solar power application," *Molten Salts Chem.*, pp. 415–438, 2013.

[25] O. J. Who, Foong Chee and Lovseth, Jorgen and Nydal, "Heat Capacity Measurements of NaNO3--KNO3 Binary System," *Submitt. Pap. to Int. J. Thermophys.*, 2011.

[26] V. D. Bhatt, K. Gohil, and A. Mishra, "Thermal Energy Storage Capacity of some Phase changing Materials and Ionic Liquids," vol. 2, no. 3, pp. 1771–1779, 2010.

[27] S. Pincemin, R. Olives, X. Py, and M. Christ, "Highly conductive composites made of phase change materials and graphite for thermal storage," vol. 92, pp. 603–613, 2008, doi: 10.1016/j.solmat.2007.11.010.

[28] Y. Tian and C. Y. Zhao, "A review of solar collectors and thermal energy storage in solar thermal applications," *Appl. Energy*, vol. 104, pp. 538–553, 2013, doi: 10.1016/j.apenergy.2012.11.051.

[29] F. Agyenim, P. Eames, and M. Smyth, "A comparison of heat transfer enhancement in a medium temperature thermal energy storage heat exchanger using fins," *Sol. Energy*, vol. 83, no. 9, pp. 1509–1520, 2009, doi: 10.1016/j.solener.2009.04.007.

[30] S. Batchelor, E. Brown, N. Scott, and J. Leary, "Two birds, one stone-reframing cooking energy policies in Africa and Asia," *Energies*, vol. 12, no. 9, pp. 1–18, 2019, doi: 10.3390/en12091591.

[31] WHO Household Air Pollution and Health, Available online:https://www.who.int/en/news-room/factsheets/detail/household-air-pollution-and-health (accessed on Mar. 27, 2021).

[32] M. Sehgal, S. A. Rizwan, and A. Krishnan, "Disease burden due to biomass cooking-fuel-related household air pollution among women in India," *Glob. Health Action*, vol. 7, no. 1,

2014, doi: 10.3402/gha.v7.25326.

[33] Y. T. Wassie and M. S. Adaramola, "Analysis of potential fuel savings, economic and environmental effects of improved biomass cookstoves in rural Ethiopia," *J. Clean. Prod.*, vol. 280, p. 124700, 2021, doi: 10.1016/j.jclepro.2020.124700.

[34] P. and D. L. Funk, "Parametric model of solar cooker performance," *Sol. Energy*, vol. 62, no. 1, pp. 63–68, 1998.

[35] P. A. Owusu and S. Asumadu-sarkodie, "sustainability issues and climate change mitigation A review of renewable energy sources , sustainability issues and climate change mitigation," *Cogent Eng.*, vol. 15, no. 1, 2016, doi: 10.1080/23311916.2016.1167990.

[36] J. Lian, Y. Zhang, C. Ma, Y. Yang, and E. Chaima, "A review on recent sizing methodologies of hybrid renewable energy systems," *Energy Convers. Manag.*, vol. 199, no. April, p. 112027, 2019, doi: 10.1016/j.enconman.2019.112027.

[37] E. Bellos and C. Tzivanidis, "Parametric investigation of nanofluids utilization in parabolic trough collectors," *Therm. Sci. Eng. Prog.*, vol. 2, pp. 71–79, 2017, doi: 10.1016/j.tsep.2017.05.001.

[38] T. Bauer, "Approximate analytical solutions for the solidification of PCMs in fin geometries using effective thermophysical properties," *Int. J. Heat Mass Transf.*, vol. 54, no. 23–24, pp. 4923–4930, 2011, doi: 10.1016/j.ijheatmasstransfer.2011.07.004.

[39] A. Gallagher, "A solar fryer," *Sol. Energy*, vol. 85, no. 3, pp. 496–505, 2011, doi: 10.1016/j.solener.2010.12.018.

[40] A. A. Badran, I. A. Yousef, N. K. Joudeh, R. Al Hamad, H. Halawa, and H. K. Hassouneh, "Portable solar cooker and water heater," *Energy Convers. Manag.*, vol. 51, no. 8, pp. 1605–1609, 2010, doi: 10.1016/j.enconman.2009.09.038.

[41] E. Bellos, C. Tzivanidis, and V. Belessiotis, "Daily performance of parabolic trough solar collectors," vol. 158, no. July, pp. 663–678, 2017.

[42] H. H. Ozturk, "Experimental determination of energy and exergy efficiency of the solar parabolic-cooker," vol. 77, pp. 67–71, 2004, doi: 10.1016/j.solener.2004.03.006.

[43] R. Petela, "Exergy analysis of the solar cylindrical-parabolic cooker," vol. 79, pp. 221–233, 2005, doi: 10.1016/j.solener.2004.12.001.

[44] G. Coccia, G. Di, and M. Sotte, "Design , manufacture , and test of a prototype for a

parabolic trough collector for industrial process heat," *Renew. Energy*, vol. 74, pp. 727–736, 2015, doi: 10.1016/j.renene.2014.08.077.

[45] P. Forman, S. Mu, K. Hennecke, and J. Kru, "ScienceDirect Light concrete shells for parabolic trough collectors – Conceptual design , prototype and proof of accuracy," vol. 111, pp. 364–377, 2015, doi: 10.1016/j.solener.2014.11.002.

[46] A. Harmim, M. Merzouk, M. Boukar, and M. Amar, "ScienceDirect Design and experimental testing of an innovative building-integrated box type solar cooker," *Sol. Energy*, vol. 98, pp. 422–433, 2013, doi: 10.1016/j.solener.2013.09.019.

[47] S. K. Shukla, "International Journal of Green Energy Comparison of Energy and Exergy Efficiency of Community and Domestic Type Parabolic Solar Cookers," no. June 2015, pp. 37–41, 2009, doi: 10.1080/15435070903227912.

[48] M. Pe, F. J. Cabrera, and A. Ferna, "Use of parabolic trough solar collectors for solar refrigeration and air-conditioning applications," vol. 20, pp. 103–118, 2013, doi: 10.1016/j.rser.2012.11.081.

[49] A. Ferna, "Parabolic-trough solar collectors and their applications," vol. 14, pp. 1695–1721, 2010, doi: 10.1016/j.rser.2010.03.012.

[50] H. Price, G. Cohen, R. Gee, and R. Mahoney, "Advances in Parabolic Trough Solar Power Technology," vol. 124, no. May 2002, pp. 109–125, 2017, doi: 10.1115/1.1467922.

[51] B. Kurs, "Thermal performance assessment of internal longitudinal fi ns with sinusoidal lateral surfaces in parabolic trough receiver tubes," vol. 140, pp. 816–827, 2019, doi: 10.1016/j.renene.2019.03.106.

[52] B. Zou, Y. Jiang, Y. Yao, and H. Yang, "Thermal performance improvement using unilateral spiral ribbed absorber tube for parabolic trough solar collector," *Sol. Energy*, vol. 183, no. March, pp. 371–385, 2019, doi: 10.1016/j.solener.2019.03.048.

[53] G. Kumaresan, P. Sudhakar, R. Santosh, and R. Velraj, "Experimental and numerical studies of thermal performance enhancement in the receiver part of solar parabolic trough collectors," *Renew. Sustain. Energy Rev.*, vol. 77, no. March, pp. 1363–1374, 2017, doi: 10.1016/j.rser.2017.01.171.

[54] W. Fuqiang, C. Ziming, T. Jianyu, Y. Yuan, S. Yong, and L. Linhua, "Progress in concentrated solar power technology with parabolic trough collector system : A comprehensive review," *Renew. Sustain. Energy Rev.*, vol. 79, no. May, pp. 1314–1328,

2017, doi: 10.1016/j.rser.2017.05.174.

[55] N. P. Trough, C. Using, T. T. Inserts, P. P. Inserts, and I. F. Absorber, "Enhancing the Performance of Evacuated and Twisted Tape Inserts , Perforated Plate Inserts and," 2018, doi: 10.3390/en11051129.

[56] X. Song, G. Dong, F. Gao, X. Diao, and L. Zheng, "A numerical study of parabolic trough receiver with nonuniform heat fl ux and helical screw-tape inserts," *Energy*, vol. 77, pp. 771–782, 2014, doi: 10.1016/j.energy.2014.09.049.

[57] E. Bellos, C. Tzivanidis, K. A. Antonopoulos, and G. Gkinis, "Thermal enhancement of solar parabolic trough collectors by using nano fluids and converging-diverging absorber tube," *Renew. Energy*, vol. 94, pp. 213–222, 2016, doi: 10.1016/j.renene.2016.03.062.

[58] P. M. Zadeh, T. Sokhansefat, A. B. Kasaeian, F. Kowsary, and A. Akbarzadeh, "Hybrid optimization algorithm for thermal analysis in a solar parabolic trough collector based on nano fl uid," *Energy*, vol. 82, pp. 857–864, 2015, doi: 10.1016/j.energy.2015.01.096.

[59] P. E. Phelan, T. P. Otanicar, and R. A. Taylor, "Solar energy harvesting using nanofluids-based concentrating solar collector," vol. 3, no. August 2012, pp. 1–9, 2013, doi: 10.1115/1.4007387.

[60] J. Chen and M. Hans, "Heat transfer enhancement in dimpled tubes," vol. 21, 2001.

[61] K. R. Kumar and K. S. Reddy, "Thermal analysis of solar parabolic trough with porous disc receiver," *Appl. Energy*, vol. 86, no. 9, pp. 1804–1812, 2009, doi: 10.1016/j.apenergy.2008.11.007.

[62] A. M. Sefidan, M. Taghilou, M. Mohammadpour, and A. Sojoudi, "Effects of different parameters on the discharging of double-layer PCM through the porous channel," *Appl. Therm. Eng.*, vol. 123, pp. 592–602, 2017, doi: 10.1016/j.applthermaleng.2017.05.131.

[63] C. Veerakumar and A. Sreekumar, "Phase change material based cold thermal energy storage: Materials, techniques and applications - A review," *Int. J. Refrig.*, vol. 67, pp. 271–289, 2016, doi: 10.1016/j.ijrefrig.2015.12.005.

[64] F. Fornarelli, V. Ceglie, B. Fortunato, S. M. Camporeale, M. Torresi, P. Oresta, A. Miliozzi, "Numerical simulation of a complete charging-discharging phase of a shell and tube thermal energy storage with phase change material," *Energy Procedia*, vol. 126, pp. 501–508, 2017, doi: 10.1016/j.egypro.2017.08.220.

[65] M. Lacroix, "Numerical simulation of a shell-and-tube latent heat thermal energy storage unit," *Sol. Energy*, vol. 50, no. 4, pp. 357–367, 1993, doi: 10.1016/0038-092X(93)90029-

N.

[66] S. Seddegh, X. Wang, and A. D. Henderson, "A comparative study of thermal behaviour of a horizontal and vertical shell-and-tube energy storage using phase change materials," *Appl. Therm. Eng.*, vol. 93, pp. 348–358, 2016, doi: 10.1016/j.applthermaleng.2015.09.107.

[67] M. Esapour, M. J. Hosseini, A. A. Ranjbar, Y. Pahamli, and R. Bahrampoury, "Phase change in multi-tube heat exchangers," *Renew. Energy*, vol. 85, pp. 1017–1025, 2016, doi: 10.1016/j.renene.2015.07.063.

[68] Hakeem Niyas and P.Muthukumar, "Performance Analysis of Latent Heat Storage Systems," *Int. J. Sci. Eng. Res.*, vol. 4, no. December 2013, 2015.

[69] E. M. Sparrow, S. V Patankar, and S. Ramadhyani, "Analysis of melting in the presence of natural convection in the melt region," *J. Heat Transfer*, vol. 99, no. 4, pp. 520–526, 1977, doi: 10.1115/1.3450736.

[70] M. Lacroix and T. Duong, "Experimental improvements of heat transfer in a latent heat thermal energy storage unit with embedded heat sources," *Energy Convers. Manag.*, vol. 39, no. 8, pp. 703–716, 1998, doi: 10.1016/S0196-8904(97)10011-5.

[71] M. A. Ezan, M. Ozdogan, and A. Erek, "Experimental study on charging and discharging periods of water in a latent heat storage unit," *Int. J. Therm. Sci.*, vol. 50, no. 11, pp. 2205–2219, 2011, doi: 10.1016/j.ijthermalsci.2011.06.010.

[72] M. Longeon, A. Soupart, J. F. Fourmigué, A. Bruch, and P. Marty, "Experimental and numerical study of annular PCM storage in the presence of natural convection," *Appl. Energy*, vol. 112, pp. 175–184, 2013, doi: 10.1016/j.apenergy.2013.06.007.

[73] Y. B. Tao, Y. K. Liu, and Y. L. He, "Effects of PCM arrangement and natural convection on charging and discharging performance of shell-and-tube LHS unit," *Int. J. Heat Mass Transf.*, vol. 115, pp. 99–107, 2017, doi: 10.1016/j.ijheatmasstransfer.2017.07.098.

[74] G. S. Han, H. S. Ding, Y. Huang, L. G. Tong, and Y. L. Ding, "A comparative study on the performances of different shell-and-tube type latent heat thermal energy storage units including the effects of natural convection," *Int. Commun. Heat Mass Transf.*, vol. 88, no. October, pp. 228–235, 2017, doi: 10.1016/j.icheatmasstransfer.2017.09.009.

[75] Y. B. Tao and Y. L. He, "Effects of natural convection on latent heat storage performance of salt in a horizontal concentric tube," *Appl. Energy*, vol. 143, pp. 38–46, 2015, doi:

10.1016/j.apenergy.2015.01.008.

[76] X. Cao, Y. Yuan, B. Xiang, and F. Highlight, "Effect of natural convection on melting performance of eccentric horizontal shell and tube latent heat storage unit," *Sustain. Cities Soc.*, vol. 38, no. December 2017, pp. 571–581, 2018, doi: 10.1016/j.scs.2018.01.025.

[77] Z. J. Zheng, Y. Xu, and M. J. Li, "Eccentricity optimization of a horizontal shell-and-tube latent-heat thermal energy storage unit based on melting and melting-solidifying performance," *Appl. Energy*, vol. 220, no. March, pp. 447–454, 2018, doi: 10.1016/j.apenergy.2018.03.126.

[78] M. M. Joybari, F. Haghighat, and S. Seddegh, "Natural convection characterization during melting of phase change materials: Development of a simplified front tracking method," *Sol. Energy*, vol. 158, no. October, pp. 711–720, 2017, doi: 10.1016/j.solener.2017.10.031.

[79] J. M. Mahdi, S. Lohrasbi, D. D. Ganji, and E. C. Nsofor, "Accelerated melting of PCM in energy storage systems via novel configuration of fins in the triplex-tube heat exchanger," *Int. J. Heat Mass Transf.*, vol. 124, pp. 663–676, 2018, doi: 10.1016/j.ijheatmasstransfer.2018.03.095.

[80] N. Kousha, M. J. Hosseini, M. R. Aligoodarz, R. Pakrouh, and R. Bahrampoury, "Effect of inclination angle on the performance of a shell and tube heat storage unit – An experimental study," *Appl. Therm. Eng.*, vol. 112, pp. 1497–1509, 2017, doi: 10.1016/j.applthermaleng.2016.10.203.

[81] F. Fornarelli, S.M. Camporeale, B. Fortunato, M. Torresi, P. Oresta, L. Magliocchetti, A. Miliozzi, G. Santo, "CFD analysis of melting process in a shell-and-tube latent heat storage for concentrated solar power plants," *Appl. Energy*, vol. 164, pp. 711–722, 2016, doi: 10.1016/j.apenergy.2015.11.106.

[82] M. K. Rathod and J. Banerjee, "Thermal performance enhancement of shell and tube Latent Heat Storage Unit using longitudinal fins," *Appl. Therm. Eng.*, vol. 75, pp. 1084–1092, 2015, doi: 10.1016/j.applthermaleng.2014.10.074.

[83] Y. Wang, L. Wang, N. Xie, X. Lin, and H. Chen, "International Journal of Heat and Mass Transfer Experimental study on the melting and solidification behavior of erythritol in a vertical shell-and-tube latent heat thermal storage unit," *Int. J. Heat Mass Transf.*, vol. 99, pp. 770–781, 2016, doi: 10.1016/j.ijheatmasstransfer.2016.03.125.

[84] U. Herrmann and D. W. Kearney, "Survey of thermal energy storage for parabolic trough power plants," *J. Sol. Energy Eng. Trans. ASME*, vol. 124, no. 2, pp. 145–152, 2002, doi: 10.1115/1.1467601.

[85] L. F. Cabeza, C. Solé, A. Castell, E. Oró, and A. Gil, "Review of solar thermal storage techniques and associated heat transfer technologies," *Proc. IEEE*, vol. 100, no. 2, pp. 525–538, 2012, doi: 10.1109/JPROC.2011.2157883.

[86] J. M. Mahdi and E. C. Nsofor, "Melting enhancement in triplex-tube latent thermal energy storage system using nanoparticles-fins combination," *Int. J. Heat Mass Transf.*, vol. 109, pp. 417–427, 2017, doi: 10.1016/j.ijheatmasstransfer.2017.02.016.

[87] K. Bhagat, M. Prabhakar, and S. K. Saha, "Estimation of thermal performance and design optimization of finned multitube latent heat thermal energy storage," *J. Energy Storage*, vol. 19, no. July, pp. 135–144, 2018, doi: 10.1016/j.est.2018.06.014.

[88] A. Sciacovelli, F. Gagliardi, and V. Verda, "Maximization of performance of a PCM latent heat storage system with innovative fins," *Appl. Energy*, vol. 137, pp. 707–715, 2015, doi: 10.1016/j.apenergy.2014.07.015.

[89] M. J. Hosseini, A. A. Ranjbar, M. Rahimi, and R. Bahrampoury, "Experimental and numerical evaluation of longitudinally finned latent heat thermal storage systems," *Energy & Build.*, vol. 99, pp. 263–272, 2015, doi: 10.1016/j.enbuild.2015.04.045.

[90] R. Pakrouh, M. J. Hosseini, A. A. Ranjbar, and R. Bahrampoury, "A numerical method for PCM-based pin fin heat sinks optimization," *Energy Convers. Manag.*, vol. 103, pp. 542–552, 2015, doi: 10.1016/j.enconman.2015.07.003.

[91] Y. Yuan, X. Cao, B. Xiang, and Y. Du, "Effect of installation angle of fins on melting characteristics of annular unit for latent heat thermal energy storage," *Sol. Energy*, vol. 136, pp. 365–378, 2016, doi: 10.1016/j.solener.2016.07.014.

[92] C. Liu and D. Groulx, "Experimental study of the phase change heat transfer inside a horizontal cylindrical latent heat energy storage system," *Int. J. Therm. Sci.*, vol. 82, no. 1, pp. 100–110, 2014, doi: 10.1016/j.ijthermalsci.2014.03.014.

[93] Y. Tang, D. Su, X. Huang, G. Alva, L. Liu, and G. Fang, "Synthesis and thermal properties of the MA / HDPE composites with nano-additives as form-stable PCM with improved thermal conductivity," vol. 180, pp. 116–129, 2016, doi: 10.1016/j.apenergy.2016.07.106.

[94] M. Tariq and H. A. Kazem, "Single slope solar distillator productivity improvement using phase change material and Al 2 O 3 nanoparticle," *Sol. Energy*, vol. 164, no. January, pp. 370–381, 2018, doi: 10.1016/j.solener.2018.02.049.

[95] A. Mwesigye and J. P. Meyer, "Optimal thermal and thermodynamic performance of a solar parabolic trough receiver with different nanofluids and at different concentration ratios," *Appl. Energy*, vol. 193, pp. 393–413, 2017, doi: 10.1016/j.apenergy.2017.02.064.

[96] Z. Khan, Z. Khan, and K. Tabeshf, "Parametric investigations to enhance thermal performance of paraffin through a novel geometrical configuration of shell and tube latent thermal storage system," *Energy Convers. Manag.*, vol. 127, pp. 355–365, 2016, doi: 10.1016/j.enconman.2016.09.030.

[97] S. Ebadi, S. H. Tasnim, A. A. Aliabadi, and S. Mahmud, "Melting of nano-PCM inside a cylindrical thermal energy storage system : Numerical study with experimental veri fi cation," *Energy Convers. Manag.*, vol. 166, no. March, pp. 241–259, 2018, doi: 10.1016/j.enconman.2018.04.016.

[98] H. Mehrjerdi and E. Rakhshani, "Optimal operation of hybrid electrical and thermal energy storage systems under uncertain loading condition," *Appl. Therm. Eng.*, vol. 160, no. May, p. 114094, 2019, doi: 10.1016/j.applthermaleng.2019.114094.

[99] K. Anoune, M. Bouya, A. Astito, and A. Ben, "Sizing methods and optimization techniques for PV-wind based hybrid renewable energy system : A review," *Renew. Sustain. Energy Rev.*, vol. 93, no. June, pp. 652–673, 2018, doi: 10.1016/j.rser.2018.05.032.

[100] A. Haileselassie, M. Bayray, and O. Jørgen, "Solar powered heat storage for Injera baking in Ethiopia," *Energy Procedia*, vol. 57, pp. 1603–1612, 2014, doi: 10.1016/j.egypro.2014.10.152.

[101] M. Mussard and O. J. Nydal, "Charging of a heat storage coupled with a low-cost small-scale solar parabolic trough for cooking purposes," *Sol. Energy*, vol. 95, pp. 144–154, 2013, doi: 10.1016/j.solener.2013.06.013.

[102] U. R. Prasanna and L. Umanand, "Modeling and design of a solar thermal system for hybrid cooking application," *Appl. Energy*, vol. 88, no. 5, pp. 1740–1755, 2011, doi: 10.1016/j.apenergy.2010.11.042.

[103] G. Kumaresan, V. S. Vigneswaran, S. Esakkimuthu, and R. Velraj, "Performance

assessment of a solar domestic cooking unit integrated with thermal energy storage system," *J. Energy Storage*, vol. 6, pp. 70–79, 2016, doi: 10.1016/j.est.2016.03.002.

[104] S. D. Sharma, "Thermal performance of a solar cooker based on an evacuated tube solar collector with a PCM storage unit," vol. 78, pp. 416–426, 2005, doi: 10.1016/j.solener.2004.08.001.

[105] G. Kumaresan, R. Sridhar, and R. Velraj, "Performance studies of a solar parabolic trough collector with a thermal energy storage system," *Energy*, vol. 47, no. 1, pp. 395–402, 2012, doi: 10.1016/j.energy.2012.09.036.

[106] E. C. Okogbue, J. A. Adedokun, and B. Holmgren, "Hourly and daily clearness index and diffuse fraction at a tropical station , Ile-Ife , Nigeria," vol. 1047, no. January, pp. 1035–1047, 2009, doi: 10.1002/joc.

[107] S. R. Kalbande, A. N. Mathur, S. Kothari, and S. N. Pawar, "Design , Development and Testing of Paraboloidal Solar Cooker," vol. 20, no. 3, pp. 571–574, 2007.

[108] S. M. M. Ahmed, M. R. Al-Amin, S. Ahammed, F. Ahmed, A. M. Saleque, and M. Abdur Rahman, "Design, construction and testing of parabolic solar cooker for rural households and refugee camp," *Sol. Energy*, vol. 205, no. May, pp. 230–240, 2020, doi: 10.1016/j.solener.2020.05.007.

[109] V. Thakkar, A. Doshi, and A. Rana, "Performance Analysis Methodology for Parabolic Dish Solar Concentrators for Process Heating Using Thermic Fluid," vol. 12, no. 1, pp. 101–114, 2015, doi: 10.9790/1684-1212101114.

[110] B. Anak, M. Farid, T. Zanariahshamsirali, and R. Abu, "Effect of rim angle to the flux distribution diameter in solar parabolic dish collector," vol. 68, pp. 45–52, 2015, doi: 10.1016/j.egypro.2015.03.231.

[111] Z. Zhang, J. Sun, L. Wang, and J. J. Wei, "Multiphysics-coupled study of wind load e ff ects on optical performance of parabolic trough collector," *Sol. Energy*, vol. 207, no. March, pp. 1078–1087, 2020, doi: 10.1016/j.solener.2020.06.107.

[112] A. Kasaeian, S. Daviran, R. Danesh, and A. Rashidi, "Performance evaluation and nanofluid using capability study of a solar parabolic trough collector," *Energy Convers. Manag.*, vol. 89, pp. 368–375, 2015, doi: 10.1016/j.enconman.2014.09.056.

[113] S. García-cortés, A. Bello-garcía, and C. Ordóñez, "Estimating intercept factor of a parabolic solar trough collector with new supporting structure using off-the-shelf

photogrammetric equipment," *Appl. Energy*, vol. 92, pp. 815–821, 2012, doi: 10.1016/j.apenergy.2011.08.032.

[114] George C.Bakos, "Design and construction of a two-axis Sun tracking system for parabolic trough collector (PTC) efficiency improvement," *Renew. Energy*, vol. 31, pp. 2411–2421, 2006, doi: 10.1016/j.renene.2005.11.008.

[115] L. Kalapala and J. K. Devanuri, "Influence of operational and design parameters on the performance of a PCM based heat exchanger for thermal energy storage – A review," *J. Energy Storage*, vol. 20, no. July, pp. 497–519, 2018, doi: 10.1016/j.est.2018.10.024.

[116] A. J. Lopes Jesus, S. C. C. Nunes, M. Ramos Silva, A. Matos Beja, and J. S. Redinha, "Erythritol: Crystal growth from the melt," *Int. J. Pharm.*, vol. 388, no. 1–2, pp. 129–135, 2010, doi: 10.1016/j.ijpharm.2009.12.043.

[117] A. Shukla, D. Buddhi, and R. L. Sawhney, "Thermal cycling test of few selected inorganic and organic phase change materials," *Renew. Energy*, vol. 33, no. 12, pp. 2606–2614, 2008, doi: 10.1016/j.renene.2008.02.026.

[118] S. D. Odeh, G. L. Morrison, and M. Behnia, "Modelling of parabolic trough direct steam generation solar collectors," vol. 62, no. 6, pp. 395–406, 1998.

[119] Evangelos Bellos and Tzivanids Christos, "Assessment of the thermal enhancement methods in parabolic trough collectors," *Int. J. Energy Environ. Eng.*, vol. 9, no. 1, pp. 59–70, 2018, doi: 10.1007/s40095-017-0255-3.

[120] K. A. Reed, P.Bendt, A.Rabl, H.W.Gaul, "Optical analysis and optimization of line focus solar collectors."

[121] E. Jacobson, N. Ketjoy, S. Nathakaranakule, and W. Rakwichian, "Solar Parabolic Trough Simulation and Application for a Hybrid Power Plant in Thailand," vol. 32, pp. 187–199, 2006, doi: 10.2306/scienceasia1513-1874.2006.32.187.

[122] M. Li and L. L. Wang, "Investigation of evacuated tube heated by solar trough concentrating system," vol. 47, pp. 3591–3601, 2006, doi: 10.1016/j.enconman.2006.03.003.

[123] E. Bellos, C. Tzivanidis, and K. A. Antonopoulos, "A detailed working fluid investigation for solar parabolic trough collectors," *Appl. Therm. Eng.*, vol. 114, pp. 374–386, 2017, doi: 10.1016/j.applthermaleng.2016.11.201.

[124] A. Kasaiean, M. Sameti, R. Daneshazarian, and Z. Noori, "Heat transfer network for a

parabolic trough collector as a heat collecting element using nano fl uid," *Renew. Energy*, vol. 123, pp. 439–449, 2018, doi: 10.1016/j.renene.2018.02.062.

[125] E. Bellos and C. Tzivanidis, "Thermal analysis of parabolic trough collector operating with mono and hybrid nano fl uids," *Sustain. Energy Technol. Assessments*, vol. 26, no. September 2017, pp. 105–115, 2018, doi: 10.1016/j.seta.2017.10.005.

[126] D. K. Vernon E. Dudley, Gregory I. Kolb, A. Roderick Mahoney, Thomas R. Mancini, Chauncey W. Matthews, Michael Sloan, *Test Results: SEGS LS-2 Solar Collector;Report of Sandia National Laboratories*, SAN94-1884th ed. Livermore,CA, USA: Sandia National Laboratories, 1994.

[127] A. A. Hawwash, A. K. Abdel, S. A. Nada, and S. Ookawara, "Numerical Investigation and Experimental Verification of Performance Enhancement of Flat Plate Solar Collector Using Nanofluids," *Appl. Therm. Eng.*, vol. 130, pp. 363–374, 2018, doi: 10.1016/j.applthermaleng.2017.11.027.

[128] H. Olia, M. Torabi, M. Bahiraei, and M. H. Ahmadi, "applied sciences Application of Nanofluids in Thermal Performance Enhancement of Parabolic Trough Solar Collector : State-of-the-Art," 2019, doi: 10.3390/app9030463.

[129] A. Mwesigye, Y. Halil, and J. P. Meyer, "Numerical analysis of the thermal and thermodynamic performance of a parabolic trough solar collector using SWCNTs-Therminol ® VP-1 nano fl uid," vol. 119, pp. 844–862, 2018, doi: 10.1016/j.renene.2017.10.047.

[130] O. O. Fasina and Z. Colley, "Viscosity and specific heat of vegetable oils as a function of temperature: 35°C to 180°C," *Int. J. Food Prop.*, vol. 11, no. 4, pp. 738–746, 2008, doi: 10.1080/10942910701586273.

[131] A. A. Al-Abidi, S. Mat, K. Sopian, M. Y. Sulaiman, and A. T. Mohammad, "Numerical study of PCM solidification in a triplex tube heat exchanger with internal and external fins," *Int. J. Heat Mass Transf.*, vol. 61, no. 1, pp. 684–695, 2013, doi: 10.1016/j.ijheatmasstransfer.2013.02.030.

[132] *ANSYS Fluent User's Guide*. Canonsburg, 2013.

[133] American Society of Heating, *Ashrae Standard*. Atlanta, 1977.

[134] W. Wang, S. He, S. Guo, J. Yan, and J. Ding, "A combined experimental and simulation study on charging process of Erythritol-HTO direct-blending based energy storage

system," *Energy Convers. Manag.*, vol. 83, pp. 306–313, 2014, doi: 10.1016/j.enconman.2014.03.054.

[135] T. Nomura, N. Okinaka, and T. Akiyama, "Impregnation of porous material with phase change material for thermal energy storage," *Mater. Chem. Phys.*, vol. 115, no. 2–3, pp. 846–850, 2009, doi: 10.1016/j.matchemphys.2009.02.045.

[136] A. Kaizawa, N. Maruoka, A. Kawai, H. Kamano, T. Jozuka, T. Senda and T.Akiyama, "Thermophysical and heat transfer properties of phase change material candidate for waste heat transportation system," *Heat Mass Transf.* vol. 44, no. 7, pp. 763–769, 2008, doi: 10.1007/s00231-007-0311-2.

[137] R. P. Singh, H. Xu, S. C. Kaushik, D. Rakshit, and A. Romagnoli, "Charging performance evaluation of finned conical thermal storage system encapsulated with nano-enhanced phase change material," *Appl. Therm. Eng.*, vol. 151, no. January, pp. 176–190, 2019, doi: 10.1016/j.applthermaleng.2019.01.072.

[138] X. Yang, Z. Lu, Q. Bai, Q. Zhang, L. Jin, and J. Yan, "Thermal performance of a shell-and-tube latent heat thermal energy storage unit : Role of annular fins," *Appl. Energy*, vol. 202, pp. 558–570, 2017, doi: 10.1016/j.apenergy.2017.05.007.

[139] V. Joshi and M. K. Rathod, "Constructal enhancement of thermal transport in latent heat storage systems assisted with fi ns," *Int. J. Therm. Sci.*, vol. 145, no. June 2018, p. 105984, 2019, doi: 10.1016/j.ijthermalsci.2019.105984.

[140] A. A. Al-Abidi, S. Bin Mat, K. Sopian, M. Y. Sulaiman, and A. T. Mohammed, "CFD applications for latent heat thermal energy storage: A review," *Renew. Sustain. Energy Rev.*, vol. 20, pp. 353–363, 2013, doi: 10.1016/j.rser.2012.11.079.

[141] H. Niyas, S. Prasad, and P. Muthukumar, "Performance investigation of a lab–scale latent heat storage prototype – Numerical results," *Energy Convers. Manag.*, vol. 135, pp. 188–199, 2017, doi: 10.1016/j.enconman.2016.12.075.

[142] V.R. Voller, C. Prakash, "A fixed grid numerical modelling methodology for convection-diffusion mushy region phase-change problems," *Int. J. Heat Mass Transf.*, vol. 30, pp. 1709–1719, 1987.

[143] Y. Hong, W. B. Ye, J. Du, and S. M. Huang, "Solid-liquid phase-change thermal storage and release behaviors in a rectangular cavity under the impacts of mushy region and low gravity," *Int. J. Heat Mass Transf.*, vol. 130, pp. 1120–1132, 2019, doi:

10.1016/j.ijheatmasstransfer.2018.11.024.

[144] R. S. Vajjha, D. K. Das, and P. K. Namburu, "International Journal of Heat and Fluid Flow Numerical study of fluid dynamic and heat transfer performance of Al 2 O 3 and CuO nanofluids in the flat tubes of a radiator," *Int. J. Heat Fluid Flow*, vol. 31, no. 4, pp. 613–621, 2010, doi: 10.1016/j.ijheatfluidflow.2010.02.016.

[145] M. Mahdavi, S. Tiari, and V. Pawar, "A numerical study on the combined e ff ect of dispersed nanoparticles and embedded heat pipes on melting and solidi fi cation of a shell and tube latent heat thermal energy storage system," vol. 27, no. September 2019, 2020, doi: 10.1016/j.est.2019.101086.

[146] S. A. Kalogirou, *Solar energy engineering: processes and systems*, Second. 2013.

[147] J. A. D. and W. A.Beckman, *Solar Engineering of Thermal Processes*. Hoboken, 2013.

[148] Kline SJ and McClintock FA, "Describing uncertainties in single-sample experiment" Mechanical Engineering, 1953

Appendix A

Fundamentals of Solar Energy

The geometric relationship between solar collector and sun is required so that the position of sun with respect to a particular place can be tracked [146]. For the estimation of solar radiation, knowledge of sun's strength and earth's correlation with the sun is very important. Local solar noon is the instant of time at which sun passes over the meridian of the observer and this is known as apparent solar time. Apparent solar time depends on the apparent motion of the sun across the sky and is used for solar energy calculations. Solar noon does not usually coincide with standard 12:00 Hrs. wall clock time. The equations of time and longitude correction are employed to convert local standard time (LST) to apparent solar time [147].

Equation of Time (EoT)

The orbital velocity of earth differs throughout the year due to the factors related with earth's orbit around the sun. As a result, the apparent solar time diverges slightly from wall clock time. The variation created due to this is known as the equation of time (EoT) and is resulted because of the non-uniform time taken by earth to complete one revolution around its own axis with reference to the sun throughout the year [147]. The EoT is approximated using the following equations and it is indicated in Fig.A.1.

$$ET = 9.87\sin(2B) - 7.53\cos(B) - 1.5\sin(B)\,[min.] \tag{A.1}$$

where

$$B = (N - 81)\frac{360}{364}[degrees] \tag{A.2}$$

Longitude Correction (LC)

For determining standard clock time at a particular location, a longitude correction term is either added or subtracted and is expressed as mentioned below [147].

$$LC = 4(l_{st}) - l_{local}) \tag{A.3}$$

where, l_{st} and l_{local} are the standard and local longitudes, respectively. Hence, the general equation to estimate apparent solar time (AST) is described by Eq. (A.4).

$$AST = LST + ET \mp 4(l_{st}) - l_{local}) \tag{A.4}$$

where, *LST* is local solar time,

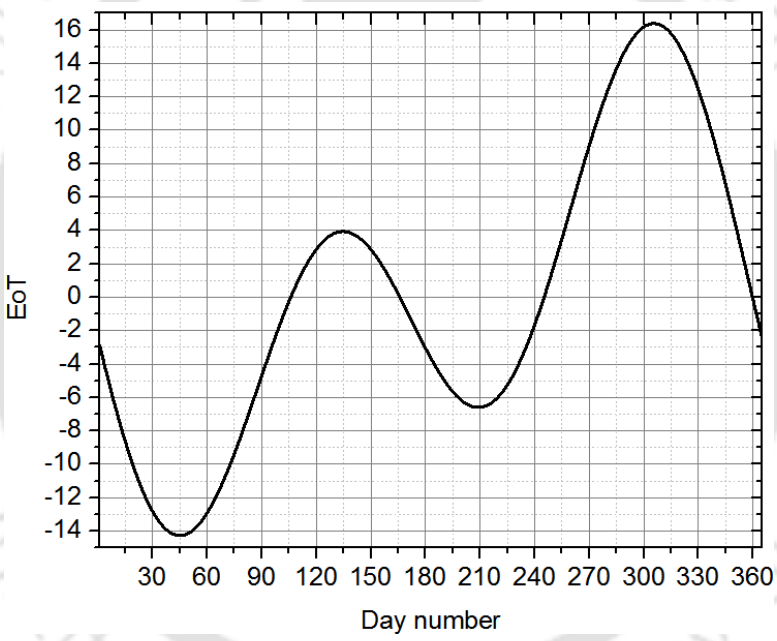

Fig.A.1.Equation of time

From the above equation, the east of Greenwich location is represented by a minus (-) sign, whereas, west is denoted by a plus (+) sign. LST is the time based on the apparent angular movement of the sun through the sky.

Basic Earth-Sun Angles

The yearly extent of solar radiation that reaches on the earth's surface varies due to the variation in the distance between the earth and the sun (see Fig.A.2). On December 21, earth and the sun has a minimum distance i.e. 1.471×10^{11}m, which is called perihelion. The maximum distance

between earth and sun occurs on June 21 of every year, which is called aphelion and its value is $1.512x10^{11}$m [146], [147]. Earth revolves about its axis and the axis is tilted with respect to earth's orbital plane axis at an angle of 23.45° [146]. This tilt is the major cause of the seasonal disparity of the solar radiation presented at any location on the surface of the earth. Therefore, the location of a point (P) on earth with respect to sun's rays can be determined at any time, if the basic Earth-Sun angles are known. These are the hour angle (ω), latitude angle (φ) and the declination angle of the sun (δ) and shown in Fig A.3- A.5.

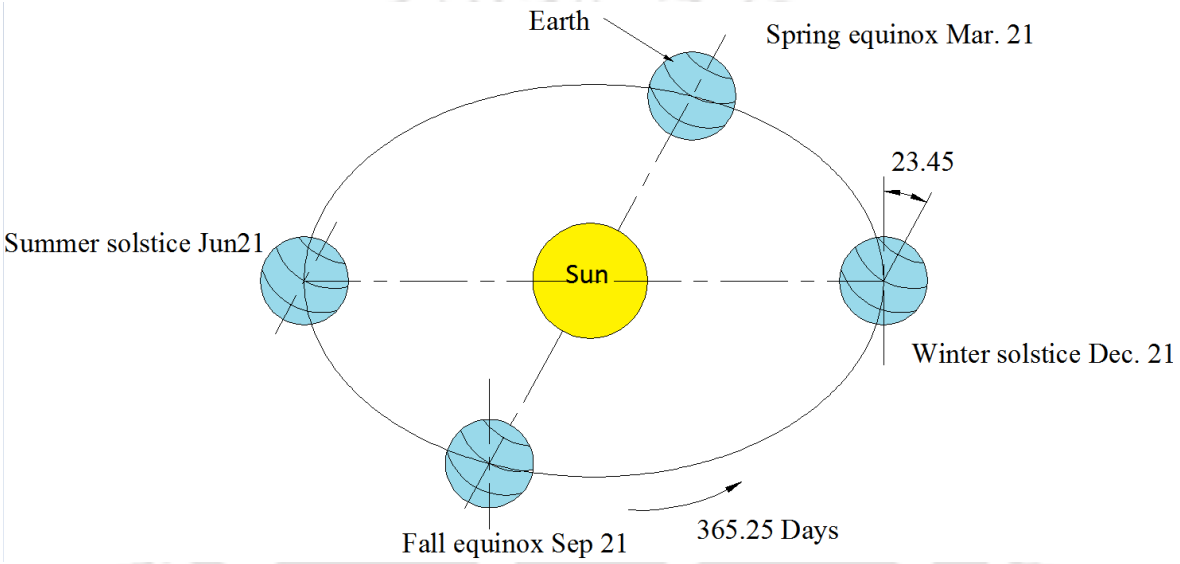

Fig.A. 2.Earth revolution around the sun [105]

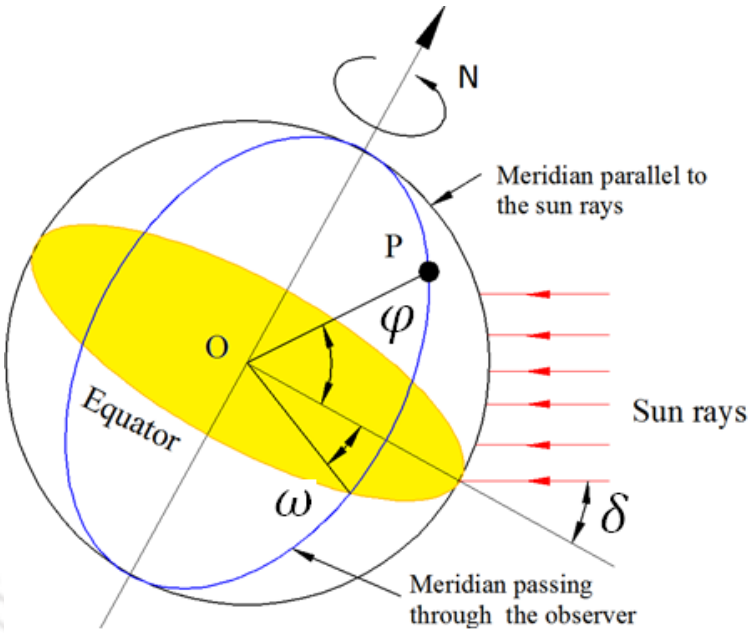

Fig.A. 3.Basic solar-Earth angles [105]

Solar declination angle (δ) is an angle between earth-sun line and the equatorial plane of the earth. The declination angle is defined as an angular position of the sun at solar noon with respect to the equator. As it can be seen from Fig. A.4, the angle varies throughout the year due to earth's revolution around its axis. The magnitude of the declination angle varies between $+23.45^0$ and -23.45^0, which is resulted on 21st of June and December, respectively [146]. The declination angle can be estimated approximately according to Eq. (A.5).

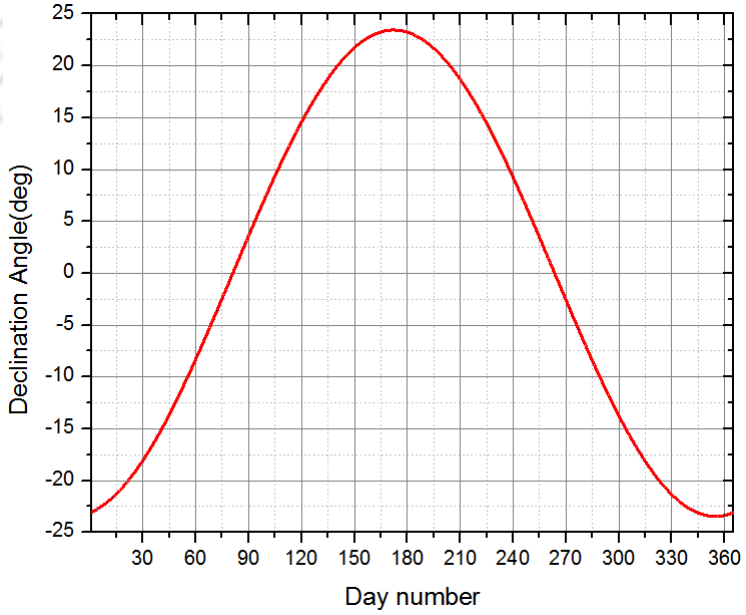

Fig.A. 4.Variation of the solar declination angle (δ) throughout the year

$$\delta = 23.45^0 \sin\left[\frac{360}{365}(284 + N)\right][Degrees] \quad \text{(A.5)}$$

where, N represents the day of the year and variation of declination angle throughout the year is illustrated in Fig.A.4.

The hour angle **(ω)** is defined as an angular distance between the meridian of the observer and the meridian whose plane encloses the sun, thus, the value of the hour angle varies the whole day. At the instance, the sun reaches its highest point in the sky, the hour angle becomes zero, which occurs at the local noon. The hour angle exhibits a maximum negative and positive value of 180^0 at sunrise and sunset, respectively at any place on the earth [147]. The hour angle can be estimated by Eq. (A.6).

$$\omega = 15(AST - 12) \quad \text{(A.6)}$$

The latitude (ϕ) is explained as an angle between the line joining a particular location to the center of the Earth and the equatorial plane. It varies between $+90^0$ to -90^0. All locations on the earth which lay at the same latitude, display same geometric relationship with respect to the sun [147].

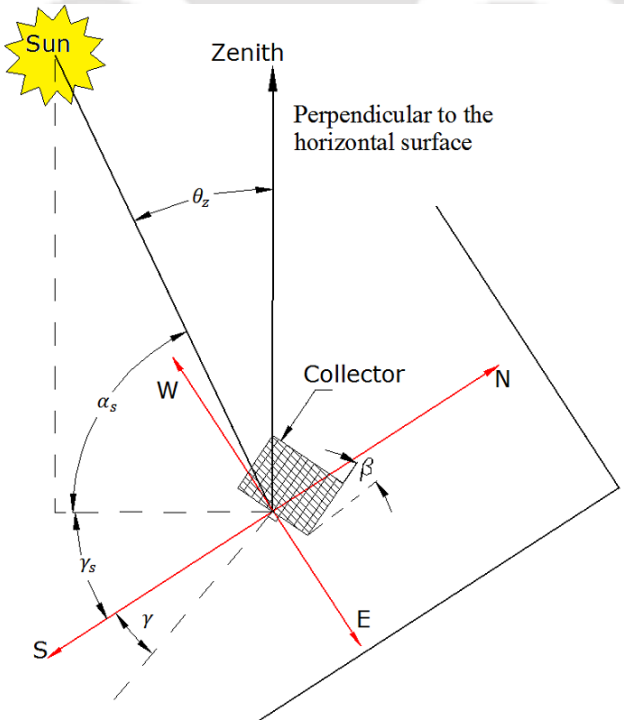

Fig.A. 5.Solar angles [106]

The solar zenith angle (θz) is defined as an angle between sun's rays and a line perpendicular to the horizontal surface at O.

The surface azimuth angle (**γ)** is described as an angle between projections of the line into horizontal plane normal to a given surface and the local longitude meridian. The value of surface azimuth angle is 0^0, positive and negative for south, west and east directions, respectively, and satisfies $-180^0 \leq \gamma \leq 180^0$ [147].

The tilt angle **(β)** or slope is defined as an angle between the surface under consideration and the horizontal plane.

The incidence angle (θ_i) is expressed as an angle between sun's ray and a line, which is normal to a surface. The angle of incidence is related to the latitude (ϕ), declination (δ), the hour angle (ω), tilt angle of the surface (β), and the surface azimuthal angle (γ) as shown on Eq. (A.7) [147].

$$\cos\theta_i = \sin\delta\, sin\,\phi\, cos\beta - sin\delta\cos\phi\, sin\beta\cos\gamma + cos\delta\, cos\phi\, cos\beta\, cos\,\omega + cos\delta\, sin\phi\, sin\beta\, cos\gamma\, cos\omega + cos\delta\, sin\beta\, sin\gamma\, sin\omega \quad \text{(A.7)}$$

If the surface is horizontal (β=0), the angle of incidence is referred as the Zenith angle

$$\cos\theta = \cos z = \sin\delta\, sin\,\phi + cos\delta\, cos\phi\, cos\,\omega \quad \text{(A.8)}$$

Appendix B

Uncertainty Analysis

While measuring various data of experimental results, uncertainties are more likely to occur due to several reasons such as reading, observation, drift and calibration. The uncertainties of the various dependent variables are calculated using the theory of perturbation technique proposed by Kline and McClintok [148]. Suppose a parameter Y depends on the independent variables such as $\vartheta_1, \vartheta_2, \vartheta_3, \ldots\ldots \vartheta_n$, therefore, P can be defined as a function of all the independent variables as per Eq. (B.1)

$$Y = Y(\vartheta_1, \vartheta_2, \vartheta_3, \ldots\ldots \vartheta_n) \tag{B.1}$$

If ΔP is the uncertainty of the results and if $\Delta Y_1, \Delta Y_2, \Delta Y_3 \ldots\ldots \Delta Y_n$ are the uncertainty in the independent variable. Then the total uncertainty of the known parameter (ΔY) in the results can be expressed as per Eq. (B.2).

$$\left[\left(\frac{\partial Y}{\partial \vartheta_1}\Delta\vartheta_1\right)^2 + \left(\frac{\partial Y}{\partial \vartheta_2}\Delta\vartheta_2\right)^2 + \left(\frac{\partial Y}{\partial \vartheta_3}\Delta\vartheta_3\right)^2 + \cdots + \left(\frac{\partial Y}{\partial \vartheta_n}\Delta\vartheta_n\right)^2\right]^{1/2} \tag{B.2}$$

The main dependent parameters which are involved in this study are thermal efficiency of the PTSC, useful heat, liquid fraction, energy stored and energy discharged of the LHS unit. Whereas, the major independent variables are the HTF temperature at the inlet and outlet of the PTSC, the temperature of the absorber tube, ambient air temperature, the mass flow rate of the HTF and solar radiation. On the other hand, the major independent parameter associated the LHS performance study is the temperature, which is measured using K-type thermocouple. As mentioned in section 5.2.3, the thermocouple is calibrated and the obtained maximum average error is ±0.35 ^{0}C. The uncertainty of the mass of the PCM in the LHS is assumed to be 1.5% and other uncertainty of physical variables are show in Table B.1.

Table.B 1

Uncertainty value of physical variables

Equipment	Measured value	Unit	Maximum uncertainity
Thermocouple	Temperature	^{0}C	0.35
Pyranometer	Direct normal irradiation	W/m^2	3
Flow meter	Mass flow rate	Kg/s	0.001
Balance weight	Mass of PCM	%	1.5
Reflector	Area	m^2	0.01

Thermal efficiency of PTSC

The thermal efficiency of the solar air heater is calculated by the equation given below.

$$\eta = \frac{\dot{m}_{HTF} C_p (T_{out} - T_{in})}{A_c \times I_b} \quad \text{(B.3)}$$

Considering C_p as fixed value, the uncertainty for the thermal efficiency ($\Delta\eta$)is determined by the following equation.

$$\Delta\eta = \left[\left(\frac{\partial\eta}{\partial\dot{m}_{HTF}}\Delta\dot{m}_{HTF}\right)^2 + \left(\frac{\partial\eta}{\partial T_{out}}\Delta T_{out}\right)^2 + \left(\frac{\partial\eta}{\partial T_{in}}\Delta T_{in}\right)^2 + \left(\frac{\partial\eta}{\partial A_c}\Delta A_C\right)^2 + \left(\frac{\partial\eta}{\partial I_b}\Delta I_b\right)^2\right]^{\frac{1}{2}} \quad \text{(B.4)}$$

$$\Delta\eta = \pm\sqrt{(21.95 \times 0.001)^2 + (0.157 \times 0.35)^2 + (0.157 \times 0.35)^2 + (1.339 \times 0.01)^2 + (0.0063 \times 3)^2}$$

$$\Delta\eta = \pm 0.084 = 8.4\%$$

Where,

$$\frac{\partial\eta}{\partial\dot{m}_{HTF}} = \frac{C_p.(T_{out} - T_{in})}{A_c \times I_b} = 21.95$$

$$\frac{\partial\eta}{\partial T_{out}} = \frac{\dot{m}_{HTF}.C_p}{A_c \times I_b} = 0.157$$

$$\frac{\partial \eta}{\partial T_{in}} = -\frac{\dot{m}_{HTF}.C_p}{A_c \times I_b} = 0.157$$

$$\frac{\partial \eta}{\partial I_b} = \frac{\dot{m}_{HTF}.C_p.(T_{out} - T_{in})}{I_b^2 \times A_c} = 0.0063$$

$$\frac{\partial \eta}{\partial A_c} = \frac{\dot{m}_{HTF}.C_p.(T_{out} - T_{in})}{A_c^2 \times I_b} = 1.339$$

Liquid fraction

The uncertainty of the liquid fraction of the PCM between the solid and liquid temperature is estimated using the following equation.

$$\theta = \frac{T - T_s}{T_l - T_s} = \frac{T - T_S}{2\Delta T_M} = \begin{cases} 0 & if\ T < T_s \\ 0 - 1 & if\ T_S \le T \le T_l \\ 1 & if\ T > T_l \end{cases} \quad \text{(B.5)}$$

The uncertainty for the liquid fraction of the PCM (Δθ)is given using the following equation.

$$\Delta\theta = \left[\left(\frac{\partial\theta}{\partial T}\Delta T\right)^2 + \left(\frac{\partial\theta}{\partial T_S}\Delta T_s\right)^2 + \left(\frac{\partial\theta}{\partial T_M}\Delta(\Delta T_M)\right)^2\right]^{\frac{1}{2}} \quad \text{(B.6)}$$

$$\Delta\theta = \pm\sqrt{(0.1 \times 0.35)^2 + (-0.1 \times 0.35)^2 + (-0.1 \times 2 \times 0.35)^2}$$

$$\Delta\theta = \pm 0.086$$

Where,

$$\frac{\partial\theta}{\partial T} = \frac{\partial}{\partial T}\left(\frac{T - T_S}{2\Delta T_M}\right) = \frac{1}{2 \times \Delta T_M} = 0.1$$

$$\frac{\partial\theta}{\partial T_S} = \frac{\partial}{\partial T}\left(\frac{T - T_S}{2\Delta T_M}\right) = -\frac{1}{2 \times \Delta T_M} = -0.1$$

$$\frac{\partial\theta}{\partial T_M} = \frac{\partial}{\partial T}\left(\frac{T - T_S}{2\Delta T_M}\right) = -\frac{(T - T_s)}{2 \times (\Delta T_M)^2} = -0.1$$

Energy stored

The uncertainty of the quantity of energy gets stored depends on the uncertainty of temperature difference, liquid fraction and mass. The total heat energy stored in PCM is estimated as per Eq.B.7.

$$Q_{tot} = mC_p(T - T_{ini}) + mL\theta = m\left(C_p\Delta T + L\theta\right) \tag{B.7}$$

The uncertainty of the energy stored is determined as follow.

$$\Delta Q_{tot} = \pm\left[\left(\frac{\partial Q_{tot}}{\partial m}\Delta m\right)^2 + \left(\frac{\partial Q_{tot}}{\partial \Delta T}\Delta(\Delta T)\right)^2 + \left(\frac{\partial Q_{tot}}{\partial \theta}(\Delta\theta)\right)^2\right]^{\frac{1}{2}} \tag{B.8}$$

$$\Delta Q_{tot} = \pm\sqrt{(592.3 \times 0.015)^2 + (125.9 \times 0.35)^2 + (20572.6 \times 0.086)^2}$$

$$\Delta Q_{tot} = \pm 1769KJ = \pm 1.7MJ$$

Where,

$$\frac{\partial Q_{tot}}{\partial m} = \frac{\partial}{\partial T}\left(m\left(C_p\Delta T + L\theta\right)\right) = C_p\Delta T + L\theta = 2.17(136.5 - 27) + 354.7 = 592.3$$

$$\frac{\partial Q_{tot}}{\partial \Delta T} = \frac{\partial}{\partial \Delta T}\left(m\left(C_p\Delta T + L\theta\right)\right) = mC_p = 2.17 \times 58 = 125.9$$

$$\frac{\partial Q_{tot}}{\partial \theta} = \frac{\partial}{\partial \Delta T}\left(m\left(C_p\Delta T + L\theta\right)\right) = mL = 58 \times 354.7 = 20572.6$$

List of Publications

International Journal Papers

1. Berihu Geberyohannes Abreha, Pinakeswar Mahanta and Gaurav Trivedi, **Performance Investigation of lab-scale shell and tube LHS prototype**. Journal of Energy Storage. 2020; 31. (DOI: https://doi.org/10.1016/j.est.2020.101527)
2. Berihu Geberyohannes Abreha, Pinakeswar Mahanta and Gaurav Trivedi, **Thermal performance evaluation of multi-tube cylindrical LHS system**. Applied Thermal Engineering. 2020; 179. (DOI: https://doi.org/10.1016/j.applthermaleng.2020.115743)
3. Berihu Geberyohannes Abreha, Pinakeswar Mahanta and Gaurav Trivedi, T**he effect of finned HTF tubes configuration on the performance of multi-tube shell and tube latent heat storage unit: Numerical investigation** "in Journal of Energy Storage (under revision)"
4. Berihu Geberyohannes Abreha, Pinakeswar Mahanta and Gaurav Trivedi, **Development and performance study of parabolic trough solar collector for solar cooking application** (Submitted to Journal of solar energy)
5. Berihu Geberyohannes Abreha, Pinakeswar Mahanta and Gaurav Trivedi, **Performance investigation of lab scale LHS unit powered by hybrid PTSC and auxiliary energy sources** (Ready for submission)

Conference Papers

1. Berihu Geberyohannes Abreha, Pinakeswar Mahanta and Gaurav Trivedi, ***Numerical Modeling and Simulation of Thermal Energy Storage for Solar Cooking Using Comsol Multiphysics Software." in*** AIP Conference Proceedings **2091**, 020004 (2019); https://doi.org/10.1063/1.5096495
2. Berihu Geberyohannes Abreha, Pinakeswar Mahanta and Gaurav Trivedi, ***Numerical Comparative Study of Thermal Energy Storage for Solar Cooking.*** National Conference on

Waste to Energy 2018 on 28-29th December 2018 December 2018 at Indian National Institute of Technology (NIT) Mizoram Aizawl), Mizoram, India.

3. Berihu Geberyohannes Abreha, Pinakeswar Mahanta and Gaurav Trivedi, ***Performance improvement techniques in shell-and-tube type of latent heat storage unit.*** International Conference on Recent Trends in Developments of Thermo-fluids and Renewable Energy (TFRE-2020) 24-26th June 2020 (Postponed) in Indian National Institute of Technology (NIT) Arunachal Pradesh, Yupia, India